Title	Tunable properties of carbon nanotube forest metamaterials -Growth control and fine patterning-
Author(s)	MICHAL PANDER, Adam
Citation	高知工科大学, 博士論文.
Date of issue	2017-03
URL	http://hdl.handle.net/10173/1509
Rights	
Text version	ETD

Tunable properties of carbon nanotube forest metamaterials

Growth control and fine patterning

by

Adam Michal Pander

Student ID Number: 1186001

A dissertation submitted to the
Engineering Course, Department of Engineering,
Graduate School of Engineering,
Kochi University of Technology,
Kochi, Japan

in partial fulfillment of the requirements for the degree of
Doctor of Engineering

Assessment Committee:
- Supervisor: Hiroshi Furuta
- Co-Supervisor: Akimitsu Hatta
- Co-Supervisor: Chaoyang Li
- Committee Member: Mamoru Furuta
- Committee Member: Hideo Kohno

March 2017

(Intentionally left blank)

Abstract

The subject of this work is a fabrication of carbon nanotube (CNT) forest metamaterials, by precise growth control of highly oriented, vertically aligned CNTs. In the present study, a systematic tuning of properties of CNT forest is presented in order to fabricate CNT metamaterials.

In the first part of the thesis, a Taguchi method of designing experiments was applied to optimize a formation of iron catalyst particles during the annealing process. For the sake of obtaining a uniform single-walled CNT (SWNT) forest, an analysis of an average roughness and a size of particles was carried out. The parameters optimized during the experiment were: annealing time, hydrogen flow rate, temperature, and argon flow rate. Plots of signal-to-noise (SN) ratios of obtained results showed that temperature and annealing time had the highest impact on the average roughness and the size of Fe particles. Moreover, a physical model of the catalyst formation process was provided for the first time with the support of the Taguchi statistical method, proving that Ostwald ripening and subsurface diffusion of catalyst atoms into AlO_x support were basic mechanisms responsible for the formation of particles. Further analysis of the results confirmed that temperature and annealing time were main parameters inducing mechanisms responsible for the reduction of the size of particles, and were also supported by additional H_2/Ar annealing atmosphere. For the final evaluation of the results, a verification experiment was conducted, in which CNT forest was grown using the optimized growth conditions, and its properties were compared to the CNT forest from before the optimization. The average diameter of CNTs was decreased by 67%, from 9.1 nm (multi-walled CNTs - MWNTs) to 3.0 nm (SWNTs).

In the second part, the Taguchi approach was utilized to tune optical properties of CNT forest by decreasing the total optical reflectance, which was required for metamaterial application. The annealing parameters optimized previously remained unchanged, while the other parameters related to catalyst deposition and CNT growth were optimized. In this part of the study acetylene gas flow rate, Fe catalyst film thickness, substrate polarization potential (bias) during AlO_x buffer layer sputtering, and acetylene/hydrogen gasses flow ratio

were tuned. Based on the SN ratio plots, the highest impact on the final results of total optical reflectance was observed for bias during the deposition of the buffer layer and the thickness of the catalyst. The introduction of bias during the deposition of AlO_x layer changes the inner structure of the film and affects the process of Fe catalyst formation, resulting in varying size and density of Fe particles. On the other hand, the higher thickness of Fe catalyst supplies more material during the process and allows the formation of a larger number of particles on the surface, improving the density of CNT forest. A verification experiment was conducted and it yielded a 45% decrease in the reflectance, to the lowest value (0.077%) ever reported for a thin CNT forest films with relatively low height (~21 μm). The effect of the structure of the CNTs was studied by obtaining Raman spectra of the grown CNT forest. It was found that for a homogeneous, vertically aligned CNT forest, the effect of the type of CNT (SWCNTs, DWCNTs, or MWCNTs) was insignificantly small and could be neglected. The analysis of the influence of the density and alignment of CNTs on the total optical reflectance was investigated for the first time and showed a significant impact of structural parameters of CNT forest on the total reflectance.

Future applications of CNT metamaterials require a low-temperature growth on various substrates. In the third part of the research, the low-temperature growth of CNTs on Al foil was presented. The growth of CNTs requires treatment of the surface to remove contaminations from the substrate. It was confirmed that both the usage of AlO_x buffer layer, and hydrogen treatment of the surface before deposition of Fe catalyst, have a positive effect on the growth of CNTs. The influence of hydrogen annealing time on the growth of CNTs was investigated. Moreover, with the introduction of water vapor during the CVD process (water-assisted CVD), the height improvement of grown CNTs from 14.7 μm (w/o H_2O) to 24.4 μm (0.07 sccm H_2O) for 10 minutes growth was observed. The investigation of the thickness of the catalyst showed that a thickness of 1.0 and 1.2 nm were the most suitable for low-temperature growth. The water-assisted CVD growth of CNTs resulted in the increase of the catalyst activity up to 120 minutes.

A new method of uniform and fine patterning of CNT forest nanostructures for metamaterials, utilizing a focused ion beam (FIB) with additional secondary etching step,

was developed for the fabrication range of hundreds of nanometers to several micrometers. The influence of FIB etching depth on the morphology of catalyst surface and growth of CNTs was investigated. By removing redeposited material and decreasing the thickness of Fe catalyst using FIB secondary etching method, fine patterning of CNT forest was proved. The influence of the FIB processing parameters on the morphology of the catalyst surface and the growth of CNT forest was investigated. The results of applying the FIB secondary etching method included the removal of redeposited material, the decrease of the average surface roughness (from 0.45 nm to 0.15 nm), and the decrease in thickness of the Fe catalyst. With a FIB patterning depth of 10 nm and a secondary etching of 0.5 nm, a catalytic growth of high-density CNT forest structures as small as about 150 nm on pre-deposited catalyst film was achieved. Additionally, the influence of FIB etching depth on the morphology of catalyst surface and growth of CNTs was studied.

In the final part of the work, infrared (IR) properties of various CNT forest patterns for metamaterials, prepared on the predeposited catalyst, were presented for the first time. The bulk properties of patterned self-standing uniform CNT forest in the IR region were investigated. The IR reflectance of CNT metamaterial patterns was presented, showing high dependence on shape, height, alignment and pitch of the patterns. Furthermore, the trail of tuning of a magnetic resonance of CNT patterns was presented. The increase in height of patterned CNT forest reduced the reflectance. It was confirmed that the absorption of infrared radiation was increased by the formation of dip shape as resonator role in SRR patterns, not by the total absorption area ratio covered by CNTs. The tuning of the magnetic resonance of CNT patterns showed insignificant changes in the FT-IR reflectance spectra. Furthermore, the decrease of the spacing between the patterns caused the reduction of reflectance, and the redshift of the phase of oscillations was observed. Apart from that, the control of the alignment from horizontal to vertical resulted in the change of the absorbance and significantly changed the phase of oscillations, due to the changes in the propagation of an electromagnetic wave through the designed CNT structures composed of horizontally aligned CNTs.

In conclusion, the optimization process allowed a growth of a high-density and high-aligned SWNT forest with very low reflectance which was required for the successful fabrication of metamaterials. By applying the FIB patterning process followed by the newly developed FIB secondary etching method, the uniform and fine fabrication of CNT metamaterial nanostructures was possible, in various sizes, shapes, and diversity. Finally, the investigation of IR properties of patterned SWNT forest for metamaterials showed the influence of shape, height, alignment, spacing, and magnetic resonance tuning on the electromagnetic response in the IR regime, proving a successful fabrication of CNT metamaterials.

Acknowledgements

Foremost, I would like to acknowledge my supervisor *Assoc. Prof. Hiroshi Furuta* for having faith in my abilities and giving me the chance to study at Kochi University of Technology. I would like to express my gratitude to him for guiding me, providing me with valuable feedback that helped me deal with many challenging problems as well as for encouragement and support in times of difficulty.

I would like to express my very sincere gratitude to *Prof. Akimitsu Hatta* and *Prof. Chaoyang Li* for being very good advisors during the course of study. Their ideas and comments very indispensable and allowed me to improve my work many times.

I would like to thank *Prof. Hideo Kohno* and *Prof. Mamoru Furuta*, for valuable feedback during the preparation of this thesis. I would also like to thank *Prof. Keisuke Takano* and *Prof. Makoto Nakajima* from Osaka University for great support and guidance during the study. I am thankful *Prof. Masahiko Isobe* and *Prof. Ryo Kimura*, for their great help, advice, and support during the course of study. A special gratitude to *Ms. Ai Nakayama* and *Ms. Satomi Ueno*, for their help and contribution to my laboratory life. I would also like to acknowledge *Mr. Shinnosuke Inami* and *Dr. Gang Xie* from Aishin Seiki Co., Ltd., for their scientific and financial support.

I am thankful to all the members of the Hatta-Furuta laboratory for their assistance during my research. I am especially thankful to *Dr. Jun-Seok Oh*, for his countless advice, ideas, and guidance. Big appreciation to my fellow doctoral students *Udorn Junthorn*, *Vladislav Gamaleev*, and *Md Abdullah Al Mamun* for being great friends during the last years. I'm also thankful to my Japanese friends, *Hirofumi Koji*, *Kouki Ishimoto*, *Tanami Sota*, and *Hiroki Miyaji*, for many interesting discussions and relaxing times. Their presence in the laboratory always introduced a spark of happiness to my daily life.

This research was supported by JSPS KAKENHI Grant (no.24560050) and the joint research project of the Institute of Laser Engineering, Osaka University (contract subject 2016B1-FURUTA).

I am also very thankful to the staff members of International Relations Division for their support, hard work and commitment. I'm especially grateful to *Kimiko Sakamoto, Mari Yamasaki, Miki Okauchi*, and *Saki Hamamura* for being great help and support during my study. Nevertheless, I am also grateful to *Prof. Shinichiro Sakikawa* for his time, guidance, big help and countless advice regarding Japanese and university life.

I had a chance to meet many extraordinary and interesting people, some of whom became my very close friends. First of all, I would like to thank *Peter, Sergey, Michelle, Rika, Erina, Mitchell, Hiyori* and *Yuka* for the introduction to the Japanese culture and life. Also big thanks to *Vlad, Ono, Rebecca*, and *Cristina*, for being great friends both in the moments of happiness and trouble. The time spent with you was a great experience and became a valuable chapter of my life. I would also like to express my gratitude to *Thai community in KUT*, *Japanese residents of International House*, *Yuuki Izumiya*, and *countless others* for making my life more interesting each time I meet you. And finally, I would really like to thank *Murasaki family* from Kanazawa, for their hospitality and all the good memories we have made together.

I would also like to thank my *Polish friends*, with whom, despite the big distance, I was able to keep contact. Their endless interest and support were invaluable to me during the last 3 years I have spent in Japan.

Finally, I take this opportunity to express my profound gratitude to my family for the unconstrained encouragement, support and truthful love they have shown me all these years. To my *mom*, who always supported me and always had good advice up her sleeve, to my *sister* who, despite the big distance, became closer to me. Finally, to my deceased *dad* who could not see this moment of my life, but would be proud.

To you all, I dedicate this work.

Disclaimer

Some passages in this work have been quoted *verbatim* from the previous publications and work of the author (listed according to the state in time of writing the thesis):

Journal Papers:

1) Adam Pander, Hiroshi Furuta, Akimitsu Hatta, *"Optimization of catalyst formation conditions for synthesis of carbon nanotubes using Taguchi method"*, Applied Surface Science **371** (2016) 425-435. DOI: 10.1016/j.apsusc.2016.02.216
2) Adam Pander, Keisuke Takano, Makoto Nakajima, Akimitsu Hatta, Hiroshi Furuta, *"Infrared properties of patterned CNT forest for metamaterials"* in Proceedings of 2016 IEEE Nanotechnology Materials and Devices Conference (NMDC) 1–2 (IEEE, 2016). DOI: 10.1109/NMDC.2016.7777129
3) Adam Pander, Hiroshi Furuta, Akimitsu Hatta, *"FIB secondary etching method for fabrication of fine CNT forest metamaterials"*, accepted to Nano-Micro Letters – March 16th 2017.
4) Adam Pander, Keisuke Takano, Makoto Nakajima, Akimitsu Hatta, Hiroshi Furuta, *"Infrared properties of patterned CNT forest for metamaterials"*, submitted to Nanoscience and Nanotechnology Letters.
5) Adam Pander, Kouki Ishimoto, Akimitsu Hatta, Hiroshi Furuta, *"Significantly low reflectance in thin CNT forest film tuned by the Taguchi method"*, submitted to Journal of Material Science.

Conference Publications:

1) Adam Pander, Hiroshi Furuta, and Akimitsu Hatta, *"Optimization of the synthesis parameters of Carbon Nanotubes (CNTs) forest using the Taguchi Method"*, The 48th Fullerenes-Nanotubes-Graphene General Symposium (FNTG 48), Tokyo (Japan), February 21st-23rd, 2015.
2) Adam Pander, Kouki Ishimoto, Hiroshi Furuta, and Akimitsu Hatta, *"Tuning of optical properties of carbon nanotube (CNT) forest grown using Taguchi method"*, The

fifteenth International Conference on the Science and Applications of Nanotubes (NT 15), Nagoya (Japan), June 29th –July 3rd, 2015.

3) Adam Pander, Keisuke Takano, Makoto Nakajima, Akimitsu Hatta, and Hiroshi Furuta, *"Infrared properties of patterned CNT forest for metamaterials"*, 11th IEEE Nanotechnology Materials and Devices Conference (NMDC 2016), Toulouse (France), October 9th-12th, 2016.
4) Adam Pander, Hiroki Miyaji, Akimitsu Hatta, and Hiroshi Furuta, *"Water-assisted low-temperature growth of carbon nanotubes on aluminum foil"*, CNT25 - INTERNATIONAL SYMPOSIUM ON CARBON NANOTUBE in Commemoration of its Quarter-Century Anniversary, Tokyo (Japan), November 15th-18th, 2016.
5) Adam Pander, Kouki Ishimoto, Hiroshi Furuta, and Akimitsu Hatta, *"Optimization of Carbon Nanotubes properties using the Taguchi approach"*, Nanotech Symposium 2015, Kochi (Japan), November 14th, 2015.
6) Adam Pander, Keisuke Takano, Makoto Nakajima, Akimitsu Hatta, and Hiroshi Furuta, *"FIB fabrication and infrared properties of patterned CNT forest"*, Nanotech Symposium 2016, Kochi (Japan), November 12th, 2016.
7) Adam Pander, Kouki Ishimoto, Akimitsu Hatta, and Hiroshi Furuta, *"Taguchi method in optimization of optical properties of CNT forest"*, レーザー研シンポジウム, Osaka (Japan), April 19-20th, 2016.

All of the quoted sources were originally written by the author of this thesis.

Table of Contents

List of Figures

List of Tables

Abbreviations

CNT	- carbon nanotube
SWNT	- single-walled carbon nanotube
DWNT	- double-walled carbon nanotube
MWNT	- multi-walled carbon nanotube
NIM	- negative index material
CVD	- chemical vapor deposition
PECVD	- plasma enhanced chemical vapor deposition
FIB	- focused ion beam
EB	- electron beam
TEM	- transmission electron microscope
SEM	- scanning electron microscope
AFM	- atomic force microscope
DFM	- dynamic force microscopy
FE-SEM	- field emission scanning electron microscope
FT-IR	- Fourier transform infrared
NIR	- near infrared
UV	- ultraviolet
SRR	- split ring resonator
ASR	- asymmetric split resonator
EM	- electromagnetic
RF	- radio frequency
MOS-FET	- metal-oxide-semiconductor-field-effect-transistor
DOE	- design of experiment
SN	- signal-to-noise

Chapter 1. Introduction

1.1. Background

Carbon nanotubes (CNTs), due to their unique structure and extraordinary physical, electrical and optical properties, have received major attention since the first discovery by Iijima [1] in 1991. The bulk structure of vertically aligned, high-density CNTs (so-called CNT forest) can provide CNTs with preferable length, diameter, and structure for mass production of CNTs [2,3]. Physical properties and the structure of CNTs directly influence mechanical, electrical, thermal and optical properties of CNT forests [4,5].

It was reported that CNTs behavior is similar to nearly ideal one-dimensional nano-rod antennas with a diameter of a several nanometers and length from tenths of nanometers to many micrometers [6]. Furthermore, the behavior of a single-walled CNTs (SWNTs) is similar to direct gap semiconductors with absorption spectra dominated by exciton lines [7]. Based on experimental observations, the nonlinear optical behavior of CNTs [8] is related to a high third-order susceptibility with sub-picosecond recovery time [9,10], in which the source of the nonlinearities is an effect of the saturation of the resonant excitation lines and allows many various applications, such as light sources in nanoscale, photodetectors, photovoltaic devices and ultrafast lasers [11,12].

Various structures of CNTs are utilized in many electronic applications such as nano-electronic devices [13], electrodes for MOS-FETs (metal oxide semiconductor field effect transistors) [14], a wiring material for large-scale integrator (LSI) interconnects [15], actuators and polymeric composites for electronic devices [16] or high emission current density emitters [17]. Recently, electrical and optical properties of CNTs are utilized in various types of solar cells, where CNTs act as electrodes [18,19], counter electrodes [20,21], active layers in solar cells [22] and conduct scaffolds for semiconducting materials used in solar cells [23]. A large number of recently developed CNT-based devices allow us to assume that CNTs can also be applied in wide-spreading fields for the successful development of new applications.

At the same time, a relatively new research field of “metamaterials” emerged. Metamaterials are artificial materials engineered to obtain properties that do not exist in nature [24] and acquire their properties from embedded subwavelength structures grouped together in order to manipulate electromagnetic waves [25,26]. Presented in 2000, by Pendry *et al.* [27], the study of the perfect lens composed of metamaterials, followed by fabrication of first negative index metamaterials in terahertz regime in 2001 by Shelby *et al.* [28], resulted in rapid development of applications [29–35]. Finally, it opened an interdisciplinary research field of nano-scale circuits and material sciences.

1.2. Motivation and research issue

Electromagnetic properties of metamaterials are derived from the shape and size of designed structures of an electromagnetic circuit, and also from the properties of the material that consist of those structures. Currently, the development of metamaterials is limited by the design and fabrication methods. However, by utilizing anisotropic materials, like CNTs, which can produce negative refraction due to their chirality, those limitations may be overcome. High shielding effectiveness accompanied by a high dielectric constant of SWNTs [36,37] can be tuned by control of growth parameters and post-processing operations such as chemical treatment or molecular functionalization [38], which is impossible with conventional materials like metals. Due to this, unique structure and properties of CNTs influence the performance of metamaterials and can be used for the design of metamaterials.

First trials allowed the utilization of the extraordinary properties of CNT forest in the fabrication of metamaterials in the terahertz regime [38,39]; however, only in the form of slits, which were cut in thin CNT films. To fully utilize the electromagnetic properties of CNT forest originated from high alignment and density, a different approach for the metamaterial fabrication is required.

Most of the metamaterial designs presented so far are in the form of Split Ring Resonators (SRRs), which can be described as an LC circuit antenna of the EM wave [23]. It is known that the LC resonance frequency scales inversely with the lateral size of SRR structures. For shorter wavelengths, obtaining high-resolution patterns on the large area samples is quite challenging. One of the ways to solve this issue is to reduce the total size of

the patterned area of metamaterials and measure their optical properties at a smaller scale of the patterned area.

There are several reasons why the successful fabrication of CNT metamaterials is complicated and was chosen as the main target of research in this thesis. For the manufacturing of electromagnetic metamaterials [16], [17] in a wide range of radiation, the successful development of following issues has to be achieved:

- The structure control of the diameter of CNTs (1 – 100 nm) and height of CNT (10 nm – 10 µm) is not a trivial task due to a high number of process parameters influencing the growth process. There are many growth methods; however, the future applications have to be taken into consideration. Furthermore, for the application of metamaterials, the precise control of the uniformity and quality of SWNTs is crucial. Also, to fully utilize the properties of CNTs in metamaterials, precise control of growth height is required.
- The structure control of the optical properties of CNT forests is required for metamaterials. For various applications, the size of metamaterial structures will differ, requiring the scaling of the growth height at the same time. The growth height of the CNT forest is one of the most important factors, which results in the increase of the absorbance of an electromagnetic wave in the CNT forests. For the optical or infrared regime, reduction of the growth height is desired while, at the same time, maintaining high absorbance in order to effectively interact with electromagnetic radiation and allow the usage of the thin CNT film.
- The fabrication of CNT forests for metamaterial application, in dependence of the application, will require direct growth of CNTs on a desired part of the device. The growth of CNT forests requires high temperature in all conventional methods, causing limitation in the applicability of the various substrates. For that purpose, the development of low-temperature growth of CNTs is necessary to fulfill the need for the future development of metamaterials for different applications.

- The design of an electromagnetic circuit of metamaterial patterns and the precise patterning process of CNT forest into the metamaterial structures are both critically important for the CNT forest metamaterials with a required specification. The nanoscale patterning of CNT forest for optical and IR metamaterial application has not been presented before, so both the design and the fabrication method should allow the possibility of testing of various designs. An appropriate design or a suitable combination of metamaterial circuits will allow a verification of the electromagnetic properties of fabricated CNT metamaterials, while the suitable choice of the fabrication method will allow precise fabrication of CNT metamaterial patterns. In the nanoscale, the fabrication method may influence the catalytic growth of CNTs, and these issues should also be considered during the patterning.

1.3. Research objectives

The main objective of this dissertation the successful fabrication of the electromagnetic metamaterials, composed of CNT forest meta-atoms, by precise growth control of highly oriented vertically aligned CNT forests. The issues listed in the previous section are addressed as following:

- The growth of single-walled carbon nanotubes (SWNTs) – a precise control of growth parameters in order to study the conditions of formation of catalyst particles during the growth process. The properties that are originated from SWNTs structure are required. For successful fabrication of the electromagnetic metamaterials, properties directly related to the structure of SWNTs have to be controlled.

- The improvement of the total optical reflectance of thin CNT forest film – the precise control of growth parameters responsible for high absorption is necessary. High absorption and behavior close to a blackbody is required for the fabrication of metamaterials.

- The development of low-temperature growth of CNTs – for future applications in photonics and electronics, direct growth of CNTs on the fabricated parts of devices is required.

- The development of a highly precise fabrication method of CNT forest for metamaterials – in order to fabricate nanostructures with high precision and for optical and IR regime.
- The investigation of the electromagnetic behavior of fabricated CNT metamaterials – in order to evaluate the properties, performance and applicability of patterned CNT forest into future applications.

1.4. Organization of this thesis

The structure of the thesis is as follows:

Chapter 1 introduces the main motivation and issues in the research field of CNT metamaterials. The requirements for the current research are presented and explained. The research objectives are demonstrated.

Chapter 2 introduces the detailed background of the presented research. The introduction to the carbon nanotube and metamaterial field is presented. A literature review of the most relevant experimental and theoretical studies in those fields is demonstrated.

Chapter 3 describes methods and experimental equipment used throughout the research. The Taguchi method of designing the experiment is presented in detail. Furthermore, the methods of catalyst deposition and carbon nanotube growth are described. Finally, the introduction to the measurement methods, which were used during the research, is presented with annotations to the conducted part of the research.

Chapter 4 presents the study on the catalyst formation condition optimized by the Taguchi method in order to decrease the diameter of CNTs and achieve growth of SWNTs. Short introduction and objectives are described and followed by a short description of methods used only in this chapter. Furthermore, the detailed study of the statistical approach to the plan of the experiment is discussed. The optimum values of optimized parameters, sensitivity analysis of parameters and analysis of mutual interaction are presented. Moreover, the model of the formation of catalyst particles is proposed and supported by the statistical analysis of the Taguchi method. The improvement of the optimization is presented.

Chapter 5 provides the investigation of the tuning of the total optical reflectance of thin CNT forest film by the Taguchi method. Introduction, objectives, and used methods are described and followed by the results of the optimization process. The optimum values of parameters, sensitivity, and interaction analysis are presented. The improvement of the reflectance, comparing to previous experiments, is defined. The elaboration over structural parameters of CNT forest (density, alignment, etc.) is performed in order to define factors crucial for obtaining low reflectance CNT forest.

Chapter 6 presents the investigation of the low-temperature water-assisted growth of CNTs on the metallic (Al) substrates. The introduction, objectives, and experimental methods are described. The investigation of the influence of the annealing atmosphere and the presence of AlO_x support layer on the catalyst is performed. Comparison of the growth of CNTs with and without hydrogen pretreatment applied before catalyst deposition is presented. In order to optimize the CNT growth, the study of annealing time, the second most important parameter after temperature, is presented. Finally, the influence of the water vapor flow on the height of CNTs, in dependence on the catalyst thickness is presented and discussed. The activity of the catalyst particles during the water-assisted CVD process is studied.

Chapter 7 provides the study over a newly developed FIB secondary etching method for fine fabrication of CNT metamaterial patterns. The introduction, objectives, and explanation of method are provided. The influence of the FIB patterning depth and the FIB secondary etching depth on the growth of CNTs in the fabricated patterns is studied. Furthermore, the investigation over the influence of FIB fabrication on the surface of the catalyst, before the CNT growth is studied. The model of the catalyst redeposition and various effects of cleaning are discussed.

Chapter 8 presents for the first time the infrared properties of patterned CNT forest for metamaterials. A brief introduction, objectives, and the experimental methods are described. The study over the infrared properties of bulk CNT forest and patterned CNT forest is presented. The effect of the height of CNTs, shape of patterns, spacing, alignment of CNT, and magnetic resonance tuning parameters on the IR spectra are presented and discussed in detail. The metamaterial response in presented structures is studied.

Chapter 9 summarizes the main achievements drawn from the research and discusses future research recommendations, which could develop the research of CNT metamaterials into the direction of new applications.

Chapter 2. Research background

2.1. Carbon nanotubes

2.1.1. Introduction

Carbon ($^{12}_{6}C$) is a polyatomic nonmetal which belongs to group 14 of the periodic table of elements with an atomic number of 6 and a mass number of 12. Carbon atoms have four valence electrons, resulting in the $2s^2\ 2p^2$ electron configuration which allows the formation of covalent chemical bonds. The electronegativity of carbon in the Pauling scale is 2.55.

Carbon is one of the most abundant elements; 4th most abundant in the universe and 15th in the Earth's crust. The very high abundance of carbon is related to two main properties of the element. First of all, carbon shows the possibility of creating simple and complicated compounds which are built only from carbon atoms, and the high durability of such compounds is related to high bonding energy between carbon atoms. The second important property is the possibility of creating double and triple bonds between carbon atoms, increasing the number of possible reactions.

Carbon isotopes possess atomic nuclei that contain six protons and a number of neutrons, varying from 2 to 16. In nature, there are 15 carbon isotopes with the most common being ^{12}C, ^{13}C, and ^{14}C. The stable ^{12}C isotope is the most common, forming 98.93% of the carbon on Earth, while the other stable ^{13}C isotope forms around 1.07% carbon compounds. On the other hand, the non-stable ^{14}C isotope is formed in the upper atmosphere by thermal neutrinos from cosmic radiation, and after being transported to the surface of Earth it is absorbed by biological material. The very long half-life of 5700 years for ^{14}C isotope allows the radiometric dating of biological material to identify the age of samples. Other isotopes worth mentioning are ^{8}C and ^{19}C. The ^{8}C isotope has the shortest lifespan due to proton emission and alpha decay, resulting in a half-life of 1.98739×10^{-21} s. On the other hand, the ^{19}C isotope possesses a radius of the nucleus larger than it would be expected for a sphere of constant density, and this property is called a nuclear halo.

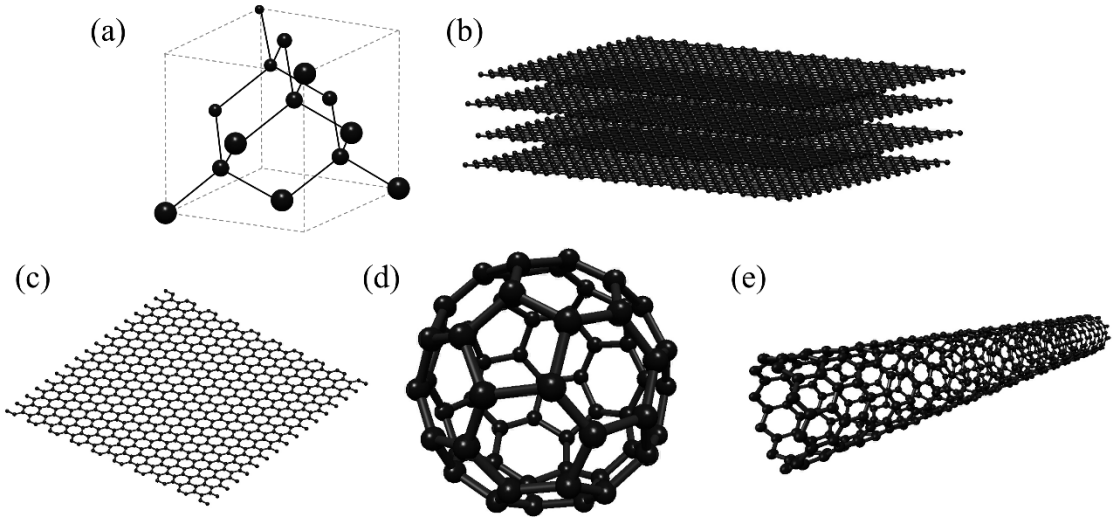

Figure 2.1. Allotropes of carbon: (a) diamond, (b) graphite, (c) graphene, (d) fullerene C60, and (e) carbon nanotube.

Due to the short life of carbon in atomic form, the stabilization of carbon occurs in multi-atomic structures, in various physical forms - allotropes. In allotropes, the whole structure is made of the same atoms, so the properties of the allotrope are originated from the same atoms joined together and aligned in the bulk structure. The first of allotropes – diamond (Fig. 2.1(a)), is well known for its very high hardness and dispersion of light. In diamond, each carbon atom is tetrahedrally bonded to four other carbon atoms by covalent bonds in the sp^3 hybridization of the electron configuration, forming the diamond lattice as a variation of the face-centered cubic structure. Diamond exhibits the highest hardness of all known materials, very high thermal conductivity of 900 – 2320 $Wm^{-1}K^{-1}$, wide bandgap of 5.5 eV, high optical dispersion [40], and insulating electric properties. The other commonly known carbon allotrope – graphite (Fig. 2.1(b)), due to altered structure, exhibits different properties. The structure of graphite is composed of individual graphene layers, organized in the hexagonal crystal. Carbon atoms in each layer are covalently bonded with a distance of 0.142 nm, while each layer is bonded by weak van der Waals bonds with a distance of 0.335 nm. Compared to diamond, graphite exhibits very low hardness, the thermal conductivity of 140 – 500 $Wm^{-1}K^{-1}$ along the layer axis and 3 – 10 $Wm^{-1}K^{-1}$ perpendicularly to the layers [41], and the band gap of -0.04 eV, which makes graphite a relatively good electrical conductor. The fabrication of single graphene sheets (Fig. 2.1(c)) was achieved only in 2004 by Novoselov *et al.* [42],

resulting in an intense investigation of 2D materials. In 1985, fullerene structure (Fig. 2.1(d)) as an allotrope of carbon was discovered by Kroto *et al.* [43]. First fullerene C_{60} was composed of 60 carbon atoms arranged in 12 pentagons and 20 hexagons, in the shape of a "soccer ball" with the typical size of 0.7 nm in diameter. Later on, the formation of various sizes of fullerenes was observed, e.g. C70, C76, C82, etc. Finally, in 1991, based on the work of Iijima [1], another carbon allotrope was defined – carbon nanotube (Fig. 2.1(e)).

2.1.2. Discovery

For researchers, the discovery of carbon nanotubes is strictly related to work published by Sumio Iijima in 1991 [1], in which the growth of helical carbon structures was presented. Despite the significant influence of this work for the current development of carbon nanotube field, the history of this extraordinary material starts in the 1950s. The first work related to carbon nanotubes was published in 1952 by Radushkievich and Lukyanovich [44]. In their study, the first micrographs of graphitic hollow tubular carbon fibers of 50 – 100 nm diameter prepared by thermal decomposition of carbon monoxide on iron catalyst at 600°C were presented. The encapsulation of iron carbides in the tips of fibers was observed and this led to the conclusion that the dissolution of carbon in iron caused the formation of iron carbides and further carbon deposition resulted in the formation of graphene layers on the filament. In the following year, a study of carbon nanofibers grown from the reaction of CO and Fe_2O_4 at 450°C was presented by Davis *et al.* [45]. In their work, the investigation of carbon fibers formation showed that the iron, or iron carbide catalyst, was formed on the surface of the iron oxide in the form of a speck which gave origin to a carbon filament growth with a diameter of 10 – 200 nm. Moreover, the tip based mechanism of growth of carbon threads was proposed. In 1955, Hofer *et al.* reported a very similar growth mechanism of carbon nanofibers [46]. In 1959, the observation of growth of nanoscale tubular carbon fibers from the decomposition of n-heptane on iron at 1000°C was reported by Hillert and Lange [47]. In 1971, Lieberman and *et al.* reported growth of various graphitic like fibers in three different shapes: tubular, twisted, and balloon like [48]. The analysis of the TEM images and diffraction data confirmed the existence of MWNTs in the obtained samples. In the 1970s a lot of research was done independently by Endo and Baker for the purpose of synthesis and study of tubular fibers of multi-layered carbon. One of the most important works in that

period was presented in 1976 by Endo *et al.* in which the growth of carbon fibers of nanometer diameter was achieved by the CVD method, by pyrolyzing a mixture of benzene and hydrogen at 1100°C. In the same work, the study of nanofibers in a shape of hollow tubes was conducted [49]. In 1985, the other carbon allotrope – fullerene was discovered by Kroto *et al*. [43]. In 1987, the U.S. patent for graphitic hollow core "fibrils" was issued for H. Tennent [50]. In his work, the carbon fibrils of 3.5 – 70 nm diameter and length of hundreds of nanometers were synthesized on a metal catalyst. Moreover, as mentioned at the beginning of this chapter, nanotubes were synthesized by arc discharge method by Iijima. In his work, the crystal structure of hollow carbon molecules was determined for the first time in the soot after the arc discharge. This work became the milestone in the research and is often referred to as the moment of the discovery of carbon nanotubes. Finally, the first single-walled CNTs were discovered independently by Iijima *et al.* [51] and Bethune *et al.* [52] in 1993, together with the introduction of methods of synthesis using transition-metal catalysts.

2.1.3. Types of carbon nanotubes

Since the first presentation of carbon nanotubes, two main types were distinguished: multi-walled carbon nanotubes (MWNTs) and single-walled carbon nanotubes (SWNTs). Sometimes, as a separate group, a type of MWNTs build of 2 graphene sheets – double-walled carbon nanotubes (DWNTs) are distinguished.

2.1.3.1. MWNTs

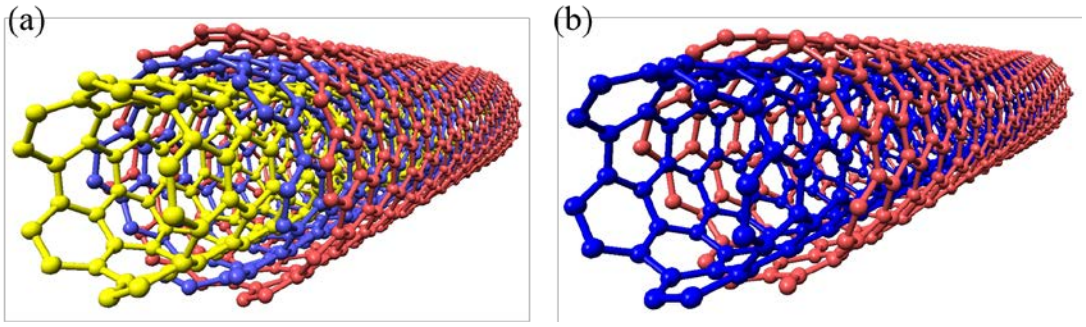

Figure 2.2. (a) Multi-walled and (b) double-walled carbon nanotube.

The structure of MWNTs can be modeled by rolling several graphene layers into a concentric seamless tube, as shown in Figure 2.2(a). The number of the walls usually varies

from 2 to 25 or more, with a diameter of tenths of nanometers. The formation of MWNTs can be described by two different models, the so-called Russian Doll model, and the Parchment model. In the Russian Doll model, the sheets of graphene are organized in the form of concentric tubes, where within a wider SWNT, the smaller SWNT can be found. The distance between each layer of the graphene (wall) is slightly bigger than in graphite, about 3.3 Å, which suggests a different mechanism of layer-stacking. The Parchment model, suggested in 1960 for carbon fibers to explain their cylindrical structure, assumes that graphene sheets scroll to form concentric cylinders.

As mentioned in chapter 2.1.3, DWNTs (Fig. 2.2(b)) are also included in the family of MWNTs. The morphology and properties of DWNTs are similar to the properties of SWNTs, while chemical properties for various applications are improved. DWNTs are especially useful during the functionalization processes, in order to obtain new properties to CNTs. During functionalization, some C=C bonds in SWNTs may break, resulting in the generation of holes in the CNT structure. On the other hand, the modification of DWNTs is applied only to the outer wall and allows preservation of the mechanical and electrical properties of CNT.

2.1.3.2. SWNTs

SWNTs are built of a one-atom-thick carbon sheet as shown in Figure 2.3. The synthesis of SWNTs can be conducted by chemical vapor deposition (CVD) [49], arc discharge [51] or disproportionation of carbon monoxide [53]; however, the most commonly used are CVD methods [54]. The typical diameter of SWNTs is below 2 nm, with length up to several centimeters.

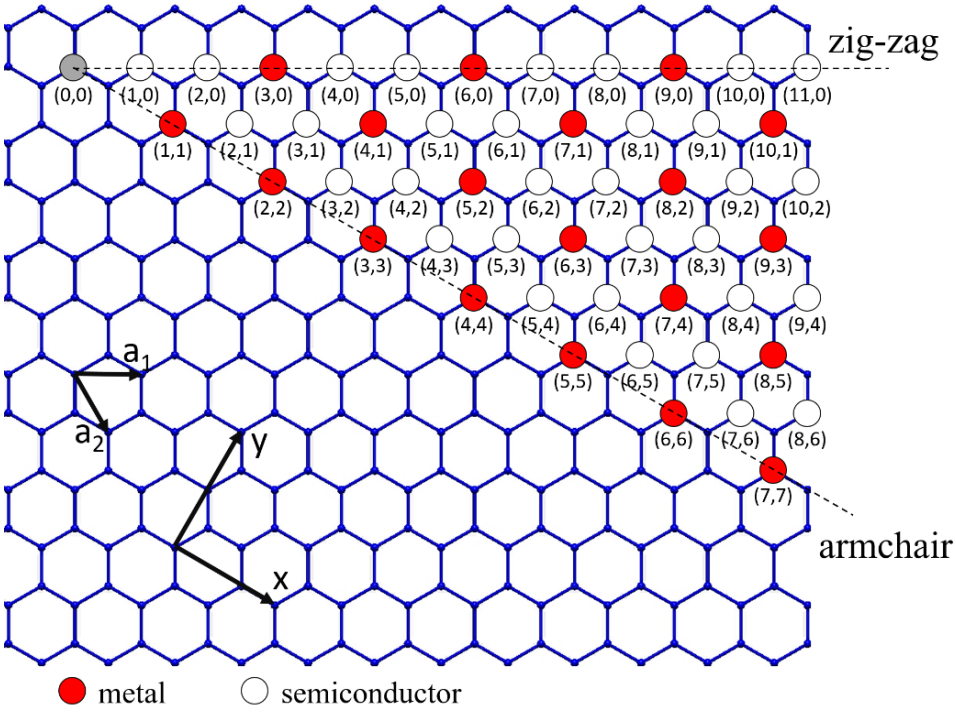

Figure 2.3. The hexagonal lattice of the graphene layer [55].

The structure of SWNTs can be described as a single layer of graphene rolled up into a cylindrical tube. The tube can be rolled up in various ways and is represented by a chiral vector $\mathbf{C_h}$, as defined:

$$\mathbf{C_h} = n\mathbf{a_1} + m\mathbf{a_2} \qquad \text{(eq. 2.1)}$$

where $\mathbf{a_1}$ and $\mathbf{a_2}$ are lattice vectors define in Figure 2.4, and (*n*, *m*) are integers which denote the number of a unit vector along two directions in the honeycomb structure lattice of graphene sheet [55]. In case the integers n = m, the SWNTs are called arm-chair, for m = 0, SWNTs are called zig-zag, and the rest are called chiral and the values of (*n*, *m*) are assigned to them. The graphic representation of chirality is shown in Figure 2.4(b-d).

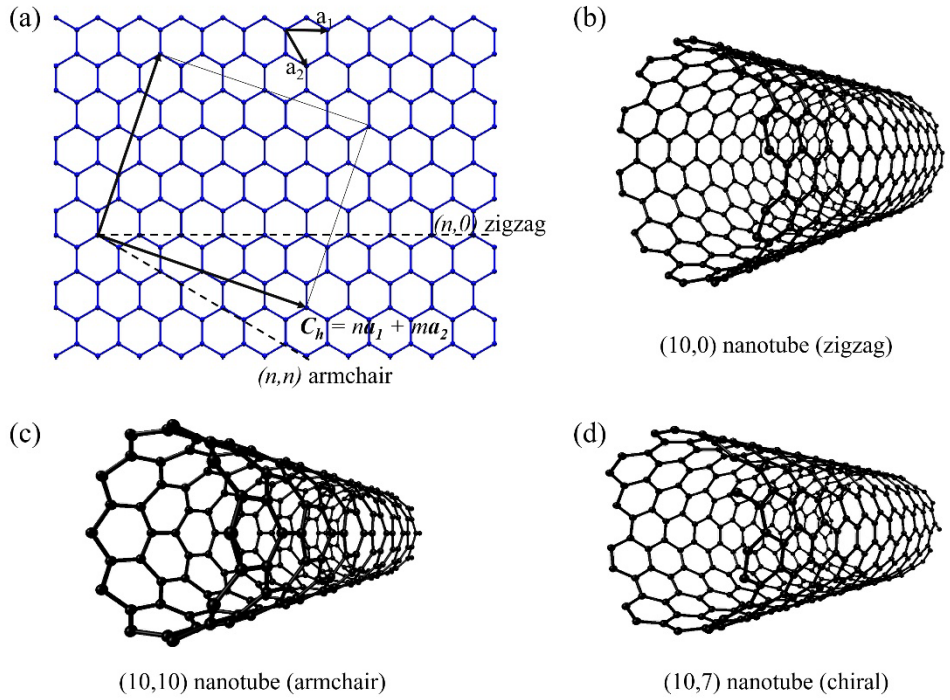

Figure 2.4. (a) Schematic of a graphene layer with (n, m) nanotube and description how a nanotube is rolled up, $\mathbf{a_1}$ and $\mathbf{a_2}$ are the lattice unit vectors of graphene sheet. (b) Zigzag SWNT (10, 0), (c) armchair nanotube (10, 10), and (d) chiral nanotube (10, 7).

The chirality of SWNTs influences their electrical properties. For a given (*n*, *m*), in the case of armchair nanotubes (*n* = *m*), the SWNTs are metallic with low energy properties defined by Luttinger liquid model [56], which describes low energy excitations in a 1D electron gas systems. On the contrary, both the chiral and zig-zag CNTs can be either metallic or semiconducting depending on the chirality or equivalently the diameter.

2.1.4. *Synthesis methods*

The growth of CNTs can be achieved by various methods, like arc discharge, laser ablation, chemical vapor deposition, etc. The synthesis by those methods is usually conducted in a vacuum or with process gasses. The modifications of the synthesis methods

allowed the production of high yield CNTs for massive scale industrial applications. In the following chapter, the most commonly used methods of CNT synthesis are introduced.

2.1.4.1. Arc discharge method

The arc discharge method presented in Figure 2.5, was invented for the synthesis of carbon nano-onions in 1980 and fullerenes in 1985. In this method, the negative electrode containing carbon sublimates due to the high temperature, as a result of high current flow responsible for the ignition of arc-discharge. The arc discharge method was used by Iijima in 1991 [1] for the first successful synthesis of MWNTs from the carbon soot of graphite electrodes. Under suitable arc-discharge conditions, the very high yield of MWNTs can be achieved. On the contrary, the addition of metallic particles (e.g. Fe, Ni, Co, etc.) as a catalyst in a graphite anode allows the growth of SWNTs [51,52] in large quantities [57].

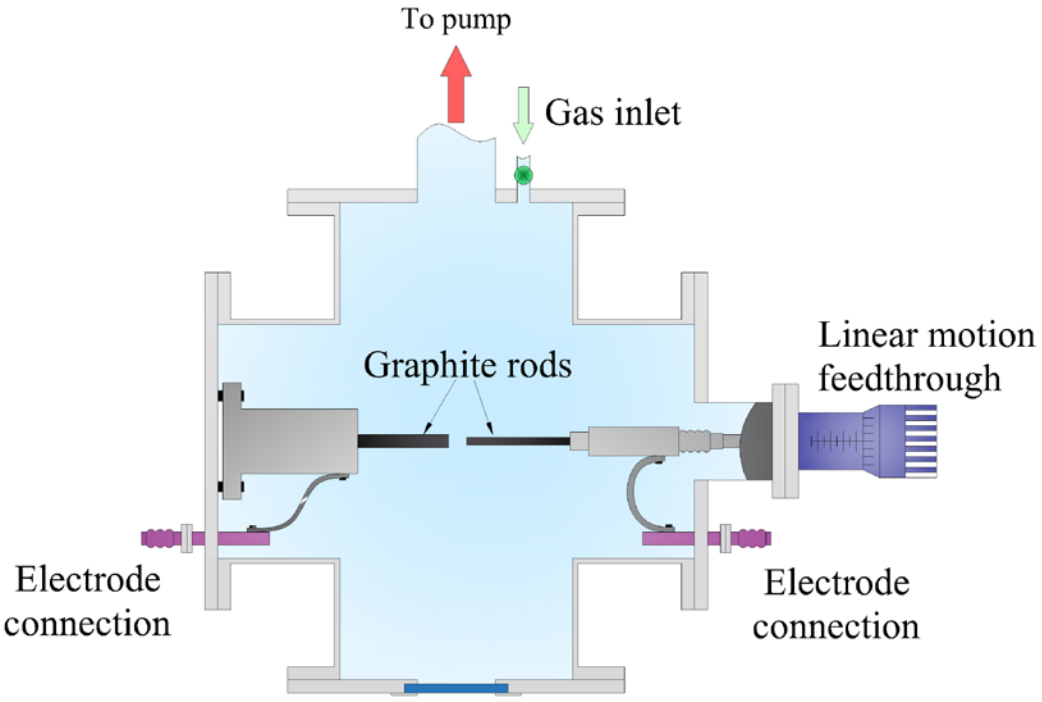

Figure 2.5. Schematic of arc discharge system used for growth of CNTs.

The arc discharge method provides a useful tool for generating the high temperatures required to vaporize carbon atoms into a plasma (>3000°C). The typical process consists of the following steps. First of all, due to high current flow through graphite electrodes, the arc discharge is generated and the evaporation of electrodes is observed. The process of

formation of a carbon soot is observed at the anode, during cooling down of the evaporation products. Typical arc product consists of a hard outer shell made of pyrolytic graphite and the soft black powder core containing a mixture of CNTs and graphitic nanoparticles. Furthermore, the process is carried out in the inert gas, such as argon or helium; however, due to higher ionization potential of He, better results are achieved. External cooling of the electrodes and arc chamber supports the increase of the CNT yield during the arc discharge process. As a result of the CNT synthesis by arc discharge method, a yield up to 30% by weight can be achieved, which contains both MWNTs and SWNTs of lengths up to 50 μm. The synthesis of CNTs on the surface of the cathode and non-constant spacing between electrodes result in a non-uniform current flow and non-homogenous electric fields. Due to those effects, the distribution of the temperature and the density of carbon vapor are non-uniform and the impurities and graphitic nanoparticles are present and always co-exist with CNTs. Moreover, the non-uniformity of the temperature and pressure results in limited control of the diameter and length of the synthesized CNTs.

The arc discharge method allows the synthesis of very high-quality CNTs; however, the separation of amorphous carbon by-products requires various purification methods for both, MWNTs and SWNTs. CNTs obtained by the arc discharge method have a very small number of structural defects and very good crystallinity. Because of that, the arc discharge method is widely used for large-scale production of SWNTs.

2.1.4.2. Laser ablation

The process of removing materials from a solid surface by laser beam irradiation of the surface is called laser ablation. In the case of the lower laser flux, a heating of solid material occurs due to laser irradiation and the evaporation or sublimation is observed. Laser ablation was developed in 1995 for the purpose of CNT synthesis [58,59]. The schematic of laser ablation method is shown in Figure 2.6.

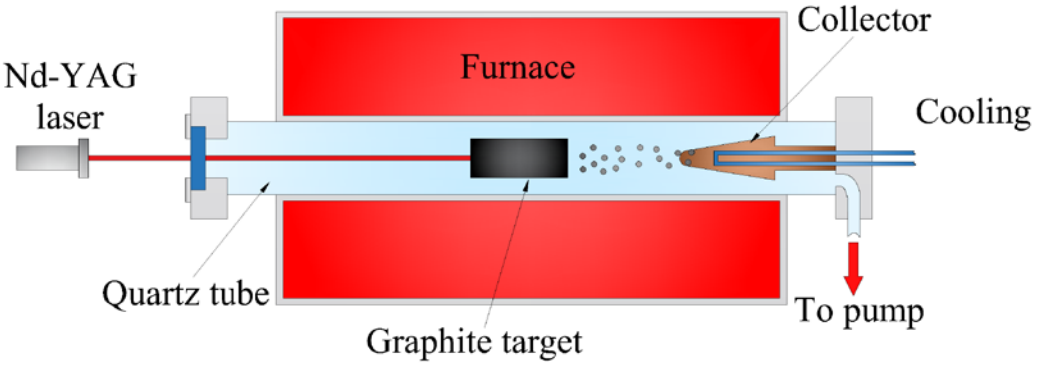

Figure 2.6. Schematic of laser ablation system used for growth of CNTs.

During the process of the synthesis of CNTs by laser ablation, a block of graphite is placed inside a furnace, heated to approximately 1200°C, and irradiated by the pulsed laser. At the same time, the flow of inert gas (e.g. Ar, He), pumped along the direction of the laser point is maintained. Laser irradiation results in the ablation of the graphite target, causing the evaporation of carbon which is transported by the flowing inert gas in the direction of a cooled copper collector. Cooled collector allows the condensation of the vaporized carbon and formation of CNTs on the surface. Similar to the arc discharge method, the growth of MWNTs can be observed from a pure block of graphite as the starting material, while the growth of SWNTs requires composite of graphite and metallic particles (e.g. Co, Ni, Co + Ni, etc.) which act as a catalyst.

In the laser ablation method, due to laser irradiation, the heating and evaporation of the target surface, containing graphite and metallic particles, is observed. During the cooling of the evaporated particles, the condensation of carbon atoms and molecules into larger, more stable clusters is noted. Moreover, the condensation of the catalyst species is observed. The catalyst attaches to carbon clusters and prevents the formation of closed cage structures. The growth of SWNTs from the clusters occurs as the diffusion of carbon continues, until the size of the catalyst particles is too large or the growth conditions have cooled down and do not allow further diffusion of carbon through catalyst particles. In this case, the catalyst particles become coated with the uniform carbon layer, and the growth of CNTs is also stopped as no more carbon atoms can be absorbed [60].

By applying the laser ablation method, the yield of CNTs is increased up to 70-90% in the total product, compared to arc discharge method [61]. Furthermore, by better control of the temperature during the process, better control of the diameter of CNTs can be achieved. On the contrary, due to high-power laser required for the growth of CNTs, the laser ablation method is more expensive. Some modification of laser ablation allows replacing the high-power laser sources with an electron beam which is used for the evaporation of graphite targets instead [62].

2.1.4.3. Chemical vapor deposition

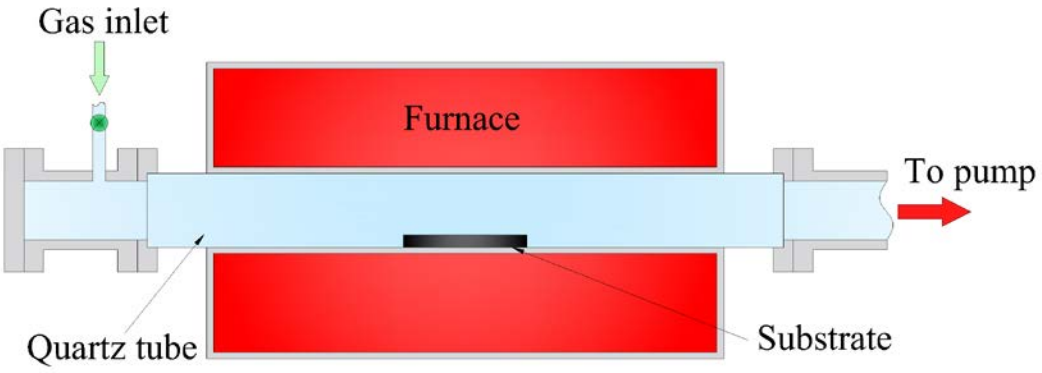

Figure 2.7. Schematic of hot-wall CVD system used for growth of CNTs.

Chemical vapor deposition is the most commonly used method of CNT growth [54] due to simplicity and relatively low cost of the process as compared to arc discharge and laser ablation. Furthermore, CVD method allows synthesis at a relatively low temperature and ambient pressure. The crystallinity of grown MWNTs is much lower than in the other two methods; however, the crystallinity of SWNTs is very similar in all the cases. Another advantage of CVD method is higher yield and higher purity of grown nanotubes. In CVD method, a big number of various substrates and hydrocarbons in any state allows very good control of the structure of CNT forest and growth of CNTs in various form (powders, films, aligned CNTs, etc.). Finally, CVD method provides better control of growth parameters than other methods [54].

The schematic of CVD process used for the growth of CNTs is shown in Figure 2.7. The furnace is usually heated above the temperature of 600°C, in which the decomposition of hydrocarbon can occur. The carbon feeding gas, such as methane, benzene, acetylene,

ethylene, etc. is introduced into the heated furnace and the pyrolysis over the metallic catalyst surface occurs, allowing the growth of CNTs on various substrates. In some cases, a solid hydrocarbon, such as camphor, naphthalene, ferrocene etc. is used and kept in the low-temperature zone of the chamber. Solid hydrocarbon directly changes state from solid to vapor, so the nucleation of CNTs can occur on the surface of the heated catalyst. In the CVD method, the catalyst used for the growth is one of the most important factors. A successful growth of CNTs has been reported on iron, nickel, cobalt, gold, platinum and stainless steel.

The growth of CNTs can occur according to two different mechanisms which depend on the interactions between the catalyst and the substrate.

(1) In the first case, when the interactions are weak, the decomposition of hydrocarbon occurs on the top surfaces of the metallic particles which act as a catalyst and result in the creation of H_2 and C_n species. The carbon atoms and molecules diffuse down through the catalyst particles, and CNT precipitates out across the bottom of the metallic particle at a lower temperature, pushing the whole particle off the surface. The process occurs as long as the top of the catalyst is open and the activity is kept, allowing decomposition of hydrocarbons. The diffusion process depends on the carbon concentration gradient inside the particle. Once the carbon species stop reacting with the exposed end and the metallic particle is fully covered with carbon, the activity of the catalyst decreases and growth of CNTs is stopped. Described model of CNT growth is called “tip-growth model” [63,64].

(2) A different mechanism is observed in the case when interactions between substrate and catalyst are strong. The beginning of the CNT growth mechanism is very similar to the first case, in which the decomposition of hydrocarbons and diffusion of carbon occur; however, due to strong interactions, the CNT precipitation cannot raise the particle up. Due to that, the CNT is compelled to grow from the place with the lowest interactions with the substrate – the top of the particle. In this mechanism, the crystallization of carbon is firstly observed in the form of a hemispherical dome, usually referred as half of fullerene. The dome extends up and forms a seamless graphitic cylinder. During the process, carbon species obtained through decomposition diffuse upwards, through the

surface of the metallic particle. For that reason, this model is called “base-growth model” [65].

The size of the catalyst particles governs the type of obtained CNT. When the size of a particle is a few nanometers, the formation of SWNT occurs, while for the size of a tenth of a nanometer, the formation of MWNT is achieved [66].

The CVD equipment used for growth is easy to modify, causing an expansion and further development of CVD methods. Based on the method of the decomposition of carbon source gasses, the CVD methods can be divided into two main groups: thermal CVD and plasma enhanced CVD (PECVD) [67].

Thermal chemical vapor deposition

Thermal chemical vapor deposition is the simplest method. During the process the pyrolysis of carbon source gasses occurs at high temperatures. The growth temperature is usually between 700-1200°C in order to allow the pyrolysis process. The successful synthesis of large arrays of vertically aligned CNT forest was achieved by thermal CVD, such as water-assisted CVD [2,68] and atmospheric thermal CVD, due to a crowding effect originated from van der Waals forces in the dense CNT forest. The thermal CVD can be divided into two types, depending on the type of heating: a hot-wall CVD and a hot-wire CVD.

A typical design of hot-wall CVD (Fig. 2.7) contains a reaction chamber in the shape of quartz tube in which the CVD process is conducted, and a heated furnace. The energy required for the heating of the reaction chamber to the temperature which allows the pyrolysis of gasses, is usually provided by electric high-temperature furnace. The temperature that is usually applied during the CVD process is above 700°C, even up to 1200°C.

The hot-wall CVD process starts from the introduction of substrates with prepared catalyst into the chamber, which is pumped to the pressure below 1×10^{-3} Pa. After the base pressure is reached, the heating of the chamber begins and after the sufficient temperature is reached, the annealing process is conducted for a precisely controlled time in order to achieve the formation of catalyst particles. The annealing process can be carried out in a vacuum or gaseous atmosphere of hydrogen (H_2), ammonia (NH_3), argon (Ar), or mixtures of those

gasses. After the annealing process, the hydrocarbon gas is introduced into the chamber for the duration of CNT growth. After the process, the chamber is cooled down and the samples are removed from the reactor.

One of the variations of hot-wall CVD is water-assisted CVD, often referred to as “supergrowth”. In this process, the small quantities of a water vapor are introduced into the reactor chamber during the experiment, in order to increase the activity and lifetime of the catalyst. Introduction of water vapor allows the growth of dense, high purity and very high SWNT arrays of length of several millimeters [2,69].

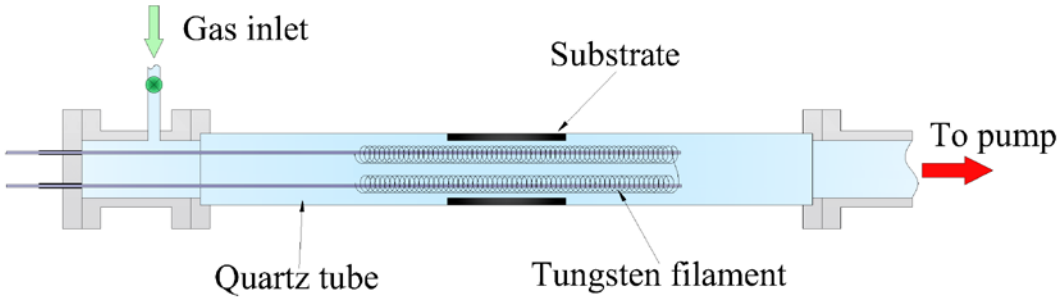

Figure 2.8. Schematic of hot-filament CVD system used for growth of CNTs.

On the other hand, hot-wire CVD is also commonly used for growth of CNTs and is presented in Fig. 2.8. The experimental setup is very similar to the hot-wall CVD method, in which instead of an electric furnace, a hot-wire (hot-filament) is used for the pyrolysis of hydrocarbon gasses. The advantage of the hot-wire CVD method is lower energy consumption required for heating the chamber. The most simple setup of the hot-wire CVD without a heater requires the activation of hydrocarbon gas by heating the filament up to 2200°C. During the process, the CNTs are deposited directly on the surface of the substrate, which is heated by the filament through the thermal irradiation. In some cases, the electric furnace is used for the independent heating of the substrates [70].

Plasma enhanced chemical vapor deposition

In plasma enhanced CVD (Fig. 2.9), chemical reactions and the deposition of thin films from a vapor to a solid state are enhanced by plasma. Compared with the thermal CVD method, the PECVD allows the growth of CNTs at significantly lower temperatures [71–73].

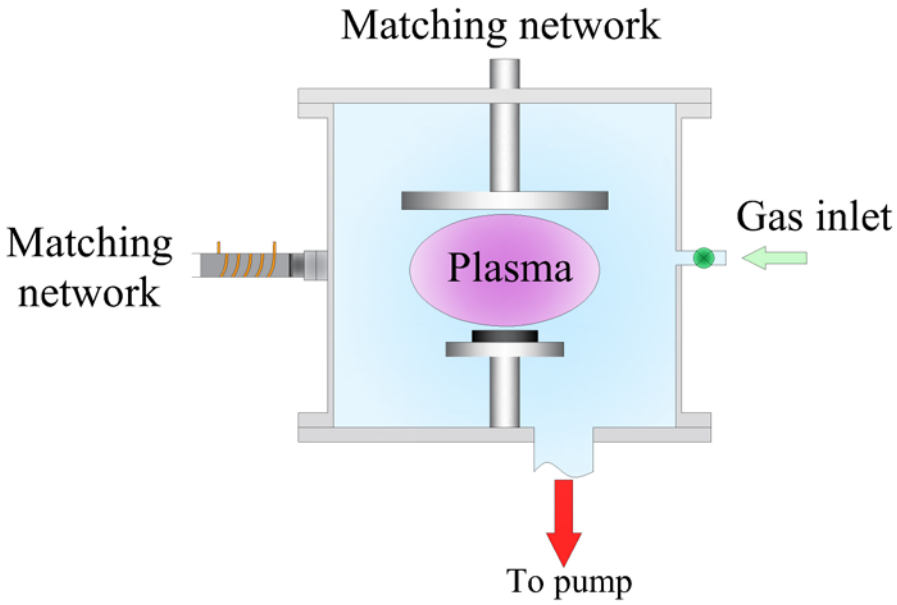

Figure 2.9. Schematic of plasma enhanced CVD system used for growth of CNTs.

The plasma occurs in the reaction chamber filled with reactive gasses between two electrodes and is usually generated by radio frequency (RF) or direct current (DC) discharge. After the ignition, plasma is involved with chemical reactions responsible for the CNT growth process. Compared with the thermal CVD, the influence of PECVD method on the properties of CNTs grown is much larger, due to big variation of parameters during the process, such as etching ability, etching rate, selectivity of etching, hydrogen content, etc.

Based on the heating methods and plasma sources, a wide range of PECVD techniques for the synthesis of CNT were developed [74,75]. In the group of PECVD techniques related to the heating methods, the following types were developed: back-heated PECVD, hot-filament PECVD and simple PECVD without heating. In the second group, related to the plasma sources, DC PECVD, RF-PECVD, microwave PECVD, etc. can be listed. For the synthesis of CNTs, various heating methods and plasma sources are used in different configurations.

In the typical DC PECVD, without additional heating source, the plate-plate or rod-plate electrode systems are usually used. The distance between cathode and anode is maintained within a range of several centimeters. The current of the plasma discharge is controlled by the DC power supply in a constant-current mode. During the process, various gasses are introduced to the reactor chamber and the decomposition of hydrocarbons occurs in DC plasma. As a result, radicals of the decomposed source gas are produced and then deposited on the surface of the substrate. The growth temperature is usually higher than the room temperature, due to the plasma heating and depends on the plasma density, energy, etc. The DC PECVD allows growth of vertically aligned CNTs of various diameters, which depend on the plasma intensity. For higher intensity the diameter increases. On the other hand, for the precise control of the temperature of the substrate, the external heating source is usually introduced to the process, in a form of an electric furnace or an IR lamp. In the back-heated PECVD, the heating of the substrate is conducted by a resistance heater mounted below the substrate holder, which allows precise control of the growth temperature [76,77]. In the hot-filament PECVD, the heating of the substrate is provided by hot filament mounted above the sample [78–80].

The typical RF-PECVD system is composed of a reactor chamber, anode and cathode electrodes, a vacuum pumping system, and a RF power supply [81]. A formation of plasma in the reactor chamber is achieved by the RF generation. The plasma generated during the process contains reactive ions and radicals of the reactive gasses introduced during the growth of CNTs. Compared with DC PECVD, the growth of CNTs by RF-PECVD is easier due to the activation and cleaning of the catalyst surface, related to the less intense ion bombarding.

The typical microwave PECVD system is composed of a microwave magnetron, a circulator, a tuner, a cavity, and a waveguide [82]. The microwave frequency of 2.45 GHz, generated by microwave magnetron allows the tuning of microwave power between 0 and 3000 W. In order to prevent the reflection of power back to the magnetron, the circulator is used. The tuner is used for the optimization of impedance matching, while the cavity, adjusted by sliding short, allows the resonance at 2.45 GHz and generation of microwaves.

During the process, reactive gasses are introduced into the chamber, in which by the decomposition occurs. Compared to DC PECVD and RF-PECVD, the cost of the microwave PECVD is lower, allowing the growth of large-scale CNT arrays in the order of kilograms due to the fast heating and cooling during the synthesis processes.

2.1.4.4. Hydrothermal methods

Hydrothermal method is generally defined by heterogeneous reaction in the presence of solvents or mineralizers, which is conducted under high pressure and temperature in order to allow a dissolution and a recrystallization of materials that under normal conditions are insoluble [83]. The hydrothermal processing is commonly used for the synthesis of metal oxides, semiconductors, nitride nanomaterials, and recently also CNTs.

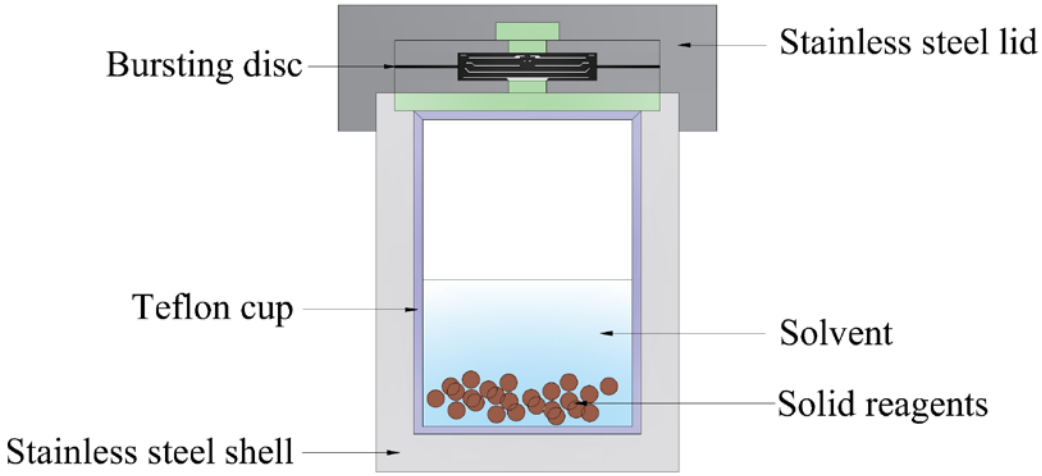

Figure 2.10. Schematic of hydrothermal reactor used for growth of CNTs.

During typical hydrothermal process (Fig. 2.10), pressure and temperature in the chamber (autoclave), applied during the experiment, are the most important parameters of growth and are crucial for the precise control of dissolution process. In a typical setup, the temperature is applied and measured by an external heater, while the pressure is controlled by the direct measurement using the Bourdon pressure gauge, or by utilizing the pressure-vapor-temperature (PVT) relation.

Compared to laser ablation and arc discharge, in which the synthesis of CNTs high temperature and metal catalysts are required, the hydrothermal process allows the growth of CNTs in a temperature from 160°C to 1000°C. The synthesis of CNTs was achieved for

various pressures and temperatures, and also utilizing various solutions, without catalyst in some cases. The growth of CNTs was achieved at 160°C using an ethyl alcohol/polyethylene glycol mixture dissolved in basic aqueous solution [84], at 180°C using ethyl alcohol only [85], while for the case of 350°C, the hexachlorobenzene and tetrachloroethylene with Ni/Co catalyst were used [86]. On the other hand, the synthesis of CNTs was also achieved in higher temperatures, e.g. at 600°C and in pressure of 12,4 MPa, using toluene and Fe alloy as a catalyst [87]; at 700-800°C and pressure of 60-100 MPa, using polyethylene and ethylene glycol [88,89]; and finally at 1000°C using supercritical CO_2 [90].

The hydrothermal method allows the growth of both, multi walled and single walled CNTs. The temperature of synthesis influences the diameter of CNTs, allowing growth of MWNTs with smaller diameter at lower temperatures and bigger diameters at higher temperature, with keeping the same number of walls [89]. Moreover, the hydrothermal method provides very high quality of grown CNTs and allows precise control over the structure and the diameter of CNTs. On the other hand, despite some advantages of the hydrothermal method over arc discharge or laser ablation method, the parameters of synthesis affect the stability of CNT growth. In time, the structure of obtained SWNTs changes to MWNTs and a formation of graphitic nanoparticles is also observed. Furthermore, the addition of oxygen in the super-critical water results in the decrease of the diameter of MWNTs to the point where SWNTs are not observed [83].

2.1.4.5. Flame method

One of the oldest methods to produce CNTs is a flame method, shown in Fig. 2.11. Some of the researchers claim that CNTs were discovered in 400-year-old sabers from Damascus [91]. In the flame method the growth of CNTs is achieved by the burning of hydrocarbon gasses, such as methane, ethylene, benzene, etc. Moreover, CNTs can be commonly found in the soot in various flame environments.

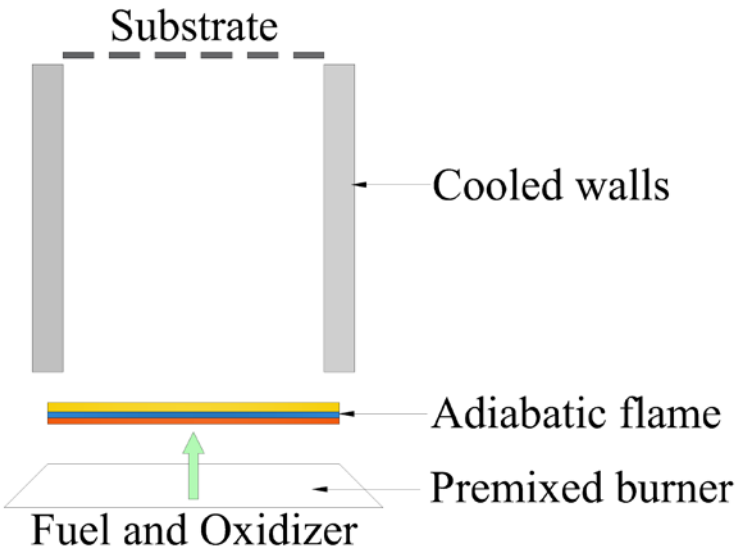

Figure 2.11. Schematic of typical system setup of flame method used for growth of CNTs.

The mechanism responsible for the growth of CNTs by the flame method is related to the diffusion of hydrocarbons during the process. The method allows the synthesis of both MWNTs and SWNTs; however, often due to uncontrolled process, the uniformity, shape, size and quality of nanotubes may significantly vary. On the other hand, by the precise control of growth process, the synthesis of highly-aligned MWNT [92] and SWNT [93,94] arrays was also achieved. For example, Hu *et al.* [95] showed possibility of growth of high-quality MWNT arrays using laminar flow of ethylene/air mixture and anodized aluminum oxide (AAO) as a template, and Co particles as the catalyst placed at the bottom of nanopores. By the flow of gasses perpendicularly to the surface of the AAO template, the growth of smooth and uniform CNTs was obtained [95].

2.1.4.6. Disproportionation of carbon monoxide

The first hollow carbon nanotubes reported in 1952 [44] and mentioned in chapter 2.1.2, were prepared by disproportionation of carbon monoxide at 450°C. Moreover, catalytic disproportionation allowed the growth of hollow structures of carbon fibers and SWNTs [53,96].

In the presented method, the disproportionation of carbon monoxide occurs according to the Boudouard equilibrium:

$$2CO \rightleftharpoons C + CO_2 \qquad \text{(eq. 2.2)}$$

Below the temperature of 700°C, the right side of the equilibrium is favored, in case the catalyst is present (Fe, Co, and Ni) [96]. Typically the carbon monoxide gas passes through the powders or particles of iron, nickel or cobalt, resulting in the growth of CNTs. The investigation of the growth mechanisms suggests that the dissociative chemisorption of the CO gas on the NiFe alloy results in the diffusion of carbon into the alloy bulk structure. Further investigation showed that the bulk diffusion is determined by an isothermal gradient with local equilibria, at the interfaces between metallic catalyst-carbon and metallic catalyst-gas. Due to that fact, the growth of CNTs is observed as a result of the precipitation of carbon at the metal-carbon interface.

The disproportionation of carbon monoxide allows the growth of SWNTs through the pyrolysis of various catalysts and carbon sources. By applying high pressures (0.1 – 1 kPa) and temperatures of 800 - 1200°C, a very efficient synthesis of high yield SWNTs is possible [97]. The high pressure modification of disproportionation method is often called HiPco (high-pressure CO) [98].

2.1.5. Properties

Carbon nanotubes, due to their unique structure, exhibit a large number of extraordinary properties. The most important are described in the following subchapters.

2.1.5.1. Mechanical properties

The ratio of diameter and length of CNTs influences the mechanical properties. Due to the extraordinary structure, the tensile strength and elastic modulus of CNTs have the highest values ever reported. In the perfect CNT, the sp^2 bonds formed between carbon atoms decide the strength of a nanotube. Due to the C-C bonds and unique geometry, CNTs have a very big tensile strength along their axes and a very high elastic modulus in their axial direction. The estimation of the Young modulus of CNTs, based on their structure, allows values between 1 TPa and 2 TPa. In the case of SWNTs, the elastic modulus depends on the diameter and chirality, while in the case of MWNTs, the crystallinity of the outer walls is the most important [99].

The theoretical study shows that the strength of a perfect nanotube is about 10 to 100 times higher than the strength of steel per unit weight, while the elastic modulus of 1000 GPa is about 5 times higher than steel. CNTs have a very big potential in various mechanical applications due to a very high strength, Young modulus, and tensile strength of 63 GPa, combined with relatively small weight of nanotubes. It should also be noted that the electronic properties of CNT are also very unusual. The change of the chirality of SWNTs, or the increase in number of walls, results in the change of type of conductivity, from semiconductor to conductor [100–102]. Table 2.1 summarizes the mechanical properties of CNTs and compares them with other string materials [103].

Table 2.1. Mechanical properties of CNTs and other string materials.

Material	Young modulus (GPa)	Tensile Strength (GPa)	Density (g/cm^3)
SWNT	1054	150	1.3
MWNT	1200	150	2.6
Epoxy	3.5	0.005	1.25
Steel	208	0.4	7.8
Wood	16	0.008	0.6

2.1.5.2. Thermal properties

Due to their unique structure, CNTs exhibit anisotropic thermal conductance. Along the axis direction CNTs show a very good thermal conductivity and a “ballistic conduction” property, and while in the lateral direction to the axis, CNTs exhibit insulator properties. The ballistic conduction refers to the transport of electrons in the material of a very low electrical resistivity, caused by the scattering [104]. At room temperature, the thermal conductivity along the aligned SWNTs is about 3500 W/mK, while the conductivity measured for isolated SWNT of (10, 10) chirality is about 6600 W/mK [105]. For comparison, the thermal conductivity of copper, which is known of its high conductivity, is about 385 W/mK. In the case of CNT forest, the thermal conductivity is improved in the case of the improvement of alignment of CNTs.

The thermal conductivity of MWNTs along the axial direction is about 0.5 – 1.2 W/mK at room temperature. Interestingly, the shortest MWNT forest exhibits the highest value of thermal conductivity, which also decreases perpendicular to the CNT axis [106].

CNTs exhibit isotropic thermal expansion and high thermal stability up to 750°C in air and up to 2800°C in vacuum [104]. On the other hand thermal diffusivity of aligned CNT arrays shows very high anisotropy along the axial direction of CNTs and perpendicular to the direction of CNT alignment. The measurements of thermal diffusivity of MWNTs were conducted by Borca-Tasciuc *et al.*[107]. Results of the thermal diffusivity of aligned CNT arrays showed a small decrease along CNTs and perpendicularly, with increase of the temperature, while the overall value was about 25 times smaller [107,108].

2.1.5.3. Chemical properties

Chemical properties of CNTs are mostly originated from their structure. In CNTs, graphene sheet is rolled up in the shape of a tube which results in the increase of the chemical reactivity of nanotubes. Due to the curvature effects, the σ and π orbitals mix, causing the hybridization of the orbitals. With the decrease of the diameter, the hybridization becomes larger and is directly derived from the mismatch of the π orbital caused by the change of the curvature of CNTs, resulting in higher chemical reactivity of SWNTs than MWNTs. Due to high chemical reactivity, it is possible to modify the caps and walls of CNTs and control e.g. the solubility of CNTs. On the contrary, the covalent modification of sp^2 bonds of carbon atoms in CNTs by attachment of various molecules is very challenging and therefore, CNTs are considered chemically inert [109].

Finally, the chemical properties of CNTs allows the modification of other properties by applying doping, wetting, charge transfer, filling, etc. The chemical properties of CNTs can be utilized in various fields for different applications, such as sensing, energy storage, electronics, biological separation, etc.

2.1.5.4. Electrical properties

The atomic structure of CNTs, described by the chirality and diameter [110], defines their extraordinary electrical properties. As mentioned in previous chapters, structure of CNT is originated from a rolled up sheet of graphene. The graphene sheet is a semimetal and

because of that, it exhibits both semiconducting and metallic properties. During the formation of CNT, the proper organization of carbon atoms and quantum mechanical wave function of the electrons has to be achieved. For the perfect CNT, the current density of 4×10^9 A/cm^2 can be achieved and is over 1000 times higher than the current density of Co [111].

The individual CNTs can be characterized by resistance, capacitance and inductance which are originated from their intrinsic structure and mutual interactions with other materials. The transport of electric charges in the structure of CNTs and the resistance originated from it depend on the scattering on structural defects and vibrations of atomic structure of CNTs [112]. However, in the 1D materials, such as CNTs, the strong covalent bonding results in changes of the resistance and the electric transport process. In the 1D materials, the small angle scattering cannot occur, so only charge carriers can move only forward and backward along the nanotube. The 1D structure of CNTs results in a new type of quantized resistance which is directly related to the interactions between three-dimensional (3D) and 1D materials, such as metal electrodes or CNTs, and is expressed by:

$$\frac{1}{R_Q} = \left(\frac{2e^2}{h}\right) M \qquad \text{(eq. 2.3)}$$

where $2e^2/h$ is quantized resistance and M is an apparent number of conducting channels which include the coupling between 2 electrons and the coupling effects between nanotubes and intrinsic channels. For metallic CNTs, the number M = 2, so the resistance is equal to 6.45 kΩ. Moreover, except the quantized resistance, other types of resistance also occur and are related to presence of Schottky barriers at semiconducting-metallic CNT interfaces or bad contact between nanotubes. Also, in the case of long CNTs or at high bias, the scattering collisions can be observed and results in the diffusive limit of transport of the charge carries, limiting the mobility of electrons. Despite this effect, CNTs exhibit very high carrier mobility, even 1000 times higher than carrier mobility in silicon.

The capacitance of CNTs is originated from the unique electronic structure and related to the density-of-states. The density-of-states of CNT describes how the states of energy are distributed in energy, and is independent of electrostatics. Typically, the quantum capacitance of CNTs is small and takes values of 10 – 16 F/μm. On the other hand, CNTs

also exhibit electrostatic capacitance which is dependent on the shape and electric structure of the surrounding conductors [111,113].

The inductance of CNTs is originated from the resistance of the current flow through the nanotubes. In the classical approach, the inductance of CNTs depends on their diameter, shape, structure, defects, permeability etc. The electrical properties of CNTs are used for various applications, such as electrodes for metal-oxide-semiconductor-field-effect-transistors (MOS-FETs) [14], a wiring material for large-scale integrator (LSI) interconnects [15], actuators and polymeric composites for electronic devices [16] or high emission current density emitters [17]. The same properties are also utilized in various types of solar cells, where CNTs act as electrodes [18,19], counter electrodes [20,21], or active layers in solar cells [22].

2.1.5.5. Optical properties

The optical properties of individual SWNTs depend on the structure of metallic and chiral nanotubes which possess second-order hyperpolarizability (a non-linear optical property of a molecule) [114]. In contrast, in the case of well-aligned MWNT bundle, the optical properties are similar to graphite and are not related to the helical structure of nanotubes [115].

The absorption of individual SWNTs shows that the zigzag nanotubes possess third-order susceptibility [116,117]. The third-order susceptibility effect increases, by increasing the diameter of CNTs, due to stronger influence of the π electron transitions than the interband transitions. For the determination of second-order hyperpolarizabilities of armchair and zigzag SWNTs, an empirical exponent law can be applied and shows increase of the second-order effect due to the increase of impurities in the inner structure of SWNTs. This effect can be utilized in the photonic devices [118].

Based on the experimental analysis of optical properties of CNT bundles, the birefringence effect was determined [119]. In the birefringent material the refractive index depends on the polarization and propagation of light. In CNTs those changes are related to the propagation of light differently along and perpendicular to CNTs. In order to determine the optical properties of CNT bundles, the calculation needs to include full electromagnetic

coupling between individual CNTs in the bundle [120]. Furthermore, by studying Raman spectra, various optical effects, such as splits of the optical phonon, or diameter-dependent dispersions related to the size of CNT, can be observed [121].

CNT arrays possess unique anisotropic optical properties [8,122,123] and exhibit high third-order susceptibility [9]. Low density, vertically aligned CNT forests have low refractive index and due to their unique structure of effectively trapping light, CNTs exhibit superior light absorbance properties [124–126]. Due to very high absorbance and low reflectance in the visible and infrared light regions [125–127], CNT forests exhibit properties close to that of a blackbody, a theoretical material, which is claimed to absorb all spectra of incident light. Many groups of researchers have presented results of very low reflectivity of CNT forests, with the lowest reflectance of incident light in UV-VIS range of 0.045% noted by Yang *et al* [125] for 633 nm wavelength for the CNT forest height of 200-300 μm. On the contrary, the very low reflectance, below 0.01%, in infrared regime (2.5 – 15 μm wavelength) was also recently reported for CNT forests of 30-50 μm height, grown on a high roughness aluminum substrates [128].

2.2. Theory of metamaterials

2.2.1. Introduction to metamaterials

The modern history of metamaterials starts from the first paper presented by Veselago in 1968 [129], in which a general model of electromagnetic wave propagation in new "left-handed" materials possessing negative permittivity ($\varepsilon < 0$) and permeability ($\mu < 0$) was theoretically presented for the first time. Despite the fact that the existence of "left-handed" materials was not observed in nature, the Maxwell equations, which describe the electric and magnetic fields, do not exclude their existence. Moreover, the theoretical study of lossless materials showed possibility of obtaining extraordinary properties, which cannot be found in nature. On the other hand, in the first experimental work presented in 2000 by Pendry [27], the fabrication of "perfect lens" was proposed, in which a focus size smaller than the diffraction limit was achieved. In his work [27], a search for an artificial material possessing specific properties not observed in natural materials was presented. The perfect lens material should possess both negative permittivity and permeability in the same frequency region;

however, no such a material has been found in nature so far. He concluded that the materials with negative refractive index could restore the phase of propagation and the amplitude of evanescent states. Furthermore, a practical implementation was simulated by a slab of silver. Pendry claimed that a “perfect lens” tuned to the surface plasma frequency of silver could be achieved. In 2001, Shelby *et al.* [28], in their work, an array of metallic wires with suitable spacing and radius of 0.03 mm was constructed to exhibit a negative permittivity at the frequency of 8 – 12 GHz for microwave region, while metallic split rings were manufactured in order to obtain a negative permeability. A schematic of such a material is shown in Figure 2.2. Their work and studies over design of lenses induced the recent active development of negative metamaterials [130–133]. The electromagnetic properties of metamaterials became a new branch of modern science, resulting in a large number of publications on this topic.

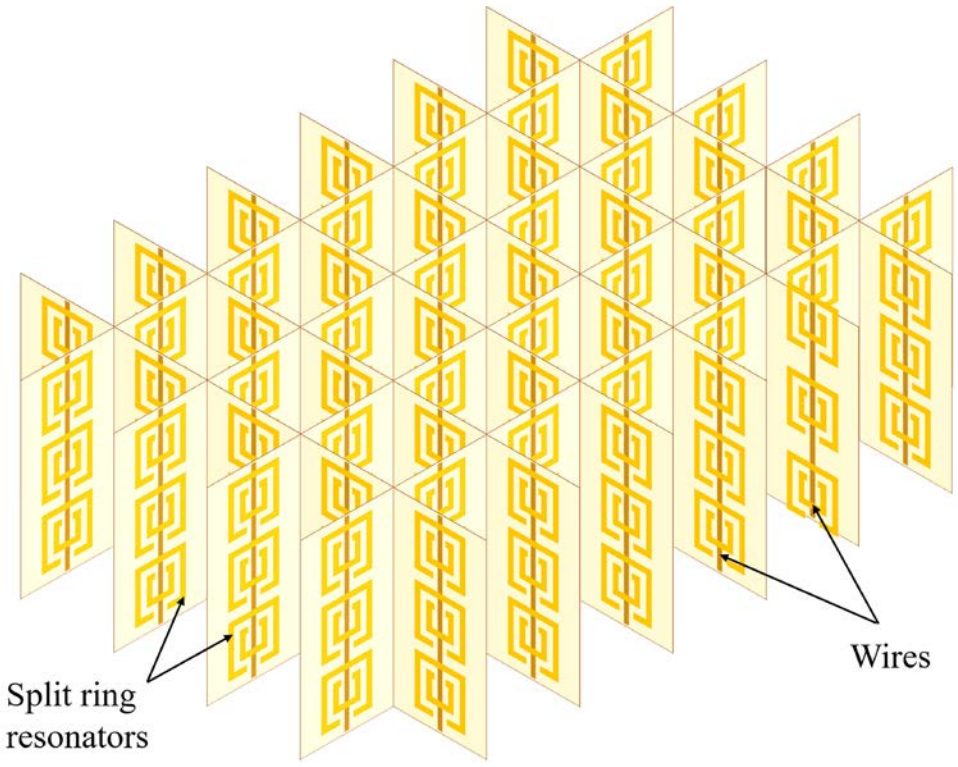

Figure 2.12. Schematic of the first metamaterial constructed of copper slit-ring resonators and wires mounted on the circuit board [28].

Starting from the work published by Pendry [27], a major effort in the fabrication of metamaterials in the visible frequencies was made. Due to many difficulties related to the scaling of the SRR structures to the optical wavelengths which would allow the interactions

with the permeability, in order to achieve negative index materials, the fabrication of optical metamaterials is still challenging. The fabrication of loops, ring resonators, and gaps is still very problematic, and various changes of the electric properties of materials used for fabrication are observed and related to the increase of the frequency in the optical range. Due to high frequencies and a very small size of the metamaterial structures, the conduction properties of the material change, resulting in the limitation of the transmission of the electromagnetic waves through arrays. For that reason, a major effort related to the development of new nanostructures was made in order to allow negative index materials in the near IR and the visible light region. Various new designs of structures were presented, such as coupled nanocones [134], plasmonic parallel nanowires and nanoplates [135,136], anisotropic waveguides [137] or even defects in regular photonic nanostructures [138]. On the other hand, in order to manipulate the transmission of the electromagnetic waves, different materials, such as carbon nanotubes [4], or Si_3N_4 [39], were also used. Despite the big improvement and the observation of the electromagnetic resonances in the optical range, the most remarkable example of utilizing optical metamaterials – an invisibility cloak [139], is yet to be achieved.

"Meta"- materials are artificial materials engineered to obtain properties that do not exist in nature [24] and which acquire their properties from embedded subwavelength metallic structures grouped together in a dielectric to exhibit the required values of permittivity and permeability in the desired frequency range in order to manipulate electromagnetic waves [25,26]. The electromagnetic properties of metamaterials are derived from the shape and size of designed resonating structures of an electromagnetic circuit, and also from the properties of the material that consist of those structures. In order to classify the material as a metamaterial, a number of requirements have to be fulfilled. First of all, the description of the structure of a material by effective homogenous electromagnetic parameters [140] has to be possible. Furthermore, the electromagnetic parameters of such a material are determined by the total response of small resonators, which have to be periodically placed in the structure. In metamaterials, the ratio of electromagnetic wavelength and the lattice constant has to be of the order of ten or more. By fulfilling those requirements, the metamaterials can be

distinguished from other structures which manipulate the electromagnetic wave, like photonic crystals, frequency selective surfaces, or arrays of metallic holes.

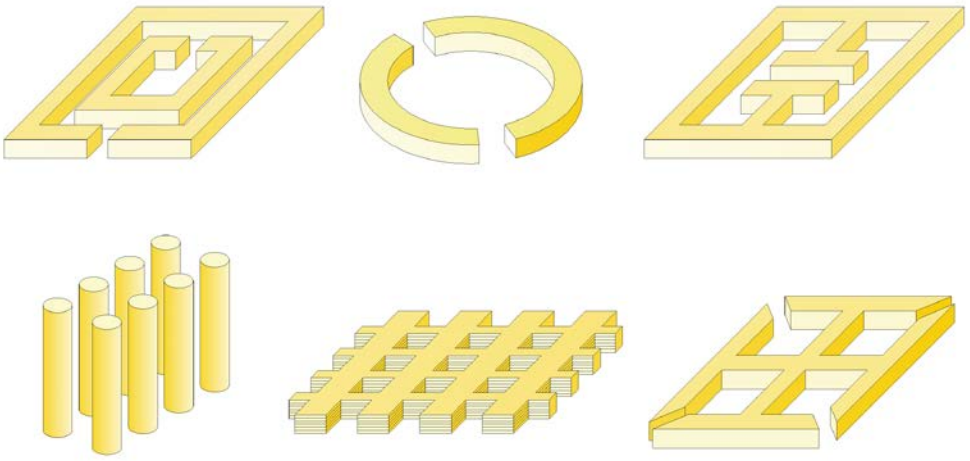

Figure 2.13. Examples of metamaterial structures (a) SRR, (b) ASR, (c) e-SSR, (d) rods, (e) fishnet, and (f) cross.

Since the work published by Pendry *et al.*, many different types of subwavelength resonators have been introduced for manufacturing the metamaterials, like split ring resonators (SRRs), asymmetric split resonators (ASRs), electric SRRs (e- SRRs), rods, fishnets, crosses, thin wires, etc. (Fig. 2.13). Some of the presented resonators are designed to interact with the electric or magnetic part of the electromagnetic radiation, while the other ones show a negative refractive index. At low frequencies, below the infrared, in order to obtain the desired electromagnetic properties of the metamaterial, simple structures like arrayed thin wires or SRRs are used. On the other hand, at higher frequencies, where the ideal conductivity of metallic resonators diminishes and the difficulty of the fabrication process rises, other advanced structures are designed to improve the performance of specific optical properties of metamaterial structures.

2.2.2. Electromagnetic behavior

The electromagnetic behavior of metamaterials depends on the type of used structures and range of frequencies. In the following part, the basics of the manipulation of the electric and magnetic part of the electromagnetic radiation are presented.

2.2.2.1. Electric resonance

For the conductive materials existing in nature, the electric response occurs typically at high frequencies, for metals at UV-VIS frequency region. This response is originated from the electric plasma frequency:

$$\omega_{\mathrm{ep}} = \sqrt{\frac{ne^2}{m\varepsilon_0}} \qquad \text{(eq. 2.4)}$$

where n is the electron density, e is a charge of the electron, ε_0 is the vacuum permittivity and m is an effective mass of the electron. For that reason, in order to obtain an electric response at lower frequencies, the modification of the plasma frequency is necessary. As can be seen from equation 2.1., the modification of frequency of plasma can be obtained by changes in electron density or effective mass. For that reason, a metamaterial structure based on the thin wires can be used (Fig. 2.14).

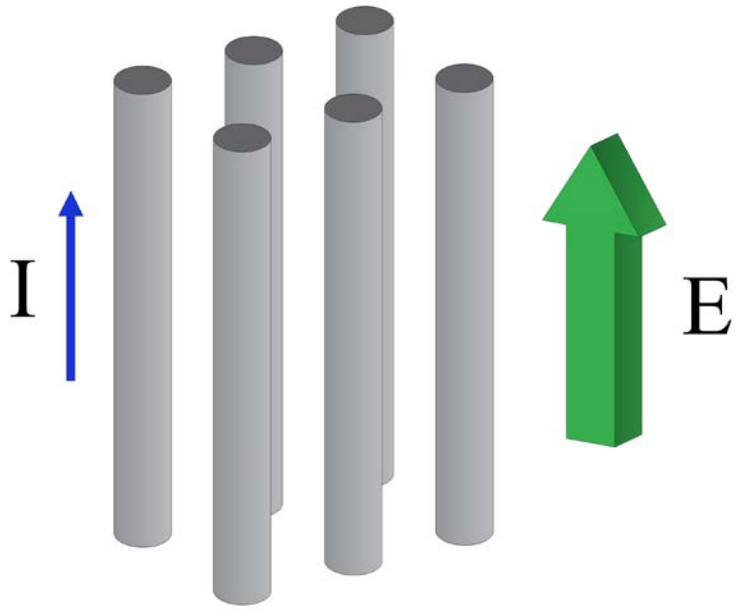

Figure 2.14. Thin metal wire structure used for the generation of electric resonance in metamaterials.

The structure constructed from the thin metal wires changes the electron density due to a distance of metal nano-rods in a unit cell and due to the mutual inductance of the wires, the effective mass of the electrons is intensified. In such a structure, the plasma frequency can be manipulated only by dimensions of the lattice spacing and the wire radius r. For that reason,

the permittivity obtained by the structure presented in Figure 14, can be explained by Drude model as:

$$\varepsilon_{\text{eff}}(\omega) = 1 - \frac{\omega_{\text{ep}}^2}{\omega^2 + j\,\Gamma\,\omega} \qquad \text{(eq. 2.5)}$$

where Γ is related to energy dissipation.

2.2.2.2. Magnetic resonance

A magnetic response from nonmagnetic materials is possible if the current loop can be supported in the material and the magnetic dipole moments can be induced. In metamaterials, a magnetic response can be obtained for certain design of SRRs, in the case a suitable alignment of the electromagnetic wave to the SRR circuit is achieved. A typical SRR design introduces two metallic concentric loops with slits or gaps directed in the opposite direction, as shown in Fig 2.13(a). For a magnetic field oscillating in the axial direction of the SSRs, a current flow is induced in the ring and a raise of magnetic dipole parallel to the magnetic field is achieved. The inductance of the SSR and the capacitance of the gap are the equivalent of an electric LC circuit, resulting in magnetic resonance (Fig. 2.15).

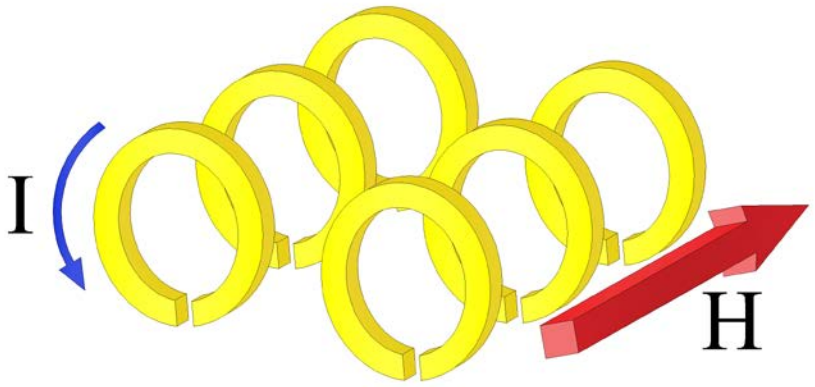

Figure 2.15. Split Ring Resonator structure used for the generation of magnetic resonance in metamaterials.

In the typical SRR (Fig. 2.13(a)), a second, inner ring is related to a net capacitance of the double SRR and is responsible for the decrease of the resonance frequency. For that reason, the ratio between the lattice constant and the electromagnetic wavelength is increased and metamaterials built from the SRRs are more homogenous to the electromagnetic

excitation. In contrast, in the case that the second ring is removed from the structure (Fig. 2.15), only the shift of the resonance frequency can be observed, without significant influence on the whole metamaterial performance [141].

The effective magnetic permeability of periodically aligned SRR arrays, under a magnetic field excitation, is given by Lorentzian model [141]:

$$\mu_{\text{eff}}(\omega) = 1 - \frac{F\omega^{w}}{\omega^{2} - \omega_{m0}^{2} + j\,\Gamma\,\omega} \qquad \text{(eq. 2.6)}$$

where ω_{m0} is magnetic resonance frequency, Γ is related to energy dissipation and F is the filling factor of the SRR patterns.

For SRR patterns, the frequency of magnetic plasma is given for the case when permeability is below zero:

$$\omega_{\text{mp}}^{2} = \omega_{m0}^{2}/(1 - F) \qquad \text{(eq. 2.7)}$$

The SRRs at lower frequencies have a positive sign of permeability, while between the resonance and plasma frequency, the magnetic response is negative. For that reason, SRR structure with negative permeability supports both paramagnetism and diamagnetism [140].

2.2.2.3. Electromagnetic resonance

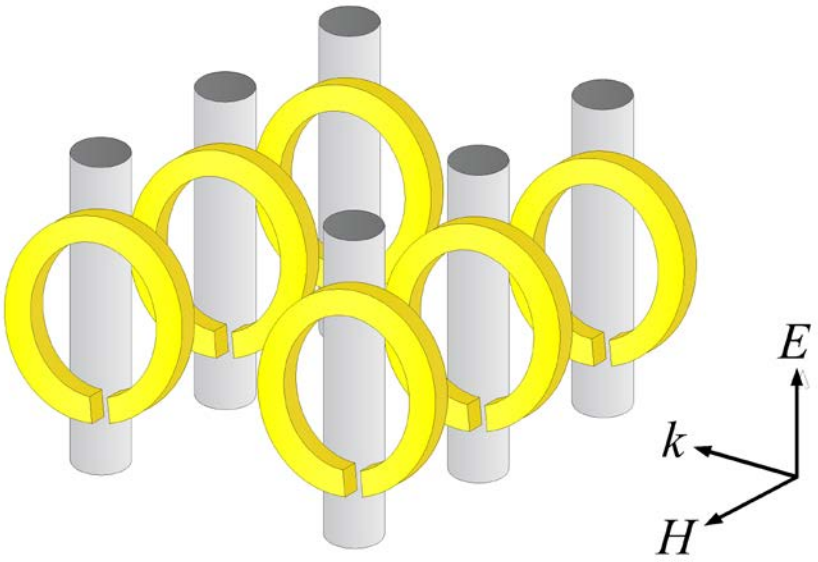

Figure 2.16. Example of structure composed of thin metal wires and split rings, used for generation of electromagnetic resonance in metamaterials.

As mentioned in chapter 2.2.1, the theory of material with both negative permittivity and permeability was proposed by Veselago. In such a case, ***E*** and ***H*** form a left-handed vector set with respect to ***k***, and the wave vector becomes negative. On the other hand, pointing vector ***S***, which indicates the direction of propagation of the energy of the wave, still form right-handed vector set with vectors ***E*** and ***H***, and results in the backward propagation of the wavefront [129]. The idea was utilized in order to develop negative index metamaterials (NIMs). For that reason, by utilizing the magnetic and electric metamaterials at the same time, the NIMs are possible [141,142]. The interactions between two classes of metamaterials are minimized due to the filling factors of both types of metamaterials which allows the preservation of negative permittivity and permeability [143]. As mentioned in chapter 2.2.1, with a combination of copper SSRs and thin wires, the first NIMs in microwave frequency were achieved in 2001 by Shelby *et al.* [28]. In NIMs, a structure composed of periodic SRRs arrays and thin wires is specifically oriented in the electric field in the electromagnetic incident wave. The vector of the electric field is parallel to the metallic wire axis, while the magnetic field is parallel to the axis of SRRs. By such an orientation and the fact that combination of SRRs and wires are responsible for magnetic and electric responses, it is

possible to achieve negative permittivity and permeability in the narrow frequency range, which allows the exhibition of the negative refractive index.

2.2.3. Applications of metamaterials

Metamaterials, due to their unique properties, allow many various applications in which a precise control of the electromagnetic wave is required. The most common applications include: antennas, absorbers, superlenses, cloaks, sensors, filters, etc.

By utilizing metamaterials for antennas, the enhancement of the radiation and a matching of properties of electric and magnetic dipole antennas were achieved. The size of a typical metamaterial antenna is about a fifth of the wavelength it interacts with. The development of antennas using metamaterials allowed a very big improvement in the radiation power, up to 95% at 350 MHz. Furthermore, the directivity of the antennas was also improved by applying patch antennas or flat horn with flat aperture which were made of zero index metamaterials. In the case of zero index metamaterials, the propagation of signal stimulates a time dependent spatially static field which results in the constant value of the phase at any point of the antenna and allows the improvement of the directivity.

In metamaterial absorbers, in order to absorb a large amount of the electromagnetic radiation, the manipulation of the permittivity and permeability of metamaterials is conducted by the precise control of the structure of metamaterials. Metamaterial absorbers can be used in photodetection and application of solar photovoltaic, in which high performance, minimum resistive losses, and low power consumption are required. Furthermore, the manipulation of the permittivity and permeability is relevant in transformation optics and negative refractive index materials.

Another application of metamaterials are superlenses which are aimed to achieve resolution beyond the diffraction limit. In conventional optics, materials used for lenses suffer a diffraction limit as only the transmission of the propagating components from a light source occurs while the transmission of the evanescent light through the lens is very limited. In order to overcome this problem, the manipulation of the refractive index is required which would allow the enhancement and recovery of the evanescent light. For that reason, the metamaterial superlenses should possess negative refractive index, resulting in the yield of

negative phase velocity. The fabrication of a perfect superlens which can constitute all evanescent waves would allow resolution beyond ordinary microscopes.

The most desired application of the metamaterials is cloaking in the optical range. In theory, a cloaking device can be achieved by cancellation of the electric and magnetic component of the electromagnetic field which is generated by an object, or by guiding the electromagnetic wave around the object. The guidance of the electromagnetic wave can be achieved by the transformation of the system in a way, that inside the cloak, the electromagnetic field will be equal to zero. In such a case, the region inside the cloak would disappear for certain wavelengths. Recently, a cloaking device for thermal invisibility was presented [144], and allowed the disappearance of the object for the propagating heat wave; however, the optical cloak is still very challenging.

Despite many difficulties related to the fabrication of metamaterials, the possibility of manipulation of electromagnetic radiation still attracts major attention and brings closer the realization of possible applications of metamaterials.

Chapter 3. Methods and experimental

In the following chapter, a method of design of experiment, sputtering and CNT synthesis equipment, and measurement equipment used in this work is introduced.

3.1. Taguchi method

The Taguchi method is one of the methods of design of experiments (DOE) which provide an efficient and systematic way to optimize the design for high performance, quality, and cost. Taguchi method allows for the definition of which controllable factors reduce the variation of results and make the product insensitive to changes caused by uncontrollable factors. In this method, parameters are set to minimize response variation, adjusting the results of the process on target at the same time.

The typical definition of quality is based on the minimum and maximum specification level of a certain parameter, in which the measured value of the product should be included. In other words, the measured value of the specific parameter should be in a certain range. In such approach, no information of the methods and techniques required to obtain such a result are presented. On the other hand, the quality defined by Taguchi is related to the minimum loss of the property of the product, by introducing a loss function. In the Taguchi method, the variation from the target decreases the quality of the product, which means that the variation should be reduced and loss function should ideally take the value of 0.

The optimization of the properties of the product by the Taguchi method should be considered in a few steps.

In the first step, the quality characteristic to be optimized is defined. The quality characteristic defines the variation of which parameters has the highest influence on the product quality. In this dissertation, the quality characteristic was defined by the average roughness and size of the catalyst particles in the first part of the research, and also by the total UV-VIS reflectance of thin CNT forest film in the second part of the research.

In the second part of the Taguchi method, the noise factors are identified. Noise factors are parameters which are uncontrollable or too expensive to control but still have an influence on the results and the quality of the product. Noise factors include changes of environmental

conditions, a variation of the parameters, and also a variation of the products prepared by the same design with the same input. In the CNT growth process, noise factors might be related to the vacuum chamber design, gas flow fluctuations, gas leaks, etc.

In the third step, the control parameters which have a significant effect on the quality of the final product are defined. Control parameters (factors) include all the parameters that can be set and easily changed, in order to control the process. For each control parameter, levels of the tested values have to be identified in order to improve the quality of the product. The number of parameters with associated values defines the experimental region in the Taguchi method.

Table 3.1. An example of an orthogonal array of L9 (3^4) matrix.

Experimental trail	Process parameters			
	A	B	C	D
1	1	1	1	1
2	1	2	2	2
3	1	3	3	3
4	2	1	2	3
5	2	2	3	1
6	2	3	1	2
7	3	1	3	2
8	3	2	1	3
9	3	3	2	1

In the next step, based on the defined experimental region, the design of the experimental matrix is conducted. In the Taguchi method, orthogonal tables of the experiment are selected (Table 3.1). The orthogonal array is a matrix of numbers arranged in columns and rows in a way that each pair of columns is orthogonal to each other. In the experiment, the row represents a value of each controlled parameter (A, B, C, D) in a given experiment, while each column represents a specific factor that can be changed between the experiments (1, 2, 3). In the orthogonal array, the effect of various parameters can be separated from each other.

After the selection of appropriate orthogonal array, the procedure of simulation of the variation of the quality characteristics is defined, based on the noise factors.

In the fifth step, the experiments prepared based on the orthogonal table are carried out. The Taguchi method can be used for any controllable process, in which the response of the variation of control parameters can be measured.

The sixth step of the optimization by the Taguchi method requires the identification of the optimal parameter configuration. In Taguchi method, the changes of the product properties dependent on noise factor (N – noise) are minimized and the changes dependent on signal factors (S – signal) are maximized. Taguchi method provides the statistical coefficient η, called signal-to-noise (SN) ratio, which is the logarithmic function of the desired output values. The SN ratio allows for the evaluation of the influence of process parameters on the properties of the final product. Taguchi method provides data that consists of statistically significant factors of the process and allows to find the optimum level of the parameters by using SN ratio analysis and experimental data analysis. Taguchi method utilizes 3 main optimization targets: the smaller-the-better; the larger-the-better and nominal-is-best. When it is preferable to minimize certain desirable properties of the product, the criterion 'the smaller-the-better' is used, and the equation for signal-to-noise ratio η is:

$$\eta = -10 \log_{10} \left(\frac{1}{n} \sum_{i=1}^{n} y_i^2 \right) \qquad \text{(eq. 3.1)}$$

In the case that it is preferable to maximize certain desirable properties of the product, the criterion 'the larger-the-better' is used for calculation, and the formula for η calculation is:

$$\eta = -10 \log_{10} \left(\frac{1}{n} \sum_{i=1}^{n} \frac{1}{y_i^2} \right) \qquad \text{(eq. 3.2)}$$

Furthermore, when it is appropriate to target the response for certain values, the criterion 'nominal-is-best' is used, and the equation for signal-to-noise ratio η is:

$$\eta = \log_{10} \left(\frac{\bar{y}_i^2}{\sigma^2} \right) \qquad \text{(eq. 3.3)}$$

In all equations, y_i is the primary response to the signals, n is the number of repetitions of each experiment, and σ^2 is the standard deviation.

In the Taguchi method, in order to define the optimum parameters, the highest SN ratio value is chosen for all 3 cases.

In the last step, the verification experiment, planned based on the optimum values of the optimized parameters, is conducted. In the case the Taguchi optimization process was designed properly, the highest quality should be observed.

One of the main advantages of the Taguchi method over the conventional methods is the possibility of the defining the sensitivity of each parameter and the interactions between individual parameters. Sensitivity analysis is performed in order to determine the mean values of experiment results when the means are widely dispersed. In such a case, the relation between input and output parameters should be proportional or linear. The better the linearity and the steeper the relation between input and output, the better the adjustability. Based on that, the slope is used as an equivalent to sensitivity. Analysis of the sensitivity allows a definition of parameters, which have the highest impact on the results. Constant SN ratio lines define the highest stability.

The analysis of interactions between individual parameters shows the condition in which the influence of factor on the parameters changes depending on the other factor. The analysis of interaction allows a more detailed analysis of optimum conditions of the optimization process. The interaction plot does not describe the degree of interaction; however, it provides many significant pieces of information about the process. The analysis of interactions supports the analysis of reproducibility, stability, and favorable combinations of parameters during the experiment, improving the overall quality of the product.

3.2. Magnetron sputtering

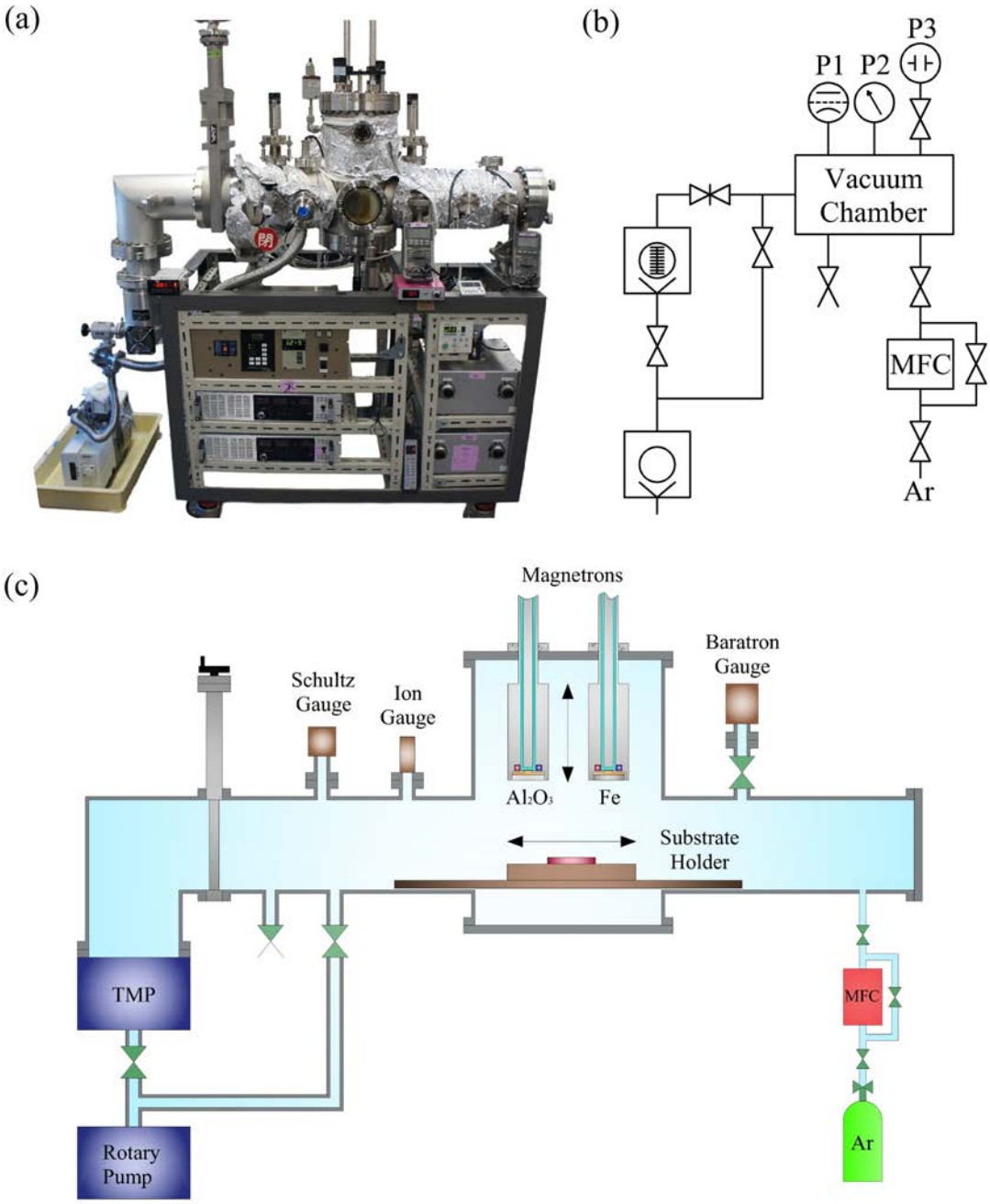

Figure 3.1. RF magnetron sputtering chamber (a) photo, (b) diagram, and (c) schematic representation.

A deposition of catalyst film for the growth of CNT forest was carried out using a radio frequency (RF) magnetron sputtering method. A photo, schematic representation, and diagram of the vacuum system are shown in Figure 3.1. In the majority of the experiments,

a 30 nm thick AlO_x support layer and a Fe catalyst layer of various thicknesses were deposited on electrochemically polished ($R_a \leq 0.15$ nm) p-type (100) silicon or aluminum foil substrates. A deposition chamber was equipped with an Al_2O_3 target of 99.99% purity (4N) and a Fe target of 99.99% purity (4N), 2 inches diameter each, mounted horizontally on the top of the chamber, 100 mm above the substrate holder. Argon gas of 99.9999% purity (6N) was supplied to the deposition chamber through a mass flow controller Horiba SEC-400MK3.

During the experiments, prior to deposition, samples were mounted on a substrate holder and introduced to a vacuum chamber. The evacuation of the chamber from the atmospheric pressure down to 100 Pa was conducted by a rotary vane pump and was followed by the evacuation by a turbomolecular pump (TMP) to a base pressure below 5.0×10^{-4} Pa. The value of the initial pressure was controlled by an active Pirani cold cathode vacuum gauge Balzers PKR 250, while the base pressure was controlled by an ionization gauge Canon Anelva MG–2F. During the pumping, the rotary pump was connected behind the TMP in order to remove gasses accumulated at the end of the pump. After the required vacuum was obtained, a water flow was introduced to the back of the magnetrons for the purpose of cooling the cathodes, while Ar gas flow of 25 sccm was introduced into the chamber through mass flow controller. The deposition pressure of 0.8 Pa was achieved by a partially closed flap valve, situated between the chamber and the pumping system, which allowed balancing of the flow of Ar gas and the pumping speed. The control of deposition pressure was conducted by the ionization gauge and a capacitance manometer gauge MKS Baratron 626A. After the stabilization of pressure was achieved, the substrate holder was moved away from the deposition area. In order to remove impurities and contaminations from the surface of the Al_2O_3 cathode, a process of target cleaning was performed for 10 min. The deposition was performed using the RF power supply and impedance matching network, with a typical frequency of 13.56 MHz and power of 50 W. After the cleaning process was stopped, the substrate holder was moved under the cathode, and sputtering of 30 nm thick AlO_x support layer was conducted. Afterwards, the holder was moved away and the presputtering of Fe target was carried out for 5 min. Similar as in the case of alumina, the substrate holder was moved under the Fe target and the deposition of Fe catalyst occurred. The deposition of Fe was conducted using RF power supply and power of 25 W. In several experiments, during

the deposition of AlO_x film, a polarization potential (bias) was applied through the direct contact of insulated substrate holder with a polarized electrode. After the deposition, Ar gas flow and water flow were stopped, and the air was introduced into the chamber by ventilation valve. The deposition rates of AlO_x and Fe films were investigated using an ellipsometry method, which allowed precise calculation of the deposition time required for the deposition of each layer. During that time, the changes in the thickness of the alumina and iron targets were observed and required systematic revisions of the sputtering rate of the catalyst.

3.3. Chemical vapor deposition

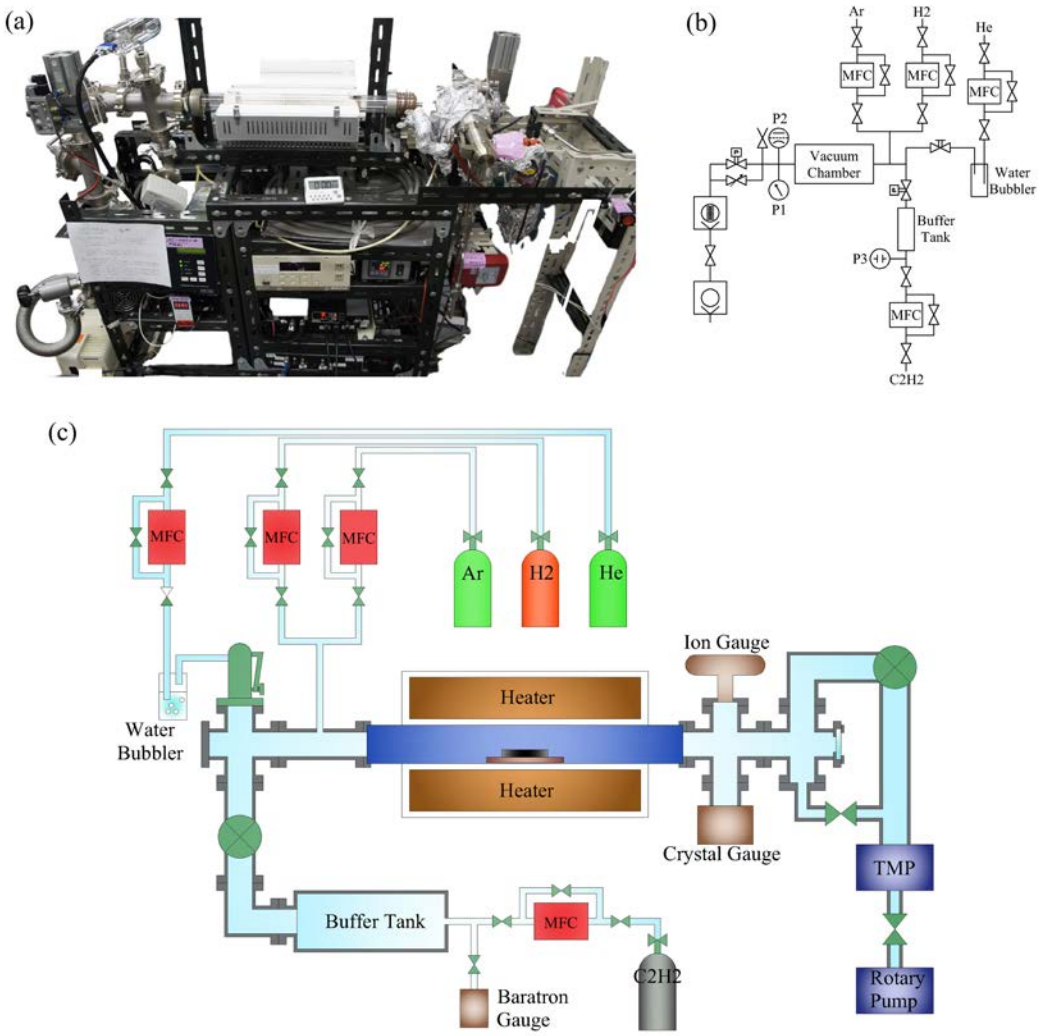

Figure 3.2. Thermal CVD chamber (a) photo, (b) diagram, and (c) schematic representation.

A growth of CNT forest was conducted using a thermal catalytic chemical vapor deposition (CCVD) method on the as-prepared AlO_x/Fe catalyst deposited by the RF magnetron sputtering method described in chapter 3.2. An image, schematic representation, and diagram of a CVD chamber are shown in Fig. 3.2. The CVD chamber was composed of a pumping system, a quartz vacuum chamber, and a buffer tank. The pumping system was used for the evacuation of the CVD chamber and was built with a rotary vane pump and a turbomolecular pump (TMP). The CVD chamber – a 50 cm long quartz tube furnace with an outer diameter of 5 cm was connected to the pumping system from one side and buffer tank from the other side, through the set of pneumatic and manual valves.

At the beginning of the CVD process, samples mounted on a substrate holder were inserted into the quartz tube and the chamber was evacuated. The pumping process started from the evacuation of the chamber by the rotary pump to the initial pressure below 100 Pa. This process was followed by the evacuation by the TMP to a base pressure of $<5\times10^{-4}$ Pa. The value of initial pressure was controlled by a crystal gauge Canon Anet M-320XG, while the base pressure was controlled by a hot-filament ionization gauge Canon Anelva BRG-1B. During the pumping, a heating of 120°C was applied to the quartz tube, while a water cooling was applied to the connections between the quartz tube and a metal piping in order to avoid the overheating of the rubber O-rings. In most of the cases, the pumping was applied to the entire vacuum chamber, including the buffer tank and gas lines. After the evacuation, a number of valves was closed to separate the buffer tank and gas lines from the vacuum chamber, and the further heating of the quartz tube in vacuum was conducted with a temperature ramping speed of 60°C/min, until the process temperature was reached. The typical value of temperature between 600 and 820°C was dependent on the experimental conditions. After the heating, an annealing process was carried out in vacuum, argon, hydrogen, or hydrogen/argon atmosphere, for various, precisely controlled times, depending on the requirements of the experiment. After the annealing process, the growth of CNTs was conducted using acetylene (C_2H_2) gas as a carbon source. The introduction of acetylene was carried out using the buffer tank presented in Fig. 3.2. First, the acetylene was introduced to the buffer tank until a certain value of pressure, controlled by a capacitance manometer MKS Baratron 626B, was obtained. After that, the pneumatic valve was automatically opened,

introducing the gas into the chamber, allowing the achievement of the required growth pressure, in a step function behavior, instead of slow increase from base to CNT growth pressure. In some cases, during the CNT growth, a hydrogen and/or helium/water vapor mixture were also introduced to the chamber with various ratios to C_2H_2. The growth time was controlled from several seconds, up to two hours. Gasses used during the process were supplied to the chamber through mass flow controllers (MFC), allowing precise flow control. Hydrogen was supplied using Horiba SEC-B40 controller, argon using Fujikin FCST 1005C controller, water/helium mixture using Horiba SEC-400MK3 controller, and acetylene using Fujikin FCST 1005LC controller. After the CNT growth process, the CVD chamber was cooled down to the room temperature by an external air flow, usually for 30 min. Finally, the turbomolecular pump was stopped, valves to the buffer tank, pump, and gas lines were closed, and the substrate holder was removed from the chamber.

The purities of argon, hydrogen during annealing, and helium and acetylene during growth, were 99.9999% (6N), 99.99999% (7N) and 99.999% (5N), 99.999% (5N), respectively.

3.4. Measurements

3.4.1. FE-SEM

The microscopic analysis was conducted using field emission scanning electron microscope (FE-SEM) JEOL JSM-5310 (Fig. 3.3). The FE-SEM provides elemental information about topography and morphology at magnification from 25× to 500 000×, with a very high depth of field. The FE-SEM produces a less distorted and clearer image than conventional SEM, with a very high spatial resolution, up to single nanometers. A field-emission cathode in an electron gun provides narrower electron beams at low and high electron energy, resulting in an improved spatial resolution and minimized charging and damage of the sample.

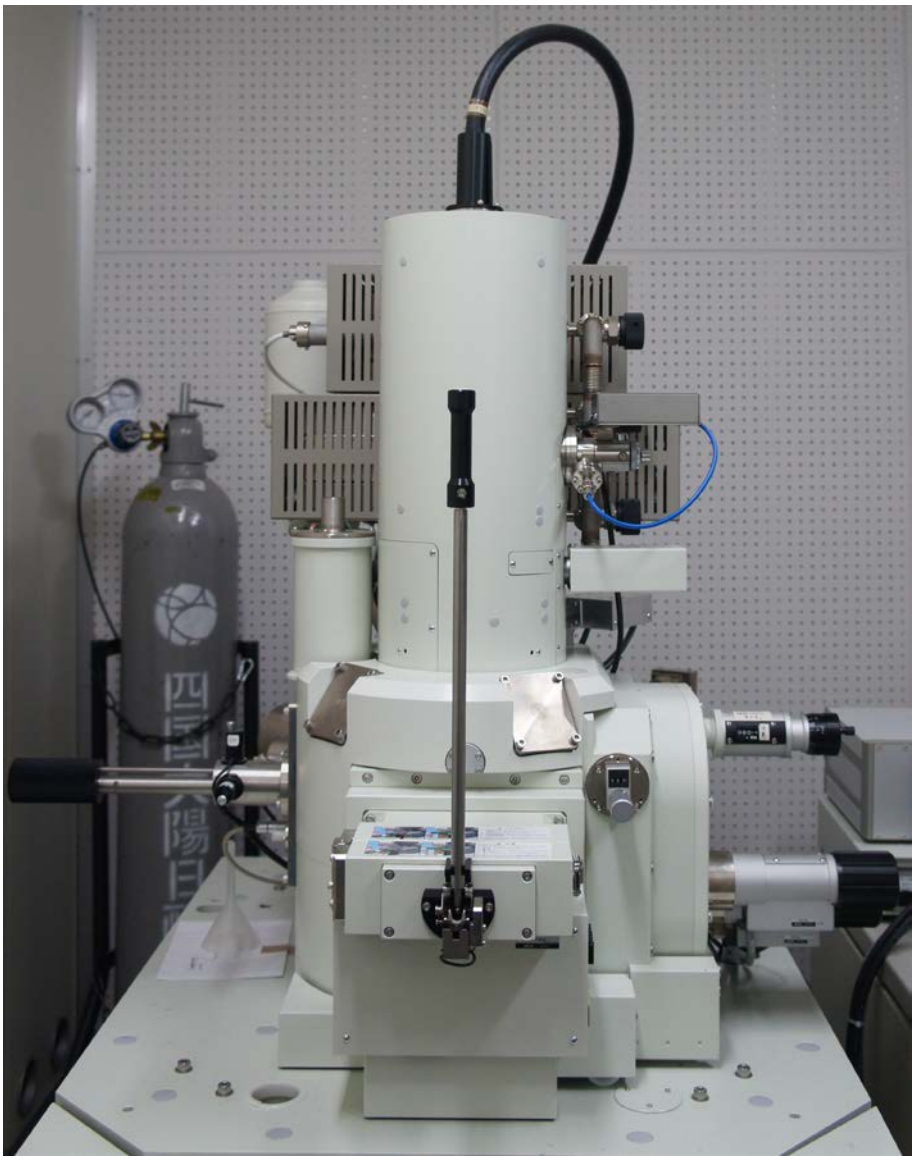

Figure 3.3. Field Emission Scanning Electron Microscope JEOL JSM-5310.

The FE-SEM observations of CNTs included measurements of the height of CNT forest, diameter for MWNTs and density. High-magnification images of bundles and individual nanotubes were used for the calculation of the CNT forest density and alignment. The FE-SEM was also used for the observation of Fe catalyst particles in the series of experiments related to the optimization of catalyst formation conditions. Additionally, the quality of the FIB patterns fabricated on the catalyst surface and after growth of CNTs was investigated

using FE-SEM imaging. The accelerating voltage of 5 kV and the electron beam current of about 22 μA were used during a majority of measurements.

3.4.2. AFM

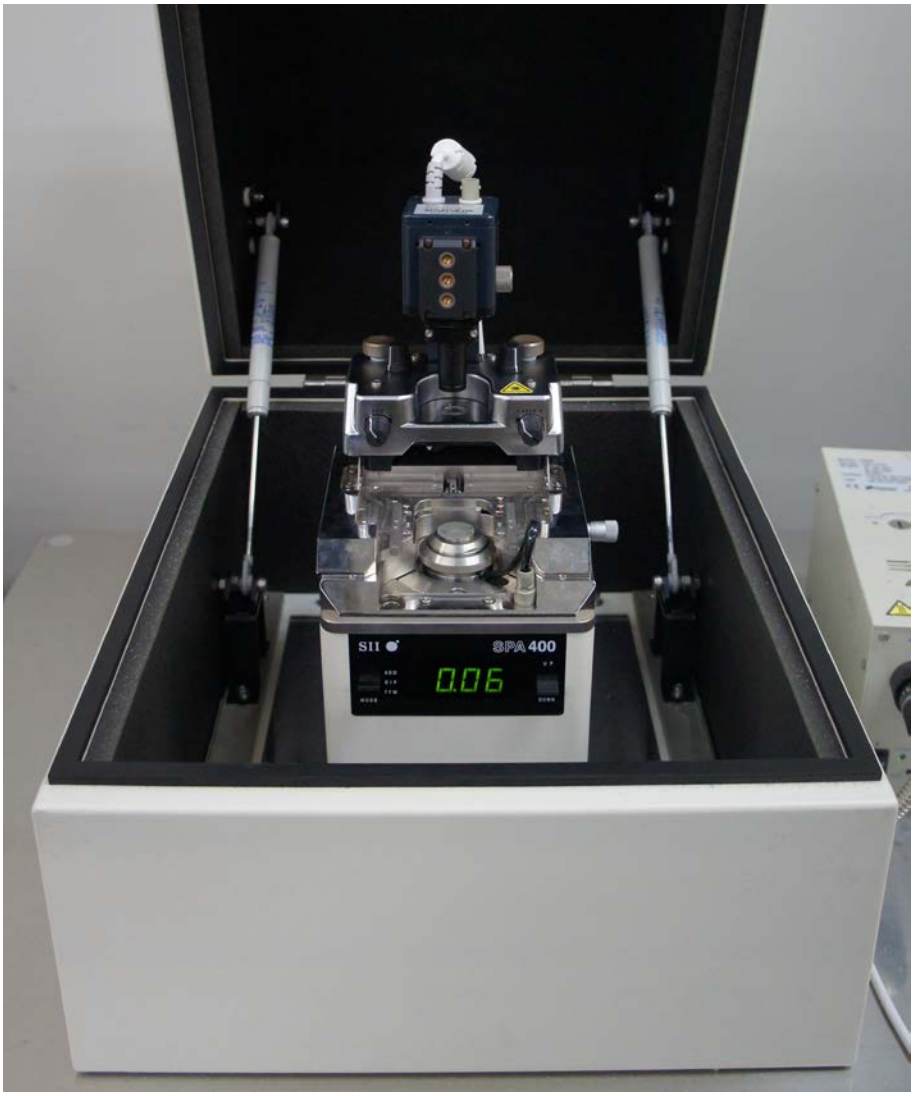

Figure 3.4. Atomic Force Microscope SPI3800N/SPA400, SII Nanotechnology Inc.

The morphology of catalyst surface was determined by an Atomic Force Microscope (AFM) SPI3800N/SPA400, SII Nanotechnology Inc. (Fig. 3.4), using a tip with a diameter of 10 nm, in a Dynamic Force Microscopy (DFM) mode. The AFM belongs to the group of scanning probe microscopes, designed for the purpose of measurement of local properties, such as roughness, height, magnetism, etc. The operation of the AFM is based on the

measurement of interaction force between the tip and the sample and allows very high vertical resolution up to 0.1 nm. To acquire the image, the measurement of vertical and lateral deflections of the cantilever, using the optical lever, is conducted. A laser beam reflected from the surface of the cantilever is directed into a position-sensitive photodetector and based on the gathered signal, the position of the laser spot and thus the angular deflection of the cantilever is defined.

The AFM was used for the measurements of the average surface roughness and size of catalyst particles during the experiments of optimization of the catalyst formation conditions. Furthermore, the AFM was used for the investigation of the influence of the FIB patterning on the catalyst surface morphology, by defining the changes of the surface, in the cases when a FIB secondary etching was applied. The AFM measurements were carried out using: vibration frequency of ~138 kHz, vibration voltage of around 1 V, I gain of 0.4 and P gain of 0.2.

3.4.3. TEM

A transmission electron microscope (TEM) allows measurements of structures as small as single nanometers. A high energy electron beam is focused into a small, coherent beam by a condenser lens which restricts the beam by excluding high angle electrons. The electron beam is then focused on the sample and partially transmitted and projected by an objective lens on a phosphor screen or a CCD camera. The transmission of the electrons depends on the thickness and electron transparency of the sample. The image is generated by the electrons which strike the screen and based on the amount of the transmitted electrons, the darker and brighter areas can be distinguished. Due to the interactions between the electrons and the atoms of the investigated material, it is possible to observe nanoscale features such as crystal structure, dislocations, etc.

Figure 3.5. Transmission Electron Microscope JEOL JEM 2100M.

In this dissertation, the transmission electron microscope JEOL JEM 2100M was used (Fig. 3.5) for measurements of the diameter of CNTs during experiments of the optimization of the catalyst formation conditions. CNTs dissolved in ethanol were placed on a copper grid covered with thin graphite film. Due to the high resolution, it was possible to observe and measure the diameter of SWNTs obtained throughout the series of experiments. The typical

parameters of the TEM operation were working pressure $<2\times10^{-5}$ Pa and accelerating voltage of 300 kV.

3.4.4. Raman

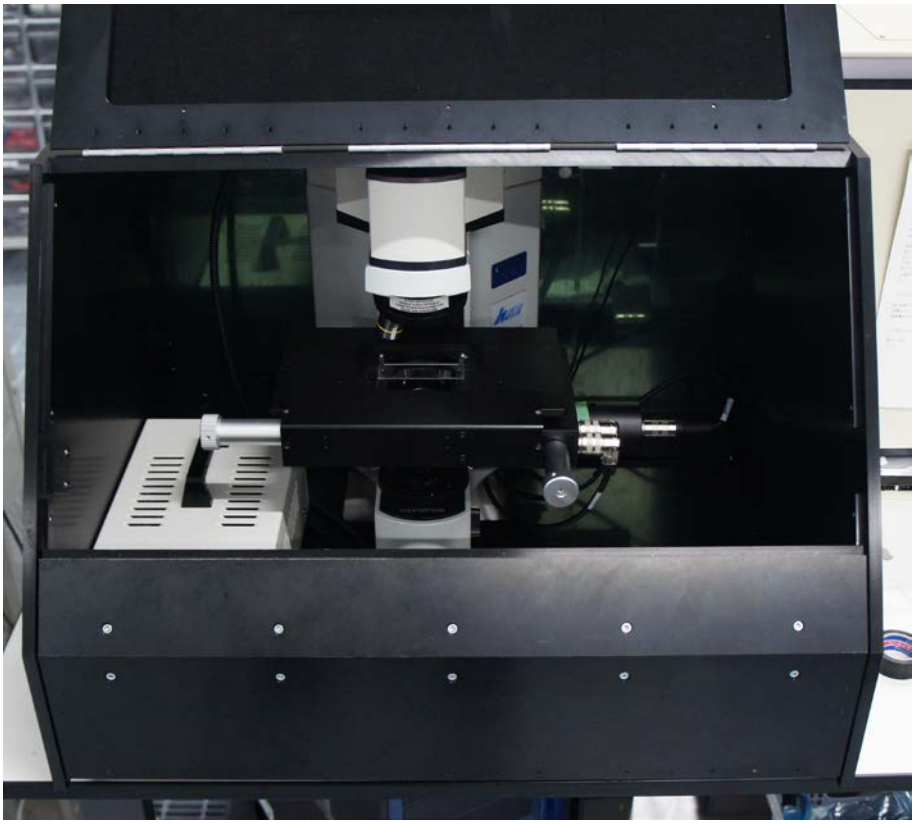

Figure 3.6. Micro-Raman spectrometer HORIBA JOBIN YVON HR-800.

Raman spectroscopy is based on an inelastic scattering of monochromatic light. During the measurement, a majority of the scattered light has the same frequency as an incident beam (Rayleigh or elastic scattering), while in the inelastic scattering the frequency of photons in the light changes upon an interaction with the sample. Photons of the monochromatic light are absorbed by the sample, reemitted with different frequency, and shifted up (Stokes radiation) or down (anti-Stokes radiation), as compared to the original frequency. An increase or decrease of the energy is connected to the vibration energy level in the electronic state of molecules and observed Raman shift is a direct measurement of the energy. Raman shift provides information about vibrational, rotational and other transitions in molecules.

Furthermore, Raman spectroscopy is a very good tool to measure bands of symmetric linkages, allowing detailed analysis of the structure of CNTs.

For Raman structural and quality analysis of CNT forests, micro-Raman HORIBA JOBIN YVON HR-800 spectrometer was used, with a laser excitation of 532.08 nm, shown in Figure 3.6. The intensity of laser light reaching the substrate was controlled by a neutral-density (ND) filter and a magnification of the objective lens. Moreover, during Raman analysis, the incident laser light beam of the diameter of 2 μm and intensity of 50.4 $\mu W/cm^2$ was maintained. For each measurement, height calibration by p-type Si substrate was carried out in order to evaluate the improvement of intensity. In presented work, Raman analysis was conducted in all parts of the research in order to evaluate the type of CNTs (SWNT, DWNT, or MWNT), the crystallinity, a number of defects and the type of conductivity (semiconducting or metallic) of CNTs. Moreover, Raman spectra were used for the evaluation of the diameter of SWNTs from the obtained radial breathing mode (RBM) bands.

3.4.5. UV-VIS spectroscopy

Figure 3.7. UV-VIS spectrometer HITACHI U-3900.

An ultraviolet-visible (UV-VIS) spectroscopy allows measurements of absorption, reflectance, and transmission of light in the near-UV, optical and near-infrared (NIR) regime. A light beam is directed on the sample and due to the structure of the material, the radiation is partially absorbed while the rest is reflected and transmitted. The absorption of UV-VIS light is related to the excitation of outer electrons. Energy absorbed by atoms or molecules results in the excitation of the electrons to a higher energy orbitals. The amount of the absorbed energy, which is used for electron excitation, defines the total absorption of a material.

During the research, the total reflectance of CNT forests in UV-VIS region was measured by a HITACHI U-3900 spectrometer, shown in Figure 3.7. For the measurements of the total UV-VIS reflectance of CNT forest, the integrating sphere was used and the incident light beam with an angle of 10° was directed at the sample. The obtained spectra were calibrated for the Al_2O_3 samples. Due to the fact that the growth of the CNTs was performed on the Si samples, it was assumed that the transmission of light was 0%, in all cases. Spectra of the total UV-VIS reflectance of CNT forests were used in the experiments of the optimization of the total reflectance for thin CNT forest.

3.4.6. FT-IR, FT-IR microscope

Figure 3.8. Fourier transform infrared spectrometer (FT-IR) JASCO FT/IR-6100.

An infrared (IR) spectroscopy is used to determine a molecular structure with a characteristic absorption of infrared radiation. During measurements, the infrared radiation is selectively absorbed, in specific wavelengths, by atoms and molecules of a material, causing the change of dipole moments of molecules. Due to the absorption of the infrared radiation, the vibrational energy levels are transferred to the excited state, and absorption peaks, related to the vibrational energy gap, appear. The intensity of absorption depends on the change of the dipole moment and the transition of energy levels. By analysis of the IR spectra, it is possible to obtain information about the structure of the molecule. The Fourier transform IR (FT-IR) spectroscopy allows measurements with very high resolution and in a very wide range. Furthermore, in the FT-IR spectrometry the signal-to-noise ratio of obtained spectrum is increased and due to that, the accuracy of the wavenumber is also improved.

In the presented work, the infrared reflectance spectra of bulk structure of CNT forest without metamaterial patterns were obtained using a Fourier transform infrared spectroscopy (FT-IR) JASCO FT/IR-6100, with an incident angle of 15°, which is shown in Figure 3.8.

The reflectance spectra were normalized to the Si substrate. The measurements of the CNT metamaterial patterns were carried out by the FT-IR spectrometer (JASCO FT/IR 660 PLUS) combined with an IR microscope JASCO IRTRON IRT-30, with an incident light perpendicular to the surface of the samples. A 28 μm diameter circular measurement area was defined by an aperture in the light path of the IR microscope. The reflectance spectra were normalized to the Si substrate. For both FT-IR spectrometers, during the measurements of reflectance, no polarization of the incident light was applied.

3.4.7. Focused ion beam

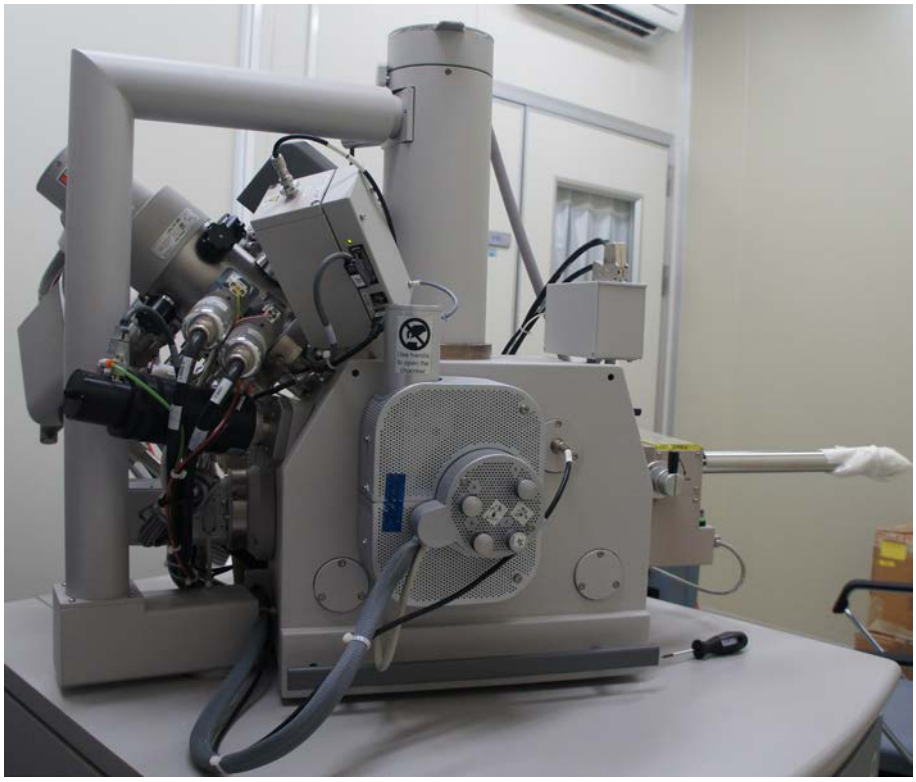

Figure 3.9. Focused Ion Beam system FEI QUANTA 3D 200i.

A focused ion beam (FIB) method allows the patterning of the surface of various materials with a resolution of tenths of nanometers. The FIB method is maskless and by precise control of energy and intensity of the beam, allows fine fabrication of various depths, size and shape of patterns; however, due to sputtering, the redeposited material can be observed on the surface of patterns. The ion beam is directed perpendicularly to the sample and focused on the surface by a series of lenses. A high-energy ion beam reaching the

substrate surface sputters the sample and allows precise milling of the specimen, down to single nanometers. The diameter of the ion beam and the lateral resolution of the FIB milling depends on the applied ion current. The FIB imagining is also possible for the low-energy ion beams.

The fabrication of patterns was conducted after the deposition of the catalyst, before the CNT growth. For that purpose, the FEI QUANTA 3D 200i FIB system was used and is shown in Figure 3.9. The total patterned area varied from 10×10 μm to 30×30 μm and contained structures of various sizes (0.8×0.8, 1×1, and 2×2 μm) and shapes (SRR, asymmetric split resonators (ASR), L-shape, squares, etc.). The fabrication of patterns was carried out utilizing prepared bitmap designs and was followed by a FIB secondary etching process, applied to the entire patterned area, including the prepared structures. The fabrication of metamaterial structures was conducted with a patterning depth of 10 nm in order to remove the top layer of catalyst and support layer with diffused Fe particles. The optimized depth of secondary etching was 0.6 nm. The secondary etching process was applied in order to remove the redeposited material from the surface of the patterns and to smoothen the catalyst surface. The FIB fabrication was conducted with 30 pA, 30 kV Ga ion beam.

Chapter 4. Optimization of catalyst formation conditions for growth of SWNTs

4.1. Introduction

To achieve the desired properties of CNTs, various methods of CNTs synthesis are used. Of the methods mentioned in chapter 2, the most popular are arc-discharge, laser ablation and chemical vapor deposition (CVD), among which the CVD method is the most commonly used [54]. Catalytic CVD method is a simple and inexpensive way to grow CNTs at a low temperature and an ambient pressure. The catalytic CVD provides higher yields and higher purity levels of grown nanotubes and allows for easier control of growth parameters and structures of CNTs [13]. Also, the equipment used for growth is easy to modify, causing an expansion and advances in development of CVD methods, such as: thermal CVD, Plasma Enhanced CVD (PECVD) [67], water-assisted (super growth) CVD [2] and others. However, despite the advantages of the CVD method, many problems associated with high-density growth of single-walled CNTs (SWNT) exist [145].

Although many years have passed since the discovery of CNTs, it remains difficult to fabricate high-density and long SWNT forests, due to the influence of the many process parameters on the growth process [73,146–148]. One of the most important factors is the annealing process, which allows for the formation of the catalyst nanoparticles which govern the diameter of CNTs [73,149]. Also, the density of the formed catalyst particles influences the density of the CNTs forest. Although many experiments have been conducted, the mechanisms of catalyst formation are not clear. For example, Sakurai *et al.* [150] explained the formation of the catalyst particles by interpretation of the role of subsurface diffusion and Ostwald ripening phenomena. In their work, the Ostwald ripening was shown to be the main cause of elimination of small particles and subsurface diffusion was the cause of the reduction in the size of larger particles, giving the high uniformity of the catalyst size. However, to utilize those phenomena in the catalyst formation process, complicated calculations are needed [151]. These complex calculations require additional time and make modifications of the process even more difficult.

The growth of CNT forest may cause many difficulties in finding optimum growth parameters, reproducibility, and mass-production, related to the large number of parameters influencing the growth during the synthesis process. Testing possible parameters separately and choosing the proper values of the CNTs growth can be a time-consuming process, which can give us a local minimum. However, there might still be a possibility of the existence of better values, which would require a large number of experiments using standardized procedures to confirm all possibilities. One of the many possible solutions to decrease the number of experiments is to apply optimization methods to the design of the experiment parameter matrix [152]. This method allows the screening of the factors and determines which parameters are important for explaining process variation. A statistical approach allows for the systematic investigation of the process and the parameters that influence the quality of the final product [153–155]. Identification of significant factors leads to improvements in the manufacturability, reliability, and quality of a product.

4.2. Objectives

In this part of the research, a statistical approach of designing CNTs growth experiments using the Taguchi method in a small number of experiments, developed to control the size and roughness of the catalyst particles after annealing process, will be presented. The study focus on the determination of the optimum parameters and mechanisms of formation of the catalyst, which determines the diameter of the CNTs. The growth of CNTs involves various steps, which cause high noise and low reproducibility of the process [156,157]. By employing the Taguchi method, it is possible to remarkably decrease or eliminate negative effects of the production process through a statistical approach. Using the Taguchi orthogonal arrays, we were able to dramatically decrease the number of experiments from 4^4 (= 256) to 16, while at the same time keeping accuracy high.. Due to the fact that all of the annealing parameters in the design were weighted equally, we were able to evaluate all factors independently, so the effect of one parameter did not influence other parameters. The aim of the experiments was to reduce the average surface roughness and size of the particles after the annealing process, based on the Taguchi method of designing experiments. Further, the physical

properties of CNT forests grown with the optimized parameters were measured and the effect of the various annealing parameters on CNTs growth is discussed.

4.3. Experimental and methods

The deposition of the catalyst and growth of CNTs was performed accordingly to methods described in chapter 3.2 and 3.3.

Based on the Taguchi method, described in chapter 3.1, an orthogonal table [158] of experiments (Table 4.1.), various temperatures, gases flow rates of argon and hydrogen, and annealing times were used. After vacuum annealing, the growth of CNTs was performed using only acetylene gas (C_2H_2) with a flow rate of 10 sccm at 54 Pa partial pressure for 10 min. No additional gases were used. Based on previous reports [159,160], the annealing parameters (ref. standard) used during the growth of CNTs were: an annealing time of 3.5 min, temperature of 730°C, hydrogen and argon flow rates of 0 sccm. These parameters were used as a base for the Taguchi optimization process, as a starting point to decrease the diameter of CNTs [161].

The optimization experiments of the catalyst formation during the annealing process has been planned and carried out according to the Taguchi design. The parameters optimized during the series of experiments were prepared using the orthogonal table L16 (4^4) – four process parameters with four different values. The parameters optimized in this research were: 1) annealing time (t_{AN}), 2) hydrogen flow rate (f_{H2}), 3) annealing temperature (T_{AN}) and 4) argon flow rate (f_{Ar}). For each parameter, four values were tested, which are summarized in Table 4.1. Argon and hydrogen were used as annealing atmospheres with different ratios. Based on the Taguchi orthogonal table design L16 (4^4), a 16 experiment plan was prepared and is presented in detail in Table 4.2.

Table 4.1. The optimized parameters and their value level applied in the experiments

No.	Parameter optimized	Variability interval			
		1.	2.	3.	4.
1)	Annealing time (t_{AN}) [min]	1	2.5	4	5
2)	Hydrogen flow rate (f_{H2}) [sccm]	0	35	65	100
3)	Annealing temperature (T_{AN}) [°C]	730	760	790	820
4)	Argon flow rate (f_{Ar}) [sccm]	0	20	40	60

The aim of the optimization was to decrease the size of catalyst particles and to decrease the surface roughness, which should influence the final diameter of the CNTs grown on the catalyst. After the experiments listed in Table 4.2 were conducted, a verification experiment was performed, which allowed fine tuning of the annealing process. Within the described research, the computer software Minitab 17 developed by Minitab® Inc. [162] was used for planning the experiment, for statistical analysis of the results, and for computing the optimal parameters of the annealing process.

The characterization of the catalyst and CNTs was conducted using three methods described in chapter 3 - FE-SEM, AFM, and TEM.

Table 4.2. Plan of experiments prepared according to the Taguchi orthogonal table L16 (4^4).

Experiment number	Parameters values			
	Annealing time (t_{AN}) [min]	Hydrogen flow rate (f_{H2}) [sccm]	Annealing temperature (T_{AN}) [°C]	Argon flow rate (f_{Ar}) [sccm]
1.	1	0	730	0
2.	1	35	760	20
3.	1	65	790	40
4.	1	100	820	60
5.	2.5	0	760	40
6.	2.5	35	730	60
7.	2.5	65	820	0
8.	2.5	100	790	20
9.	4	0	790	60
10.	4	35	820	40
11.	4	65	730	20
12.	4	100	760	0
13.	5	0	820	20
14.	5	35	790	0
15.	5	65	760	60
16.	5	100	730	40

4.4. Results and discussion

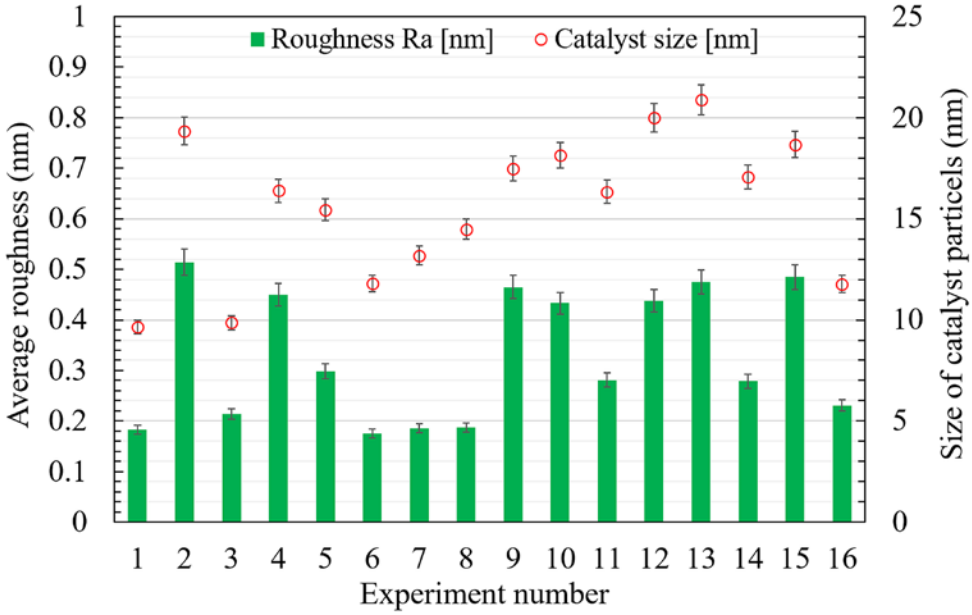

Figure 4.1. Average catalyst surface roughness and diameter of Fe catalyst particles in 16 experiments at selected parameters in Table 4.2 [161].

The goal of the experiments, presented in this part of the research, was to decrease the size of the particles and the surface roughness of the iron catalyst after the annealing process, based on the Taguchi method. Figure 4.1 shows the average roughness of the catalyst surface and the average size of the particles after annealing under different conditions, which were set according to the Taguchi orthogonal table (Table 4.2). Due to a wide range of tested parameters, the results of measurements achieve different values, without a strong correlation between them. The highest average roughness was measured for experiment 2 (0.51 nm), while results show the lowest value of 0.17 nm for experiment 6. At the same time, the highest and the lowest values of the average size of the catalyst are 20.9 nm and 9.7 nm, for experiment 13 and experiment 1, respectively.

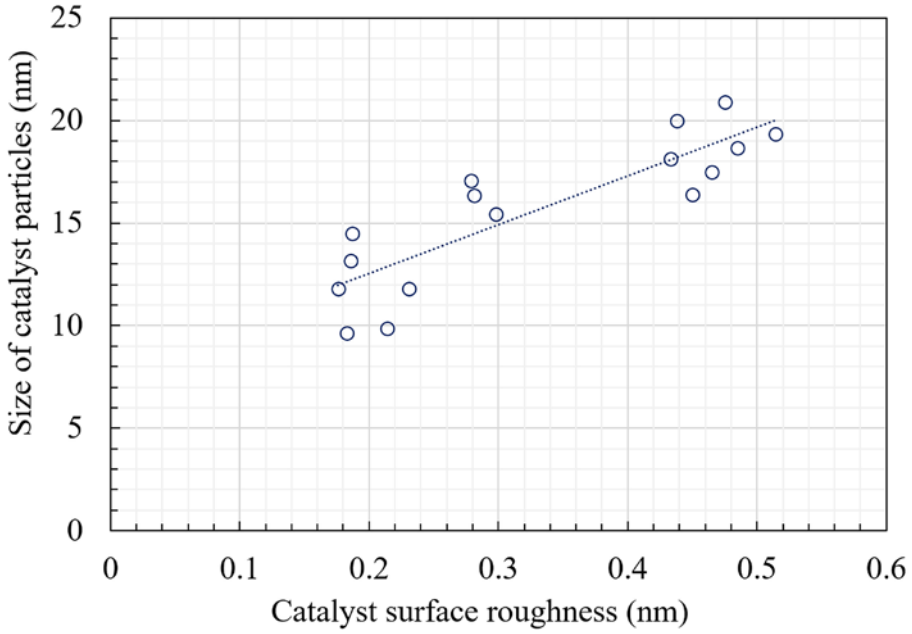

Figure 4.2. Dependence of average surface roughness and size of Fe catalyst particles.

As can be seen in Figure 4.2, changes in the annealing conditions caused similar types of changes in both the average size of the catalyst particles and in the roughness of the catalyst surface. With the growth in size of the catalyst particles, the roughness of the surface also increased. It can be assumed that both catalyst surface roughness and the size of the catalyst particles play similar roles in the growth of CNTs [73,147]. Further, roughness and size of the catalyst particles were analyzed, by dividing the experiments into 4 groups, according to the annealing time during the experiments.

Figure 4.3(a) shows the plot of roughness measurements of catalyst surfaces of the first four experiments performed with a fixed annealing time t_{AN} of 1min, according to the Taguchi plan of experiments (Table 4.2). Experiment 1 (Fig. 4.3(a) – blue curve) presents a catalyst surface with small, barely distinguishable, single particles. The average diameter of the particles was d = 9.7 nm and the roughness was R_a = 0.18 nm. Figure 4.3(b) shows an AFM image of experiment 1, which demonstrated the lowest average roughness and the lowest average size of particles among the experiments with an annealing time of 1 min.

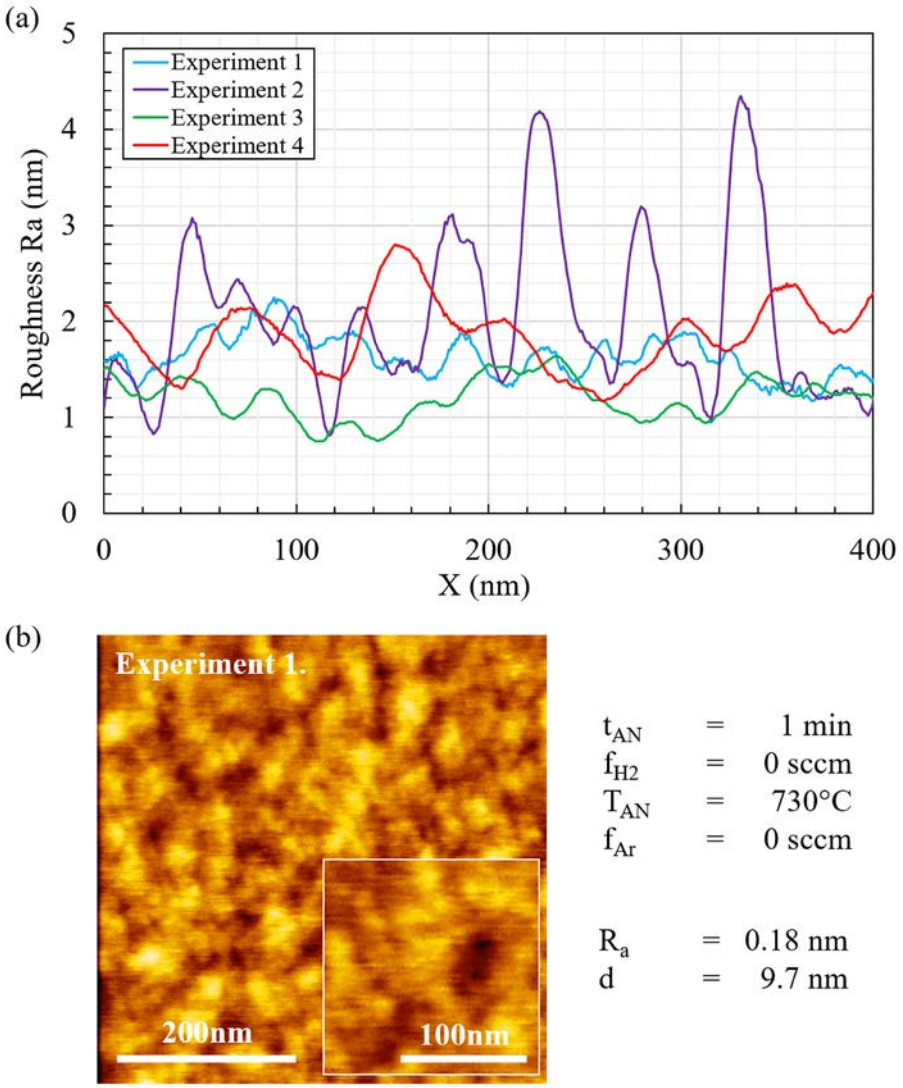

Figure 4.3. (a) AFM line profiles of Fe catalyst particles after annealing process for Taguchi experiments 1-4, (b) AFM scan of surface of experiment 1, with process parameters and results of measurements. (t_{AN} – annealing time, f_{H2} – H_2 flow rate, T_{AN} – temperature, f_{Ar} – Ar flow rate, R_a – roughness, d – average diameter). Fixed parameter in Exp. 1-4 was the annealing time of 1 min [161].

In experiment 2 (Fig. 4.3(a) – violet curve), the rapid growth of catalyst particles was observed. During the annealing, hydrogen gas was introduced to assists with the catalyst iron oxides (Fe_2O_3, Fe_3O_4. FeO) reduction to pure metallic Fe particles. Hydrogen influences the subsurface diffusion processes and helps in catalyst particles formation at the same time by increasing the surface mobility [163,164]. As can be seen, in this case, both the mean

diameter of the particles (d = 19.3 nm) and the surface roughness (R_a = 0.51 nm) exhibit high values, which are not suitable for the growth of SWNTs [165].

In experiment 3 (Fig. 4.3(a) – green curve), a decrease in roughness (0.21 nm) and particle size (9.9 nm) is observed. Due to a high temperature which causes higher subsurface diffusion, and higher hydrogen flows which reduce oxidized Fe [163], increasing surface mobility at the same time, smaller particles are formed [164]. On the other hand, in experiment 4 (Fig. 4.3(a) – red curve), a further increment of temperature and gas flow seem to cause substantial growth of particles. It is assumed that around a temperature of 820°C, the Ostwald ripening phenomenon has a higher impact on the particles formation than subsurface diffusion. In addition, higher flows of argon gas decrease the total partial pressure of hydrogen, which also decreases its influence on the formation and final size of Fe particles (16.4 nm) and surface roughness (0.45 nm).

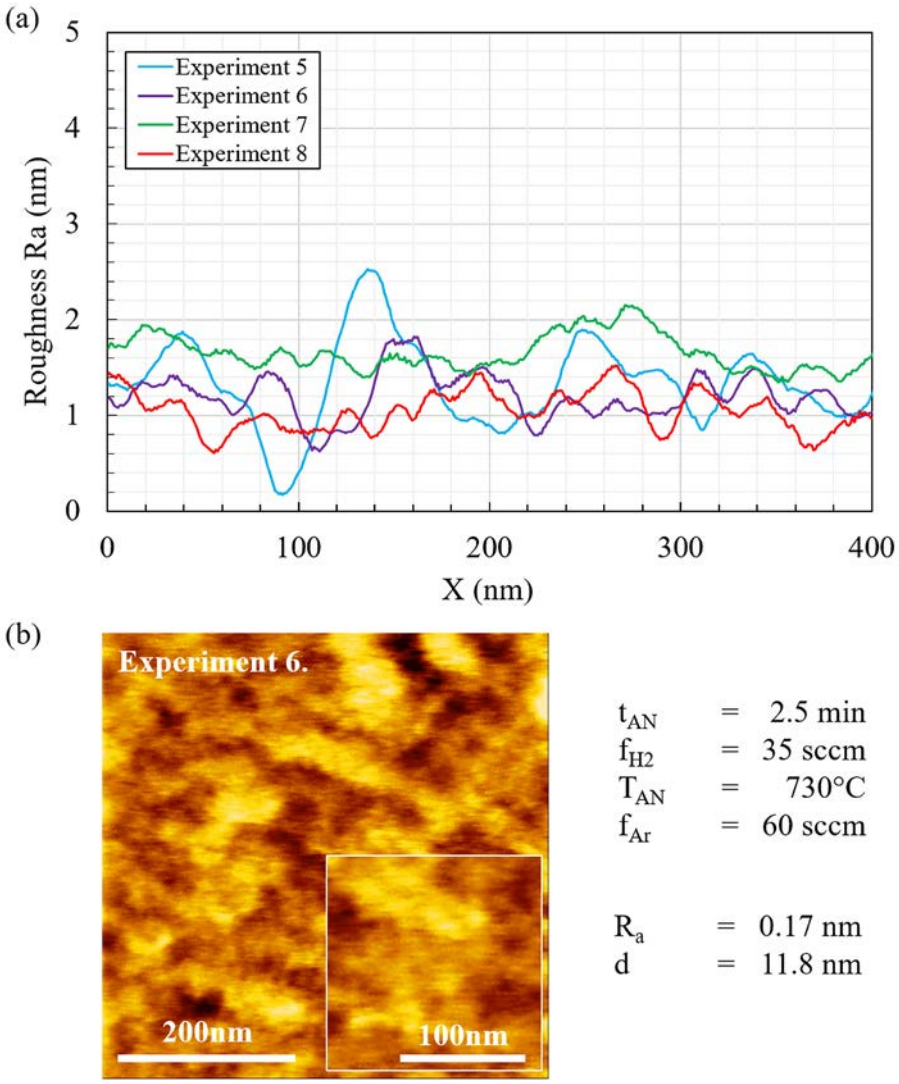

Figure 4.4. (a) AFM line profiles of Fe catalyst particles after annealing process for the Taguchi experiments 5-8, (b) AFM scan of surface of experiment 6, with process parameters and results of measurements. Fixed parameter in Exp. 5-8 was annealing time of 2.5 min [161].

Figure 4.4(a) shows the AFM line profiles of Fe thin films after annealing for runs 5-8, based on the Taguchi plan of experiments (Table 4.2). Experiment 5 (Fig. 4.4(a) - blue curve) presents catalyst surface after annealing with relatively large, distinguishable particles. The average roughness R_a = 0.3 nm and the average particles diameter of 15.4 nm in Exp. 5 are the effect of annealing in a temperature of 760°C for 2.5 min in the Ar atmosphere. The presence of argon gas during the annealing, according to Pisana *et al.* [149], helps in

decreasing the size of the catalyst in a small degree. Experiments 6-8 (Fig. 4.4(a)) exhibit similar values of average roughness and particle diameters; however, the mechanisms behind such results are slightly different in each case. In experiment 6, because of the relatively low temperature and the hydrogen/argon atmosphere of annealing, formation of small diameter particles (d = 11.8 nm) with the lowest average surface roughness (R_a = 0.17 nm) was possible, which is shown in Figure 4.4(b). In experiment 7, the annealing process was performed at 820°C in a hydrogen atmosphere. Due to this fact, the expansion of the catalyst particles, caused by the influence of the Ostwald ripening effect, was suppressed, giving the particles an average diameter of 13.2 nm and a roughness of 0.19 nm. Experiment 8 was also performed in a relatively high temperature of 790°C and in a mixture of hydrogen and argon. It is believed that the influence of hydrogen on the formation of the catalyst particles was reduced due to the argon flow, which decreased the partial pressure of hydrogen, increasing average roughness (R_a = 0.19 nm) and the size of Fe particles (d = 14.5 nm).

Figure 4.5(a) shows the AFM line profiles of experiments 9-12 based on the Taguchi plan (Table 4.2). The fixed parameter in experiments 9-12 is an annealing time of 4 min, which caused a significant increase in both the average diameter of particles and roughness. In experiment 9 (Fig. 4.5(a) – blue curve), due to a relatively high temperature, a longer time of process and annealing in an argon atmosphere, the average size of the particles (d = 17.5 nm) and roughness (R_a = 0.47 nm) exhibit higher values. A higher temperature and a longer annealing time without hydrogen supported the Ostwald ripening process during annealing and enhanced the increment of the size of particles and surface roughness.

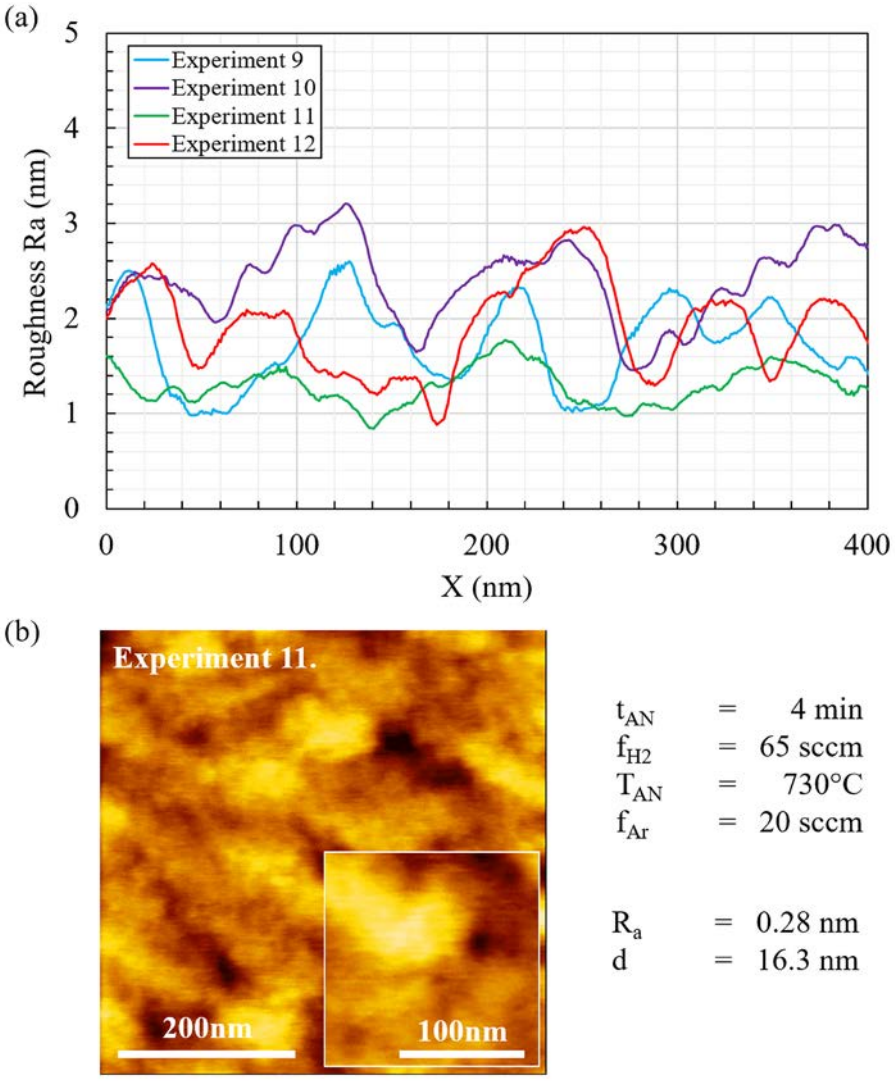

Figure 4.5. (a) AFM line profiles of Fe catalyst particles after annealing process for the Taguchi experiments 9-12, (b) AFM scan of surface of experiment 11, with process parameters and results of measurements. Fixed parameter in Exp. 9-12 was annealing time of 4 min [161].

Annealing parameters in experiment 10 (Fig. 4.5(a) – violet curve) are: annealing for 4 min, a temperature of 820°C and an Ar/H_2 atmosphere. Due to the presence of hydrogen gas during the annealing process, it is expected that the size of Fe particles will decrease. However, due to an Ar flow of 60 sccm, a temperature of 790°C, and a process time of 4 min, the hydrogen effect on catalyst formation seems to be suppressed, which can be observed on

the AFM image, where the increased average catalyst size of d = 18.1 nm and the increased average surface roughness of R_a = 0.43 nm were observed.

Experiment 11, shown in Figure 4.5(a) (green curve), presents a decrease in the size of particles (d = 16.3 nm) and surface roughness (R_a = 0.28 nm). A temperature of 730°C and a high H_2 flow (65 sccm) compared to the Ar flow (20 sccm) resulted in reducing the size of the Fe particles. Due to a lower temperature of 730°C and to the hydrogen flow, and its reducing effect on oxidized Fe particles [150,163], the Ostwald ripening phenomenon effect was decreased and the subsurface diffusion effect was improved. The AFM scans of the catalyst surface of experiment 11, shown in Figure 4.5(b), demonstrate the lowest roughness and smallest size of particles for experiments performed with an annealing time of 4 min. On the other hand, in experiment 12 (Fig. 4.5(a) – red curve), an increase of temperature (760°C) and H_2 gas flow (100 sccm) did not result in a further decrease of Fe particle size. It is noted that, for this combination of conditions where the annealing time is 4 min and the temperature is 760°C, the Ostwald ripening effect dominates over the subsurface diffusion phenomenon and oxide reduction caused by hydrogen flow is less significant for catalyst formation process.

Figure 4.6(a) shows the AFM plots of the average roughness of Fe catalyst surface after annealing for runs 13-16 of the Taguchi plan of experiments (Table 4.2). According to this plan, experiment 13 (Fig. 4.6(a) – blue curve) was performed at an annealing temperature of 820°C in an Ar atmosphere (20 sccm) for 5 min. This set of parameters resulted in the highest average particle size (d = 20.9 nm) among all of the experiments and a high surface roughness R_a = 0.48 nm. Due to the high temperature, long annealing time and non-reducing atmosphere, extensive growth of Fe particles was observed.

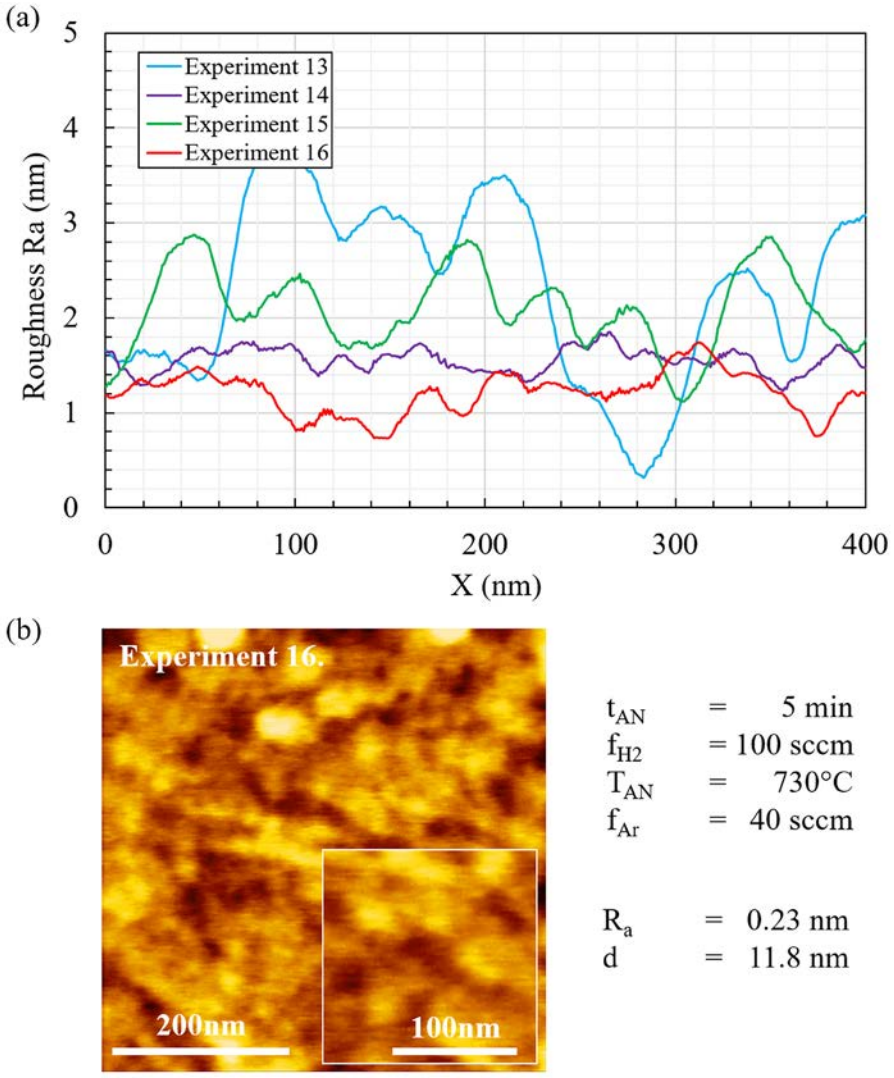

Figure 4.6. (a) AFM line profiles of Fe catalyst particles after annealing process for Taguchi experiments 13-16, (b) AFM scans of experiment 16 surface with process parameters and results of measurements. Fixed parameter in Exp. 13-16 was annealing time of 5 min [161].

In experiment 14 (Fig. 4.6(a) – violet curve), for the same annealing time, a reduction of the average size (d = 17.1 nm) of the Fe catalyst and average roughness (R_a = 0.28 nm) was observed. It can be seen that the reduction in temperature to 790°C and the change of the annealing atmosphere for hydrogen, resulted in a decrease of average values. As can be seen in Figure 4.6(a) (green curve), in experiment 15, an increase in the size of Fe particles was observed. Although, the temperature of annealing was reduced to 760°C and the hydrogen gas flow was increased to 65 sccm, the introduction of 60 sccm of Ar gas decreased the partial

pressure of H_2, reducing its effect on the oxidized Fe particles. Finally, the average size of the catalyst particles (d = 18.7 nm) and average roughness (R_a = 0.49 nm) increased. The last experiment (Fig. 4.6(a) – red curve) based on the Taguchi plan of experiments (Table 4.2) was performed at a temperature of 730°C and with a hydrogen gas flow of 100 sccm. As can be seen, both the average diameter (d = 11.8 nm) of the Fe particles and the average roughness (R_a = 0.23 nm) were reduced; however, due to the time of annealing (5 min) and the presence of Ar gas, the achieved values are not as good favorable as in experiment 6-8. A longer annealing time caused a larger growth of particles when Ar decreased the partial pressure of H_2, reducing its influence on the process. The AFM scans (Fig. 4.6(b)) show that the Fe catalyst surface in experiment 16 with the smallest size of particles was achieved with an annealing time of 5 min.

The influence of individual process parameters on the average diameter of Fe catalyst particles and average catalyst surface roughness was determined by the Taguchi method, using the computer software Minitab 17, and is shown in Figure 4.7. The goal of the experiments was to reduce the size and roughness of the Fe catalyst particles to values sufficient for SWNT forest growth. Accordingly, the criterion 'the smaller-the better' was applied to evaluate the influence of the annealing parameters on the average particle size and surface roughness; based on the results of measurements, SN ratios response graphs were prepared. Based on the diagram in Figure 4.7(a), in order to obtain the minimum average roughness of the catalyst surface, the annealing process should be performed using the following process values: an annealing time of 2.5 min (level 2), a hydrogen gas flow of 65 sccm (level 3), an annealing temperature of 730°C (level 1), and an argon gas flow of 0 sccm (level 1). Moreover, the analysis of SN ratios showed the highest influence of the temperature and the annealing time on the final values of the average roughness of catalyst surface, with a percentage effect of 44.49% and 37.75%, respectively. Interestingly, the argon flow rate has a higher influence (12.92%) on the roughness than the hydrogen flow rate (3.76%), which is related to the changes in the partial pressure of hydrogen in the Ar/H_2 mixture atmosphere. The percentage value of the residual error of the statistical calculations is 1.09%.

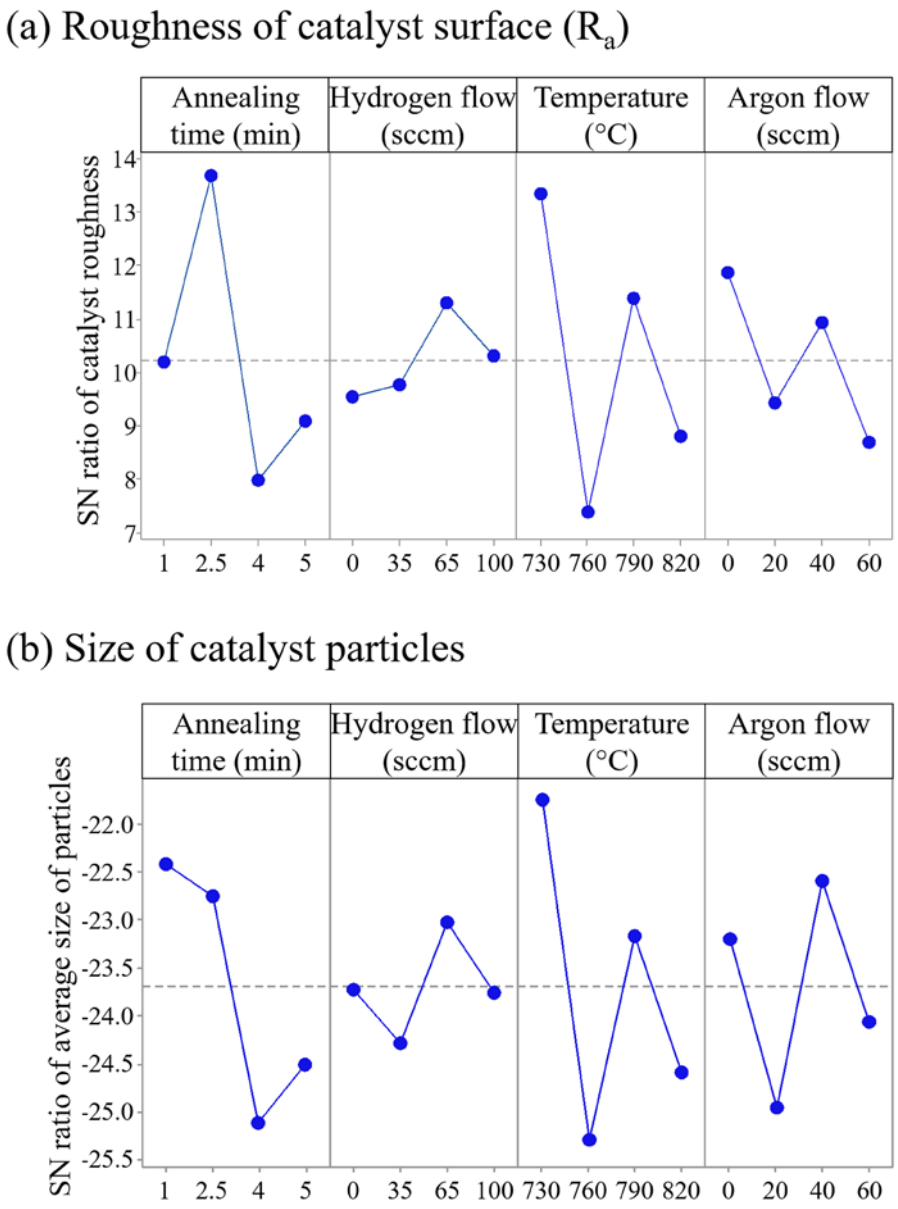

Figure 4.7. The influence of the individual process parameters on the properties catalyst layer: (a) roughness of surface (b) size of particles [161].

The diagram shown in Figure 4.7(b) represents the SN ratios of the results obtained for the Fe catalyst particle diameter. The lowest diameter of particles can be obtained in the annealing process carried out for 1 min (level 1 of annealing time), in an hydrogen atmosphere with a flow rate of 65 sccm (level 3 H_2 flow rate), at a temperature of 730°C (level 2), and with a flow of argon gas at 40 sccm (level 3 of Ar flow rate). Similar to the SN

ratios of the roughness measurement results, temperature and annealing time seem to play the most important role in the formation of the particles, with the percentage effects of 44.78% and 31.08% respectively. Also in this case, an argon gas flow rate of (18.08%) seems to have a higher impact on the average size of Fe particles than the hydrogen flow. rate (4.7%). For the calculation of particle size optimization SN ratios, the percentage value of residual error is 1.37%. As can be seen in Fig. 4.7(a, b), to achieve a small average diameter of particles and a lower surface roughness, annealing temperature and hydrogen flow rates, in both cases, should take the same values of 730°C and 65 sccm, respectively. However, as described above, the annealing time and argon flow should take different values.

In order to clarify the mechanisms behind the formation of Fe catalyst particles, a sensitivity analysis of tested parameters was conducted, based on SN ratio graphs (Fig. 4.7). In the Taguchi method, the flat SN ratio lines indicate that particular parameters have low sensitivity.

As can be seen in Figure 4.7, the catalyst formation process was highly sensitive to temperature and annealing time. In other words, changes of temperature and annealing time during the process, markedly increased or decreased the average size of Fe particles and average surface roughness. Comparison of sensitivity also showed that during the annealing process, the argon flow was more sensitive to change than the hydrogen flow, but not as much as the temperature and annealing time. It means, that the size and roughness of Fe catalyst changes less rapidly with argon adjustments from the baseline.

Additionally, for temperature, the highest sensitivity change was noted between 730°C and 760°C. It means that, changes in that range of temperatures caused the most rapid changes in the size of Fe particles and roughness values. The highest sensitivity of annealing time was noted in the case where the time increased from 2.5 min to 4 min, causing rapid changes and resulting in a decrease in the SN ratio value.

As can be seen from the sensitivity analysis, temperature and annealing time caused the biggest changes of catalyst structure, which supports Ostwald ripening and subsurface diffusion as mechanism responsible for the formation of catalyst particles. Both of these mechanisms are temperature and time dependent.

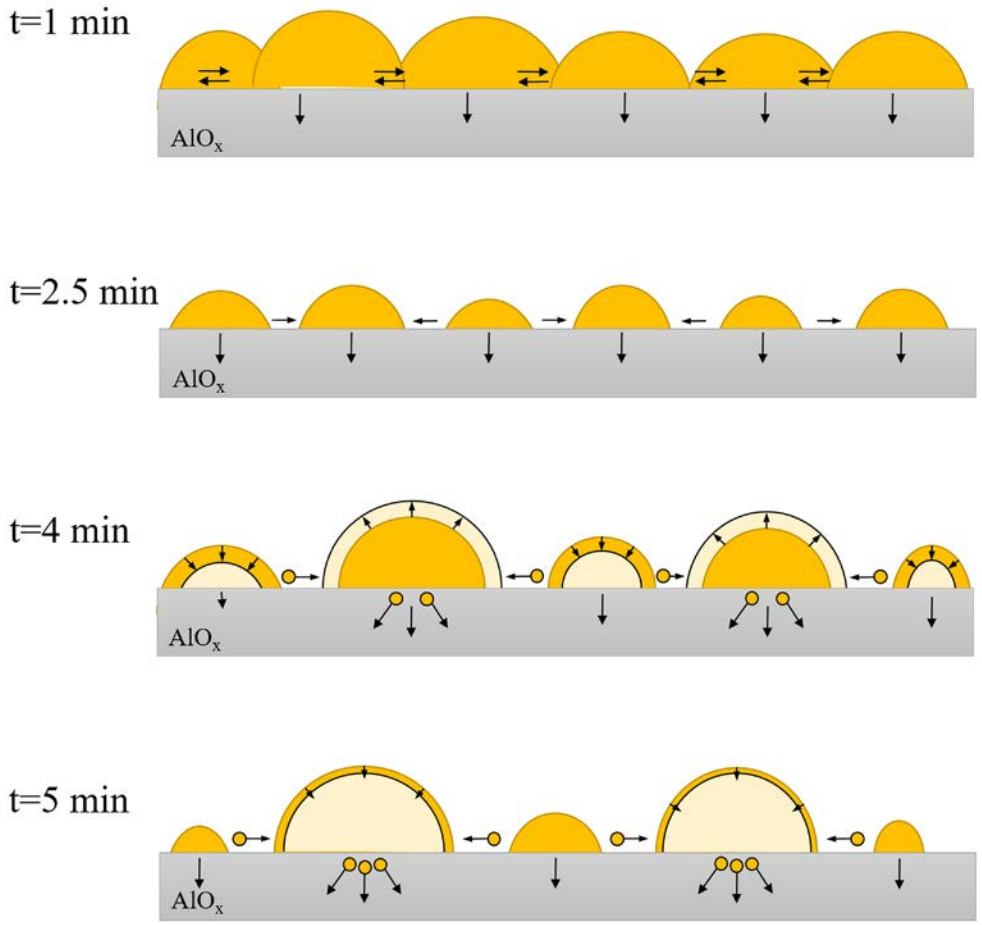

Figure 4.8. Diagram schematic of catalyst formation mechanisms in dependence of annealing time (temperature = const. (730°C)) [161].

For an annealing time of 1 min, formation of particles of various sizes and shapes from a catalyst film is noticed (Fig. 4.8). Due to a short time, the influence of Ostwald ripening and subsurface diffusion seems too weak to influence the formation of the catalyst particles in a major way [151]. Increase in time causes further recrystallization of the catalyst film into small particles and migration of the Fe atoms begins, as a part of the Ostwald ripening process, where Fe atoms migrate from smaller particles into the direction of larger ones. In the time range between 2.5 min and 4 min, sensitivity is increased. It means that in this phase, the formation of particles is highly affected by time changes. Furthermore, an increase of time to 4 min, connected with a sudden drop of the SN ratio, can also be explained by the Ostwald ripening mechanism. With an increase of time, due to the effect of Ostwald ripening, the size

of particles dramatically increases. Additionally, with the improvement of particle size, the subsurface diffusion also increases, as it depends on the cross section of nanoparticles. With a further increase in time, the Ostwald effect of Ostwald ripening starts to slow down, as the quantity of small particles decreases. On the other hand, due to the fact that a certain particle size was achieved, the subsurface diffusion starts to dominate and the bigger nanoparticles start to decrease in size. This effect is confirmed by the SN ratios graphs (Fig. 4.7 – annealing time curve).

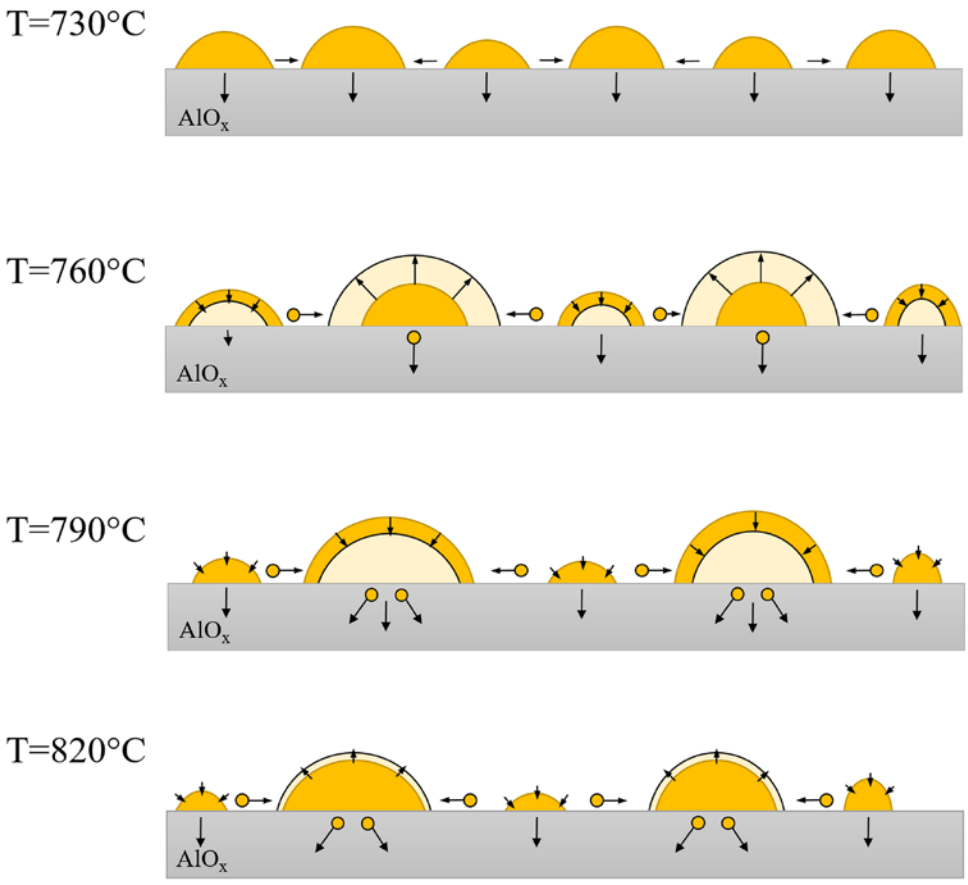

Figure 4.9. Diagram schematic of catalyst formation mechanisms in dependence of annealing temperature (annealing time = const. (2.5 min)) [161].

Simultaneously, the formation mechanisms depend on temperature (Fig. 4.9). With a relatively low temperature of 730°C, the Ostwald ripening and subsurface diffusion occurs, however at a relatively low speed which, is the reason that the particles are small. Between 730°C and 760°C, a rapid drop of the SN ratio was observed. Due to the increase of temperature, the atom migration correlated with the Ostwald ripening was enhanced, causing

the increase in catalyst particle size. At the same time, subsurface diffusion also occurs, however, to a smaller degree than with surface diffusion. A further increase in temperature causes an increase of subsurface diffusion. The pace of change of Ostwald ripening and subsurface diffusion are different. At lower temperatures the Ostwald ripening mechanism has a much higher speed than subsurface diffusion; however, with an increase in temperature, the subsurface diffusion effect starts to dominate in order to achieve an equilibrium state with the Ostwald ripening mechanism. This state continues also at a temperature of 820°C. The observation of sensitivity at various temperature shows its slow decrease. It is assumed that at higher temperatures, above 820°C, sensitivity of changes in catalyst structure would decrease even more, meaning the SN ratio lines would become flatter.

To better understand the influence of each parameter on the process and the final results, interaction plots were prepared. Due to a lower values of the diameter of CNT, the interactions in the roughness optimization process were analyzed. The interaction plot does not describe the degree of interaction; however, it provides many significant pieces of information about the process. Additionally, interaction plots are one of the most important feature of the Taguchi method, which support the analysis of reproducibility, stability and favorable combinations of parameters during the experiment.

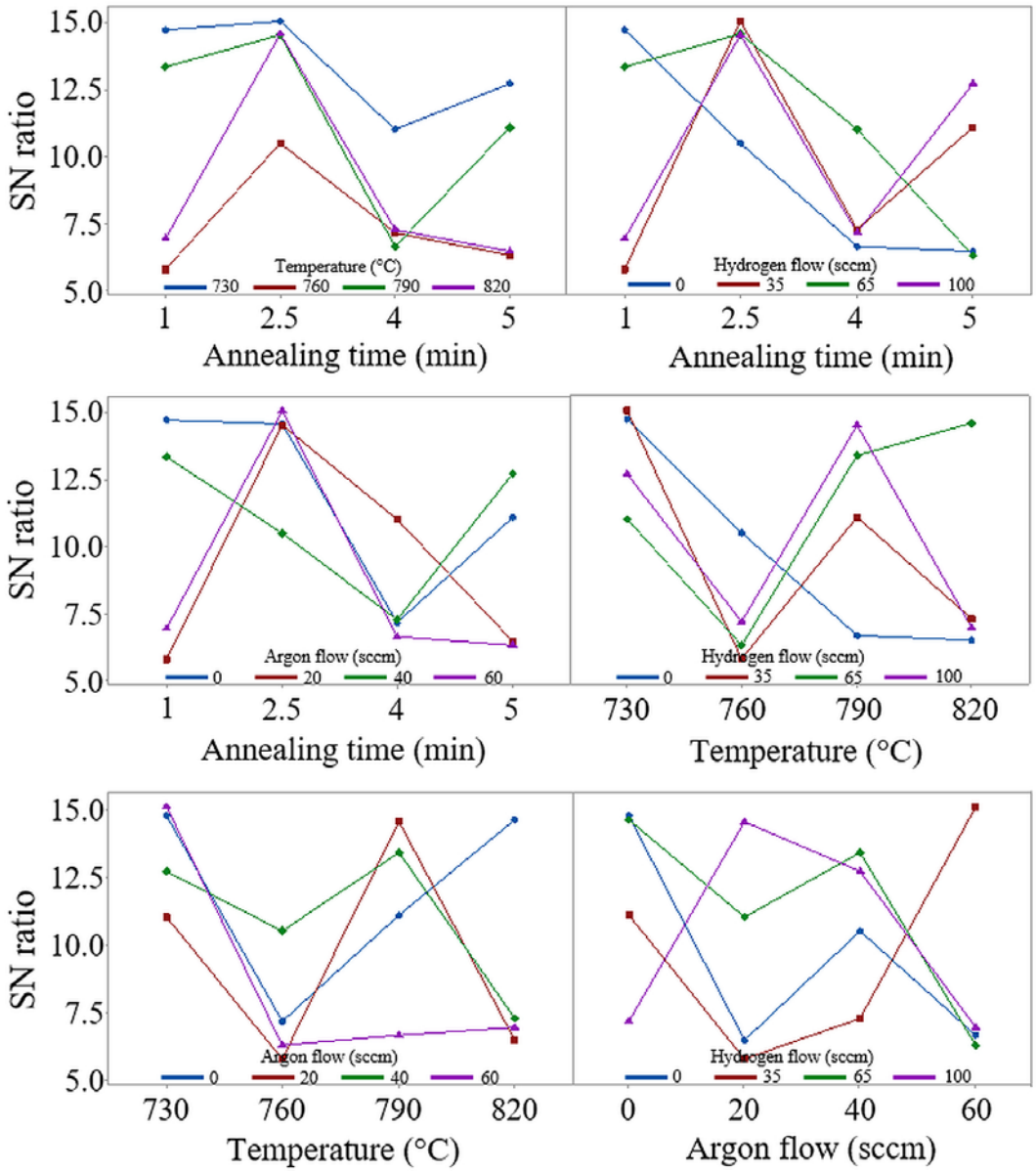

Figure 4.10. Interaction plots of tested parameters in dependence on SN ratios (Fig. 4.7) [161].

Figure 4.10(a) shows interactions between the annealing time and temperature. The analyzed results of the interactions show strong interactions between those parameters, implied by many crossovers and slopes in the curves. As can be seen, in every case of annealing time, a temperature of 730°C achieves the highest values of the SN ratio, which implies that the processes performed at that temperature are the most stable and reliable. Also the highest SN ratio values were achieved with the 2.5 min annealing. On the other hand, the

lowest SN ratio value was achieved at a temperature of 760°C and with an annealing time of 4 min, a temperature of 790°C resulted in a smaller value. An annealing temperature of 2.5 min seems to promote the stability of the process by increasing the signal-to-noise ratio for every temperature value, whereas 4 min of annealing seems to decrease the signal ratio. It seems that the lower annealing temperature produced a more stable environment during the process and achieves better results.

Additionally, the mechanism of catalyst formation is also confirmed by the temperature – annealing time interaction plot (Fig. 4.10(a)). In various temperatures with a small annealing time, the homogenous catalyst film recrystallizes into particles of various size, which is visible on the interaction plot. With an increase in time to 2.5 min, the size of the particles decreases to either a greater or lesser degree, depending on the Ostwald ripening and subsurface diffusion effect at different temperatures. With a further extension of the annealing time, rapid changes in catalyst particles size are observed, as a result of the Ostwald ripening effect. In the case of an annealing time of 5 min, at various temperatures, the Ostwald ripening and subsurface diffusion mechanisms are close to equilibrium. Small changes in catalyst size are observed.

Figure 4.10(b) shows the relationship between the annealing time and hydrogen flow during the process. Strong interactions between parameters can be observed, the sensitivity of the annealing time is much higher than the sensitivity of the hydrogen flow rate. It can be noticed that by increasing the time of annealing, in the case where no hydrogen was used during the process, the SN ratio drops quickly, which is due to the expansion of particles over an extended time. Also with a hydrogen flow of 65 sccm, after the peak in 2.5 min of annealing (the highest SN value), the SN ratio drops to a similar value as in the case of 0 sccm. Similar to Figure 4.10(a), the annealing time of 2.5 min promotes the increase in the signal-to-noise ratio when hydrogen is introduced to the chamber during the process.

Figure 4.10(c) shows a plot of the interaction between the annealing time versus the argon flow. Due to many crossovers and curve slopes, strong interactions between parameters are observed. As can be seen, for 1 min of annealing, an argon flow rate of 0 sccm has the highest SN ratio. On the other hand, for the same time, a flow of 20 sccm of argon gas exhibits

the lowest SN ratio. For an annealing time of 2.5 min, the argon flow rates of 0, 20 and 60 sccm show similar values of SN ratios. As in previous interactions plots (Fig. 4.10(a, b)), an annealing time of 2.5 min seems to be favorable for increasing the SN ratio and maintaining stability and reproducibility of the annealing process.

Interactions between temperature and the hydrogen flow rate are shown in Figure 4.10(d). With a hydrogen flow of 0 sccm, the increase in temperature results in a decrease of the SN ratio, due to enhanced growth of Fe catalyst particles at a higher temperature. On the other hand, the signal-to-noise ratio changes for the hydrogen flow rates of 35, 65 and 100 sccm, are similar in all 3 cases, and are similar to the Fig. 4.7(a) temperature changes. As can be seen, a temperature of 730°C seems favorable for catalyst formation with all of the hydrogen flow rates, maintaining high SN ratio values, which results in higher stability levels of the annealing process.

Figure 4.10(e) indicates strong interactions between the temperature of the process and the argon gas flow rate. For a temperature of 730°C, argon flow rates of 0 and 60 sccm seem to be optimal to achieve the smallest roughness of the Fe catalyst surface. On the other hand, a temperature of 760°C caused a decrease in the average signal-to-noise ratios for all argon gas flows; whereas at 790°C, the SN ratio values improved again. This behavior is related to the catalyst formation mechanism described previously. As can be noticed with the argon flow of 0 sccm, the most favorable temperatures are 730°C and 820°C. Similar to previous interaction plots, a temperature of 730°C is favorable for achieving the highest SN ratios, as well as for improving the reliability, stability and reproducibility of the annealing process.

Figure 4.10(f) illustrates the interaction plot for the argon flow rate and the hydrogen flow rate. It should be noted that the sensitivity of both parameters is lower than the annealing time and temperature. It can be assumed, therefore, that even strong interactions between those parameters might not be critical for final evaluation. As can be seen, strong interactions exist between the analyzed parameters. Different ratios of argon and hydrogen during the annealing process seem to affect SN ratios to various degrees. For example, a hydrogen flow rate of 35 sccm seems to be optimal with Ar gas flow rates of 0 and 60 sccm. However, with Ar flow rates of 20 and 40 sccm, the SN ratios take the lowest values. A similar trend is

observed with a hydrogen flow of 100 sccm with reversed values, when the highest signal-to-noise ratio is observed for 20 and 40 sccm. Hydrogen flow rates of 0 sccm and 65 sccm have similar trends, with the highest SN ratios for 0 sccm of Ar gas flow.

In Figure 4.10(a-c), an annealing time of 2.5 min seems the most favorable for increasing the signal-to-noise ratio of the results of experiments. In every interaction plot, an annealing time of 2.5 min increased the value of the signal compared to noise, which promotes the stability and reproducibility of the process. Results of the interaction plots correspond to SN plots (Figure 4.7(a)) and sensitivity analysis, where the optimized time of the annealing process was also set to 2.5 min. From analysis of the mechanisms of catalyst formation process, based on the annealing time SN ratio, Ostwald ripening and the subsurface diffusion influence were responsible for enhancing the growth of small particles.

Finally, based on the SN ratios diagrams (Fig. 4.7) with optimized annealing process values, two verification experiments were planned and performed (Table 4.3).

Table 4.3. Parameters of verification the Taguchi experiments**.**

Experiment	Annealing time (t_{AN}) [min]	Hydrogen flow rate (f_{H2}) [sccm]	Annealing temperature (T_{AN}) [°C]	Argon flow rate (f_{Ar}) [sccm]
Roughness optimization – condition 1	2.5	65	730	0
Catalyst size optimization – condition 2	1	65	730	40

Verification experiments were conducted in 2 stages. First silicon samples with a Fe catalyst were annealed according to the parameters shown in Table 4.3, then the average size of catalyst particles and surface roughness were measured. After that, a second set of samples was prepared for CNTs growth. The experiment performed according to the parameters optimized for the lowest surface roughness of the catalyst showed an average particle size of d = 11.8 nm and an average roughness of R_a = 0.159 nm, which was the lowest achieved during all experiments. For optimization of the size of the particles, the AFM measurements showed an average roughness of 0.18 nm and an Fe particle diameter of 11 nm which was not the lowest size achieved during the experiments (9.7 nm). Based on the results of the

verification experiments, CNT growth was performed on both samples using acetylene gas with a flow rate of 10 sccm (partial pressure 54 Pa) for 10 min.

Figure 4.11(a, b) shows the SEM analysis of grown CNT forests using optimized conditions 1 and 2 respectively. As can be seen, in both cases high, vertically-aligned CNT forests were grown; however, the measurements of the diameter of CNTs showed a mean diameter of 4.8 nm for a process with an optimized particle size and a diameter of 3.02 nm for the optimization of the catalyst surface roughness. TEM observations of a CNT forest grown according to condition 1 (Fig. 4.11(c)) confirmed that the CNT forest contains mostly SWNTs and DWNTs.

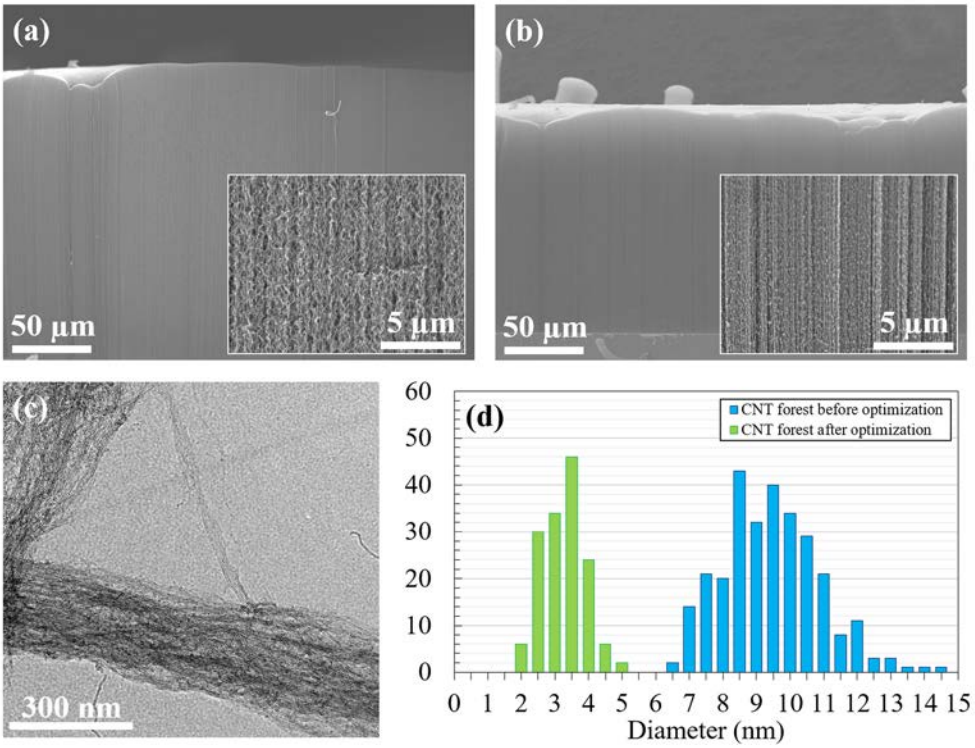

Figure 4.11. SEM image of as-grown CNT forest synthesized under (a) optimized condition 1, (b) optimized condition 2, (c) TEM image of as-grown products of condition 1 (Table 4.3), (d) diameter distribution of grown CNTs before (standard condition) and after the Taguchi optimization (condition 1) [161].

For a final evaluation of the Taguchi optimization method, the average diameter of the CNTs grown by the standard conditions (before optimization) and optimized conditions were compared (Figure 4.11(d)). As can be seen, after the optimization process, the diameter

distribution of CNTs became narrower, also the average diameter decreased from 9.18 nm for the CNT forest before optimization to 3.02 nm after the optimized condition 1. The Taguchi optimization method allowed for transition from MWNTs to SWNTs in 16 experiments based on Taguchi orthogonal table of experiments.

4.5. Conclusions

The studies described in this part of the research concerned the tuning of the annealing parameters of CNTs growth by a thermal CVD method. The Taguchi method of experiment design proved to be very effective for planning the experiments, processing the experimental results, and optimizing the parameters of the annealing process. The Taguchi method allowed fine tuning of catalyst formation for CNTs growth, in the case of the control of independent and dependent parameters. Using the Taguchi approach, the number of necessary experiments was dramatically reduced to one series of experiments, containing 16 experiments in total. One series of experiments was enough to determine individual influence of each parameter on the final properties of the catalyst. Among the optimized parameters, temperature and annealing time have a higher impact on the control of the average diameter of the Fe catalyst particles and surface roughness. Using the Taguchi method it was possible to tune out CNTs (diameter) properties without interference in the growth process itself. By dividing the average diameter of CNTs from before the optimization (9.1 nm) and after optimization (3.0 nm), a 67% diameter reduction in 9 experiments was successfully achieved by employing the Taguchi method. During the process, the structure of the CNTs was changed from MWNTs to SWNTs and DWNTs.

Experimental results and the Taguchi statistical analysis of the SN ratios and sensitivity demonstrate that Ostwald ripening and subsurface diffusion of catalyst atoms into AlO_x support layer were the basic mechanisms responsible for the formation of catalyst particles. Analysis of these results confirmed that temperature and time are the main parameters inducing the mechanisms of the particle size reduction, which is also supported by additional H_2/Ar annealing atmosphere.

In the future, it would be advisable to conduct a further optimization process in the vicinity of the optimal SN ratios values, in order to further investigate the optimal annealing

process. Furthermore, additional unknown parameters of the annealing process might be better understood. In future experiments, we plan to the optimize growth process, in order to tune the optical properties of the CNT forest for optical applications.

Chapter 5. Optimization of total reflectance of SWNT forest

5.1. Introduction

In order to achieve desired optical properties of CNT forest, various growth methods are used, with the most common, a thermal CCVD. It provides high yield and relatively high purity of grown CNTs and allows easier control of growth parameters and structures [54]. However, even though many years have passed and great improvement has been made to control the growth of CNTs, fabrication of high-density, high-aligned and high absorbance CNT forest, is still difficult due to a large number of process parameters influencing CNT growth [146–148,166]. The CNT growth process is still challenging due to a wide range of parameters, starting from catalyst preparation methods, and finishing on annealing and growth processes. One of the solutions is the reduction of the number of experiments by applying optimization methods, like Taguchi method [153]. This method can be applied for systematic investigation of the process and parameters that influence the quality of the final product [155,167,168] in order to improve manufacturability, reliability, and quality of a product.

Due to a very high absorbance and a low reflectance in the visible and infrared light regions [125–127], CNT forests exhibit properties close to that of a blackbody, described in chapter 2. Many groups of researchers have presented results of very low reflectivity of CNT forests, with the lowest reflectance of incident light in UV-VIS range of 0.045% noted by Yang *et al.* [125] for 633 nm wavelength for the CNT forest height of 200-300 μm. Additionally, the very low reflectance, below 0.01%, in the infrared regime (2.5 – 15 μm wavelength) was also recently reported for CNT forests of 30-50 μm height, grown on a high roughness aluminum substrates [128]. Blackbody properties of CNT forest were recently used in designing metamaterials [38,39]. Properties of metamaterials are derived from a shape and size of designed structures and also from the properties of the material that consist of those structures. Due to that, the density, alignment and other electrical and optical properties of CNTs, influence the performance of metamaterials. One of the most important features of CNTs for metamaterial applications is a total reflectance of CNT forest, which should possibly be the lowest [38].

Although in many experiments the very low reflectance of CNT forest has been already achieved, mechanisms responsible for a variation of absorbance are still not clearly explained. Recently, a research on the influence of the height of vertically aligned multi-walled CNT (MWNT) forest [169] showed changes in CNT absorbance in dependence of forest height for the same structure of CNTs. Also, the influence of chirality of individual CNTs on the optical properties was studied, revealing strong dependence in this matter [170]. Furthermore, electromagnetic response simulations of CNT arrays were performed using the finite-difference-time-domain (FDTD) method, in order to study the effect of structural randomness, like random position, diameter, length or orientation [170], and also to investigate total visible absorbance of two-dimensional nanotube arrays [171].

5.2. Objective

In presented part of the dissertation, a statistical approach to the design of experiment of CNT growth by the Taguchi method developed to tune the optical properties of CNT forest, is presented. The work is focused on the examination of the optimum growth parameters responsible for the decrease of total reflectance of CNT forest, and the investigation of the dependence of structural parameters (density, alignment, etc.) of thin CNT forest film on the reflectance results. For various industrial applications, high absorbance uniform materials are needed; however, for most of the cases, the height of the highest absorbance CNT forest is above 200 μm. In presented research, the remarkably low total reflectance for the thin CNT forest of 20 μm height, over 10 times smaller than conventional forests of high absorption, is presented. The main purpose of the experiments was to reduce the total reflectance of relatively thin CNT forest film grown by thermal CCVD method, based on the Taguchi method of design of experiments. Moreover, the alignment and growth density of structure of CNT forest structure, and optical properties originated from it, were measured and the effect of various growth parameters was discussed.

5.3. Experimental and methods

The methods of catalyst preparation and CNT forest growth were described in chapter 3.2 and 3.3.

The optimized growth parameters presented in chapter 4, were used in chapter 5 to define the improvement of the total reflectance, which was achieved throughout optimization process. The parameters used during growth of CNTs were: Fe catalyst thickness of 0.5 nm, an annealing time of 2.5 min, a temperature of 730°C, hydrogen flow of 65 sccm, argon flow rate of 0 sccm, and C_2H_2 gas flow rate of 10 sccm. The total reflectance of CNT forest grown by standard parameters was compared to results obtained after the Taguchi optimization, and the improvement of reduction in reflectance was calculated.

In chapter 4, the Taguchi method was used to decrease the diameter of CNTs by investigating the influence of annealing temperature, annealing time, hydrogen flow rate, and argon flow rate on the annealing process. On the contrary, in this study, the experiments of optimizing optical properties, were designed to tune parameters of the catalyst deposition and the growth of CNTs which influence the optical properties. It should be noted, that previously optimized annealing parameters remained unchanged during the Taguchi optimization of the total reflectance. For that purpose, the orthogonal table L9 (3^4) [172] was used, four process parameters with three different values were optimized. The parameters optimized during presented series of experiments were: (1) acetylene gas flow rate (f_{C2H2}), (2) Fe catalyst film thickness (d_{Fe}), (3) substrate polarization potential (bias) during AlO_x buffer layer sputtering (V_{bias}), (4) C_2H_2/H_2 gas flow ratio ($R_{C2H2/H2}$). Values of parameters are summarized in Table 5.1. Moreover, a plan of 9 experiments was prepared and presented in detail in Table 5.2. It should be noted that in order to avoid major growth fluctuations during the analysis, in the case of the observable variation of CNT growth yield (insufficient height, etc.), the experiment was repeated. Throughout the experiments, due to a different CNT growth rate, only the variation of height was observed and required additional experiments in some cases.

Table 5.1. Optimized parameters and their value level applied in the experiments.

No.	Parameter optimized	Variability interval		
		1.	2.	3.
1)	Acetylene flow (f_{C2H2}) [sccm]	5	10	15
2)	Fe catalyst thickness (d_{Fe}) [nm]	0.5	0.7	0.9
3)	bias of AlO_x support layer (V_{bias}) [V]	0	-75	-150
4)	C_2H_2/H_2 ratio ($R_{C2H2/H2}$)	1:0	1:1	1:2

The aim of this optimization was to decrease the total reflectance of CNT forest in UV-VIS light range. The optimization of acetylene flow rate (f_{C2H2}) was chosen to control the crystallinity and purity of CNT forest. Higher crystallinity is expected to increase the absorbance of visible light. The thickness of Fe catalyst (d_{Fe}) has an impact on a formation process of catalyst particles which affects size and density of catalyst particles, determining the structure, density, and alignment of CNT forest. The increase of substrate polarization voltage during AlO_x deposition (V_{bias}) is the direct cause of the increase of ions energy reaching Si substrate surface, and affects the structure of alumina layer support. The structural changes of the supporting layer, influence the catalyst formation process, due to changes in surface roughness and subsurface diffusion processes. Finally, a C_2H_2/H_2 ratio ($R_{C2H2/H2}$) changes the alignment of CNTs in the forest [166], resulting in changes of visible light absorbance. All the presented parameters are anticipated to decrease the total reflectance of CNT forest in UV-VIS region.

Table 5.2. Plan of experiments prepared according to Taguchi orthogonal table L9 [172].

Experiment number	Parameters values			
	Acetylene gas flow rate (f_{C2H2}) [sccm]	Fe catalyst thickness (d_{Fe}) [nm]	bias of AlO_x layer deposition (V_{bias}) [V]	C_2H_2/H_2 gas ratio ($R_{C2H2/H2}$)
1.	5	0.5	0	1:0
2.	5	0.7	-75	1:1
3.	5	0.9	-150	1:2
4.	10	0.5	-75	1:2
5.	10	0.7	-150	1:0
6.	10	0.9	0	1:1
7.	15	0.5	-150	1:1
8.	15	0.7	0	1:2
9.	15	0.9	-75	1:0

The characterization methods of CNT forest, used in this part of research were described in chapters 3.4.1, 3.4.4, and 3.4.5 (FE-SEM, UV-VIS spectroscopy, and Raman spectroscopy). Additionally, Python software ver. 3.5 was used to calculate fast Fourier transform (FFT) of the cross-sectional SEM image of CNT forests to evaluate alignment. For density analysis, filling factor of CNTs was determined from SEM observations and calculated using ImageJ 1.50b software. The value of filling factor was expressed by calculation of the sum of diameters of CNTs observed in the SEM photo, divided by the SEM field width [173]. Due to that, filling factor of SWNT and MWNT forests should be similar; however, a number of CNTs may differ.

5.4. Results and discussion

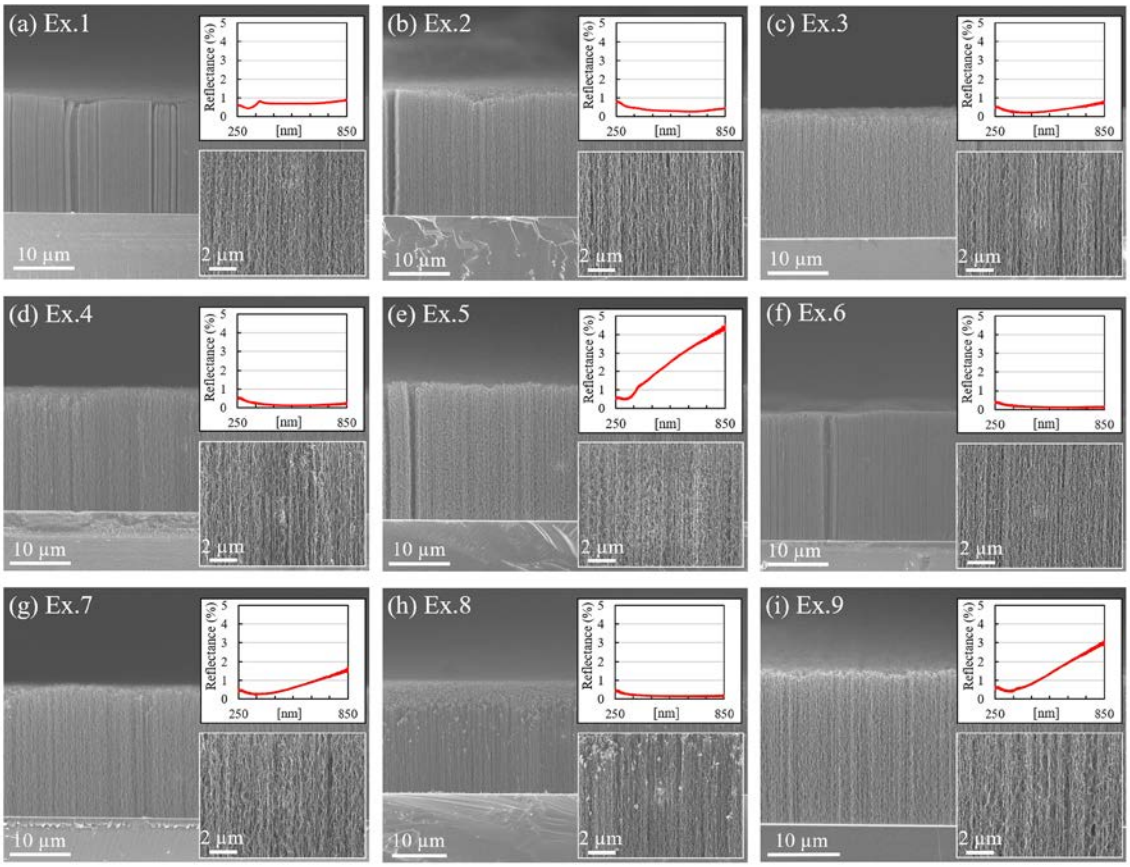

Figure 5.1. SEM images of CNT forest grown according to Taguchi plan of experiments, and spectra of total reflectance for experiments 1-9 in Table 5.2 [submitted to Journal of Material Science].

Figure 5.1 shows the SEM images of CNT forest grown according to applied Taguchi plan of experiments (Table 5.2). To avoid the influence of CNT forest height on the measurements of the total reflectance, the time of growth was precisely controlled to achieve growth height of 22±0.75 µm. In all experiments, uniform CNT forests were observed. Various densities of vertically aligned CNT forest were observed as shown in high magnification insets in Figure 5.1. Accordingly, insets of reflectance spectra showed major changes in the total reflectance of CNT forest, in dependence on experimental conditions. Furthermore, as the growth experiments were planned to keep the similar height of the forest in all experiments, it was assumed that the influence of height variation on the total reflectance of CNT forest can be neglected, as it is known that absorbance raises exponentially by increasing forest height [169]. In table 5.2, the average CNT forest height

and total reflectance measured for 350, 550 and 750 nm wavelengths, are presented, and represent beginning, middle, and end of the visible region. The height difference between the shortest CNT forest (21.22 µm) and the highest (22.68 µm) CNT forest was less than 1.5 µm, resulting in unnoticeable reflectance changes.

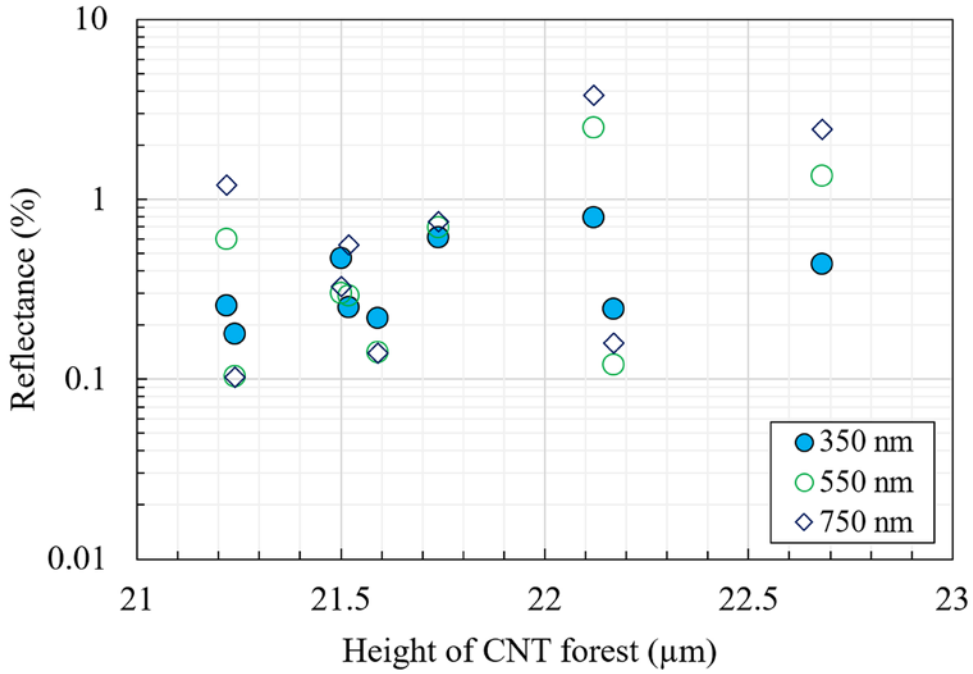

Figure 5.2. Height of CNTs vs total optical reflectance for 350 nm, 550 nm, and 750 nm [submitted to Journal of Materials Science].

It was confirmed (Fig. 5.2) that for the similar height of CNT forest, significant changes in total reflectance were observed. Additionally, the lowest reflectance in all 3 measured points was defined for experiment 6 (%R = 0.102% for 750 nm), and the highest for experiment 5 (%R = 3.76% for 750 nm).). From the first observations, it appears that higher density and alignment of CNT forest observed for experiment 6 or 8 caused the decrease of total optical reflectance, while a lower density and wavy-like structure of CNT forest, observed in experiment 5 or 9, resulted in a higher reflectance. It seems that for the same height, the variation of density and alignment of CNT forest results in different values of the reflectance. The rise of the reflectance in the UV region and observed in a few cases peaks around 370 nm are caused by the presence of Si substrate. For SWNTs, the absorption in the UV region is caused by $\pi \rightarrow \pi^*$ excitations of the electron system in nanotubes [53].

Table 5.3. Height and total reflectance of CNT forests.

Experiment No.	Average Height (μm)	Total Reflectance (%)		
		%R (350 nm)	%R (550 nm)	%R (750 nm)
1.	21.74	0.612	0.692	0.753
2.	21.50	0.471	0.301	0.327
3.	21.52	0.251	0.290	0.557
4.	22.17	0.246	0.120	0.158
5.	22.12	0.789	2.507	3.760
6.	21.24	0.178	0.104	0.102
7.	21.22	0.256	0.597	1.201
8.	21.59	0.218	0.141	0.140
9.	22.68	0.434	1.339	2.447

By utilizing Taguchi orthogonal arrays of experiments, we were able to remarkably decrease the number of experiments from 3^4 (=81) to 9, while keeping a high level of accuracy. Due to the fact that the parameters in the design were weighted equally, we were able to evaluate factors independently.

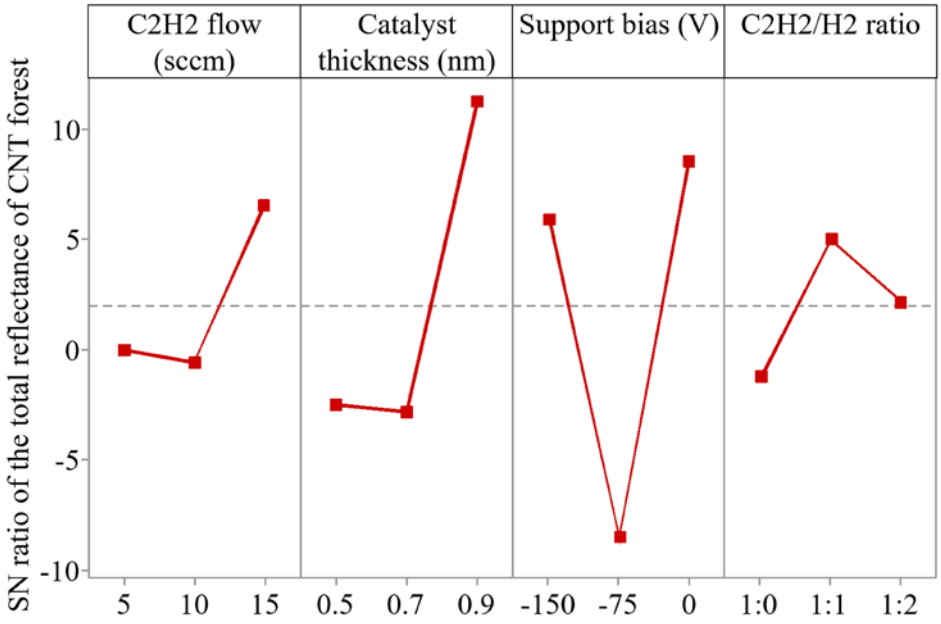

Figure 5.3. The SN ratio of the individual parameters, a higher SN ratio value indicates lower reflectance [submitted to Journal of Material Science].

The impact of process parameters on the average total reflectance of CNT forest in the range of 250 – 850 nm was determined by the Taguchi method using software Minitab 17, and the SN ratio of impact is shown in Fig. 5.3. Accordingly, the SN ratio plots based on the criterion 'the lower-the-better', were prepared for the purpose of evaluation of the influence of individual parameters on the reflectance results of the experiments. Based on the results acquired from statistical analysis, in order to obtain minimum value of the total reflectance of CNT forest, the growth process should be conducted according to following values of optimized parameters: acetylene gas flow rate of 15 sccm, thickness of Fe catalyst of 0.9 nm, bias during AlO_x support layer deposition of 0 V and acetylene/hydrogen flow ratio of 1:1. It was concluded that acetylene gas flow rate and acetylene/hydrogen flow ratio improved the crystallinity and alignment of CNTs. Furthermore, the Fe catalyst thickness of 0.9 nm deposited on the AlO_x allowed the formation of high-density nanoparticles during the annealing process, which induced the high-density CNT forest growth, observed in experiment 6 (Fig. 5.1).

The statistical analysis of SN ratios provided the influence of each parameter on the results, in which the impact of bias during deposition and thickness of Fe catalyst layer, were

defined as 48.53% and 36.94%, respectively. Additionally, the influence of C_2H_2 gas flow was calculated as 8.9%, and the influence of C_2H_2/H_2 gas ratio as 5.5%. The percentage value of the residual error of the statistical analysis was calculated as 0.13%. Based on the results, it was concluded that parameters responsible for catalyst formation (Fe thickness and support bias) had the highest effect on the total reflectance of CNT forest. It was assumed that formation of the high-density catalyst particles was the main reason behind the decrease of the reflectance as the growth of high-density CNT forest was possible. Moreover, it appeared that the density of the CNT forest was the main reason behind the decrease in the reflectance.

For the purpose of analyzing the influence of parameters on results, based on SN ratio plots in Fig. 5.3, the sensitivity analysis of tested parameters was conducted. In the Taguchi method, the lowest sensitivity of parameters was indicated by constant lines of SN ratios. As indicated in Figure 5.3, the reflectance optimization process was highly sensitive to the bias value during deposition of AlO_x support layer and the thickness of a catalyst. In other words, changes of the bias voltage and the thickness of catalyst, noticeably increased or decreased total reflectance of CNT forests. Comparison of sensitivity showed that C_2H_2 gas flow rate during the growth process was more sensitive to changes than the C_2H_2/H_2 gas ratio, although not as much as the bias of support and thickness of Fe catalyst. It means, that changes of total reflectance of CNT forest, were less rapid with C_2H_2 gas flow rate adjustments from the baseline.

For bias adjustments, the highest change of sensitivity was observed between 0 and -75 V, as shown in Fig. 5.3. Changes of polarization voltage in this range resulted in the most rapid changes in the total reflectance of CNT forests. Interestingly, the sensitivity changes of bias in the range of -75 and -150 V were almost as large, indicating a significant change of AlO_x structure during deposition with different polarization voltage. The highest change of sensitivity of the catalyst thickness was noted in the case of the increase from 0.7 to 0.9 nm, causing a rapid increase of SN ratio value. A bigger amount of material provided due to the increase the Fe catalyst layer thickness resulted in the formation of higher density particles, which were responsible for the high-density growth of CNTs and the decrease of the reflectance value. As can be seen from sensitivity analysis, bias and catalyst thickness caused

the most significant changes of the reflectance, which supported changes of catalyst formation mechanisms, due to change of the AlO_x/Fe catalyst structure, as the reason of reflectance variation.

One of the main advantages of the Taguchi method is the possibility of defining interactions between individual parameters. To clarify the influence of each pair of optimized parameters, the contour plots of interactions were prepared as shown in Figure 5.4.

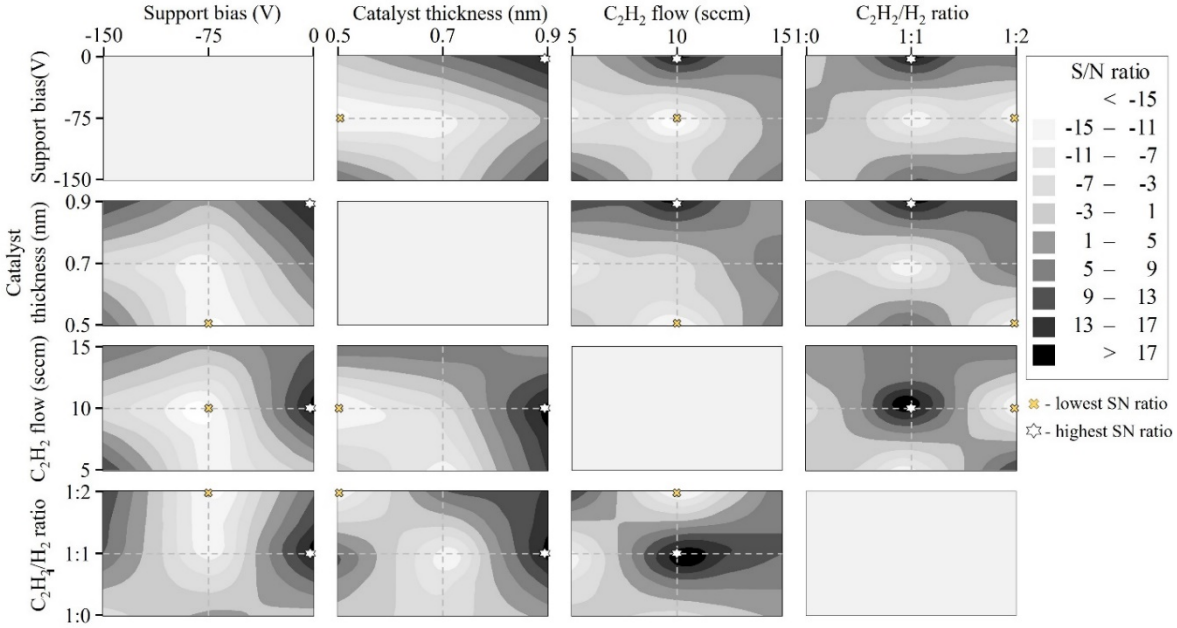

Figure 5.4. Contour plots of the SN ratio of the total reflectance reduction interaction of parameters [submitted to Journal of Materials Science].

The relationship between the bias voltage during deposition of AlO_x support layer and thickness of Fe catalyst layer, is defined in Fig. 5.4. Strong interactions of both parameters are defined as a result of high sensitivity to changes in the growth process. The highest value of the SN ratio can be observed for the bias of 0 V and thickness of Fe layer of 0.9 nm, while the lowest SN ratio can be noted for the bias of -75 V and catalyst thickness of 0.5 nm. Bias voltage of -75 V in interaction with Fe layer thickness, in all cases, provides the lowest SN ratio values. Interestingly, while for catalyst layer thickness of 0.7 nm and 0.9 nm, a bias voltage of 0 V seems to improve total reflectance of CNT forest, for the case of the thickness of 0.5 nm, the voltage of -150 V seems to provide better results. The strong effect of the bias and the catalyst thickness on catalyst formation processes, responsible for the density and

alignment of CNT forest, is also confirmed. The increase of the bias voltage during the deposition, results in the increase of the energy of ions reaching the Si surface. For the bias of 0 V, the energy of ions is relatively low and allows a deposition of uniform AlO_x layer. For a relatively low sputtering pressure, the increase of the bias to -75 V causes the increase of the ion energy and results in the resputtering of material from the Si substrate. The resputtering effect leads to the decrease of the growth rate and changes in the inner structure of AlO_x buffer layer. As a result, the change of a surface roughness [56] and mechanisms responsible for the formation of Fe catalyst particles can be expected. Interestingly, a further increase of the bias to – 150 V leads to further changes. It was assumed, that high energy ions causes a significant resputtering and the increase of the surface temperature, enhancing the surface diffusion of particles during the formation of AlO_x film. Higher diffusion during formation of a thin film allows the decrease of the roughness and due to that, the increase of the SN ratio is observed. Additionally, the variation of the thickness of Fe layer influences the amount of the catalyst material involved in the process of particles formation. Typically, larger amounts of material result in the formation of big high-density particles. The size and density of catalyst particles directly affect the diameter, density, and alignment of CNTs [31], which govern the total reflectance of CNT forest. These effects are confirmed by the high SN ratio values.

The analysis of the contour plots of the SN ratio in the interactions between acetylene flow rate and bias voltage (Fig. 5.4), shows the highest SN ratio value for combination of acetylene flow rate of 10 sccm and bias voltage of 0 V, while the lowest value is observed for voltage of -75 V for the same gas flow. It should be noted, that voltage of -75 V in combination with all acetylene flow rates results in the lowest SN ratio value in every case. Effect of SN ratio variation can be explained by changes of AlO_x support layer structure, which affects the formation of catalyst particles [174], by influencing Ostwald ripening and subsurface diffusion mechanisms [150,175]. Moreover, further increase of bias voltage to -150 V during the AlO_x sputtering process, seems to increase the SN ratio value, resulting in decreasing the total reflectance of CNT forest. The variation of the structure of AlO_x support layer affects the process of catalyst formation, resulting in various size and density of Fe particles. Due to higher influence of the bias than the acetylene flow rate, the growth of CNTs,

despite an improved crystallinity caused by acetylene, is still mostly affected by the density of CNTs and the total reflectance is changing accordingly.

Interactions between bias and C_2H_2/H_2 ratio are shown in Fig. 5.4. It should be noted, that the impact of bias voltage (48.53%) on the total reflectance is much stronger than the influence of gas flow ratio (5.5%). The highest SN ratio is observed for the bias of 0 V and 1:1 flow ratio, while the lowest SN ratio is observed for voltage of −75 V and acetylene/hydrogen flow ratio of 1:2. For all bias values, the ratio of 1:1 exhibits the highest values of the SN ratio, supporting the stability and reproducibility of the experiments. Additionally, acetylene/hydrogen flow ratio of 1:0 has the lowest sensitivity to changes during the growth process. Similar to the previous case, the improvement of the total reflectance, followed by the increase of SN ratio, is mostly a result of changes of AlO_x layer, due to the variation of bias value. The alignment improvement related to the variation of C_2H_2/H_2 ratio seems to be less significant than the alignment improvement related to the formation of catalyst particles.

Interactions between catalyst thickness and acetylene flow rate show the highest SN ratio value for the thickness of 0.9 nm and flow rate of 10 sccm (Fig. 5.4). On the other hand, the same acetylene flow rate combined with Fe catalyst thickness of 0.5 nm shows the lowest SN ratio. Interestingly, the higher thickness of the Fe catalyst and higher acetylene flow, seem favorable to improve reflectance of CNT forest. Furthermore, the changes of acetylene flow rate of 15 sccm seem to be the least sensitive to the final values of reflectance, improving the stability of the process at the same time. It was concluded that higher thickness of Fe catalyst supplies more material during annealing process and allows the formation of a higher number of particles on the surface, while the higher flow of acetylene improves the crystallinity of CNTs, resulting in the improvement of total reflectance CNT forest.

Interactions between the thickness of Fe catalyst and the C_2H_2/H_2 flow ratio are shown in Fig. 5.4. As can be seen, the highest SN ratio is observed for the combination of Fe layer thickness of 0.9 nm and 1:1 gas flow ratio, while the lowest value is noted for the thickness of 0.5 nm and 1:2 acetylene/hydrogen gas ratio. Moreover, the highest SN ratios are achieved for catalyst thickness of 0.9 nm for various flow ratios. Additionally, the gas flow ratio of 1:0

(without hydrogen) seems to have the lowest sensitivity, and shows only a small changes of total reflectance. Similar to the previous case, higher thickness of the catalyst supplies more material and supports the agglomeration of the catalyst into small particles, resulting in growth of high-density CNT forest. Despite the small influence of C_2H_2/H_2 flow ratio, the balanced flow of gasses seems to improve the alignment of CNT forest and decrease the reflectance.

The contour plot of interactions between C_2H_2 flow rate and C_2H_2/H_2 flow ratio is shown in Fig. 5.4. It should be noted, that based on SN ratios plot (Fig. 5.3), C_2H_2 flow rate and C_2H_2/H_2 ratio had the lowest sensitivity and the lowest influence on the CNT growth process during experiments of total reflectance optimization. As can be seen, the most suitable combination of parameters for total reflectance improvement was achieved with a flow rate of 10 sccm and 1:1 ratio, while increasing hydrogen flow during the process caused a dramatic decrease of SN ratio. It was concluded that too high partial pressure of hydrogen reduces the alignment of CNT forest by an extensive decrease of the size of catalyst particles, resulting in decreasing the total reflectance. Furthermore, higher percentage ratio of acetylene resulted in a decrease of the alignment, which seemed to have a higher influence on the total reflectance, than on the crystallinity of CNTs. These results correlated with the results obtained in [166]. Additionally, it could be observed that acetylene flow rate of 15 sccm and the ratio of 1:0 flow, seemed the most stable in various combinations of parameters, due to relatively low changes of SN ratios.

Finally, for interaction analysis of bias voltage, the highest SN ratio values were achieved for voltage of 0 V in every case. Also, analysis of Fe catalyst layer thickness in interaction with other parameters, showed that in every case thickness of 0.9 nm resulted in the highest SN ratio. Furthermore, C_2H_2/H_2 ratio of 1:1 gave the highest SN ratios in combination with other parameters. Results obtained from analysis of interactions correlating to results of the SN plot of individual parameters during the experiments are shown in Fig. 5.3. On the other hand, the analysis of interactions shows the highest values of SN ratio for acetylene flow rate of 10 sccm, which is lower than the value of 15 sccm achieved from SN plots in Fig. 5.3. Alternatively, during analysis of interactions, the C_2H_2 gas flow rate of 15

sccm attained high values of SN ratios for every value of interacting parameters, while the flow of 10 sccm achieved the highest and the lowest values of SN ratios, depending on the value of other tested parameters. It seems that higher stability and reproducibility of the process is crucial for defining acetylene flow rate of 15 sccm as the optimal value.

Table 5.4. Parameters of Taguchi verification experiment.

Experiment	Acetylene gas flow rate [sccm]	Fe catalyst thickness [nm]	bias of AlO_x layer deposition [V]	C2H2/H2 gas ratio
Reflectance optimization	15	0.9	0	1:1
Standard parameters (chapter 4)	10	0.5	0	1:0

Based on the results of optimization, the verification experiment using optimized values of parameters, was carried out. Experimental conditions are shown in table 5.4. The experiment conducted according to growth conditions chosen during the optimization process for total reflectance improvement, showed average height of 21.88 μm and reflectance %R of 0.198%, 0.104% and 0.077% for 350, 550 and 750 nm wavelengths, respectively. Figure 5.5(a) shows SEM image of grown CNT forest using standard condition. As can be seen, verification experiment allowed growth of homogenous vertically aligned CNT forest, with very low reflectance (Fig. 5.5(b)). Reflectance results were compared to results obtained for the CNT forest grown according to the standard condition from before the optimization process. While for 350 nm wavelength, the reflectance of CNT forest was decreased by 11% (from 0.218% to 0.194%), the improvement for 550 nm and 750 nm wavelengths was calculated as 26% (from 0.14% to 0.104%) and 45% (from 0.14% to 0.077%), respectively.

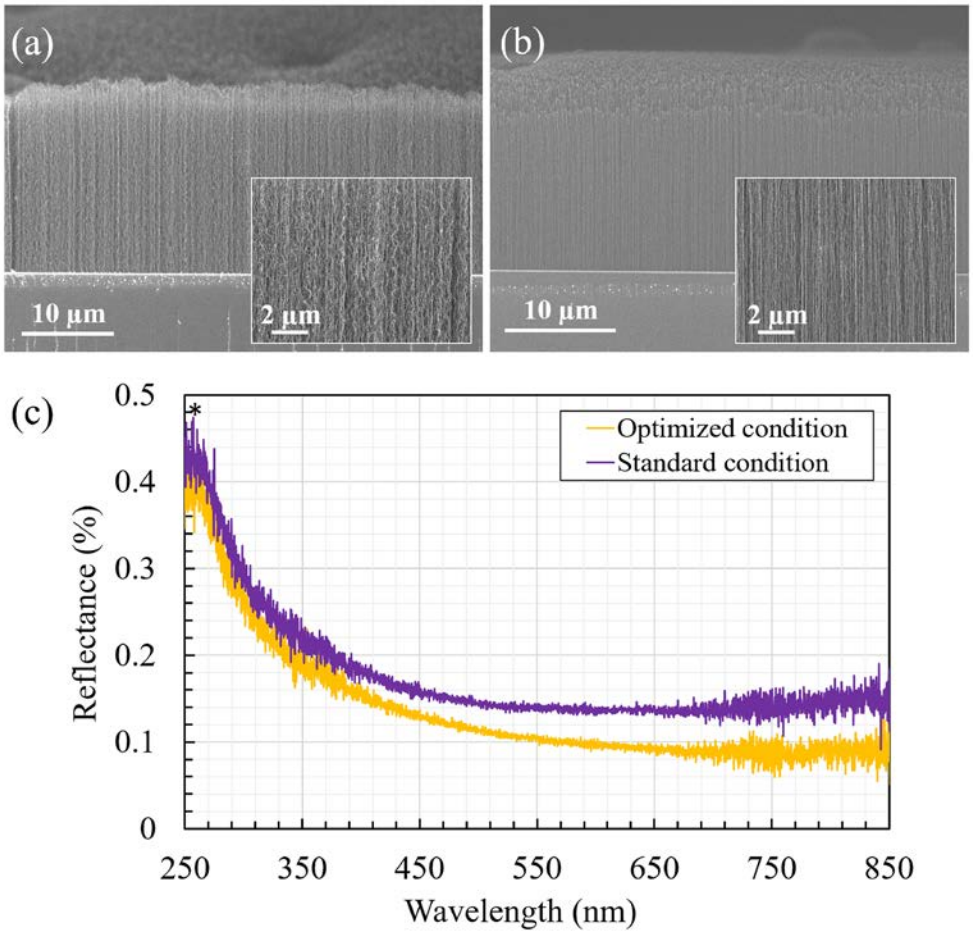

Figure 5.5. SEM images of CNT forest grown according to (a) standard condition, (b) optimized parameters condition in Table 5.4; (c) reduced total reflectance for sample before and after optimization, (∗ - Si peak) [submitted to Journal of Materials Science].

As should be noted, the verification experiment conditions, chosen based on the SN ratio analysis graph in Figure 5.3, were similar to experiment 6 from table 5.2, with a change in acetylene gas flow rate. Furthermore, by increasing acetylene and hydrogen flows, in order to keep same flow ratio, it was also possible to improve the already low reflectance of experiment 6 (%R = 0.102% for 750 nm). Through statistical optimization, the most suitable values of bias and catalyst thickness were chosen, and allowed the formation of relatively small, high-density catalyst particles, which resulted in the growth of high-density CNT forest with improved alignment and crystallinity, achieved by the control of growth atmosphere (acetylene flow, ratio).

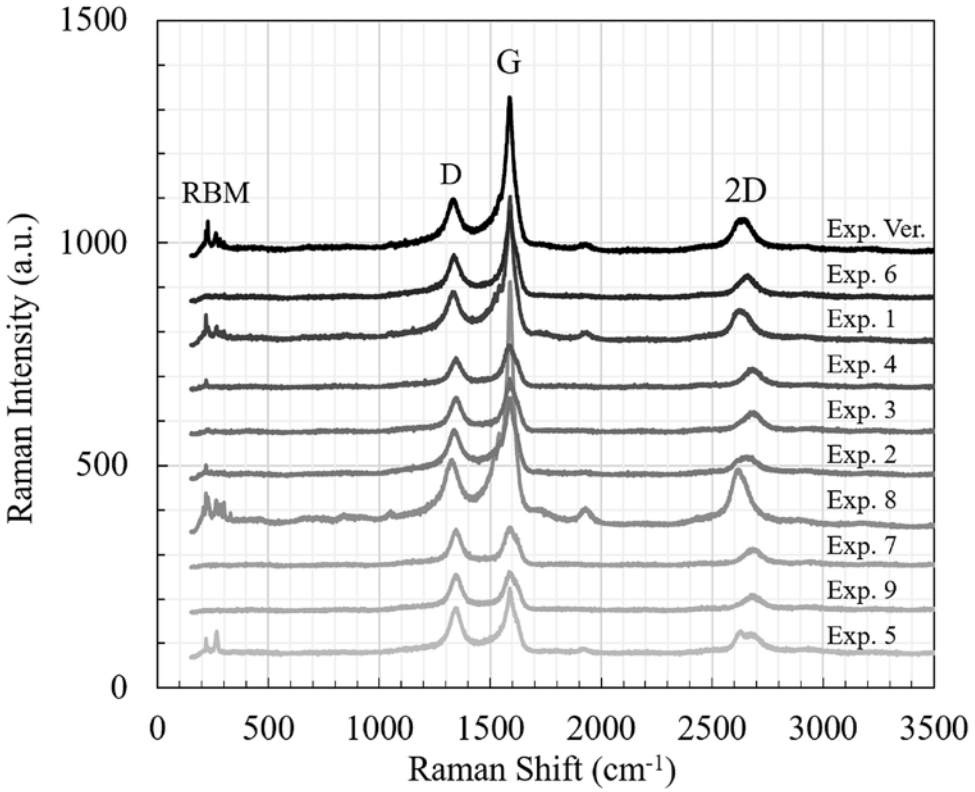

Figure 5.6. Raman spectra of CNT forest grown according to Taguchi plan of experiments (Table 5.2) [submitted to Journal of Materials Science].

In order to explain the influence of CNT structure on optical reflectance, Raman spectroscopy was used for CNT forest characterization. Figure 5.6 shows the overall Raman spectra of samples grown according to Taguchi plan of experiments, ordered from the highest measured value of reflectance (bottom spectrum) to the lowest value (top spectrum). The radial breathing mode peaks (RBM), which are an indicator of the existence of SWNTs [145,176], were defined in experiment 1, 5, 8 and in the verification experiment (Exp. Ver.). For those samples, based on peaks observed in the RBM bands, the diameter of SWNTs (0.8 – 1.2 nm) was calculated. Additionally, the RBM peaks of very low intensity could be observed for sample 2, 4 and 6, implying the presence of SWNTs in the MWNT forest. For large diameter MWNTs, the intensity of RBM band was very weak and hardly observable [177].

The intensity ratio of the G and D band indicates the quality of CNTs in the samples. The I_G/I_D ratio close to 1, indicates the high quantity of structural defects and is usually

correlated to MWNTs, due to a greater number of defects, originated from multiple graphite layers. Alternatively, SWNTs and DWNTs show higher differences in the G and D band intensities [178]. Based on that, the existence of SWNTs in experiment 1, 8 and in the verification experiment was confirmed. Interestingly, in experiment 5, despite visible RBM band, the intensity of the G band is relatively low in comparison to the D band. This results might indicate a mixture of SWNT, DWNT, and MWNT in the sample. Furthermore, for samples in which the low-intensity RBM bands are observed, higher G band intensity is noticed. It is assumed, that also in those samples, despite the high quantity of MWNTs, SWNTs are also present. For the rest of samples (exp. 3, 7, and 9), the I_G/I_D ratio is close to 1, indicating MWNTs in the CNT forest volume.

Additionally, the G band frequency might be used to define electrical properties of SWNTs, due to differences in Raman line shapes [177]. The G band consists of two main components, the G^+ band and the G^-, the existence of which is related to vibrations of carbon atoms and stretching C-C bonds in the high-frequency region [179]. Due to that, it was defined that SWNTs identified in the experiments 1, 8 and in the verification experiment are semiconducting. Due to relatively low intensities of G bands and presence of MWNTs in structure, the type of SWNTs present in other samples was not defined.

As can be seen, throughout the experiments, various types of CNTs were observed, from semiconducting SWNTs to metallic MWNTs, and no clear relation to reflectance measurements was defined. High crystallinity of individual SWNTs results in the improvement of the total reflectance, due to the higher optical density and improved propagation of light in CNT structure. Furthermore, the total reflectance of the typical MWNTs is higher than the one of the SWNTs, due to a higher number of the defects related to a higher number of graphene sheets in their structure. This could imply that CNT forests composed of SWNTs should result in the lowest values of the reflectance. However, due to a large number of structural defects accumulated in the whole volume of CNT forest, the effect of the crystallinity improvement is dramatically decreased. It is also known, that chirality and diameter of SWNTs affect optical reflectance; however, for uniform, vertically aligned CNT forest, this influence also seems to be insignificantly small and can be neglected.

For that reason, the order of Raman spectra in Fig. 5.6 do not show the dependency between the type of CNTs and the total reflectance values.

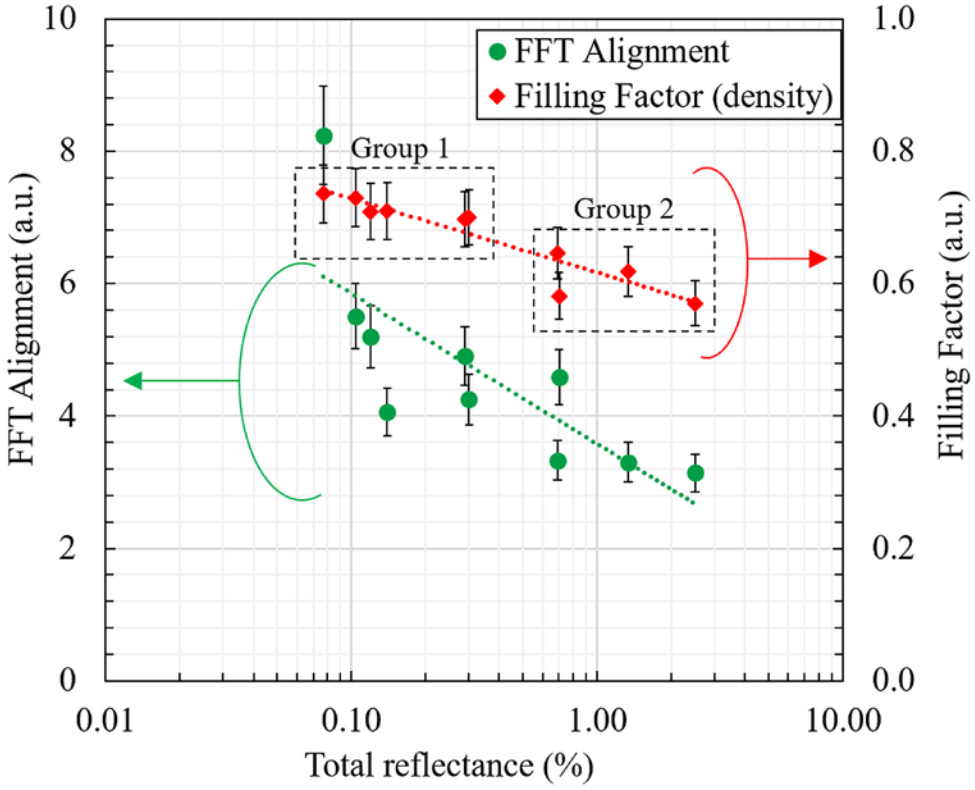

Figure 5.7. FFT Alignment and filling factor of CNT forest grown according to plan of experiments, ordered by reflectance value [submitted to Journal of Materials Science].

Figure 5.7 shows FFT alignment and filling factor (density) of CNT forests calculated for the experiments carried out during the optimization process. Results were ordered from the lowest to the highest value of the total optical reflectance. During the experiments, various density and alignment of CNTs in the forests were calculated.

The results of density measurements of CNT forests were divided into 2 groups. The first group (Group 1) of relatively high-density forests, with similar values of filling factor, exhibited low total reflectance in UV-VIS light range. For higher values of filling factor of CNT forest, changes of density seemed to be the main reason behind the changes of reflectance, while the effect of alignment could not be clearly defined. On the other hand, in the case of very similar values of filling factor, alignment of CNTs was a crucial factor deciding the value of the total reflectance, as shown in experiment 8 and 4, or experiment 3

and 2. In those experiments, for the same densities of CNT forest, an increase of alignment seemed to decrease the total reflectance values. Additionally, high-density CNT forest seemed to improve overall alignment, through supporting an effect of neighbor nanotubes [170].

In the second group (Group 2), relatively high change of density was observed and was followed by a noticeable variation of reflectance of CNT forest. Due to the lower density of CNT forest, the specular part of total reflectance spectra was affected in a higher degree by the reflected light of the incident beam. Additionally, low density of CNT forest was usually the origin to low alignment, as the CNT-supporting effect was decreased. It seems that for lower density forest, the role of high alignment of CNTs increases. For example, in experiment 7, despite the very low value of filling factor, high alignment of CNTs was observed in the sample, causing a decrease of the total reflectance compared to experiment 9, which exhibited higher density yet much lower alignment. Lower density, while maintaining relatively high alignment, resulted in the decrease of the reflectance, as compared to experiment 5 and 9, in which low-density was followed by a low alignment.

Additionally, as was visible in Raman spectra, in Figure 5.6, CNT forest of experiment 5 contained a mixture of SWNT, DWNT, and MWNT, compared to experiment 9, in which only MWNT were observed. As MWNTs have higher stiffness, compared to DWNT and SWNT, alignment of such a forest, in the case of lower density, should be kept on a higher level. This observation was also confirmed in experiment 3 and experiment 7, in which only MWNTs were observed.

As can be noted in Fig. 5.5(b), the alignment of CNT forest was very high and shows almost ideal vertical alignment perpendicular to the surface of Si substrate. Moreover, a higher density of CNT forest observed in the sample results in the increase of the total absorption area and the decrease of the average distance between individual nanotubes. For a small incident angle of 10°, each interaction between the light and CNTs can result in the reflection, transmission or absorption of the radiation, while the probability of the occurrence of the back reflection for small angles strongly decreases. The propagation of the light in the CNT forest body continues until it is completely absorbed or scattered within the forest.

The changes of alignment can be considered as changes of the incident light angle. Numerous experiments shows that the increase of the incident angle results in the increase of the total reflectance; however, the change is not significant [21, 22]. In the high-density CNT forest, due to a smaller distance between nanotubes, the probability of reflection and transmission of the propagating light decreases, as the amount of absorbing CNTs increases. In Fig. 5.7, the improvement of alignment, in the case of similar density, allowed the decrease of the total reflectance as a result of the decrease of the angle between CNTs and incident light. High-density, followed by high alignment of CNT forest allowed the most efficient absorption of incident light propagating within the forest, and resulted in a blackbody behavior in thin CNT forest film. The influence of the density and alignment was also confirmed by the SN ratio analysis, in which the highest value represented the lowest reflectance.

In conclusion, the total reflectance of CNT forest, in the case of the same height, is governed first by the density, and second by alignment of CNTs. It was confirmed that for the highest density and the highest alignment of CNT forest, the lowest value of the total reflectance was observed (%R = 0.077%), in the verification experiment. Furthermore, in the opposite case, in which the lowest values of density and alignment were observed, the reflectance of CNT forest was increased (%R = 3.76%), as observed in experiment 5.

5.5. Conclusions

The tuning of optical properties of a CNT forest grown by thermal CVD has been demonstrated. The Taguchi method of statistical analysis was used to plan the experiments and analyze the obtained results. The Taguchi method proved to be very effective for planning experiments of CNT growth, processing the obtained results, and optimizing the parameters of the growth process. Using this method, the number of necessary experiments was drastically reduced to one series of nine experiments in total, without sacrificing high accuracy of the results.

The experimental results and Taguchi analysis of the signal-to-noise ratios and interactions showed that the alumina bias potential during sputtering (48.53%) and the thickness of the catalyst layer (36.94%), which were both parameters of the catalyst

formation process, had the highest impact on the total reflectance. Furthermore, the process of catalyst formation affected the size and density of the particles, which were crucial factors of the diameter, density, and alignment of CNTs in the forest. This means that it was possible to improve the total reflectance of the CNT forest by optimizing the conditions of catalyst formation.

During the series of nine experiments and one verification experiment, the total reflectance of the CNT forest was reduced by 11% (from 0.218% to 0.194%), 26% (from 0.14% to 0.104%), and 45% (from 0.14% to 0.077%) at wavelengths of 350, 550, and 750 nm, respectively, which represent the lowest values of reflectance ever reported for a relatively low CNT forest.

The effect of the structure of the CNTs was studied by obtaining Raman spectra of the grown CNT forest. It was found that for a homogeneous, vertically aligned CNT forest, the effect of the type of CNT (SWCNTs, DWCNTs, or MWCNTs) was insignificantly small and could be neglected. There was no observable relationship between the CNT type and values of total reflectance.

The experimental results showed that the changes in reflectance were more strongly affected by the CNT density, defined by the filling factor of CNTs, than the alignment of CNTs. For a high-density CNT forest, changes in the filling factor affected the results of reflectance measurements. For forests with the same densities, however, a higher alignment of CNTs resulted in a further decrease in reflectance. Moreover, in a forest with a lower density of CNTs and thus more unoccupied space, CNT alignment had a stronger impact on the optical reflectance.

Chapter 6. Low-temperature growth of carbon nanotubes on aluminum substrates

6.1. Introduction

A high-density and high-alignment CNT forest may provide uniform CNTs with desirable length, diameter, and structure [161,180]. In recent years, CNTs were used for various electronic applications such as nanoelectronic devices [13], wiring material for Large-Scale Integrators (LSI) interconnects [15] or current emitters [17]. Methods of a direct growth of carbon nanotubes on various conductive parts of fabricated devices are very limited and mainly narrowed to the CVD methods. In the contrary, the CVD method requires higher temperature of substrates during the growth of CNTs, as compared to laser ablation, or hydrothermal methods. For different devices, a thermal durability of the actual elements is usually limited, typically to the temperature below the growth temperature of CNTs in the CVD process. In order to allow further development of various applications of CNTs in electronics, photonics, and various types of metamaterials, the direct growth of CNTs on the conducting metallic elements of the real devices is necessary and the growth of high yield and high-density CNTs at lower temperatures is required [181].

6.2. Objectives

Aluminum (Al) is a commonly used material for various applications in electronics, such as electronic storage, semiconductors, electrolytic capacitor foils, and electrodes. Furthermore, the thermal properties of aluminum allow effective thermal dissipation of heat. However, at the same time, it possess a relatively low melting point of 660°C. For this reason, in order to allow successful growth of highly-aligned CNTs, the synthesis temperature has to be significantly decreased, as compared to the typical temperatures used during the CVD process. In the following chapter, for the first time, a low-temperature growth of CNT forest at temperatures below 600°C was conducted using water-assisted catalytic chemical vapor deposition (CCVD) [2,68] on aluminum foil substrates [182]. In this chapter, the influence of preparation operation of Al foil surface on the growth of CNTs is investigated. Two main processes are studied: the influence of AlO_x buffer layer deposited on the Al foil directly before the deposition of Fe catalyst, and a hydrogen pretreatment of Al foil at higher

temperatures. Moreover, due to the overall decrease of the growth temperature, the investigation and tuning of the annealing time of Al substrates during the low-temperature growth was carried out. Finally, the systematic study of the influence of water vapor flow rate, iron catalyst thickness and catalyst lifetime was conducted, in order to increase the yield and density of CNT forest growth on Al substrates [183].

6.3. Experimental and methods

The deposition of the AlO_x buffer layer and Fe catalyst thin film were carried out using the RF magnetron sputtering method, while the growth of CNTs was carried out using the CVD method. Both methods are described in detail in chapters 3.2 and 3.3. Properties of grown CNT forest were measured using an FE-SEM microscope and micro-Raman spectroscopy, which are described in detail in chapters 3.4.1 and 3.4.4.

As mentioned previously, for future applications of CNTs in electronic, photonics, and metamaterials, a high conductivity of the substrate and the interface between the substrate and the CNT forest may be required in some cases. For that reason, an Fe catalyst of various thickness (0.8, 1, 1.2, 1.4, and 1.6 nm) was deposited either on the AlO_x buffer layer or directly on the Al foil substrate. The AlO_x layer was aimed to support a higher stability and yield of CNT forest, while direct growth was aimed to increase the conductivity of the substrate/CNT forest interface.

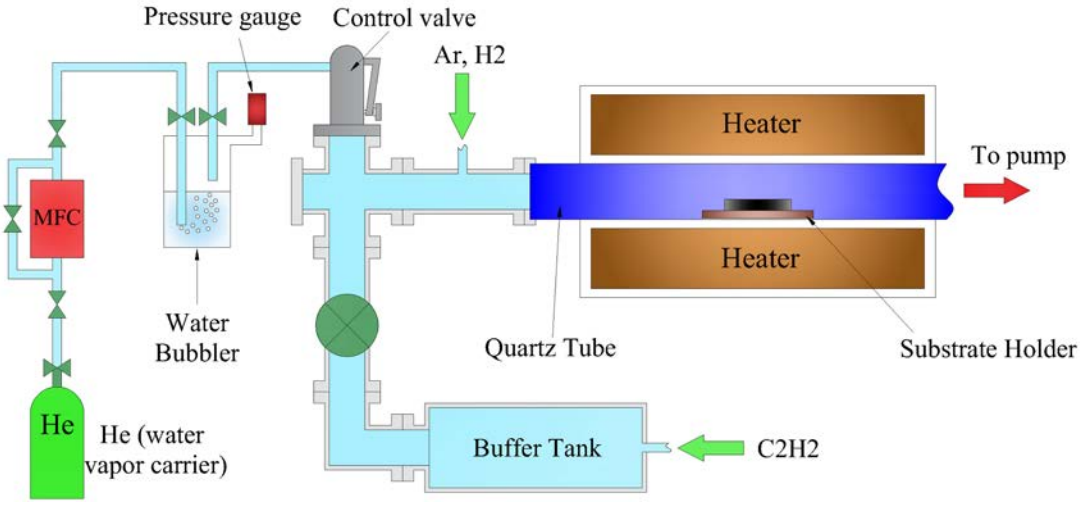

Figure 6.1. The schematic of modifications of CVD chamber for water-assisted CNT growth [183].

For the low-temperature growth of the CNT forest, a water-assisted CVD was used. For that purpose, the modifications of the CVD system were applied (Fig. 6.1). A water bubbler with two pipes introduced into the tank, one of which was long and the other is short, was filled with deionized water to the level between the mouths of both pipes. During the process, helium gas was introduced at a rate of 1 sccm by MFC controller to the water bubbler through the longer pipe which exited below the water level in the tank. The second pipe was connected to the vacuum chamber and a controlled flow of He/water vapor was introduced to the vacuum chamber. The purity of the He gas was 99.999% (5N).

Before the experiment, the pressure in the water tank was increased by introducing He gas, in order to avoid a high concentration of H_2O vapor at the beginning of process. After the annealing process was started, a further introduction of He to the water bubbler was conducted. At the same time, a control valve responsible for precise control of He/H_2O mixture flow, was opened, which allowed the introduction of water vapor into the vacuum chamber. The control of the H_2O amount in the mixture was performed by keeping constant pressure in the tank. The pressure of water vapor at temperature of 35°C, was constant and took a value of 5.63×10^3 Pa. By knowing the value of the pressure in water bubbler, the water flow can be calculated.

In order to fulfill the requirements of low-temperature growth, the temperature during all experiments was set to 600°C. Based on chapter 4, in which the influence of the temperature and annealing time was studied, an investigation of suitable annealing time for the growth of CNTs was carried out.

6.4. Results and discussion

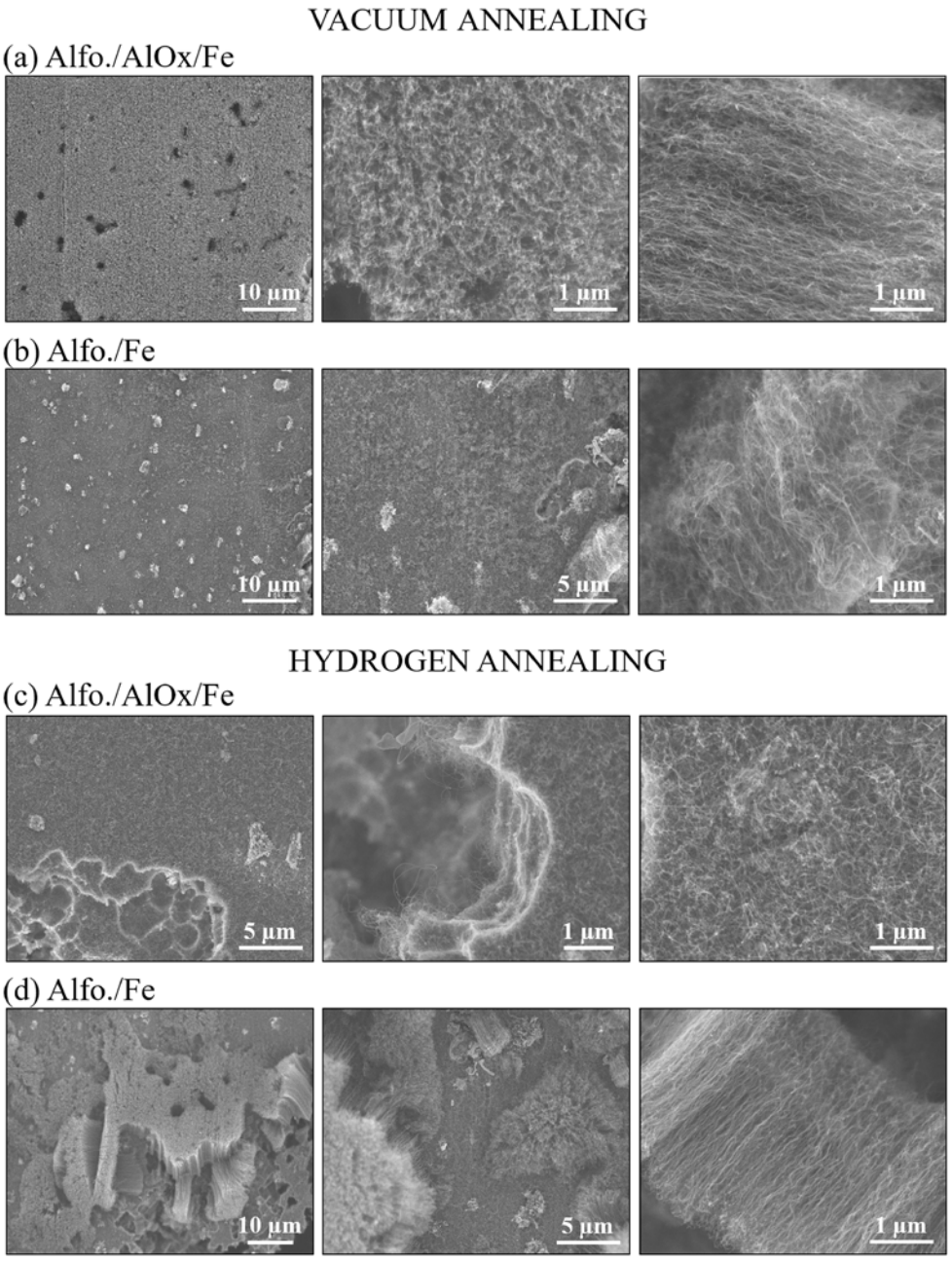

Figure 6.2. Growth of CNT forest on Al foil in dependence of annealing atmosphere and catalyst [183].

For the purpose of the investigation of growth parameters, the growth of the CNT forest in a vacuum and hydrogen atmosphere was conducted, in which the deposition of the catalyst was carried out on an AlO_x buffer layer or directly on the Al substrate. As can be seen in Fig.

6.2(a), annealing in a vacuum of AlO_x/Fe catalyst resulted in a relatively high density, randomly aligned and low uniformity CNT forest. For the same catalyst setup, the growth of a CNT forest in the hydrogen atmosphere (Fig. 6.2(c)) resulted in more uniform growth of very short, low-density CNT forest. On the other hand, the growth of CNTs using only on an Fe catalyst deposited directly on the Al foil resulted in a low-uniformity and randomly aligned CNT growth, which is shown in Figure 6.2(b). In contrast, in the case of hydrogen annealing, in some areas, a high density CNT forest was observed. It was assumed that the presence of an AlO_x buffer layer would improve the uniformity of CNT forest growth; however, the highest observed density was confirmed for samples without AlO_x. Moreover, it was concluded that the reason behind the low uniformity of grown CNTs is related to the contamination of the Al substrates, which occurs during the preparation of the catalyst. The presence of 30 nm thick AlO_x buffer layer resulted in the coverage and separation of contaminations from the Fe catalyst that existed on the surface of Al foil, and allowed the improvement of the uniformity and density of the growth of CNTs. During the annealing process, the majority of the catalyst has no contact with the possibly contaminated surface of the Al foil, so the formation of the catalyst can occur in relatively a stable environment. On the other hand, the presence of the AlO_x layer may influence the total conductance on the interface between Al substrate and CNT forest. For that reason, in order to fulfill requirements for high conductivity of the system, the cleaning procedure needs to be applied. The following part of the research focused on the improvement of the CNT forest growth using an Fe catalyst deposited directly on the Al foil.

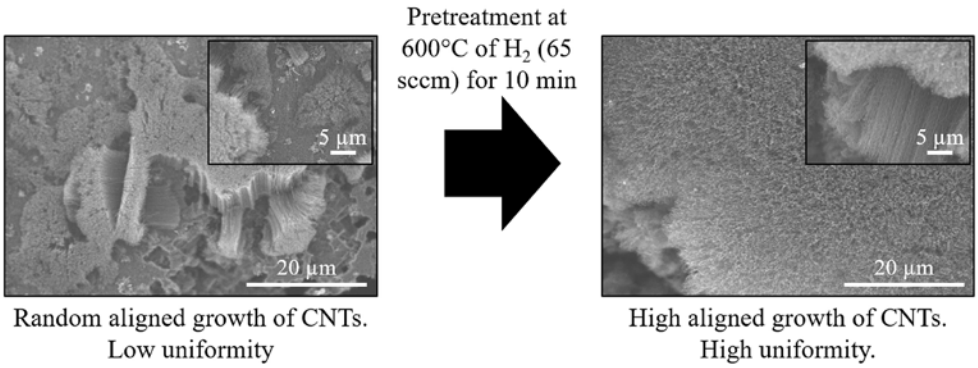

Figure 6.3. Hydrogen annealing time dependency on the growth of CNTs [183].

For the purpose of cleaning the surface of the Al substrate, before the deposition of the Fe catalyst, a pretreatment of samples in hydrogen atmosphere was carried out. The pretreatment was conducted at a temperature of 600°C, under a hydrogen flow rate of 65 sccm, for 10 minutes. As can be seen in Figure 6.3, due to the hydrogen pretreatment of Al substrates, the growth of CNTs was significantly improved. It was concluded, that at higher temperatures, hydrogen molecules reduced the surface of the Al foil with the simultaneous removal of organic contamination. During the process, the natural oxide layer is reduced by hydrogen and removed from the surface, which results in a pure metallic surface of the substrate. After the pretreatment process was finished, samples are removed from the vacuum chamber and oxidation of the substrates in air occurs, resulting in new thin layer of aluminum oxides. The pretreatment process described in this section was applied in the following part of the research before each deposition of Fe catalyst in all conducted experiments.

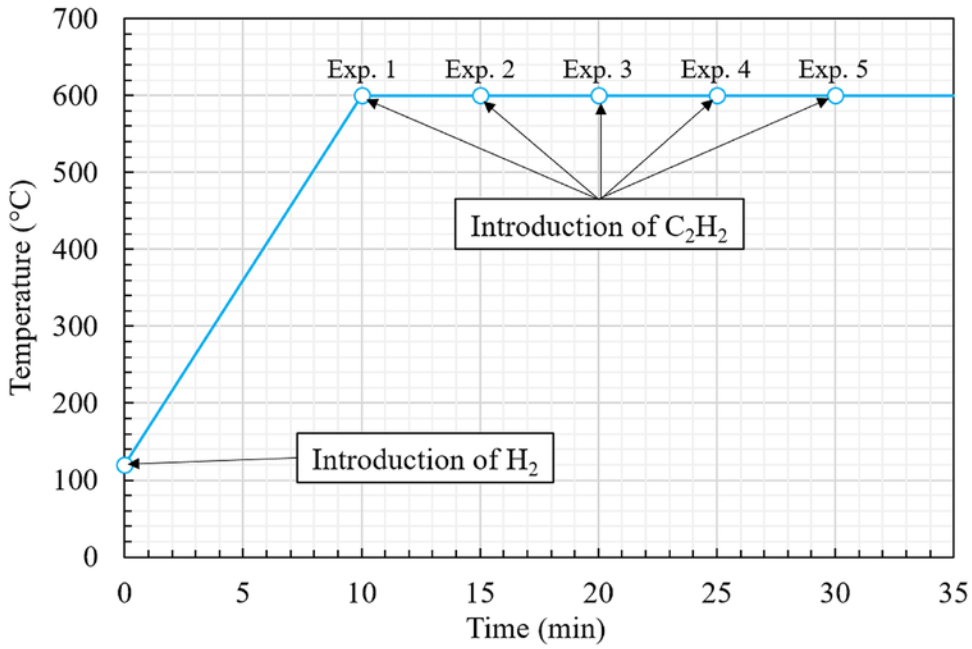

Figure 6.4. Observed improvement for CNT growth (a) without and (b) with hydrogen pretreatment [183].

For the low-temperature growth, the annealing time is the most important parameter [161] and for that reason the investigation of the influence of the annealing time on the growth of the CNT forest was conducted. After the evacuation of the CVD chamber to the base pressure of 5×10^{-4} Pa, hydrogen gas was introduced during the heating from 120°C to 600°C,

for various time of 10, 15, 20, 25, or 30 minutes, after which acetylene was introduced, in the manner shown in Figure 6.4. It should be noted, that the total time required to obtain the temperature of 600°C was about 10 min.

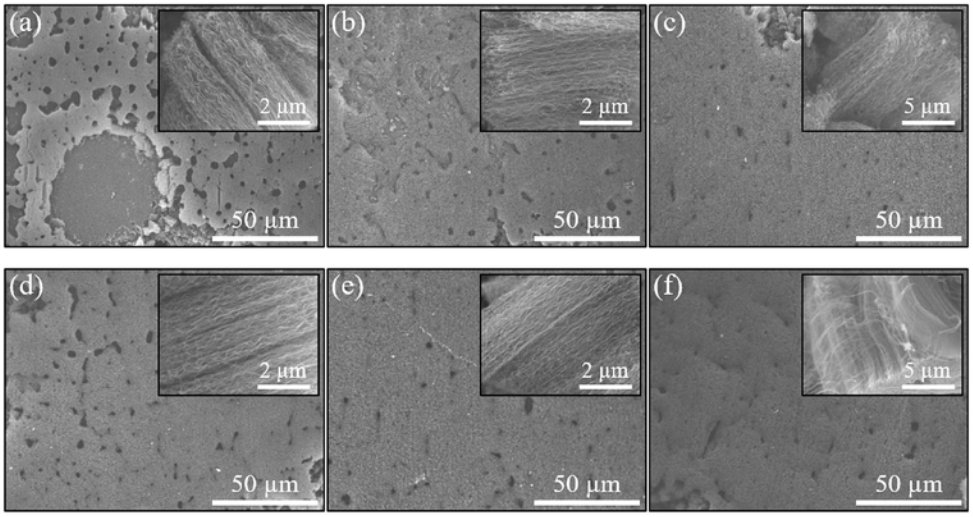

Figure 6.5. Influence of the annealing time on the growth of CNT forest [183].

The influence of the annealing time on the growth of CNT forest was investigated and results are presented in Figure 6.5. For the time growth of 10 min (Fig. 6.5(a)), relatively low density and low uniformity CNT forest of 6 – 7.5 µm height was observed. With the increase of the annealing time to 15 and 20 min (Fig. 6.5(b, c)), the height and uniformity of the CNT forest were improved; however, the density was still relatively low and no significant improvement was observed. For the annealing time of 25 min (Fig. 6.5(d)), the highest CNT forest of 11 µm was observed. Furthermore the density and the uniformity were also improved, as compared to the cases of shorter annealing time. A further increase of the annealing time (Fig. 6.5(e)) resulted in the decrease of the height (9 µm) and density. It was assumed that the formation of catalyst particles depended on the temperature and time of annealing. In the case of low-temperature growth, a shorter time did not allow the formation of particles of sufficient size and density for uniform growth of CNT forest. On the contrary, a longer annealing time resulted in the formation of relatively big particles, which were directly responsible for the increase of the diameter and a slower growth of CNTs within the forest. As can be noted, the time of 25 minutes seemed the most sufficient for the low-temperature growth of CNT forest. A suitable combination of temperature and annealing

allowed the growth of a relatively high quality CNT forest. For that reason, an additional experiment was conducted, in which hydrogen was introduced for 15 min; however, after about 10 min, when the temperature of 600°C was reached (Fig. 6.5(f)). The results of SEM measurements showed the highest density and height of the CNT forest observed throughout all the conducted experiments. It was assumed, that heating in a vacuum allowed the maintenance of a relatively unchanged surface of the Fe catalyst film, which allowed a more rapid annealing process after the introduction of hydrogen at 600°C. The introduction of hydrogen at the beginning of the heating process, seemed to have a more significant impact on the formation of catalyst particles during the heating, as compared to vacuum annealing. The presence of hydrogen gas during the heating stage induced changes of catalyst much faster and eventually affected the size of particles, and finally the density and height of grown CNT forest.

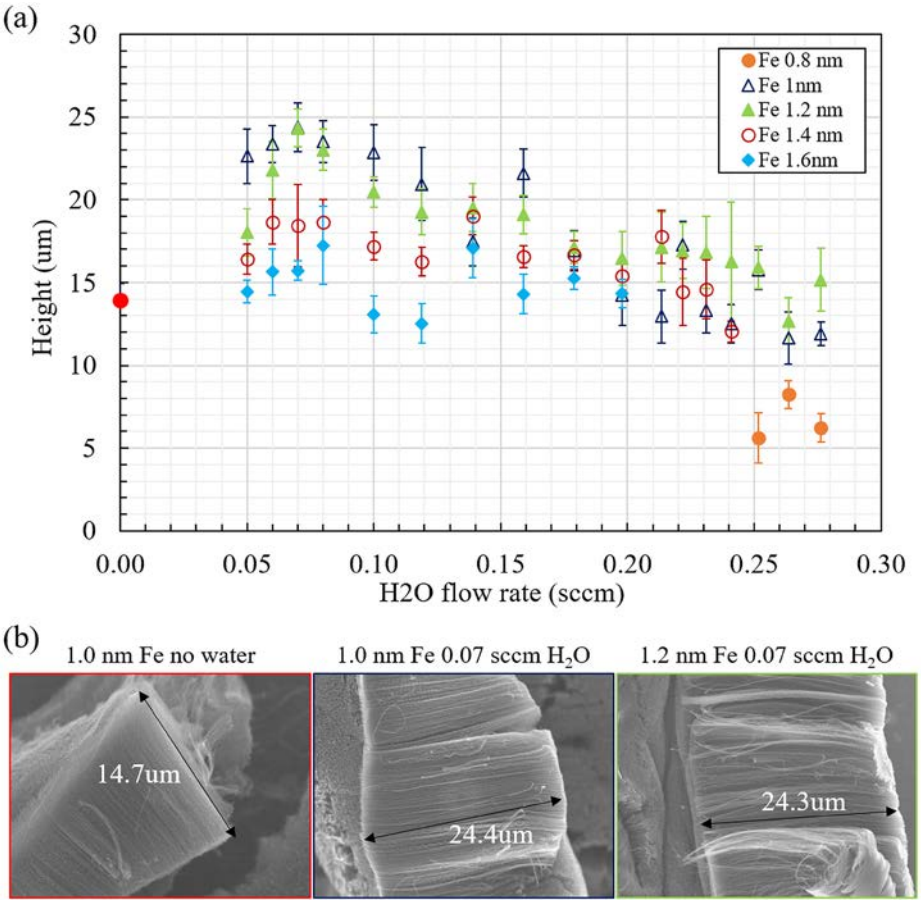

Figure 6.6. (a) Water flow rate vs height of CNT forest, and (b) CNT forest grown for the case without and with water flow of 0.07 sccm [183].

Following the investigation of pretreatment process and optimization of annealing time, water-assisted growth of CNTs was performed. Various water flows from 0.05 sccm H_2O to 0.28 sccm H_2O, and various catalyst thicknesses of 0.8 – 1.6 nm, were used during the growth of CNTs on Al substrates. At first, catalyst thickness of 0.8, 1.0, 1.2 nm were used for the growth; however, due to the low height and density of CNTs grown using 0.8 nm, it was replaced with an Fe catalyst thickness of 1.4 nm. Furthermore, an Fe catalyst thickness of 1.6 nm was added to the experiments, in order to study the influence of the catalyst thickness on the growth. As can be seen in Figure 6.6, the initial growth of CNTs of 14.7 μm for no water vapor flow case, was improved to around 24 μm for H_2O flow of 0.07 sccm. The decrease of the H_2O flow during the process resulted in the improvement of CNT height as observed in Fig. 6.6; however, after the peak of growth was reached, around 0.07 sccm H_2O, a decrease of the height of the CNT forest was noted. Based on the obtained results, it was concluded that the optimal ratio of H_2O and C_2H_2 gases is about 7/1000 and for this value, the growth rate of the CNT forest was improved in the highest degree. The observed peak of the water flow rate indicated a close relation between acetylene and water vapor flows and was one of the most critical factors in water-assisted CVD growth of CNTs. During the growth of CNTs, the water vapor acts like a weak oxidizer that removes amorphous carbons from the nanotubes, without damaging them at the same time. Moreover, amorphous carbons create a coating at the surface of the catalyst particles, which results in the reduction of their activity their activity. It was concluded, that the H_2O vapor preserved and stimulated catalyst activity, allowing growth of higher yield CNT forest. As can be seen in Fig. 6.6, the catalyst thickness of 1.0 and 1.2 nm seemed to be the most stable during the series of experiment. For more detailed investigation, a dependency between the Fe catalyst thickness and height of CNT forest was prepared and is presented in Figure 6.7.

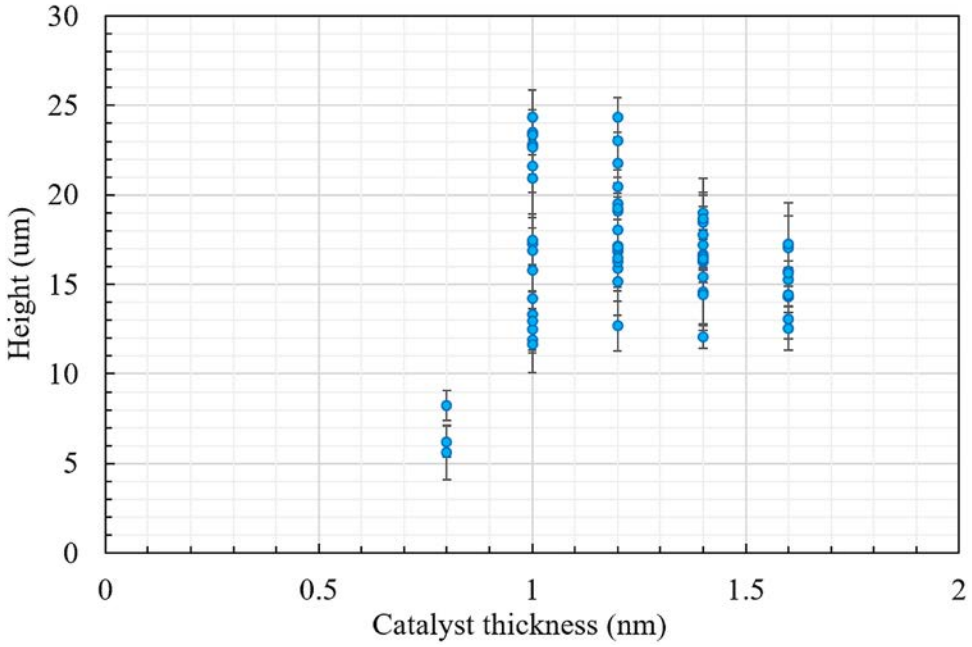

Figure 6.7. CNT height vs. Fe catalyst thickness [183].

As can be seen, the catalyst thickness of 0.8 nm resulted in the lowest height of CNT forest, which was also lower than the height of CNT forest grown in the case of no water flow. It was assumed that due to the relatively high roughness of the Al foil, the deposition of homogenous thin catalyst film become more difficult. Due to non-homogenous film and small amount of the catalyst material, the formation of catalyst particles during the annealing process resulted in low density particles which were the direct cause of growth of low density and non-uniform CNT forest. On the other hand, for the catalyst thickness of 1.4 and 1.6 nm, the improvement of height was observed; however, not as big as for the Fe catalyst thickness of 1.0 and 1.2 nm. It was concluded that during the annealing process, the formation of bigger particles occurred and was related to the extensive amount of catalyst material, as compared to the other cases. Due to the bigger size of the catalyst particles, the diameter of CNTs was increased resulting in the slower growth of CNTs within the forest. Finally, it was assumed, that catalyst thicknesses of 1.0 and 1.2 nm were the most suitable for the presented combination of parameters, including surface roughness, temperature, and H_2O flow rate. The height of 14.7 µm for no water flow case for 1.0 nm Fe catalyst was improved by almost 70%, to the height of 24.4 µm.

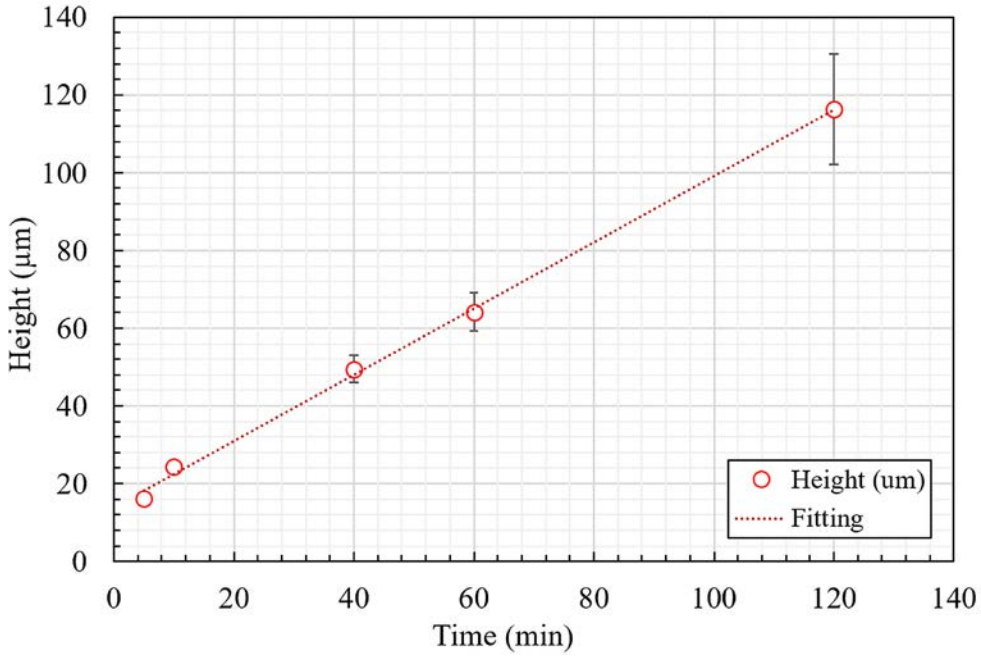

Figure 6.8. Fe catalyst activity in low-temperature water-assisted CNT growth [183].

In the typical case, the activity of the catalyst during the CNT growth is limited to 20 – 30 min and strongly depends on the temperature, time, height and water vapor presence in the process [2,68,69]. Figure 6.8 shows the catalyst activity for the Fe catalyst thickness of 1.0 nm. As can be seen, for low-temperature water-assisted CVD growth, the catalyst activity of 120 min was observed and resulted in an average height of CNT forest of 119±15 µm. The initial growth of CNT forest was improved in the first 10 min of growth and slightly decreased in time, which resulted in overall growth rate of 1.1 µm/min for 120 min growth and 2.4 µm/min for 10 min growth. Furthermore, based on the linear shape of growth rate curve, it was assumed that the activity of catalyst was larger and the height of CNT forest could still be improved. Low temperature of the growth process was the main reason behind low growth rate of CNT forest. On the other hand, the presence of water vapor in the process improved the growth rate and allowed the achievement of much higher CNT forest yield.

6.5. Conclusions

Low-temperature growth of CNTs on Al foil substrates at 600°C required treatment of the surface, in order to remove contaminations present on the samples. It was confirmed, that both, the deposition of the AlO_x buffer layer and hydrogen treatment of the surface before

deposition of the Fe catalyst, had a positive effect on the growth of CNTs. The dependence of hydrogen annealing time showed that 15 min of hydrogen annealing allowed growth of relatively high density and uniform CNTs on the surface of aluminum.

The usage of the water-assisted CVD method resulted in the improvement of the overall growth height of CNTs on Al substrate, from 14.7 μm (w/o H_2O) to 24.4 μm (0.07 sccm H_2O) for 10 min growth, at 600°C. Furthermore, the investigation of catalyst thickness showed that Fe catalyst thicknesses of 1.0 and 1.2 nm are the most suitable for low temperature growth. Catalyst thickness of 0.8 nm, due to high roughness of Al foil surface, did not allow growth of a high-density CNT forest. Due to slower growth of thicker MWNTs, a low height of CNT forest was observed for thicker catalyst films. Finally, due to the introduction of water vapor during the CNT growth, the catalyst activity was improved to 120 min and allowed a growth of 119±15 μm thick CNT forest.

Chapter 7. Fabrication of fine CNT metamaterial nanostructures by FIB

7.1. Introduction

Carbon nanotubes (CNTs) possess extraordinary electrical, chemical, physical and optical properties [180], which are directly derived from their unique structure [184] such as anisotropic electrical conductivity of horizontally aligned CNTs [185], and anisotropic optical absorption of vertically aligned CNTs [186]. Highly controlled PVD/CVD processes, including self-organization of the catalyst particles, are desired to achieve unique highly-oriented and periodically positioned CNT forests for new electronic and optronic applications.

The extraordinary properties of CNT forest, were recently used for fabrication of metamaterials and nonlinear photonic devices in the form of multi-walled CNT (MWNT) arrays, [6,187,188] slits cut in the CNT films [38], or spray-coated CNT films on ceramic metamaterials [39,189]; however, none of these examples employed the unique properties of CNT forest. To fully utilize the properties of CNT forest, originated from high alignment, density, and CNT forest structure, a different method of patterning is required. Patterned growth of carbon nanotubes in the scale of tenths of micrometers has been successfully reported on silica [190–192], silicon [193] substrates, and also on predeposited catalyst [194–196]. On the other hand, the patterning of predeposited catalyst in nanoscale, which would allow a uniform, vertically aligned single-walled CNT forest growth on various shape nanosize structures, is still challenging and is yet to be achieved [195,197–199]. A high-quality CNT structures of various shape and micrometer size were achieved by utilizing various fabrication methods. Standard lithography methods, like photolithography [194,200], electron beam lithography (EBL) [201], or soft-lithography [202] were utilized and allowed growth of fine CNT patterns. A laser machining method was used for fabrication of one-dimensional grating patterns [203], while laser etching method was utilized to obtain microstructures of CNT brushes [199]. Moreover, a patterned growth of CNTs was also achieved using anodic aluminum oxide (AAO) templates [204] and inkjet-printing of the catalyst [196]. Finally, a focused ion beam (FIB) and electron beam (EB) were used for the

patterning of catalyst nanodots and allowed fabrication of arrays of individual MWNTs [4,6,188].

For the patterning of nanostructures on the predeposited catalyst, high precision in nanoscale is required. The ability of patterning of thin films by the FIB method was presented before and allowed successful fabrication of metamaterial nanostructures from metals [205]. The FIB method is maskless and allows fabrication of nanoscale patterns of various shape and size; however, due to sputtering, redeposited material is observed on the surface of the out-of-patterned area [206]. In this study, in order to overcome the major disadvantage of the redeposition of material, a FIB secondary etching method has been developed to clean the patterned surface from the redeposited material by low depth ion beam irradiation [206] and to improve the growth of CNTs in patterned areas.

7.2. Objectives

The purpose of this part of the research was to provide a reliable method of precise fabrication of CNT patterns for metamaterial size ranged from around 150 nm to single micrometers, for the optical and infrared regime, and future applications for superlenses, antennas, and thermal metamaterials.

In the following chapter, the way of fabrication of CNT forest metamaterial nanostructures using FIB was demonstrated. Primary FIB etching was used for patterning of nanostructures and caused a redeposition of the sputtered material, while the secondary etching method was developed to remove the redeposited material and clean the surface of patterns. The influence of FIB fabrication parameters of metamaterial patterns on the catalyst surface morphology and CNT forest internal structure (uniformity, alignment, etc.) was investigated. By controlled FIB processing, the synergy between the top-down (shape of CNT metamaterial nanostructures) and bottom-up (structure of CNT forest) approaches was achieved [207].

7.3. Experimental and methods

A 30 nm thick AlO_x support layer and a 0.9 nm thick Fe catalyst layer, were deposited using the RF magnetron sputtering method described in chapter 3.2. The growth of CNTs was conducted using thermal CCVD method described in detail in chapter 3.3. The

morphology of CNTs was measured by FE-SEM, and the morphology of the catalyst surface after the patterning was measured by AFM, described in chapters 3.4.1 and 3.4.2, respectively. The TEM analysis was performed using JEOL JEM 2100M microscope, presented in chapter 3.4.3. The catalyst films were patterned using FEI QUANTA 3D 200i FIB system, described in chapter 3.4.7.

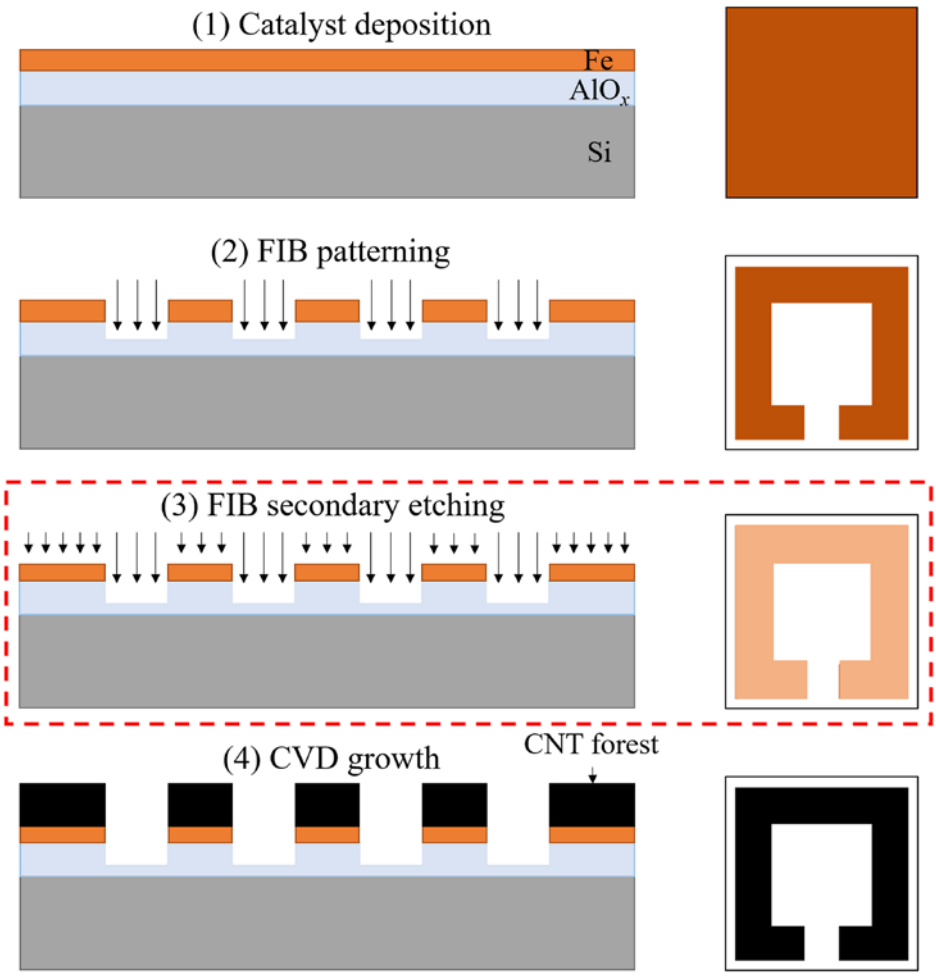

Figure 7.1. Schematic of fabrication process of CNT metamaterials. (1) Catalyst deposition, (2) FIB patterning, (3) FIB secondary etching, and (4) CVD growth [207].

The experiments were conducted according to the following procedure: (1) deposition of AlO_x/Fe catalyst on Si substrates by the RF magnetron sputtering; (2) FIB patterning of metamaterial patterns on the catalyst, followed by (3) FIB secondary etching process, continuously, without breaking vacuum; (4) CVD growth of CNT on the prepared samples (Fig. 7.1).

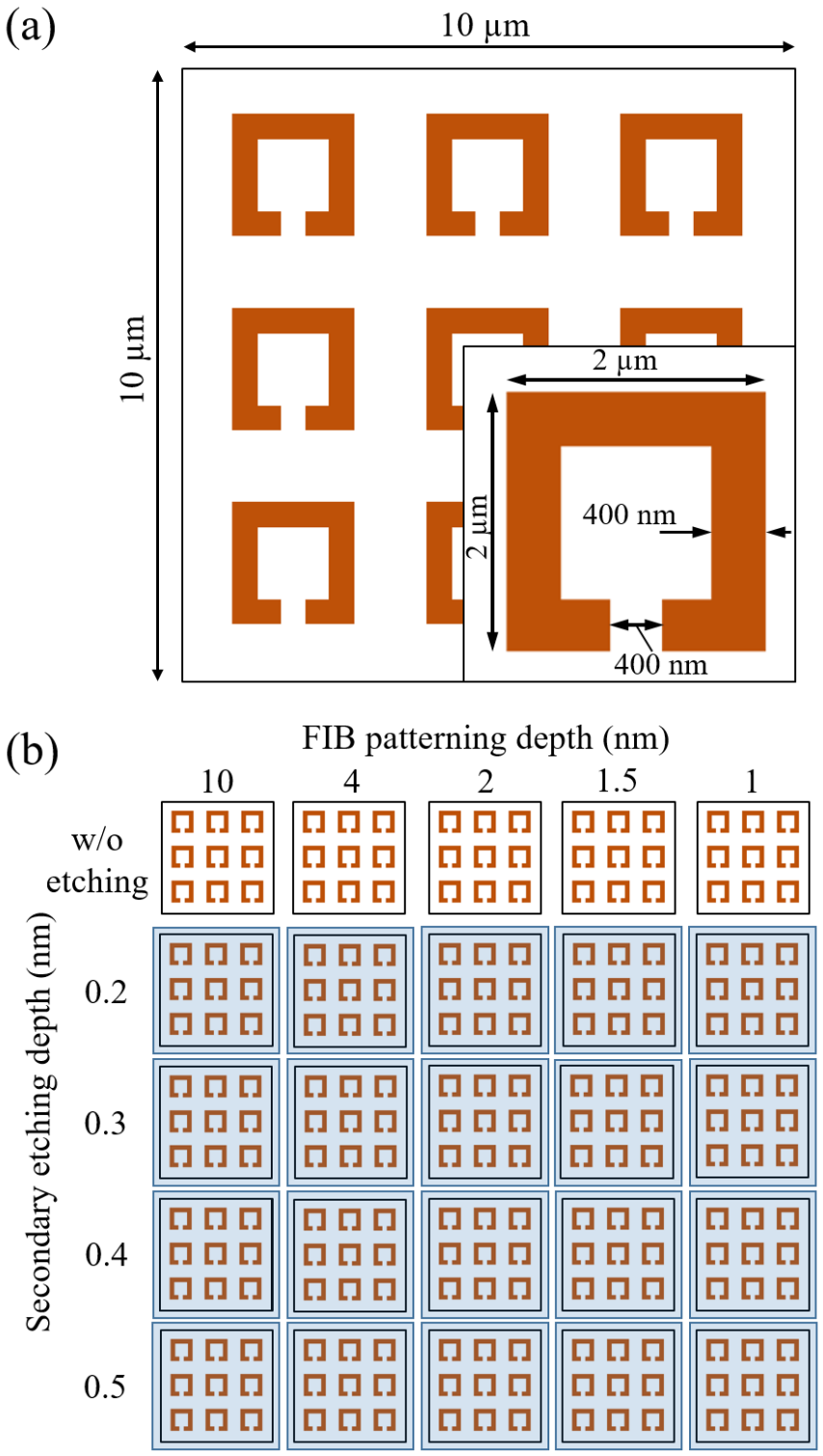

Figure 7.2. (a) Schematic of metamaterial patterns used for fabrication, (b) map of FIB milling with patterning and secondary etching depths [207].

Figure 7.2(a) shows a design of CNT metamaterial patterns used in FIB fabrication. The patterned area of 10×10 μm^2 contained 9 SRR patterns of 2×2 μm^2 size and a wall thickness of 400 nm. It should be noted that the FIB etching was selectively applied to the surface during the fabrication, to obtain non-etched SSR pattern areas which kept pristine deposited catalyst, while the secondary etching was applied to the entire surface, including SRR patterns. To study the effects of the patterning depth (10 – 1 nm) and the secondary etching depth (0.2 – 0.5 nm), a map containing 25 SRR pattern arrays was prepared (Fig. 2(b)).

The fabrication of Split Ring Resonator (SRR) patterns using various patterning depth was conducted using a prepared bitmap design and was followed by the FIB secondary etching process, continuously, without breaking vacuum (Fig. 7.1). The FIB fabrication was conducted with 30 pA, 30 kV Ga ion beam, which resulted in the diameter of the beam of 17 nm. The value of the current of 30 pA was determined based on the application and conducted tests. For lower values of current (1.5 and 10 pA) very slow etching rate was observed, while for the currents above 30 pA, an extensive etching of the edges of the patterns was noted.

For the presented FIB system the sputtering rate of Fe and stoichiometric Al_2O_3, defined by volume per dose of charge was defined as 0.29 and 0.08 μm^3/nC, respectively. As can be seen, the sputtering rate of Fe films is over 3 times higher than for the Al_2O_3. On the other hand, during the experiments, non-stoichiometric AlO_x was defined, so the sputtering rate might be higher, due to lower density of the deposited film.

7.4. Results and discussion

The results of FIB patterning depth and FIB secondary etching depth are shown in Figure 7.3.

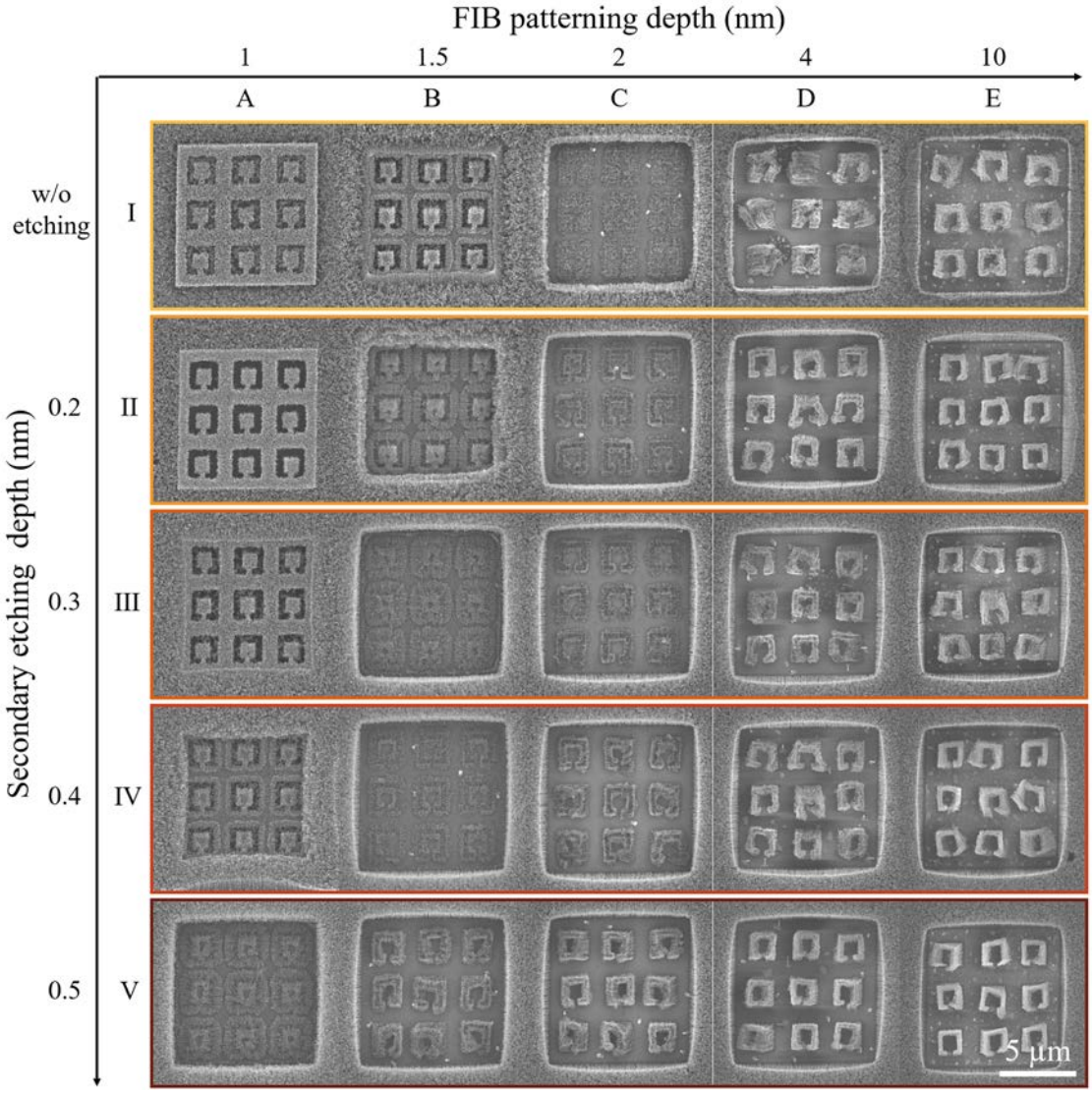

Figure 7.3. SEM images of patterned surface after CNT forest growth. Arabic numerals refer to depths in nm, while letters and Roman numeral were introduced for the purpose of analysis [207].

The patterning depth of 10 nm allowed the growth of CNT SRR arrays (Fig. 7.3 – E (I-V)). The quality and density of CNTs in those patterns were improved by applying the secondary etching of 0.2 – 0.5 nm. A similar trend was noticed for other patterning depths, and was the most noticeable for the patterning depth of 2 nm (Fig. 7.3 – C (I-V)), in which,

without the secondary etching, very low and random-aligned CNTs in the SRR patterns were grown. After the introduction of the FIB secondary etching process, gradually the pattern appeared, as the more vertically oriented growth of CNTs was observed. Interestingly, in the area of the patterning depth of 1 nm and for secondary etching depths of 0.2 and 0.3 nm (Fig. 7.3 – A (II-III)), the inverted SRR arrays were observed. The high-aligned growth of CNTs in SRR arrays for the depths of 4 and 10 nm (Fig. 7.3 – D, E) was successfully obtained, and a very small diameter of 2 - 3 nm scale was observed in a high-resolution SEM image (Fig. 7.4).

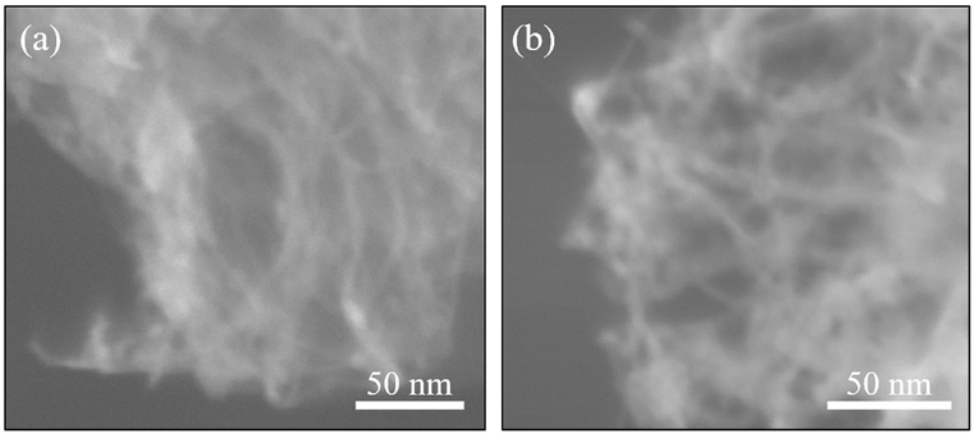

Figure 7.4. High resolution SEM images of CNT arrays grown using patterning depth of 10 nm and FIB secondary etching depth of 0.5 nm. Magnification of (a) ×400 000, and (b) ×500 000 [207].

It was concluded that the entire catalyst of 0.9 nm thickness and part of AlO_x support layer, including diffused Fe catalyst, were completely removed for 4 and 10 nm patterning depths, leaving only non-etched SRR areas with the preserved catalyst, allowing growth of CNT forests. For a patterning depth of 2 nm (Fig. 7.3 – C), short and randomly oriented CNTs were observed in SRR patterns and improved by the secondary etching process (C (II-V)). By reducing patterning depth to 1 and 1.5 nm (Fig. 7.3 – A (I), B (I)), without secondary etching, the growth of CNTs was observed in the etched area, while the growth of CNTs in the patterns was suppressed. It was found that in those cases patterning depths were not sufficient enough to completely remove catalyst film from the surface by the secondary etching, resulting in the improvement of growth height on thinner catalyst [67], while the redeposited material reduced the growth of CNTs in the designated SRR patterned areas.

Applying the secondary etching removed the redeposited material from patterns, allowing growth of randomly oriented CNTs. As a result, it was concluded that the secondary etching affected the catalyst surface morphology and was the primary reason for changes in CNT growth.

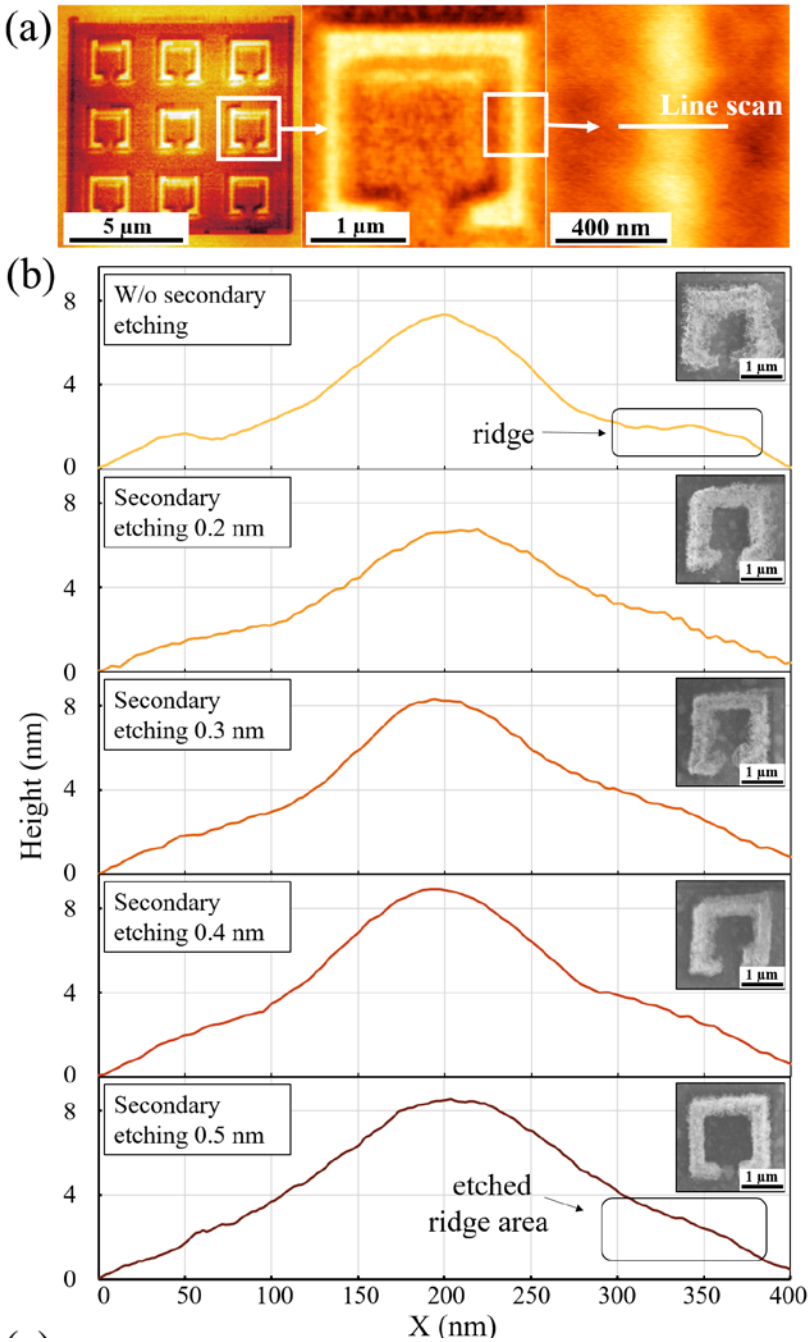

Figure 7.5. (a) AFM images of patterned catalyst, and (b) line profiles of pattern with applied secondary etching (0 – 0.5 nm) [207].

In order to investigate the secondary effect caused by the secondary etching, the AFM analysis of the patterned area was conducted (Fig. 7.5) before CNT growth. The AFM image of fabricated patterns of a depth of 10 nm and secondary etching of 0.5 nm are shown in Fig. 7.5(a). To examine the morphology of the patterned surface, line profiles of secondary etching (0 – 0.5 nm) were prepared (Fig. 7.5(b)).

As shown in Fig. 7.5(b) (w/o secondary etching), on both sides of the profile, around 50 and 350 nm, the formation of ridges was noticed, as a result of resputtering during the FIB patterning. Similar ridges were observed in [193,206] after the FIB patterning process. By applying the secondary etching to the surface, the top layer of material was removed, and the height of the ridges diminished to the point where it was no longer observable (for 0.4, 0.5 nm etching depths).

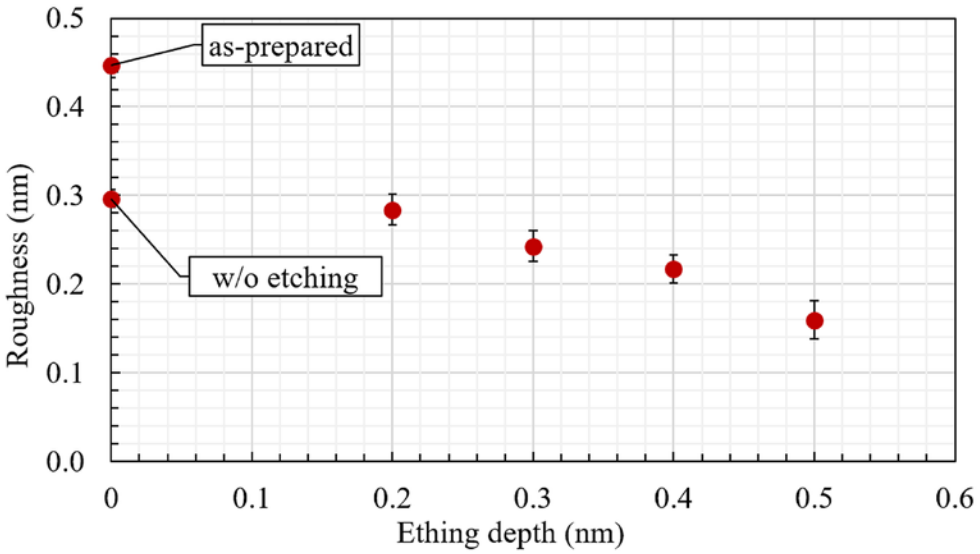

Figure 7.6. Roughness analysis of the catalyst surface [207].

A more detailed analysis of the average roughness of the Fe catalyst surface, after FIB patterning and secondary etching, was conducted and presented in Fig. 7.6. For comparison, the average roughness of as-prepared catalyst was also shown. The FIB patterning resulted in the decrease of the average roughness. It was assumed that the sputtered material, which was redeposited on the patterns, smoothed the surface by uniform redeposition. Furthermore, by applying the FIB secondary etching process, the average roughness was further decreased, from R_a = 0.45 nm for an as-prepared catalyst, to 0.15 nm for secondary etching depth of 0.5

nm. Lower roughness supported the formation of uniform catalyst particles and resulted in the growth of high-density CNT forests.

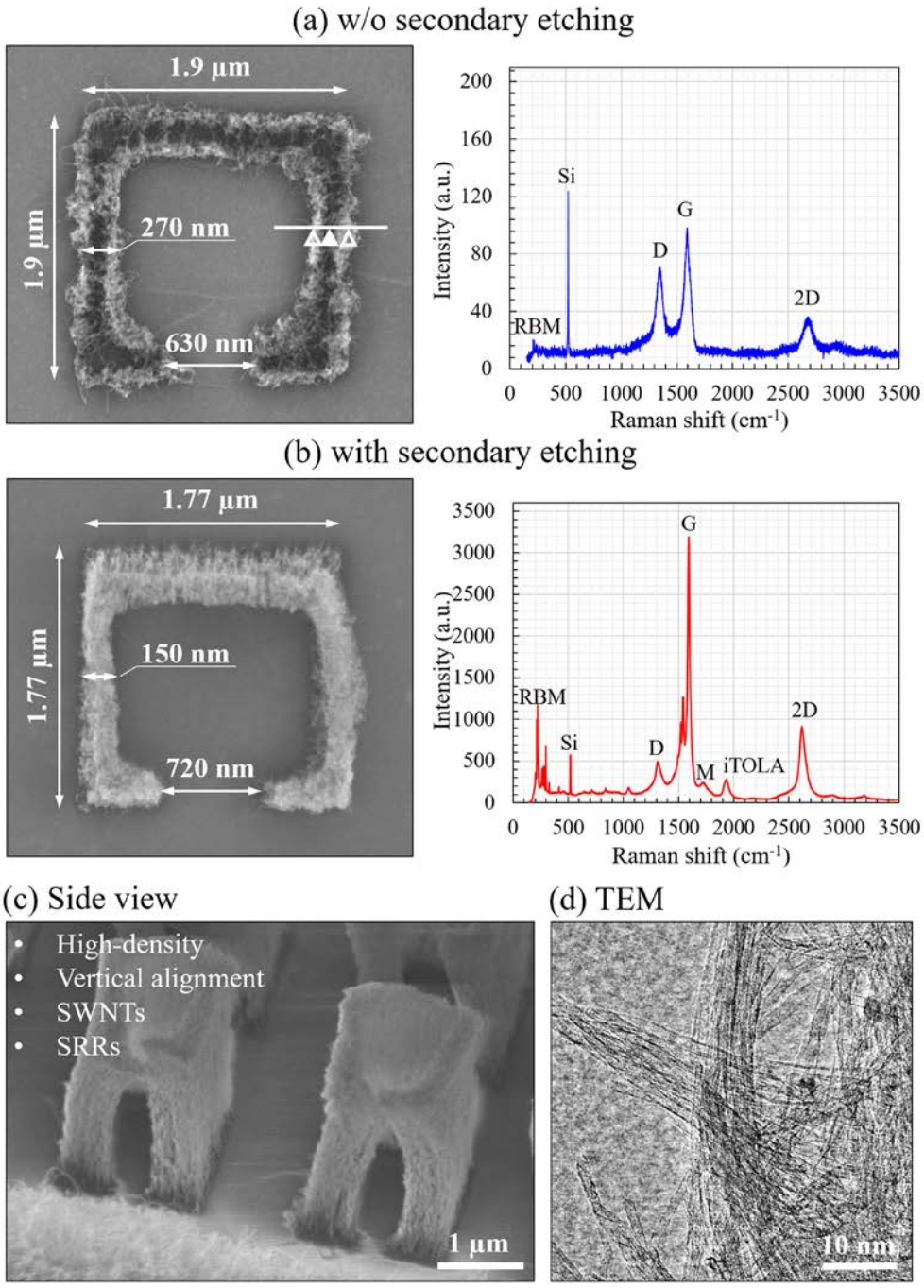

Figure 7.7. SEM images and Raman spectra of CNT patterns: (a) without secondary etching; (b) with secondary etching of 0.5 nm depth; (c) with secondary etching of 0.5 nm depth – side view (Δ - edge, ▲- body). (d) TEM image of a CNT array grown under the optimized condition of the FIB processing shown in (c) [207].

The effects of removal of the redeposited material from SRR structures and the decrease of the average roughness, after the secondary etching process, were revealed after CNT growth (Fig. 7.7). In Fig. 7.7(a), for the case without applying secondary etching, based on the numerous not grown areas in CNT forest, highly inhomogeneous, low density and low alignment growth of CNT forest on the patterns was found. The growth of CNTs was mostly observed on the edges of fabricated patterns in Fig. 7.7(a). Furthermore, despite the fact that the as-prepared CNT forest was SWNT, the Raman spectra of the SRR pattern revealed the mixture of multi-walled CNTs (MWNTs) and SWNTs. It could be observed by the G/D peak intensity ratio of 1.45 and very low signal of radial breathing mode (RBM), originated from the presence of SWNTs. In contrary, after the secondary etching of 0.5 nm depth, the growth of CNT was greatly improved as shown in Fig. 7.7(b, c). Both, the density and alignment, as well as the uniformity, were improved, allowing the growth of CNTs on the entire surface of patterns. Raman measurements of CNTs, after the secondary etching, showed very big improvement of CNT forest structure. For the relatively low height of the CNT metamaterial structures, the overall intensity was significantly improved, for the same parameters of the measurement. The analysis of spectra showed a very high intensity of RBM peaks, indicating a very high number of SWNTs in the structure, while significantly high G/D peak ratio of 10.47 indicated a very high crystallinity and a very low number of defects in the graphene layers building CNTs. This conclusion was also confirmed by a very high intensity of 2D band. Finally, the presence of additional M, iTOLA, and G^- bands [177] was also observed in Raman spectra as a result of the enhanced quality of graphene in CNTs. The detection of Raman peaks of SWNTs was also confirmed by the TEM observation, which revealed that patterned CNT forest arrays contained SWNTs (Fig. 7.7(d)).

The reason behind the changes between the cases, with and without secondary etching, was related to the annealing process at high temperature. For the case without secondary etching, the surface diffusion of catalyst particles was limited by the layer of redeposited material at the ridges. The catalyst particles agglomerated in the area before the ridges, which became the barrier for the further catalyst surface diffusion to the area outside the ridges, resulting in higher area density of the particles, and finally allowing growth of CNTs on the edges.

On the other hand, the effect of the secondary etching was determined by the amount of removed material and the decrease of surface roughness. During the patterning of SRR arrays, the sputtered material was mainly redeposited on the edges of patterns, forming ridges (Fig. 7.5(b)), and in the smaller degree in the middle of the walls. Furthermore, it was assumed, that the mass density of the redeposited film was lower than the mass density of catalyst film, and due to that, the sputtering rate was high, resulting in faster etching at the ridge area as shown in Fig. 7.5(b). By applying secondary etching of 0.5 nm, the majority of resputtered material and the top layer of Fe catalyst film, was removed. By additional ion irradiation during the secondary etching process, the cleaning of the surface and decrease in the thickness of the Fe catalyst, is to be expected, and results in the decrease of the roughness, allowing the improvement of the growth height, uniformity, and quality of CNTs. Finally, as a result of the etching, due to the thinner catalyst and significantly decreased roughness, the growth of thin SWNTs with higher growth rate was achieved [67], which was also observed in Fig. 7.3 (A (I-II)).

In the presented study, the 30 kV of accelerating voltage of Ga ions, was the direct cause of sputtering and redeposition of the material in the patterned areas; however, the other possible effects should also be noted. High accelerating voltage may cause implantation and diffusion of Ga ions caused by irradiation of ion beam. During the FIB patterning process, the depth of patterning was sufficient to remove the catalyst from the designated area, resulting in no growth of CNTs. On the other hand, the FIB secondary etching treatment of the patterned catalyst was used to clean the surface from the redeposited material. During the process, most of the deposited catalyst remained, and despite a relatively low ion energy, the implantation of Ga ions was possible. However, due to significant improvement of CNT forest observed after the secondary etching, the possible influence was insignificantly small and could be omitted.

Finally, as can be seen in Fig. 7.2 and Fig. 7.7, the size of the patterns after the patterning and the FIB secondary etching was significantly decreased. It was assumed that this shrinking effect was related to the FIB patterning process. During the patterning, the ion beam was oriented perpendicularly to the surface and the material of the surface was sputtered. Typical patterns milled using FIB do not possess vertical walls and flat bottom, but are V-shaped,

with a maximum depth in the middle [206,208,209]. Furthermore, the mouth width of V-shaped patterns is usually much larger than the diameter of the ion beam. This effect can be explained by high ion intensity of the ions outside the core region, which results in relatively higher sputtering of the material on the sides of walls, resulting in the creation of slopes. For that reason, with the increase of the etching depth, the increase of the time of ion beam irradiation also increases, and more material from the walls is sputtered. During the spattering, a part of the surface with the pristine catalyst is also removed from the edges of the walls, causing overall shrinking of the patterns. This shrinking effect should be taken into consideration during the design of fine patterning of CNT forest metamaterials in visible region.

7.5. Conclusions

This chapter presents the combination of precise FIB patterning process with additional newly developed secondary FIB etching steps in order to remove redeposited material from the surface and improve the growth of CNT forest in the SRR array nanostructures. This method allows fabrication of nanoscale metamaterial patterns and catalytic growth of high-density CNT structures as small as about 150 nm on pre-deposited catalyst film in designated areas, for the first time. The patterning depth of 10 nm and the secondary etching of 0.5 nm allowed the growth of uniform, high-density, and high-aligned CNT forest metamaterials. The FIB secondary etching method decreased the average roughness of the catalyst surface, resulting in significant improvement of CNT forest quality. The top-down process of the FIB patterning, allowed precise fabrication of SRR structures, while by influencing the catalyst preparation, the control of CNT forest could be obtained, as a bottom-up approach for fabrication of CNT forest metamaterials.

In the future, an investigation of the redeposited material, catalyst film and mutual interactions between them, should be conducted to assist in the design of light wave-sized CNT metamaterials for optical, thermal and optronic devices. The development of this method opens a wide range of applications, as uniform and precise growth of aligned CNT forest nanostructures has not been presented before. The further development of the FIB secondary etching method will contribute to the fabrication of metamaterials using CNTs, in

various spectrum of electromagnetic radiation, from optical range to far infrared, and terahertz range and will proved the designed light wave-sized metamaterials.

Chapter 8. IR properties of patterned CNT forest for metamaterials

8.1. Introduction

CNTs act as a nearly ideal one-dimensional nanorod antennas with a diameter of a few nanometers and length from tenths of nanometers to many micrometers [6]. Furthermore, the behavior of single-walled CNTs (SWNTs) is similar to direct gap semiconductors with absorption spectra dominated by exciton lines [7]. Based on experimental observations, the nonlinear optical behavior of CNTs [8] is related to a high third-order susceptibility with sub-picosecond recovery time [9,10], in which the source of the nonlinearities is an effect of the saturation of the resonant excitation lines and allows many various applications like light sources in nanoscale, photodetectors, photovoltaic devices and ultrafast lasers [11,12]. In addition, those extraordinary properties of CNTs were also recently used for the design and fabrication of metamaterials in form of metallic nanorods [4,6], SWNT films [38], and composites [39]; however, the fabrication of CNT forest metamaterials has not been presented before.

Properties of metamaterials are derived from a shape and size of designed structures of an electromagnetic circuit, and also from the properties of the material that consist of those structures. Currently, metamaterial development is limited by the design and fabrication methods; however, by utilizing anisotropic materials, like CNTs, which can produce negative refraction due to their chirality, those limitations may be overcome. A high shielding effectiveness accompanied by a high dielectric constant of SWNTs [36,37], can be tuned by a control of growth parameters and post-processing operations, such as chemical treatment or molecular functionalization [38], which is not possible with conventional materials like metals. Due to that, unique structure and properties of CNT forest influence the performance of metamaterials, and can be used for their design and fabrication.

8.2. Objectives

In the following chapter, an investigation of a bulk behavior of CNT forest and an influence of geometrical parameters (shape, height, etc.) of CNT forest metamaterials on a total reflectance in the infrared (IR) regime was investigated. Due to a successful fabrication of CNT forest metamaterials, presented in chapter 7, the infrared behavior of metamaterial

patterns on a predeposited catalyst could be examined. The work is focused on the investigation of the infrared behavior of metamaterial patterns in various shapes, sizes, alignment, and pitch. Furthermore, the influence of CNT forest structure on the absorption of IR radiation was discussed. The fast prototyping of metamaterial patterns of CNT forest on the predeposited catalyst was carried out using Focused Ion Beam (FIB) and a secondary etching process, described in detail in chapter 7. The FIB processing for the first time allowed the fabrication of CNT forest metamaterials in the shape of SRRs. In the presented experiments, the shape dependence of metamaterial structures composed of uniform high-quality SWNT forest on the IR spectra, was presented. The influence of the size of the gap in the SRR patterns, the dip size of metamaterial structures, the spacing between individual structures, and the height of metamaterials on the reflectance spectra was studied. The study of the coupling effects originated from the structure of metamaterial patterns, not CNT forest, was conducted [210].

8.3. Experimental and methods

The preparation of CNT forest metamaterials was conducted as follows: (1) a deposition of the AlO_x/Fe catalyst, (2) a FIB patterning, followed by (3) FIB secondary etching process, continuously, without breaking the vacuum, and finally (4) the growth of CNTs on the patterned samples by CVD method.

The deposition of the catalyst film for carbon nanotube forest growth was carried out using optimized conditions described in chapter 5, and the RF magnetron sputtering method described in chapter 3.2. The growth of carbon nanotubes was conducted using a thermal CCVD method introduced in chapter 3.3.

After the catalyst deposition, but before the CNT forest growth, the sample was introduced into the FIB chamber in order to perform a patterning of metamaterial structures on the surface. For the preparation of CNT forest patterns, a FIB system described in chapter 3.4.7 was used. The total size of patterns was 30×30 μm and contained structures of various sizes and shapes (SRR, asymmetric split resonators (ASR), L-shape, squares, etc.). The fabrication of patterns was conducted utilizing prepared bitmap designs and was followed by a FIB secondary etching process, applied to the entire patterned area, including the prepared

structures. During the fabrication, the FIB patterning depth of 10 nm was used, and was followed by the FIB secondary etching depth of 0.7 nm. After the patterning, samples were moved into the CVD chamber for growth of high-aligned, high absorbance CNT forest. The time of growth was precisely controlled and limited to a few seconds, in order to decrease the total height of CNT forest to a single micrometers.

The quality of FIB patterns was confirmed by FE-SEM (chapter 3.4.1). The structural and quality analysis of CNT was performed using Raman spectroscopy (chapter 3.4.4), while for the measurements of the total IR reflectance, FT-IR spectrometers described in chapter 3.4.6 were used. For FT-IR microscope, a 28 μm diameter circular measurement area was defined by an aperture in the light path of the IR microscope.

8.4. Results and discussion

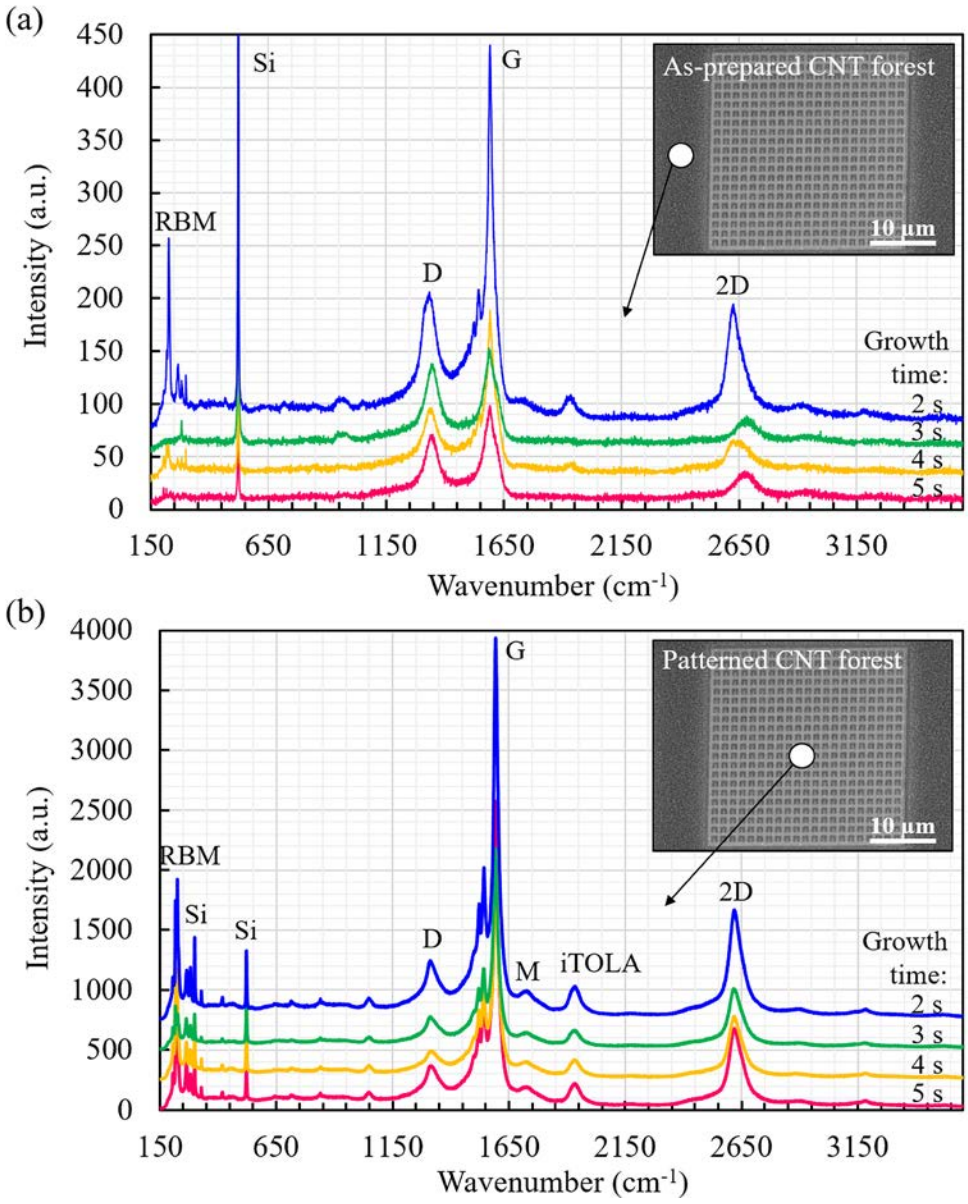

Figure 8.1. Raman spectra of (a) as-prepared CNT forest area and (b) patterned CNT forest, for growth time of 2, 3, 4, and 5 s [submitted to Nanoscience and Nanotechnology Letters].

The quality of as-grown CNT forest and CNT forest patterns of various height after the fabrication was investigated by Raman spectroscopy, and is presented in Figure 8.1. As can be seen, for 3 and 5 s growth, due to low G/D peaks intensity ratio (I_G/I_D = 1.23 and 1.28, respectively) and no peaks indicating the existence of SWNTs, MWNT forests were observed. On the other hand for the growth of 2 and 4 s, the growth of SWNT forest was confirmed.

Raman spectra showed higher intensity ratio I_G/I_D of 3.5 and 1.92, respectively, and a Radial Breathing Mode (RBM) peaks. The RBM is a mode originated from bond-stretching phonons for which all the carbon atoms move coherently in the radial direction, with typical frequency about 100–500 cm^{-1}. The RBM is an indicator of the existence of SWNTs [145,176] and scales inversely proportional to the diameter of CNTs [211]. For the diameter of CNTs above 2 nm, the RBM peaks are no longer recognizable [212].

The difference in Raman spectra observed between individual samples in Fig. 8.1(a), was originated from a preparation method, starting from the deposition of the catalyst system and finishing on the growth of CNT forests. In the case of short time growth of CNTs, a precise control of the process is required and even the smallest changes can affect the structure of CNT forest. For that reason, the growth of MWNTs, SWNTs, and mixture of those two, was observed in various samples.

Figure 8.1(b) demonstrates Raman spectra of the same samples; however, measured in the patterned area. As compared to Fig. 8.1(a), for each growth time, a very high improvement of the overall intensity of spectra could be observed. Furthermore, a very high intensity of the RBM peaks indicated a presence of SWNTs, while a very high peak intensity ratio I_G/I_D of 8.03, 9.6, 10.87 and 9.24 for 2, 3, 4, and 5 s, respectively, indicated a very high crystallinity and a high order of graphene sheets of CNTs in the patterns, which was also confirmed by high intensity of the 2D peak. A shape of a G peak can be used to distinguish the type of nanotubes, between metallic and semiconducting CNTs [213]. Due to the presence of a G^- peak around 1560 cm^{-1}, it was possible to confirm that SWNTs in the patterns were semiconducting. The presence of the M peak and the iTOLA peak was also confirmed in each Raman spectra. The M band is composed of M+ and M- bands and is related to overtones of the out-of-plane infrared-active mode in graphene. The M-band modes were enhanced by various effects related to the curvature of SWNTs. The high-frequency iTOLA peak is a combination of two phonons, one from the in-plane transverse optical branch (iTO), while the second phonon is related to the longitudinal acoustic branch (LA). The iTOLA peak observation was related to the dispersion of phonon branches in a low defective graphite [212,214].

As compared to Fig. 8.1(a), the changes of an overall intensity of spectra and intensities of individual peaks were observed. The FIB processing (patterning and secondary etching) stimulated changes of the catalyst surface resulting in the variation of CNT structure. The FIB patterning allowed fabrication of nanoscale metamaterial structures with high precision; however, the redeposition of the sputtered material was observed. It was assumed that the redeposited material covers the surface of patterns and hinders the growth of nanotubes. The deposition was non-uniform, stronger in areas close to the edges of the patterns and weaker in the middle, while the density of the deposited layer was relatively low. The secondary etching process, was designed for the purpose of cleaning of the surface from the redeposited material, and to allow the growth of uniform CNT forest structures. The effects of the secondary etching include the cleaning of the surface of the redeposited material, the decrease of the catalyst thickness, and the decrease of the surface roughness, and were described in detail in chapter 7. By cleaning the surface, the obstacle in the form of the redeposited material was removed and mechanisms (Ostwald ripening, diffusion) responsible for the formation of the catalyst particles could easily occur. Moreover, the decrease of the roughness and thickness of the catalyst layer supported the formation of small, high-density, and uniform in size catalyst particles, which reinforced the growth of high-quality SWNTs within the forest.

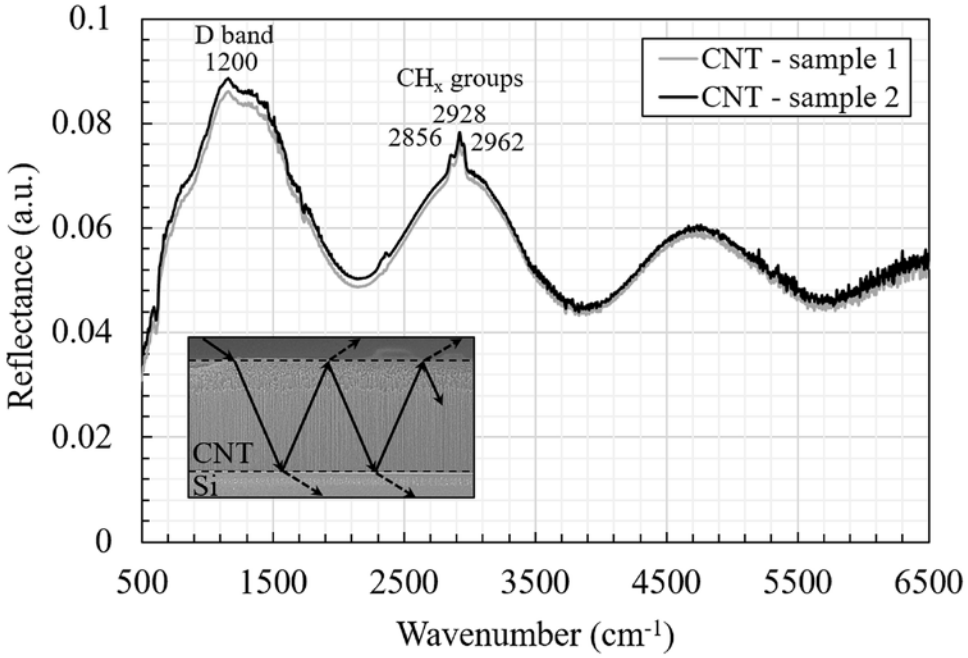

Figure 8.2. The IR absorbance spectra of CNT forests (thickness of 4 μm), with IR-active peaks at 1200 cm^{-1} (D band) and peaks at ~ 3000 cm^{-1} range, attributed to CH_x groups [submitted to Nanoscience and Nanotechnology Letters].

The IR reflectance of bulk CNT forest, measured for 3 μm high-aligned and high-density forest is shown in Figure 8.2. As can be seen, the IR reflectance spectra of CNT forest showed periodic oscillations with peaks around 1264, 2966 and 4748 cm^{-1}. Such oscillations could be experimentally observed for the first time for CNT in the IR regime. Obtained oscillations of the reflectance spectra could be explained by the Fabry-Perot effect and are commonly observed for the thin film materials. Visible oscillations were originated from an interference of a reflected wave at the top and the bottom interfaces, and for thin films with a light beam of incident angle 0°, the positions of the peaks could be easily obtained from the equation:

$$2nd = m\lambda \qquad \text{(eq. 8.1)}$$

where n is a refractive index of the thin film, d is the thickness of the film, λ is a wavelength of light in vacuum, and m is an integer. In the case of short CNT forest, the oscillations were originated from multiple reflections between the bottom and the top of CNT forest. The reflection from the bottom of CNT forest was related to the interface between CNT forest

and polished Si substrate, while the reflection from the top was connected to the high-density, carpet-like structure at the top of the CNT forest.

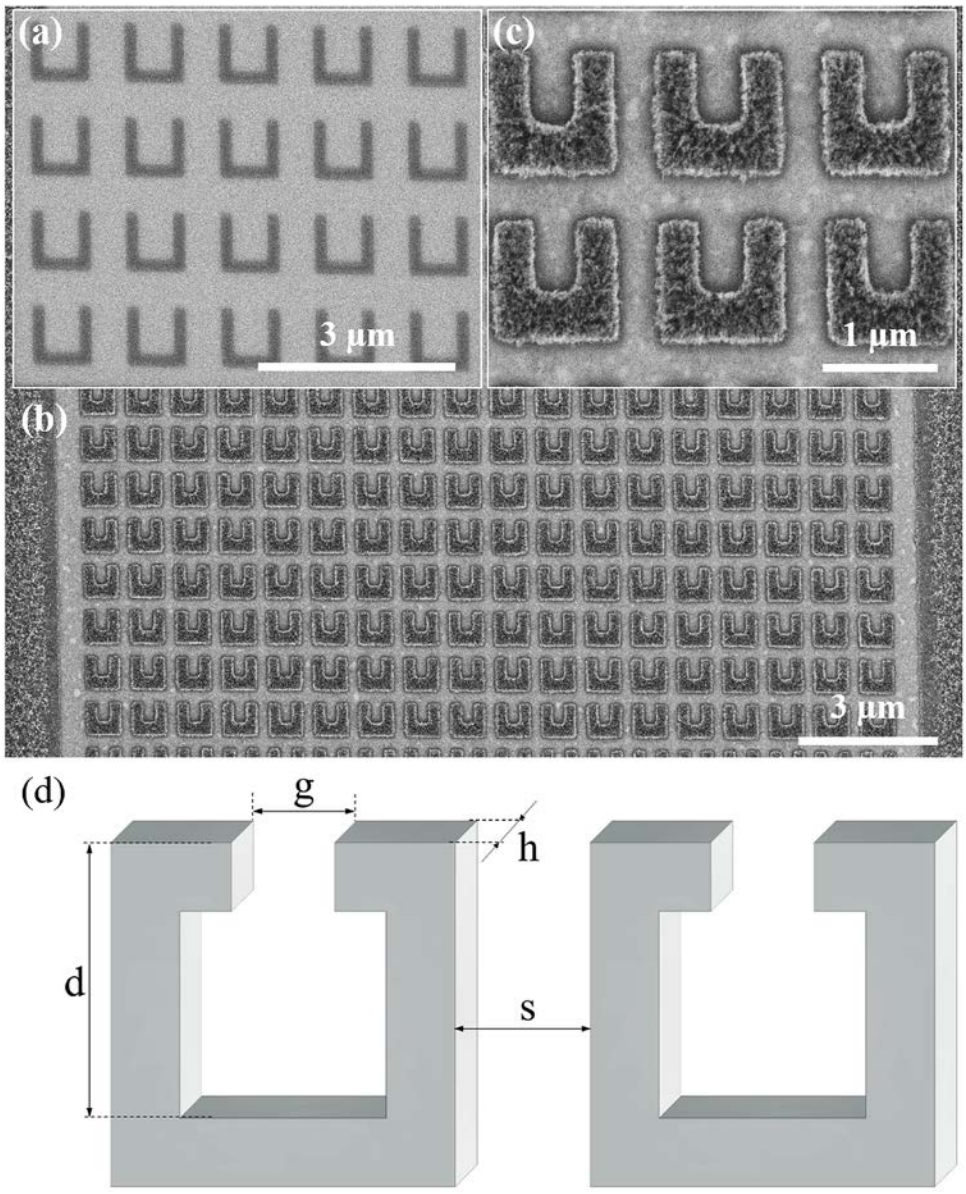

Figure 8.3. Catalyst and CNT SRR metamaterial patterns: (a) pattern surface of AlO_x/Fe catalyst; (b) top view of patterned surface with grown CNTs; (c) high magnification image of CNT metamaterial structures. (d) Investigated geometrical parameters of CNT forest metamaterials [submitted to Nanoscience and Nanotechnology Letters].

Figure 8.3 shows an example of the catalyst SRR patterns and CNT forest SRR patterns fabricated on Si substrates. Fig. 8.3(a) shows the surface of the catalyst after the patterning, although before the growth of CNT forest. As can be seen, high-quality patterns of size 1×1

μm are visible in the catalyst, before the growth of CNTs. It was confirmed that by using the FIB method with the secondary etching process, the patterning of catalyst surface resulting in the growth of high-density CNT patterns (Fig. 8.3(b, c)), as small as 200 nm, was possible. The size and the shape of electromagnetic structures were precisely designed (Fig. 8.3(d)), in order to interact with the electromagnetic radiation in the infrared region.

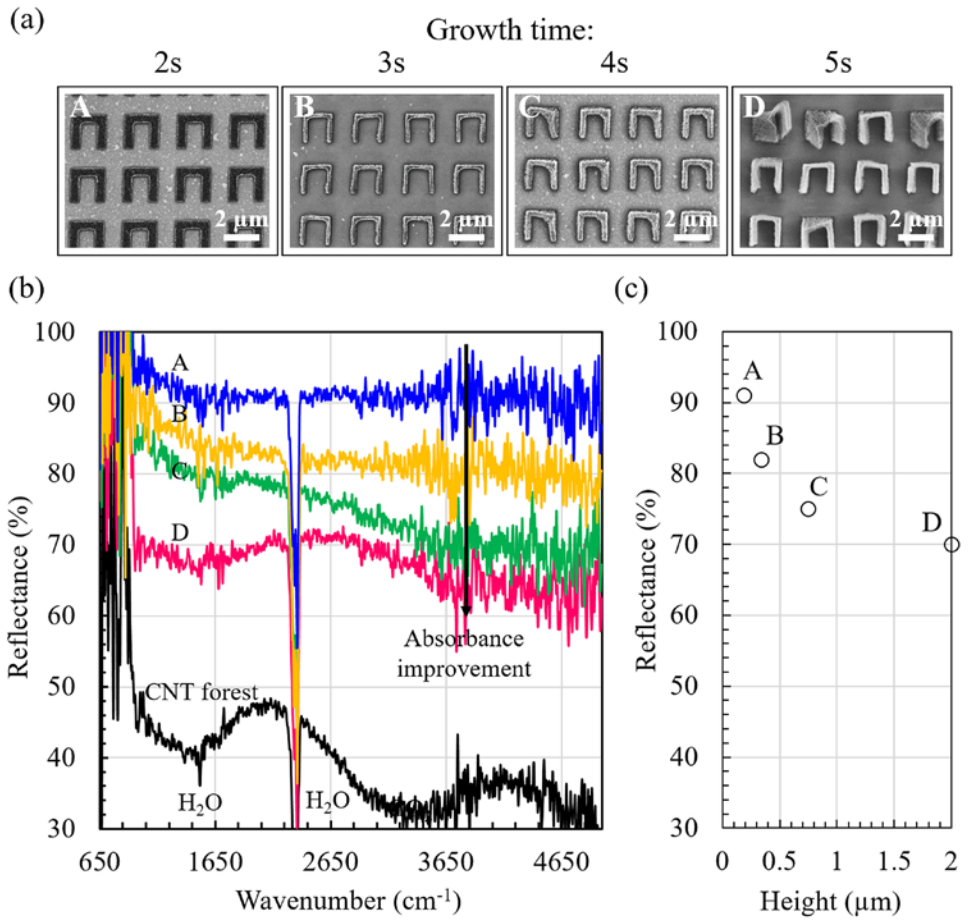

Figure 8.4. (a) CNT forest patterns of simplified SRRs in dependence of growth time. (b) FT-IR reflectance spectra of simplified SRR patterns. (c) Height of CNT patterns vs. total IR reflectance [submitted to Nanoscience and Nanotechnology Letters].

The influence of the height of CNT forest, originated from the growth time of 2, 3, 4, and 5 s, on the FT-IR spectra of simplified SRRs patterns, is shown in Figure 8.4. The calculated heights of SRRs were 190, 340, 750, and 2000 nm, for the growth time of 2, 3, 4, and 5 s, respectively. As shown in Fig. 8.4(a), the increase of the height of CNTs in the patterned areas with growth time was observed. For the growth time of 5 s, small defects of patterns,

correlated to the extended height of CNT forest were observed and were related to a smaller self-supporting effect of neighbor CNTs. Fig. 8.4(b) shows the FT-IR spectra of the patterned area for the simplified SRR patterns. The intensity of the total IR reflectance decreased exponentially with the increase of the CNT height. The dependence of the CNT height and the absorption of light is well known [125,169,215,216]. For the same shape, spacing, and type of CNTs, the height of the CNT forest metamaterials was the main reason behind changes of the total reflectance. Typically, for small angles of incident light, the interaction of light with the CNT structure results in the reflection, absorption, and transmission of the light beam. For higher CNT forest, a possible distance of propagation of light in the structure was larger than for short CNTs, resulting in a higher number of absorption points, before the reflection of light from the bottom interface of CNT-Si occurred. In theory, the height of CNT forest metamaterials could be increased in order to increase the total absorption of IR radiation; however, due to the fact, that the self-supporting effect of neighbor CNTs is also related to the surface area of the structures, the increase in the size of the individual structures would also be required. Furthermore, for the growth time of 5 s, the oscillations in the IR reflectance spectra appear were observed, while for the growth time of 4 s, changes of the reflectance in the higher wavenumber region appear. It was assumed that due to the improvements of the growth uniformity, at the top of the structures, high-density carpet like structures appeared and allowed the reflection of IR radiation, which was observed in the IR spectra. Additionally, it can be noted that despite the same height of the as-prepared CNT forest and patterned structures, the frequency of the observed oscillations was different for the growth time of 5 s. This minor change in growth height or low orientation of CNTs could be attributed to the additional influence of the metamaterial patterns shapes, which could affect the shape of the obtained IR spectra.

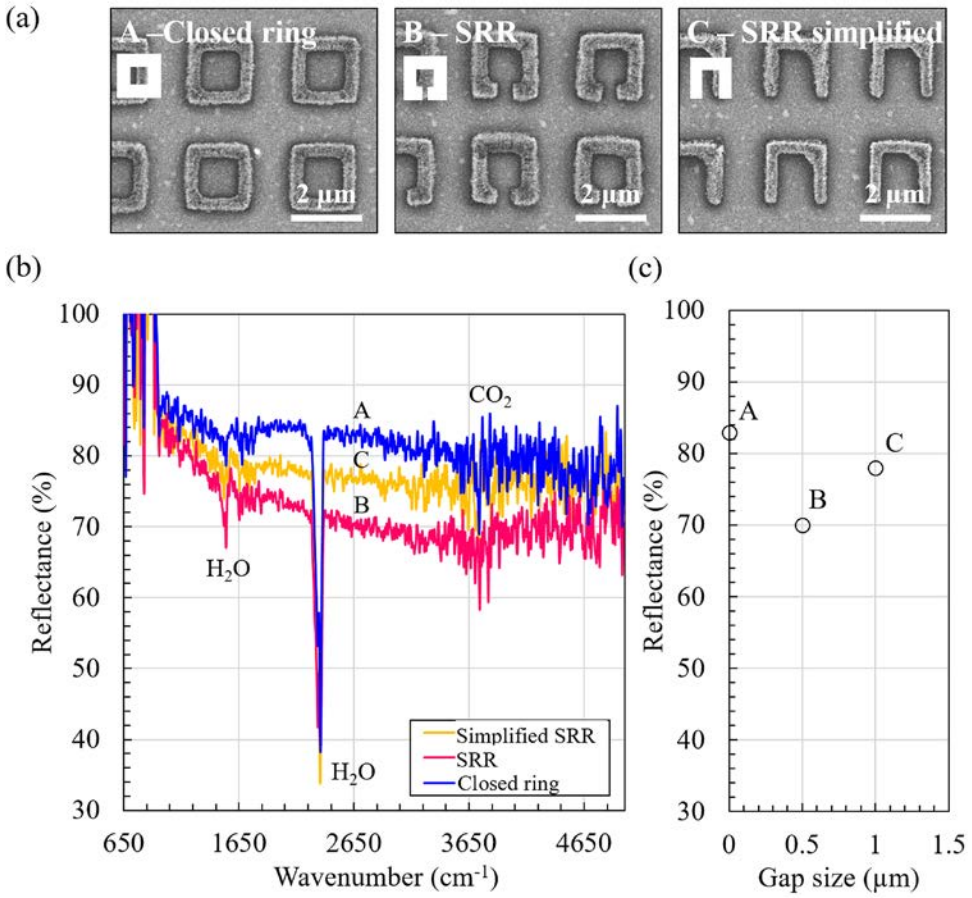

Figure 8.5. (a) CNT patterns shapes dependency on the IR reflectance, (b) infrared reflectance spectra of fabricated patterns. (c) Gap size vs. total IR reflectance [submitted to Nanoscience and Nanotechnology Letters].

Figure 8.5 shows the influence of the shape of patterned CNT forest on the total IR reflectance. For the analysis, three different shapes of structures were chosen and tested: a SRR, a simplified SRR, and a closed ring. Due to the small overall size of the patterned area, all the presented arrays were fabricated on the same sample, which allowed to obtain uniform height of SWNTs in all patterns. As can be seen in Fig. 8.5(b), the highest value of the total IR reflectance was observed for closed ring patterns, while the lowest reflectance was observed for the SRR patterns. Measurements of the IR reflectance of the simplified SRR array (Fig. 8.5(a) - B) showed a lower reflectance than for the closed rings; however, higher than the SRR pattern. Interestingly, as compared to SRR and simplified SRR patterns, the reflectance of closed ring patterns, which possessed the highest absorption area did not result in the lowest reflectance. It was assumed that despite the variation of the total absorption area,

the absorbance was directly correlated with the shape of the CNT metamaterial structures in the arrays. The lowest reflectance was demonstrated by SRR patterns, which are well known from their high interaction with electromagnetic radiation.

A typical electromagnetic resonators require splits (gaps) in the ring in order to support the resonant wavelengths larger than the diameter of the structure. If the resonator ring possesses the split, a large capacitance is generated, and the decrease of the resonant frequency is observed, while the degree of changes depends on the design of the individual structures. One of the important parameters is the size of the gap (g). The increase of the size of gap results in the decrease of the resonance intensity and the total absorption is reduced, while the decrease of the size results in the increase of the effective capacitance, and the redshift of the resonant frequency is observed. The frequency of electric resonance can be tuned by the change of the gap size. In the case of the closed rings, due to the natural absence of the gap, such a resonance does not occur and the absorption is related only to the area covered with CNTs.

In Fig. 8.5(b), the high reflectance of closed ring patterns is related to the absence of the split in their structure and for that reason, the value of the reflectance is related only to the absorption of IR radiation in the body of CNT forest. On the contrary, apart from the absorption in the CNT body, the IR reflectance of SRRs is also reduced by the resonance which occurred, due to the presence of the splits. The measurements of the total size of the gaps showed 1 μm for simplified SRRs and 0.5 μm for SRR. By introducing splits in the CNT SRR metamaterials, the generation of the capacitance could occur and the variation of the reflectance was observed. The decrease of the size of the gap allowed the generation of a larger capacitance and due to that, a stronger resonance related to the electric part of the IR radiation occurred, resulting in the bigger decrease of the IR reflectance. This typical for the metamaterial arrays behavior was observed for the first time in CNT SRR metamaterials. By precise control of the size of the gap size, a generation of larger capacitance is expected, which could result in the further decrease of the reflectance.

The observations of the reflectance between the 1650 and 3800 cm^{-1} showed the variation in the IR spectra of much higher scale than in the other regions. Though the resonance peak

was not clearly observed for the investigated CNT metamaterials, the broadband absorption of the patterns seemed to occur. CNT forest is well known for his absorption properties in a very wide range of frequencies, allowing the broadband absorption of the IR radiation. However; this phenomenon was not clearly confirmed and require further investigation.

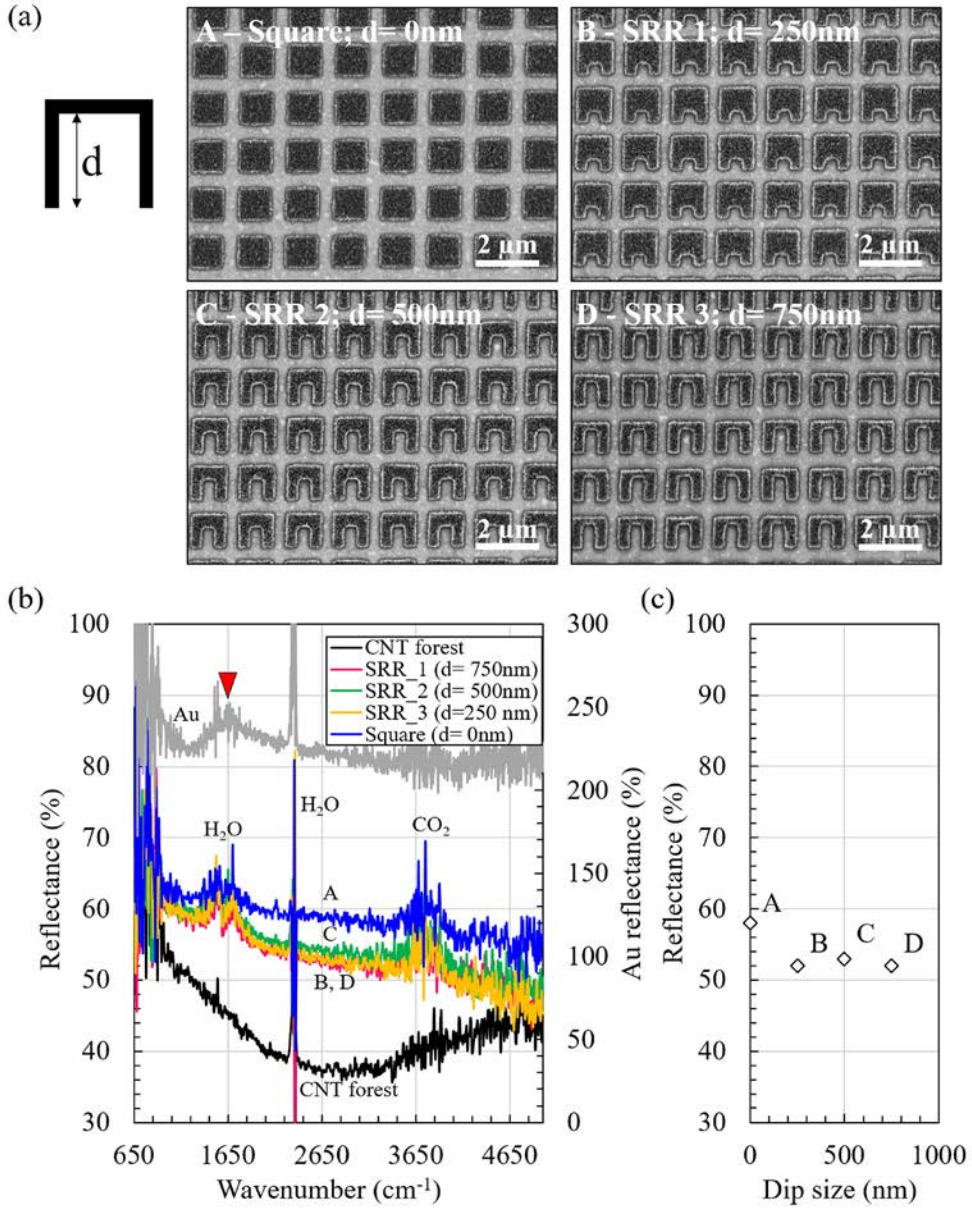

Figure 8.6. (a) SEM images of the simplified SRR patterns with different value of d parameter (0, 250, 500, and 750 nm) used for tuning the magnetic resonance; (b) FT-IR reflectance spectra of the designed patterns for magnetic resonance tuning. (c) Dip size vs. total IR reflectance [submitted to Nanoscience and Nanotechnology Letters].

The resonance of metamaterial arrays, composed entirely from the high-quality semiconducting SWNTs was proven and allowed the decrease of the total IR reflectance.

Figure 8.6 shows results of the tuning of the dip size of simplified SRR CNT patterns by changing the d parameter from 0 to 750 nm (illustrated in Fig. 8.6(a)). The height of the structures is similar (~190 nm) while the size of each structure is 1×1 μm. As shown in Fig. 8.6(b), similar to the previous example of the closed rings (Fig. 8.5), the square-shaped CNT arrays exhibited the lowest absorbance, despite the highest absorption area, as compared to the other three simplified SRR patterns. The absence of the gap in the structure forbade the generation of the capacitance and the existence of electromagnetic resonances, so the absorption was governed only by the body of CNT forest. On the other hand, the total IR reflectance of simplified SRR patterns with a value of parameter d between 750 and 250 nm showed a significant decrease in the intensity of the IR spectra. Due to the existence of splits, the resonance could occur in the CNT SRR arrays. The dip formation in simplified SRR shape clearly reduced the reflectance (increased absorption), which corresponded to the wave shift of reflectance in reference [205] by Enkrich for the dip size dependence of reflectance on metal SRR pattern. For the CNT SRR patterns, CNT forests might enhance the reduction of reflectance in the case of highly resonant SRR shapes. Interestingly, the IR reflectance spectra showed very similar values of intensity for all 3 values of parameter d. Typically, the variation of the dip size of metamaterials results in the shift of the position of the peaks related to the magnetic resonance which occurs in the metamaterials, while the position of the peaks assigned to electric resonance does not change [205]. In the presented research, due to the absence of clearly visible resonant peaks, the influence of the variation of the d parameter could not be clearly explained. Moreover, in the case of the tuning of the magnetic resonance, changes of the intensity of the total reflectance spectra were negligible, due to small interaction with CNTs [4]. For that reason, changes between intensities of the IR reflectance in observed samples were insignificantly small. On the other hand, the decrease of the total absorption area of CNT arrays, due to the change of parameter d, did not result in significant changes of the IR reflectance. It was assumed that a relatively small magnetic resonance appeared, and was enough to compensate losses of reflectance due to decrease of the absorption area.

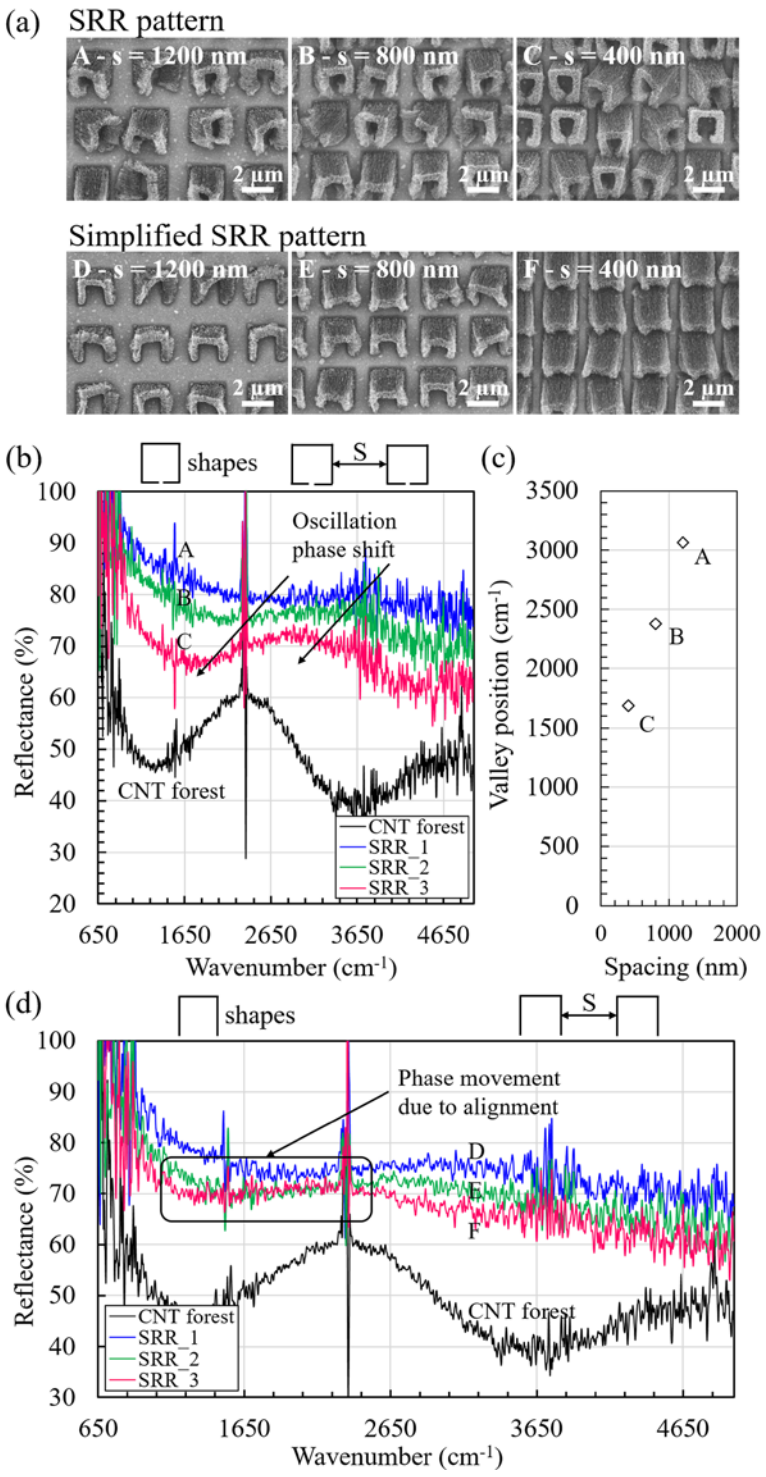

Figure 8.7. (a) SEM photos of SRR and simplified SRR patterns with different spacing of 1.2, 0.8, and 0.4 μm, (b) IR reflectance spectra of simplified SRR CNT patterns and (d) SRR patterns for various spacing. (c) Valley position vs. the spacing size between SRRs. [submitted to Nanoscience and Nanotechnology Letters].

In comparison, a Si normalized total IR reflectance of a simplified Au SRR patterns of 1×1 μm size and height of 100, nm was measured (Fig. 8.6(b)). As can be seen, for the dip size of 750 nm and same spacing, the intensity of total reflectance has been increased about 4-5 times. The reflectance of Au film was much higher than the reflectance of CNT forest, and for that reason, the application of CNTs in the metamaterials seemed justified. Finally, on the contrary to the CNT metamaterial patterns, the Au metamaterials resulted in the resonance peak, observed around 1694 cm^{-1} (Fig. 8.6(b)).

The investigation of spacing (lattice constant) between the individual structures in SRR and simplified SRR arrays, is presented in Figure 8.7. All the arrays were prepared during the same experiment on the same substrate, in order to reduce the variation of height and density of CNTs within the forest. For both cases, the distance between structures was modulated between 1.2, 0.8, and 0.4 μm (Fig. 8.7(a)). The decrease of the distance between patterns caused the overall decrease of the intensity of the total IR reflectance. Moreover, a redshift of the oscillations in measured spectra was observed. In Fig. 8.7(b, d), the decrease of the total reflectance can be explained in two ways. Firstly, the decrease of the spacing between individual structures in both arrays resulted in a larger number of structures in the same measurement area. Higher number of patterns resulted in the increase of the absorption area covered with CNT forest, and finally reduced the reflectance by improved absorption in the body of CNTs. On the other hand, by the increase of the total number of SRRs in the arrays, the number of the possible areas which could interact with the electromagnetic radiation was also increased. As a result, the decrease of the total reflectance was observed and was noted in Fig. 8.6. The introduction of higher number of SRR nanostructures capable of the resonance resulted in a higher number of coupling areas and was responsible for the decrease of the total reflectance.

As mentioned above, the height of the structures was kept on a very similar level, in order to avoid the influence of multiple reflections between the top and bottom interface of CNT forest of various height on the shift of oscillations. Due to the reduction of the spacing and the increase of the area-filling, the propagation of the electromagnetic wave through the patterned area was changed and resulted in the observed shift of oscillations in SRR and simplified SRR

arrays (Fig. 8.7(b, d)). The calculated position of valleys in the IR spectra of the SRR patterns showed nearly an ideal linear dependency to the variation of spacing between individual SRRs (Fig. 8.7(c)). The reduction of the spacing resulted in the enhanced interactions between SRRs; however, the spectral position resonances remained unchanged [217].

Interactions between individual SRRs could be explained by dipole-dipole interaction model proposed for pairs of SRRs [218]. The coupling of SRRs depends on the presence of additional SRRs in the area. Each SRR acts as an antenna and transfers the electromagnetic field through the metamaterial. The transfer of the electromagnetic near-field to the far-field causes the increase of the width of the resonant lines. Moreover, in the case of the decrease of the spacing between individual SRRs, the antenna behavior results in the changes of the resonant frequency. Despite the fact, that the resonance was not clearly observed, some of those effects could be observed during the analysis of the phase shift of oscillations.

In the case of the side-to-side position of the SRRs, typically the redshift of the resonant peak can be observed, and is related to the strong electric dipole-dipole coupling. In the SRR arrays, the parallel orientation of the electric dipoles and perpendicular orientation of the magnetic dipoles, can be observed. The interaction in the longitudinal direction, responsible for the redshift, is related to strong electric resonance, while the magnetic resonance tends to have opposite effect. On the other hand, in the on-top position of the SRR, the decrease of the spacing between individual structures results in the small increase in the resonant frequency, due to the transverse coupling of the electric and the magnetic dipoles, and the blue shift is usually observed.

In the case of side-to-side and the on-top configurations of uniformly arranged structures in the arrays, the interaction between each SRR is dominated by the side-to-side effect. The redshift originated from the side-by-side interactions between SRRs is much stronger than the blue shift originated from the on-top configuration. For that reason, the resultant redshift of the oscillations in the IR spectra was observed (Fig. 8.7(b, d)).

For simplified SRR arrays with the spacing of 0.4 μm (Fig. 8.7(a)), a much higher shift of oscillations towards lower wavenumbers, was observed and was related to a horizontally aligned CNTs found in the patterned area. As a result, direction of CNTs in relation to the E-

field of IR beam was changed from perpendicular to parallel. Due to the horizontal alignment of CNTs, the interaction of electromagnetic wave changed the coupling effect, and the propagation of the wave through the patterned area. Moreover, the variation of alignment resulted in the small increase of the total reflectance. In the case of similar height and density of CNT forest, the variation of alignment resulted in the changes of reflectance. For incident beam perpendicular to the substrate, a high vertical alignment of CNT forest resulted in low reflectance, while a horizontal alignment increased the overall intensity of the total reflectance [28, 29]. The influence of the alignment of CNTs within the forest was investigated and is presented below in Figure 8.8.

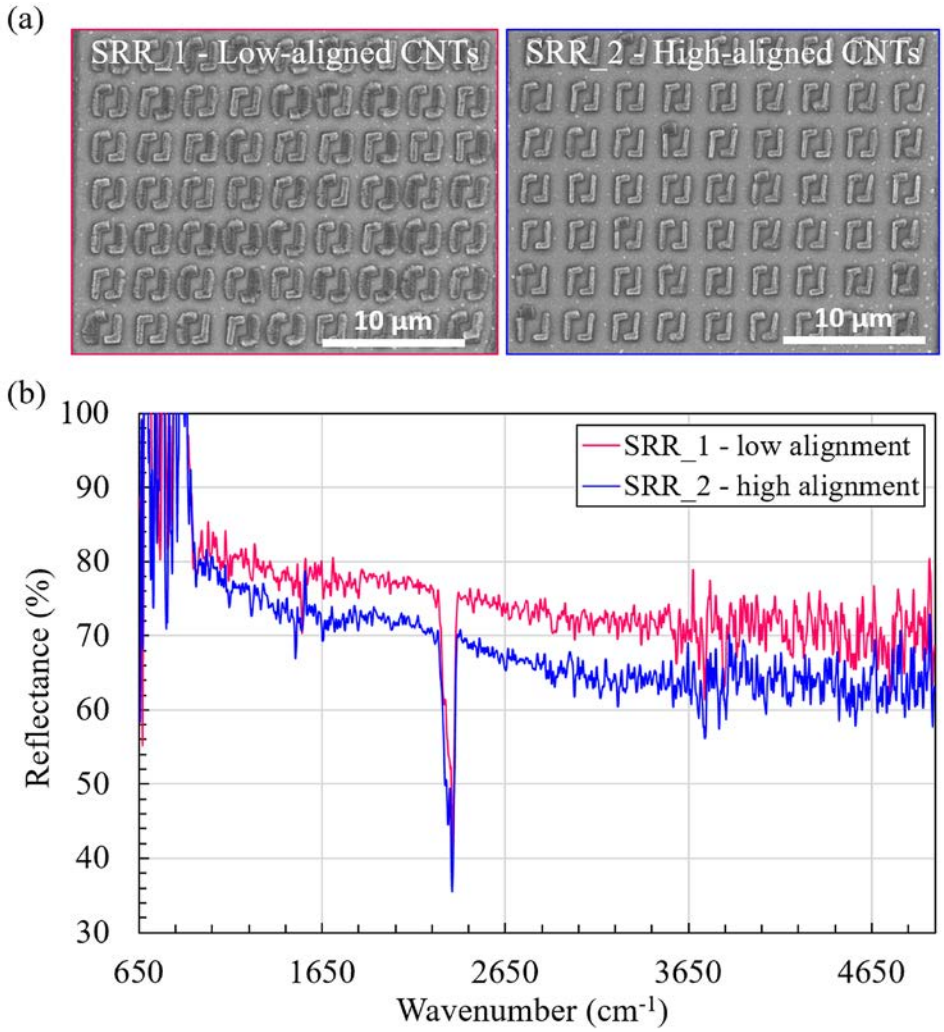

Figure 8.8. (a) SEM images of the low- and high-aligned CNT ASR L-shape patterns; (b) FT-IR spectra of reflectance in dependence of the alignment of CNTs [submitted to Nanoscience and Nanotechnology Letters].

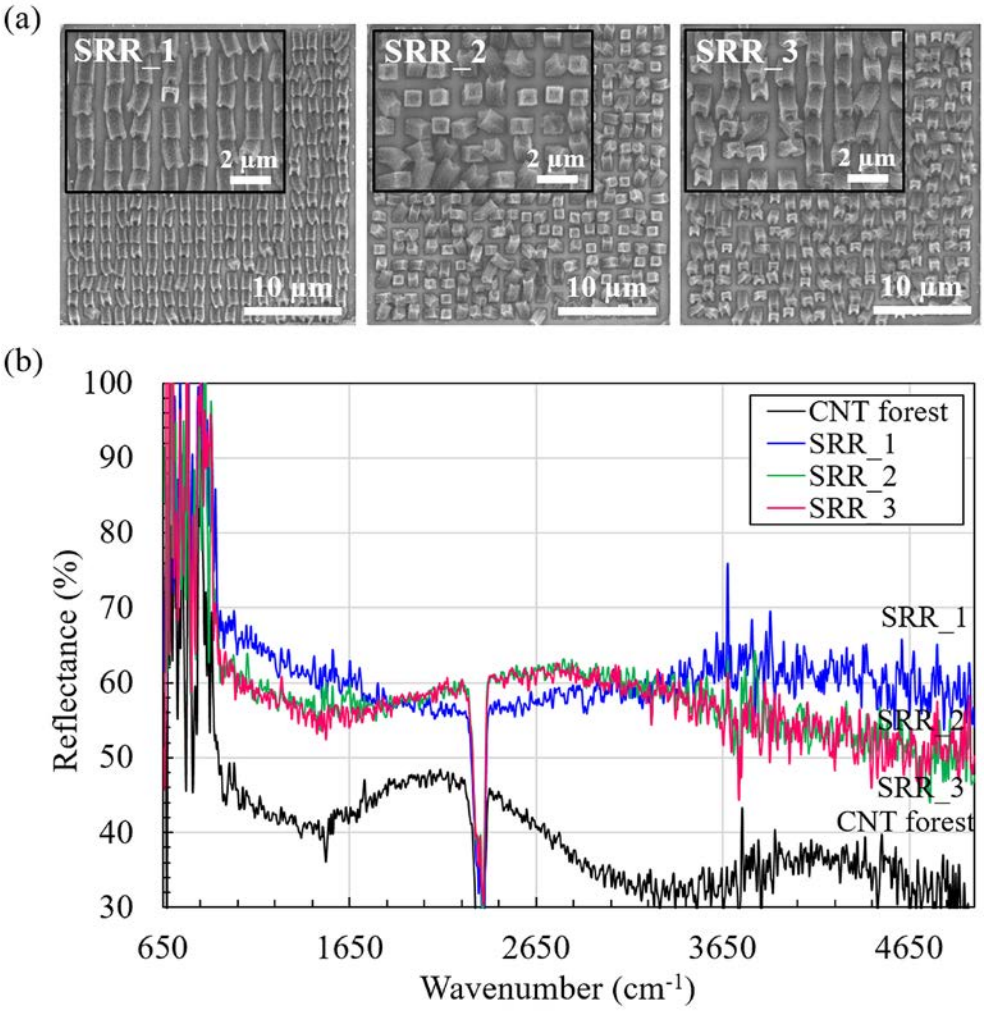

Figure 8.9. (a) SEM images of horizontally and vertically (random) aligned CNT patterns; (b) FT-IR reflectance spectra in dependence of the direction of CNT growth [submitted to Nanoscience and Nanotechnology Letters].

In Figure 8.8(a, b), the dependency between the low and high alignment of CNT forest in the patterned area is presented. As can be seen, for the same shape of the ASR L-shaped patterns with the same height, the reflectance of high alignment forest was much lower than for the low alignment one. The absorption of the CNT forest in the case of similar height was related to the density and the alignment of the forest, in which higher density and higher alignment for CNT axis parallel to incident light, was the direct cause of the lower reflectance. For the presented patterns, the density was similar, as all patterns were prepared on the same sample, under the same conditions, indicating that the change of the reflectance was originated from the alignment of the fabricated structures. In Figure 8.9(a, b), the influence of horizontal

and vertical alignment of CNTs in the patterns was studied. Values of the total IR reflectance for horizontally and vertically aligned CNT forest were similar and in the range of 55 - 70%; however, due to the change of the alignment, the phase of the oscillations was strongly inverted. For the vertically aligned CNT patterns, as compared with horizontally aligned CNTs, the peak of oscillations (~2600 cm^{-1}) was in the position, in which for horizontally aligned CNT patterns the valley is observed. It should be noted that the height of horizontally aligned CNTs was 1.1-1.3 µm, while the height of vertically aligned patterns was 1.3-1.5 µm, which showed that the change of the oscillations was not related to the interference of top and bottom surface of the CNT structures.

8.5. Conclusions

In this chapter, the investigation of the IR reflectance of patterned CNT forest in the infrared regime was presented. The method of patterning of small size (~200 nm) CNT patterns on predeposited Fe catalyst by applying FIB secondary etching was shown for the first time and allowed the fabrication of high density and high alignment SWNT patterns.

The influence of geometrical parameters of SWNT forest metamaterial patterns on the total IR reflectance was investigated. The dependency of the SRR gap (split) size, the dip size, the spacing between individual SRRs, and the height of metamaterial structures were studied and showed considerable influence on the IR spectra. The decrease of the gap size resulted in the decrease of the total reflectance, due to the increase of capacitance and stronger coupling effect. The change of the dip size caused the decrease of the IR reflectance, as compared to the square patterns. It was confirmed that the absorption of infrared radiation was increased by the formation of a dip shape, which acted as a resonator in SRR patterns, and was not related to the total absorption area ratio covered by CNTs. Observed reflectance of CNT SRR metamaterial patterns was about 4-5 times lower than the total reflectance of the Au sample. Furthermore, the decrease in the value of the spacing s between the patterns caused the reduction of reflectance, and the red shift of the phase of oscillations was observed. Apart from that, the control of the alignment from the horizontal to vertical resulted in the change of the absorbance, and significantly shifted the phase of oscillations, due to the changes in the propagation of the electromagnetic wave, through the designed CNT structures

composed of horizontally aligned CNTs. Finally, the increase of height of patterned CNT forest reduced the reflectance, due to the increase of the volume of CNTs.

During the experiments, the electromagnetic resonance, typical for metamaterial structures was not clearly observed. It was assumed, that the high absorption in CNT body, and also the transverse direction of IR radiation to the CNT axis, could be potential reasons.

In future, further investigation of the design of CNT patterns is expected for the highly controlled metamaterials with anisotropic refractive index material. In this paper, metamaterial patterns composed of semiconducting SWNTs were demonstrated; however, due to possible challenging applications, the performance of metallic MWNTs should also be investigated and open a new research of functional metamaterials.

Chapter 9. Summary

The aim of this research was the successful fabrication of the CNT metamaterials, by precise control of highly oriented vertically aligned CNT forest. Several problems were recognized during the research. First of all, in order to precisely control the growth of SWNTs, the Taguchi method of design of the experiment was applied to the CNT growth process. The Taguchi approach was used for the first time in the analysis of the catalyst particles formation conditions in CNT growth processes. Based on the analyzed results, the influence of the growth parameters on the formation of the catalyst was investigated, showing the highest impact of temperature and annealing time on the process. Moreover, based on the statistical analysis of SN ratios and interactions, the model of the formation of catalyst particles was proposed, explaining the Ostwald ripening and subsurface diffusion process as the main mechanism behind the catalyst formation.

Secondly, the study over the growth control of the low total reflectance CNT forest was conducted. For that reason, the Taguchi method was applied for the first time to the optical reflectance optimizations process. Throughout the experiments, the lowest ever reported value of the total reflectance (0.077%) for thin SWNT forest film of 21 μm in height was recorded. The effect of the intrinsic structure of the CNTs was studied by Raman spectroscopy of the grown CNT forest. It was found that for a homogeneous, vertically aligned CNT forest, the effect of the type of CNT (SWCNTs, DWCNTs, or MWCNTs) was insignificantly small and could be neglected. There was no observable relationship between the CNT type and values of total reflectance, unexpectedly. On the other hand, the influence of the filling factor (density) and alignment of CNTs on the total optical reflectance were investigated, showing the highest impact of density and alignment of the CNT forest. The significantly low-reflectance SWNT forest was successfully obtained as a base material for the fabrication of CNT metamaterials.

For the fabrication of CNT forest on the Al substrates, the low-temperature water-assisted growth of CNTs was developed. The investigation of the presence of support layer for catalysts was performed and was followed by the investigation of the hydrogen pretreatment method applied before the growth of CNTs. The Taguchi analysis of the catalyst

formation condition, allowed to define that for the low-temperature growth, the second most important growth parameter is annealing time. For that reason, in the case of the constant low-temperature, the investigation of annealing time was conducted and resulted with optimized time. Furthermore, for the first time, water-assisted CVD method was applied for low-temperature growth on the Al foil, at the low temperature of 600 °C, allowing successful growth of a high-density CNT forest. The application of water-assisted CVD method increased the density, uniformity, yield and height of CNT forest. The possibility of growth of CNT directly on the parts of real devices was shown and could contribute to future development of CNT metamaterials.

Fabrication of metamaterial required a method which would allow the growth of fine nanostructures in the range of hundreds of nanometers. For that reason, a focused ion beam method was chosen. A novel FIB secondary etching method, applied after the FIB patterning, was developed for the fabrication of uniform and fine CNT metamaterial nanostructures. The combination of precise FIB patterning process with additional secondary FIB etching steps to remove redeposited material from the surface and improve the growth of CNT forest in the SRR array nanostructures, was achieved. Applying secondary etching after the FIB patterning, for the first time allowed the growth of fine, high–density, and high-aligned CNT patterns in designated areas and the fabrication of fine metamaterial patterns of various size and shapes (SRRs, ASRs, etc.).

The successful development of precise fabrication method of CNT metamaterial nanostructures, for the first time, allowed the investigation of exceptional properties of CNT metamaterials. The IR properties of various SWNT forest patterns for metamaterials, prepared on the pre-deposited catalyst, were presented for the first time. The bulk properties of patterned self-standing uniform thin CNT forest in the IR region were investigated and showed interesting oscillating spectra for the first time in IR region. The dependency of patterned SWNT forest height, shape, pitch, alignment and magnetic resonance control was investigated. The increase of height of patterned CNT forest reduced the reflectance. It was confirmed that the absorption of infrared radiation was increased by the formation of dip shape as resonator role in SRR patterns and was not related to the total absorption area ratio

covered by CNTs. The tuning of magnetic resonance showed insignificant changes in the FT-IR reflectance spectra. Furthermore, the decrease in the value of the spacing *S* between the patterns caused the reduction of reflectance and the shift of the phase of oscillations was observed. The control of the alignment from the horizontal to vertical resulted in the change of the absorbance and significantly changed the phase of oscillations, due to the changes in the propagation of an electromagnetic wave through the designed CNT structures composed of horizontally aligned CNTs. For the first time, the investigation of the properties of metamaterial originated from the CNT forest were successfully demonstrated.

Finally, the optimization process allowed a growth of a high-density and high-aligned SWNT forest with very low reflectance, which was required for the successful fabrication of metamaterials. The low-temperature growth was achieved on metals allowing growth of CNTs directly on the parts of real electronics devices. By applying a FIB patterning process followed by newly developed FIB secondary etching method, the uniform and fine fabrication of CNT metamaterial nanostructures in various sizes, shapes, and diversity was possible. Finally, the investigation of IR properties of patterned SWNT forest for metamaterials showed the influence of shape, height, alignment, spacing, magnetic resonance tuning on the electromagnetic response in the IR regime, proving that a fabrication of CNT forest metamaterials is possible. The successful fabrication of the CNT metamaterials opened a new path in the carbon nanotube and metamaterial research, and will allow successful development of future electronic and optical applications, like antennas, superlenses, and many others. In order to fully utilize the properties of CNT metamaterials, the further investigation of the CNT physical phenomena and mechanisms is required.

References

[1] S. Iijima, Helical microtubules of graphitic carbon, Nature. 354 (1991) 56–58. doi:10.1038/354056a0.

[2] K. Hata, D.N. Futaba, K. Mizuno, T. Namai, M. Yumura, S. Iijima, Water-assisted highly efficient synthesis of impurity-free single-walled carbon nanotubes, Science. 306 (2004) 1362–1364. doi:10.1126/science.1104962.

[3] O. Suekane, T. Nagasaka, K. Kiyotaki, T. Nosaka, Y. Nakayama, Rapid growth of vertically aligned carbon nanotubes, Jpn. J. Appl. Phys. 43 (2004) L1214–L1216. doi:10.1143/JJAP.43.L1214.

[4] H. Butt, Q. Dai, R. Rajesekharan, T.D. Wilkinson, G. a J. Amaratunga, Plasmonic band gaps and waveguide effects in carbon nanotube arrays based metamaterials, ACS Nano. 5 (2011) 9138–9143. doi:10.1021/nn203363x.

[5] W.A. de Heer, A. Chatelain, D. Ugarte, A carbon nanotube field-emission electron source, Science. 270 (1995) 1179–1180. doi:10.1126/science.270.5239.1179.

[6] H. Butt, Q. Dai, P. Farah, T. Butler, T.D. Wilkinson, J.J. Baumberg, et al., Metamaterial high pass filter based on periodic wire arrays of multiwalled carbon nanotubes, Appl. Phys. Lett. 97 (2010) 163102. doi:10.1063/1.3491840.

[7] P. Avouris, J. Chen, M. Freitag, V. Perebeinos, J.C. Tsang, Carbon nanotube optoelectronics, Phys. Status Solidi. 243 (2006) 3197–3203. doi:10.1002/pssb.200669137.

[8] P. Avouris, M. Freitag, V. Perebeinos, Carbon-nanotube photonics and optoelectronics, Nat. Photonics. 2 (2008) 341–350. doi:10.1038/nphoton.2008.94.

[9] Y.-C. Chen, N.R. Raravikar, L.S. Schadler, P.M. Ajayan, Y.-P. Zhao, T.-M. Lu, et al., Ultrafast optical switching properties of single-wall carbon nanotube polymer composites at 1.55 μm, Appl. Phys. Lett. 81 (2002) 975. doi:10.1063/1.1498007.

[10] S. Tatsuura, M. Furuki, Y. Sato, I. Iwasa, M. Tian, H. Mitsu, Semiconductor carbon nanotubes as ultrafast switching materials for optical telecommunications, Adv. Mater. 15 (2003) 534–537. doi:10.1002/adma.200390125.

[11] S.Y. Set, H. Yaguchi, Y. Tanaka, M. Jablonski, Laser mode locking using a saturable absorber incorporating carbon nanotubes, J. Light. Technol. 22 (2004) 51–56. doi:10.1109/JLT.2003.822205.

[12] J.W. Nicholson, R.S. Windeler, D.J. Digiovanni, Optically driven deposition of single-walled carbon-nanotube saturable absorbers on optical fiber end-faces, Opt. Express.

15 (2007) 9176–9183. doi:10.1364/OE.15.009176.

[13] P.L. McEuen, M.S. Fuhrer, Single-walled carbon nanotube electronics, IEEE Trans. Nanotechnol. 1 (2002) 78–85. doi:10.1109/TNANO.2002.1005429.

[14] M. Nihei, A. Kawabata, Y. Awano, Direct diameter-controlled growth of multiwall carbon nanotubes on nickel-silicide layer, Jpn. J. Appl. Phys. 42 (2003) L721–L723. doi:10.1143/JJAP.42.L721.

[15] M. Nihei, A. Kawabata, D. Kondo, M. Horibe, S. Sato, Y. Awano, Electrical properties of carbon nanotube bundles for future via interconnects, Jpn. J. Appl. Phys. 44 (2005) 1626–1628. doi:10.1143/JJAP.44.1626.

[16] Y.J. Jung, S. Kar, S. Talapatra, C. Soldano, G. Viswanathan, X. Li, et al., Aligned carbon nanotube-polymer hybrid architectures for diverse flexible electronic applications, Nano Lett. 6 (2006) 413–418. doi:10.1021/nl052238x.

[17] M. Katayama, K.-Y. Lee, S. Honda, T. Hirao, K. Oura, Ultra-low-threshold field electron emission from pillar array of aligned carbon nanotube bundles, Jpn. J. Appl. Phys. 43 (2004) L774–L776. doi:10.1143/JJAP.43.L774.

[18] S. Fukutomi, K. Tamiya, T. Watanabe, K. Taguchi, Electrophoretic deposition of carbon nanotubes electrode for dye-sensitized solar cells, in: Int. Conf. Electr. Autom. Mech. Eng. (EAME 2015), 2015: pp. 55–58. doi:10.1016/j.electacta.2011.09.028.

[19] J. van de Lagemaat, T.M. Barnes, G. Rumbles, S.E. Shaheen, T.J. Coutts, C. Weeks, et al., Organic solar cells with carbon nanotubes replacing In2O3:Sn as the transparent electrode, Appl. Phys. Lett. 88 (2006) 233503. doi:10.1063/1.2210081.

[20] G. Zhu, L. Pan, T. Lu, X. Liu, T. Lv, T. Xu, et al., Electrophoretic deposition of carbon nanotubes films as counter electrodes of dye-sensitized solar cells, Electrochim. Acta. 56 (2011) 10288–10291. doi:10.1016/j.electacta.2011.09.028.

[21] K. Suzuki, M. Yamaguchi, M. Kumagai, S. Yanagida, Application of carbon nanotubes to counter electrodes of dye-sensitized solar cells, Chem. Lett. 32 (2003) 28–29. doi:10.1246/cl.2003.28.

[22] S. Ren, M. Bernardi, R.R. Lunt, V. Bulovic, J.C. Grossman, S. Gradečak, Toward efficient carbon nanotube/P3HT solar cells: active layer, Nano Lett. 11 (2011) 5316–5321. doi:10.1021/nl202796u.

[23] A. Kongkanand, R.M. Domínguez, P. V Kamat, Single wall carbon nanotube scaffolds for photoelectrochemical solar cells. Capture and transport of photogenerated electrons., Nano Lett. 7 (2007) 676–680. doi:10.1021/nl0627238.

[24] R.S. Kshetrimayum, A brief intro to metamaterials, IEEE Potentials. 23 (2005) 44–46.

doi:10.1109/MP.2005.1368916.

[25] S.J. Pendry, Metamaterials and the control of electromagnetic fields, Conf. Coherence Quantum Opt. (2007) CMB2. doi:10.1364/CQO.2007.CMB2.

[26] A.C. Sparavigna, Vibrations of a one-dimensional host-guest system, Mater. Sci. Appl. 2 (2011) 314–318. doi:10.4236/msa.2011.25041.

[27] J.B. Pendry, Negative refraction makes a perfect lens, Phys. Rev. Lett. 85 (2000) 3966–3969. doi:10.1103/PhysRevLett.85.3966.

[28] R.A. Shelby, D.R. Smith, S.C. Nemat-Nasser, S. Schultz, Microwave transmission through a two-dimensional, isotropic, left-handed metamaterial, Appl. Phys. Lett. 78 (2001) 489. doi:10.1063/1.1343489.

[29] M.F. Karim, A.Q. Liu, A. Alphones, A.B. Yu, A tunable bandstop filter via the capacitance change of micromachined switches, J. Micromechanics Microengineering. 16 (2006) 851–861. doi:10.1088/0960-1317/16/4/023.

[30] X. He, Z. Lv, B. Liu, Z. Li, Tunable magnetic metamaterial based multi-split-ring resonator (MSRR) using MEMS switch components, Microsyst. Technol. 17 (2011) 1263–1269. doi:10.1007/s00542-011-1313-z.

[31] I.M. Pryce, K. Aydin, Y.A. Kelaita, R.M. Briggs, H.A. Atwater, Highly strained compliant optical metamaterials with large frequency yunability, Nano Lett. 10 (2010) 4222–4227. doi:10.1021/nl102684x.

[32] W.L. Chan, H.-T. Chen, A.J. Taylor, I. Brener, M.J. Cich, D.M. Mittleman, A spatial light modulator for terahertz beams, Appl. Phys. Lett. 94 (2009) 213511. doi:10.1063/1.3147221.

[33] A. Minovich, J. Farnell, D.N. Neshev, I. McKerracher, F. Karouta, J. Tian, et al., Liquid crystal based nonlinear fishnet metamaterials, Appl. Phys. Lett. 100 (2012) 121113. doi:10.1063/1.3695165.

[34] B. Jin, C. Zhang, S. Engelbrecht, A. Pimenov, J. Wu, Q. Xu, et al., Low loss and magnetic field-tunable superconducting terahertz metamaterial, Opt. Express. 18 (2010) 17504. doi:10.1364/OE.18.017504.

[35] L. Gao, Y. Kim, A. Vazquez-Guardado, K. Shigeta, S. Hartanto, D. Franklin, et al., Materials selections and growth conditions for large-area, multilayered, visible negative index metamaterials formed by nanotransfer printing, Adv. Opt. Mater. 2 (2014) 256–261. doi:10.1002/adom.201300356.

[36] M.A. Seo, J.H. Yim, Y.H. Ahn, F. Rotermund, D.S. Kim, S. Lee, et al., Terahertz electromagnetic interference shielding using single-walled carbon nanotube flexible

films, Appl. Phys. Lett. 93 (2008) 231905. doi:10.1063/1.3046126.

[37] G.B. Jung, Y. Myung, Y.J. Cho, Y.J. Sohn, D.M. Jang, H.S. Kim, et al., Terahertz spectroscopy of nanocrystal−carbon nanotube and −graphene oxide hybrid nanostructures, J. Phys. Chem. C. 114 (2010) 11258–11265. doi:10.1021/jp1019894.

[38] J.T. Hong, D.J. Park, J.H. Yim, J.K. Park, J.-Y. Park, S. Lee, et al., Dielectric constant engineering of single-walled carbon nanotube films for metamaterials and plasmonic devices, J. Phys. Chem. Lett. 4 (2013) 3950–3957. doi:10.1021/jz4020053.

[39] A.E. Nikolaenko, F. De Angelis, S.A. Boden, N. Papasimakis, P. Ashburn, E. Di Fabrizio, et al., Carbon nanotubes in a photonic metamaterial., Phys. Rev. Lett. 104 (2010) 153902. doi:10.1103/PhysRevLett.104.153902.

[40] J. Walker, Optical absorption and luminescence in diamond, Reports Prog. Phys. 42 (1979) 1605–1659. doi:10.1088/0034-4885/42/10/001.

[41] M. Smalc, G. Shives, G. Chen, S. Guggari, J. Norley, R. Andy, et al., Thermal performance of natural graphite heat spreaders, in: Proc. IPACK 2005, 2005.

[42] K.S. Novoselov, A.K. Geim, S. V. Morozov, D. Jiang, Y. Zhang, S. V. Dubonos, et al., Electric field effect in atomically thin carbon films, Science (80-.). 306 (2004) 666–669. doi:10.1126/science.1102896.

[43] H.W. Kroto, J.R. Heath, S.C. O'Brien, R.F. Curl, R.E. Smalley, C60: Buckminsterfullerene, Nature. 318 (1985) 162–163. doi:10.1038/318162a0.

[44] L. Radushkevich, V. Lukyanovich, O strukture ugleroda, obrazujuce gosja pri termiceskom razlozenii okisi ugleroda na zeleznom kontakte, Zurn Fis. Chim. (1952) 88–95.

[45] W.R. Davis, R.J. Slawson, G.R. Rigby, An unusual form of carbon, Nature. 171 (1953) 756–756. doi:10.1038/171756a0.

[46] L.J.E. Hofer, E. Sterling, J.T. McCartney, Structure of carbon deposited from carbon monoxide on iron, cobalt and nickel, J. Phys. Chem. 59 (1955) 1153–1155. doi:10.1021/j150533a010.

[47] M. Hillert, N. Lange, The structure of graphite filaments, Zeitschrift Für Krist. 111 (1959) 24–34. doi:10.1524/zkri.1959.111.1-6.24.

[48] M.L. Lieberman, C.R. Hills, C.J. Miglionico, Growth of graphite filaments, Carbon N. Y. 9 (1971) 633–635. doi:10.1016/0008-6223(71)90085-6.

[49] A. Oberlin, M. Endo, T. Koyama, Filamentous growth of carbon through benzene decomposition, J. Cryst. Growth. 32 (1976) 335–349. doi:10.1016/0022-0248(76)90115-9.

[50] H.G. Tennent, Carbon fibrils, method for producing same and compositions containing same, US 4663230A, 1984.

[51] S. Iijima, T. Ichihashi, Single-shell carbon nanotubes of 1-nm diameter, Nature. 363 (1993) 603–605. doi:10.1038/363603a0.

[52] D.S. Bethune, C.H. Klang, M.S. de Vries, G. Gorman, R. Savoy, J. Vazquez, et al., Cobalt-catalysed growth of carbon nanotubes with single-atomic-layer walls, Nature. 363 (1993) 605–607. doi:10.1038/363605a0.

[53] H. Dai, A.G. Rinzler, P. Nikolaev, A. Thess, D.T. Colbert, R.E. Smalley, Single-wall nanotubes produced by metal-catalyzed disproportionation of carbon monoxide, Chem. Phys. Lett. 260 (1996) 471–475. doi:10.1016/0009-2614(96)00862-7.

[54] M. Kumar, Y. Ando, Chemical vapor deposition of carbon nanotubes: a review on growth mechanism and mass production, J. Nanosci. Nanotechnol. 10 (2010) 3739–3758. doi:10.1166/jnn.2010.2939.

[55] M.S. Dresselhaus, G. Dresselhaus, P.C. Eklund, Science of fullerenes and carbon nanotubes, Academic Press, 1996.

[56] C. Kane, L. Balents, M.P.A. Fisher, Coulomb interactions and mesoscopic effects in carbon nanotubes, 79 (1997) 5086–5089. doi:10.1103/PhysRevLett.79.5086.

[57] P. Bernier, C. Journet, W.K. Maser, A. Loiseau, M.L. de la Chapelle, S. Lefrant, et al., Large-scale production of single-walled carbon nanotubes by the electric-arc technique, Nature. 388 (1997) 756–758. doi:10.1038/41972.

[58] T. Guo, P. Nikolaev, A.G. Rinzler, D. Tomanek, D.T. Colbert, R.E. Smalley, Self-Assembly of Tubular Fullerenes, J. Phys. Chem. 99 (1995) 10694–10697. doi:10.1021/j100027a002.

[59] T. Guo, P. Nikolaev, A. Thess, D.T. Colbert, R.E. Smalley, Catalytic growth of single-walled nanotubes by laser vaporization, Chem. Phys. Lett. 243 (1995) 49–54. doi:10.1016/0009-2614(95)00825-O.

[60] C.D. Scott, S. Arepalli, P. Nikolaev, R.E. Smalley, Growth mechanisms for single-wall carbon nanotubes in a laser-ablation process, Appl. Phys. A Mater. Sci. Process. 72 (2001) 573–580. doi:10.1007/s003390100761.

[61] A. Thess, R. Lee, P. Nikolaev, H. Dai, P. Petit, J. Robert, et al., Crystalline Ropes of Metallic Carbon Nanotubes, Science (80-.). 273 (1996).

[62] M. Ge, K. Sattler, Vapor-condensation generation and STM analysis of fullerene tubes, Science. 260 (1993) 515–518. doi:10.1126/science.260.5107.515.

[63] R.T.K. Baker, M.A. Barber, P.S. Harris, F.S. Feates, R.J. Waite, Nucleation and

growth of carbon deposits from the nickel catalyzed decomposition of acetylene, J. Catal. 26 (1972) 51–62. doi:10.1016/0021-9517(72)90032-2.

[64] R.T.K. Baker, P.S. Harris, R.B. Thomas, R.J. Waite, Formation of filamentous carbon from iron, cobalt and chromium catalyzed decomposition of acetylene, J. Catal. 30 (1973) 86–95. doi:10.1016/0021-9517(73)90055-9.

[65] R.T.K. Baker, R.J. Waite, Formation of carbonaceous deposits from the platinum-iron catalyzed decomposition of acetylene, J. Catal. 37 (1975) 101–105. doi:10.1016/0021-9517(75)90137-2.

[66] S.B. Sinnott, R. Andrews, D. Qian, A.M. Rao, Z. Mao, E.C. Dickey, et al., Model of carbon nanotube growth through chemical vapor deposition, Chem. Phys. Lett. 315 (1999) 25–30. doi:10.1016/S0009-2614(99)01216-6.

[67] S. Hofmann, M. Cantoro, B. Kleinsorge, C. Casiraghi, a. Parvez, J. Robertson, et al., Effects of catalyst film thickness on plasma-enhanced carbon nanotube growth, J. Appl. Phys. 98 (2005) 1–8. doi:10.1063/1.1989432.

[68] D. Futaba, K. Hata, T. Yamada, K. Mizuno, M. Yumura, S. Iijima, Kinetics of Water-Assisted Single-Walled Carbon Nanotube Synthesis Revealed by a Time-Evolution Analysis, Phys. Rev. Lett. 95 (2005) 56104. doi:10.1103/PhysRevLett.95.056104.

[69] D.N. Futaba, K. Hata, T. Namai, T. Yamada, K. Mizuno, Y. Hayamizu, et al., 84% catalyst activity of water-assisted growth of single walled carbon nanotube forest characterization by a statistical and macroscopic approach, J. Phys. Chem. B. 110 (2006) 8035–8038. doi:10.1021/jp060080e.

[70] T. Sugai, T. Okazaki, H. Yoshida, H. Shinohara, Syntheses of single- and double-wall carbon nanotubes by the HTPAD and HFCVD methods, New J. Phys. 6 (2004) 21–21. doi:10.1088/1367-2630/6/1/021.

[71] S. Hofmann, C. Ducati, J. Robertson, B. Kleinsorge, Low-temperature growth of carbon nanotubes by plasma-enhanced chemical vapor deposition, Appl. Phys. Lett. 83 (2003) 135–137. doi:10.1063/1.1589187.

[72] S. Hofmann, C. Ducati, B. Kleinsorge, J. Robertson, Direct growth of aligned carbon nanotube field emitter arrays onto plastic substrates, Appl. Phys. Lett. 83 (2003) 4661–4663. doi:10.1063/1.1630167.

[73] M. Cantoro, S. Hofmann, S. Pisana, C. Ducati, a. Parvez, a. C. Ferrari, et al., Effects of pre-treatment and plasma enhancement on chemical vapor deposition of carbon nanotubes from ultra-thin catalyst films, Diam. Relat. Mater. 15 (2006) 1029–1035. doi:10.1016/j.diamond.2006.01.007.

[74] M. Meyyappan, L. Delzeit, A. Cassell, D. Hash, Carbon nanotube growth by PECVD:

a review, Plasma Sources Sci. Technol. 12 (2003) 205–216. doi:10.1088/0963-0252/12/2/312.

[75] M. Meyyappan, A review of plasma enhanced chemical vapour deposition of carbon nanotubes, J. Phys. D. Appl. Phys. 42 (2009) 213001. doi:10.1088/0022-3727/42/21/213001.

[76] V.I. Merkulov, A.V. Melechko, M.A. Guillorn, D.H. Lowndes, M.L. Simpson, Growth rate of plasma-synthesized vertically aligned carbon nanofibers, Chem. Phys. Lett. 361 (2002) 492–498. doi:10.1016/S0009-2614(02)01016-3.

[77] K.B.K. Teo, M. Chhowalla, G.A.J. Amaratunga, W.I. Milne, D.G. Hasko, G. Pirio, et al., Uniform patterned growth of carbon nanotubes without surface carbon, Appl. Phys. Lett. 79 (2001) 1534–1536. doi:10.1063/1.1400085.

[78] K.B.K. Teo, D.B. Hash, R.G. Lacerda, N.L. Rupesinghe, M.S. Bell, S.H. Dalal, et al., The significance of plasma heating in carbon nanotube and nanofiber growth, Nano Lett. 4 (2004) 921–926. doi:10.1021/NL049629G.

[79] J. Han, W.-S. Yang, J.-B. YooChong-Yun Park, J.-B. Yoo, C.-Y. Park, Growth and emission characteristics of vertically well-aligned carbon nanotubes grown on glass substrate by hot filament plasma-enhanced chemical vapor deposition, J. Appl. Phys. 88 (2000) 7363–7365. doi:10.1063/1.1322378.

[80] B.A. Cruden, A.M. Cassell, Q. Ye, M. Meyyappan, Reactor design considerations in the hot filament/direct current plasma synthesis of carbon nanofibers, J. Appl. Phys. 94 (2003) 4070–4078. doi:10.1063/1.1601293.

[81] Y. Shiratori, H. Hiraoka, Y. Takeuchi, S. Itoh, M. Yamamoto, One-step formation of aligned carbon nanotube field emitters at 400°C, Appl. Phys. Lett. 82 (2003) 2485–2487. doi:10.1063/1.1566803.

[82] V.K. Varadan, J. Xie, Large-scale synthesis of multi-walled carbon nanotubes by microwave CVD, Smart Mater. Struct. 11 (2002) 318. doi:10.1088/0964-1726/11/4/318.

[83] K. Byrappa, T. Adschiri, Hydrothermal technology for nanotechnology, Prog. Cryst. Growth Charact. Mater. 53 (2007) 117–166. doi:10.1016/j.pcrysgrow.2007.04.001.

[84] W. Wang, S. Kunwar, J.Y. Huang, D.Z. Wang, Z.F. Ren, Low temperature solvothermal synthesis of multiwall carbon nanotubes, Nanotechnology. 16 (2005) 21–23. doi:10.1088/0957-4484/16/1/005.

[85] W. Wang, B. Poudel, D.Z. Wang, Z.F. Ren, Synthesis of Multiwalled Carbon Nanotubes through a Modified Wolff−Kishner Reduction Process, J. Am. Chem. Soc. 127 (2005) 18018–18019. doi:10.1021/ja056654v.

[86] Y. Jiang, Y. Wu, S. Zhang, C. Xu, W. Yu, Y. Xie, et al., A catalytic-assembly solvothermal route to multiwall carbon nanotubes at a moderate temperature, J. Am. Chem. Soc. 122 (2000) 12383–12384. doi:10.1021/ja002387b.

[87] D.C. Lee, F. V. Mikulec, B.A. Korgel, Carbon nanotube synthesis in supercritical toluene, J. Am. Chem. Soc. 126 (2004) 4951–4957. doi:10.1021/ja031522s.

[88] J.M. Calderon Moreno, M. Yoshimura, Hydrothermal processing of high-quality multiwall nanotubes from amorphous carbon, J. Am. Chem. Soc. 123 (2001) 741–742. doi:10.1021/JA003008H.

[89] Y. Gogotsi, J.A. Libera, M. Yoshimura, Hydrothermal synthesis of multiwall carbon nanotubes, J. Mater. Res. 15 (2000) 2591–2594. doi:10.1557/JMR.2000.0370.

[90] M. Motiei, Y.R. Hacohen, Jose Calderon-Moreno, A. Gedanken, Preparing carbon nanotubes and nested fullerenes from supercritical CO2 by a chemical reaction, J. Am. Chem. Soc. 123 (2001) 8624–8625. doi:10.1021/JA015859A.

[91] M. Reibold, P. Paufler, A.A. Levin, W. Kochmann, N. Pätzke, D.C. Meyer, Materials: Carbon nanotubes in an ancient Damascus sabre, Nature. 444 (2006) 286–286. doi:10.1038/444286a.

[92] L. Yuan, K. Saito, W. Hu, Z. Chen, Ethylene flame synthesis of well-aligned multi-walled carbon nanotubes, Chem. Phys. Lett. 346 (2001) 23–28. doi:10.1016/S0009-2614(01)00959-9.

[93] W. Merchan-Merchan, A. Saveliev, L.A. Kennedy, A. Fridman, Formation of carbon nanotubes in counter-flow, oxy-methane diffusion flames without catalysts, Chem. Phys. Lett. 354 (2002) 20–24. doi:10.1016/S0009-2614(02)00027-1.

[94] R.L. Vander Wal, G.M. Berger, L.J. Hall, Single-walled carbon nanotube synthesis via a multi-stage flame configuration, J. Phys. Chem. B. 106 (2002) 3564–3567. doi:10.1021/JP012844Q.

[95] W. Hu, D. Gong, Z. Chen, L. Yuan, K. Saito, C.A. Grimes, et al., Growth of well-aligned carbon nanotube arrays on silicon substrates using porous alumina film as a nanotemplate, Appl. Phys. Lett. 79 (2001) 3083–3085. doi:10.1063/1.1415406.

[96] H.P. Boehm, Carbon from carbon monoxide disproportionation on nickel and iron catalysts: Morphological studies and possible growth mechanisms, Carbon N. Y. 11 (1973) 583–590. doi:10.1016/0008-6223(73)90323-0.

[97] P. Nikolaev, M.J. Bronikowski, R.K. Bradley, F. Rohmund, D.T. Colbert, K.. Smith, et al., Gas-phase catalytic growth of single-walled carbon nanotubes from carbon monoxide, Chem. Phys. Lett. 313 (1999) 91–97. doi:10.1016/S0009-2614(99)01029-5.

[98] P. Nikolaev, Gas-phase production of single-walled carbon nanotubes from carbon monoxide: a review of the hipco process, J. Nanosci. Nanotechnol. 4 (2004) 307–316. doi:10.1002/chin.200444248.

[99] P.J.F. Harris, Carbon nanotubes and related structures: new materials for the twenty-first century, Cambridge University Press, 2001.

[100] M. Meo, M. Rossi, Prediction of Young's modulus of single wall carbon nanotubes by molecular-mechanics based finite element modelling, Compos. Sci. Technol. 66 (2006) 1597–1605. doi:10.1016/j.compscitech.2005.11.015.

[101] M.-F. Yu, B.S. Files, S. Arepalli, R.S. Ruoff, Tensile loading of ropes of single wall carbon nanotubes and their mechanical properties, Phys. Rev. Lett. 84 (2000) 5552–5555. doi:10.1103/PhysRevLett.84.5552.

[102] M. Buongiorno Nardelli, J.-L. Fattebert, D. Orlikowski, C. Roland, Q. Zhao, J. Bernholc, Mechanical properties, defects and electronic behavior of carbon nanotubes, Carbon N. Y. 38 (2000) 1703–1711. doi:10.1016/S0008-6223(99)00291-2.

[103] J.P. Lu, J. Han, Carbon nanotubes and nanotubes-based nano devices, Int. J. High Speed Electron. Syst. 9 (1998) 101–123. doi:10.1142/S0129156498000063.

[104] E. Pop, D. Mann, Q. Wang, K. Goodson, H. Dai, Thermal conductance of an individual single-wall carbon nanotube above room temperature, Nano Lett. 6 (2006) 96–100. doi:10.1021/nl052145f.

[105] S. Berber, Y.-K. Kwon, D. Tománek, Thermal conductivity of carbon nanotubes, Phys. Rev. Lett. 84 (2000) 4613–4616. doi:10.1103/PhysRevLett.84.4613.

[106] M.B. Jakubinek, M.A. White, G. Li, C. Jayasinghe, W. Cho, M.J. Schulz, et al., Thermal and electrical conductivity of tall, vertically aligned carbon nanotube arrays, Carbon N. Y. 48 (2010) 3947–3952. doi:10.1016/j.carbon.2010.06.063.

[107] T. Borca-Tasciuc, S. Vafaei, D.-A. Borca-Tasciuc, B.Q. Wei, R. Vajtai, P.M. Ajayan, Anisotropic thermal diffusivity of aligned multiwall carbon nanotube arrays, J. Appl. Phys. 98 (2005) 54309. doi:10.1063/1.2034079.

[108] W. Yi, L. Lu, Z. Dian-lin, Z.W. Pan, S.S. Xie, Linear specific heat of carbon nanotubes, Phys. Rev. B. 59 (1999) R9015–R9018. doi:10.1103/PhysRevB.59.R9015.

[109] V. Lordi, N. Yao, M.M.J. Treacy, T.W. Ebbesen, J.M. Gibson, E.W. Wong, et al., Molecular mechanics of binding in carbon-nanotube–polymer composites, J. Mater. Res. 15 (2000) 2770–2779. doi:10.1557/JMR.2000.0396.

[110] Teri Wang Odom, Jin-Lin Huang, A. Philip Kim, C.M. Lieber, Structure and electronic properties of carbon nanotubes, J. Phys. Chem. B. 104 (2000) 2794–2809.

doi:10.1021/JP993592K.

[111] H. Dai, A. Javey, E. Pop, D. Mann, W. Kim, Y. Lu, Electrical transport properties and field effect transistors of carbon nanotubes, Nano. 1 (2006) 1–13. doi:10.1142/S1793292006000070.

[112] A.N. Andriotis, M. Menon, G.E. Froudakis, Various bonding configurations of transition-metal atoms on carbon nanotubes: Their effect on contact resistance, Appl. Phys. Lett. 76 (2000) 3890–3892. doi:10.1063/1.126811.

[113] P.R. Bandaru, Electrical properties and applications of carbon nanotube structures, J. Nanosci. Nanotechnol. 7 (2007) 1239–1267. doi:10.1166/jnn.2007.307.

[114] R.H. Xie, Q. Rao, Third-order optical nonlinearities of chiral graphene tubules, Chem. Phys. Lett. 313 (1999) 211–216. doi:10.1016/S0009-2614(99)01044-1.

[115] M.F. Lin, F.L. Shyu, R.B. Chen, Optical properties of well-aligned multiwalled carbon nanotube bundles, Phys. Rev. B. 61 (2000) 14114–14118. doi:10.1103/PhysRevB.61.14114.

[116] X. Liu, J. Si, B. Chang, G. Xu, Q. Yang, Z. Pan, et al., Third-order optical nonlinearity of the carbon nanotubes, Appl. Phys. Lett. 74 (1999) 164–166. doi:10.1063/1.123282.

[117] V.. Margulis, E.. Gaiduk, E.. Zhidkin, Third-order optical nonlinearity of semiconductor carbon nanotubes: third harmonic generation, Diam. Relat. Mater. 8 (1999) 1240–1245. doi:10.1016/S0925-9635(99)00109-0.

[118] R.-H. Xie, Empirical exponent law of the second-order hyperpolarizability in small armchair and zig–zag nanotubes, J. Chem. Phys. 108 (1998) 3626–3629. doi:10.1063/1.475757.

[119] W.A. de Heer, W.S. Bacsa, A. Chatelain, T. Gerfin, R. Humphrey-Baker, L. Forro, et al., Aligned carbon nanotube films: production and optical and electronic properties, Science. 268 (1995) 845–847. doi:10.1126/science.268.5212.845.

[120] F.J. García-Vidal, J.M. Pitarke, J.B. Pendry, Effective medium theory of the optical properties of aligned carbon nanotubes, Phys. Rev. Lett. 78 (1997) 4289–4292. doi:10.1103/PhysRevLett.78.4289.

[121] A. Kasuya, Y. Sasaki, Y. Saito, K. Tohji, Y. Nishina, Evidence for size-dependent discrete dispersions in single-wall nanotubes, Phys. Rev. Lett. 78 (1997) 4434–4437. doi:10.1103/PhysRevLett.78.4434.

[122] D.S. Bychanok, M.A. Kanygin, A. V. Okotrub, M. V. Shuba, A.G. Paddubskaya, A.O. Pliushch, et al., Anisotropy of the electromagnetic properties of polymer composites based on multiwall carbon nanotubes in the gigahertz frequency range, JETP Lett. 93

(2011) 607–611. doi:10.1134/S0021364011100043.

[123] K. Kempa, J. Rybczynski, Z. Huang, K. Gregorczyk, A. Vidan, B. Kimball, et al., Carbon nanotubes as optical antennae, Adv. Mater. 19 (2007) 421–426. doi:10.1002/adma.200601187.

[124] X.J. Wang, J.D. Flicker, B.J. Lee, W.J. Ready, Z.M. Zhang, Visible and near-infrared radiative properties of vertically aligned multi-walled carbon nanotubes., Nanotechnology. 20 (2009) 215704. doi:10.1088/0957-4484/20/21/215704.

[125] Z.P. Yang, L. Ci, J. a. Bur, S.Y. Lin, P.M. Ajayan, Experimental observation of an extremely dark material made by a low-density nanotube array, Nano Lett. 8 (2008) 446–451. doi:10.1021/nl072369t.

[126] K. Mizuno, J. Ishii, H. Kishida, Y. Hayamizu, S. Yasuda, D.N. Futaba, et al., A black body absorber from vertically aligned single-walled carbon nanotubes., Proc. Natl. Acad. Sci. U. S. A. 106 (2009) 6044–6047. doi:10.1073/pnas.0900155106.

[127] A. Ugawa, J. Hwang, H.H. Gommans, H. Tashiro, A.G. Rinzler, D.B. Tanner, Far-infrared to visible optical conductivity of single-wall carbon nanotubes, Curr. Appl. Phys. 1 (2001) 45–49. doi:10.1016/S1567-1739(00)00009-2.

[128] E. Theocharous, C.J. Chunnilall, R. Mole, D. Gibbs, N. Fox, N. Shang, et al., The partial space qualification of a vertically aligned carbon nanotube coating on aluminium substrates for EO applications, Opt. Express. 22 (2014) 7290–7307. doi:10.1364/oe.22.007290.

[129] V.G. Veselago, The electrodynamic of substances with simultaneously negative values of ε and μ, Sov. Phys. Uspekhi. 10 (1968) 509–514. doi:10.1070/PU1968v010n04ABEH003699.

[130] V.M. Shalaev, Optical negative-index metamaterials, Nat. Photonics. 1 (2007) 41–48. doi:10.1038/nphoton.2006.49.

[131] A. Alu, N. Engheta, Guided modes in a waveguide filled with a pair of single-negative (SNG), double-negative (DNG), and/or double-positive (DPS) layers, IEEE Trans. Microw. Theory Tech. 52 (2004) 199–210. doi:10.1109/TMTT.2003.821274.

[132] M. Beruete, M. Navarro-Cía, M. Sorolla, I. Campillo, Planoconcave lens by negative refraction of stacked subwavelength hole arrays, Opt. Express. 16 (2008) 9677. doi:10.1364/OE.16.009677.

[133] Nader Engheta, R.W. Ziolkowski, A positive future for double-negative metamaterials, IEEE Trans. Microw. Theory Tech. 53 (2005) 1535–1556. doi:10.1109/TMTT.2005.845188.

[134] A.N. Grigorenko, A.K. Geim, H.F. Gleeson, Y. Zhang, A.A. Firsov, I.Y. Khrushchev, et al., Nanofabricated media with negative permeability at visible frequencies, Nature. 438 (2005) 335–338. doi:10.1038/nature04242.

[135] V. Podolskiy, A. Sarychev, V. Shalaev, Plasmon modes and negative refraction in metal nanowire composites, Opt. Express. 11 (2003) 735. doi:10.1364/OE.11.000735.

[136] A.K. Sarychev, V.M. Shalaev, Magnetic resonance in metal nanoantennas, in: Proc. SPIE - Int. Soc. Opt. Eng., 2004: p. 128. doi:10.1117/12.560547.

[137] V.A. Podolskiy, E.E. Narimanov, Strongly anisotropic waveguide as a nonmagnetic left-handed system, Phys. Rev. B. 71 (2005) 201101. doi:10.1103/PhysRevB.71.201101.

[138] G. Shvets, Y.A. Urzhumov, Engineering the electromagnetic properties of periodic nanostructures using electrostatic resonances, Phys. Rev. Lett. 93 (2004) 243902. doi:10.1103/PhysRevLett.93.243902.

[139] U. Leonhardt, Optical conformal mapping, Science. 312 (2006) 1777–1780. doi:10.1126/science.1126493.

[140] W. Withayachumnankul, D. Abbott, Metamaterials in the terahertz regime, IEEE Photonics J. 1 (2009) 99–118. doi:10.1109/JPHOT.2009.2026288.

[141] J.B. Pendry, A.J. Holden, D.J. Robbins, W.J. Stewart, Magnetism from conductors and enhanced nonlinear phenomena, IEEE Trans. Microw. Theory Tech. 47 (1999) 2075–2084. doi:10.1109/22.798002.

[142] J.B. Pendry, A.J. Holden, W.J. Stewart, I. Youngs, Extremely low frequency plasmons in metallic mesostructures, Phys. Rev. Lett. 76 (1996) 4773–4776. doi:10.1103/PhysRevLett.76.4773.

[143] R. Marqués, D.R. Smith, Comment on “Electrodynamics of metallic photonic crystals and the problem of left-handed materials,” Phys. Rev. Lett. 92 (2004) 59401. doi:10.1103/PhysRevLett.92.059401.

[144] R. Schittny, M. Kadic, S. Guenneau, M. Wegener, Experiments on transformation thermodynamics: Molding the flow of heat, Phys. Rev. Lett. 110 (2013) 195901. doi:10.1103/PhysRevLett.110.195901.

[145] G. Zhong, J.H. Warner, M. Fouquet, A.W. Robertson, B. Chen, J. Robertson, Growth of ultrahigh density single-walled carbon nanotube forests by improved catalyst design, ACS Nano. 6 (2012) 2893–903. doi:10.1021/nn203035x.

[146] O.A. Nerushev, S. Dittmar, R.-E. Morjan, F. Rohmund, E.E.B. Campbell, Particle size dependence and model for iron-catalyzed growth of carbon nanotubes by thermal

chemical vapor deposition, J. Appl. Phys. 93 (2003) 4185. doi:10.1063/1.1559433.

[147] H. Zhang, G. Cao, Z. Wang, Y. Yang, Z. Shi, Z. Gu, Influence of hydrogen pretreatment condition on the morphology of Fe/Al2O3 catalyst film and growth of millimeter-long carbon nanotube array, J. Phys. Chem. C. 112 (2008) 4524–4530. doi:10.1021/jp710338d.

[148] Y.Y. Wei, G. Eres, V.I. Merkulov, D.H. Lowndes, Effect of catalyst film thickness on carbon nanotube growth by selective area chemical vapor deposition, Appl. Phys. Lett. 78 (2001) 1394–1396. doi:Doi 10.1063/1.1354658.

[149] S. Pisana, M. Cantoro, a. Parvez, S. Hofmann, a. C. Ferrari, J. Robertson, The role of precursor gases on the surface restructuring of catalyst films during carbon nanotube growth, Phys. E Low-Dimensional Syst. Nanostructures. 37 (2007) 1–5. doi:10.1016/j.physe.2006.06.014.

[150] S. Sakurai, H. Nishino, D.N. Futaba, S. Yasuda, T. Yamada, A. Maigne, et al., Role of subsurface diffusion and Ostwald ripening in catalyst formation for single-walled carbon nanotube forest growth, J. Am. Chem. Soc. 134 (2012) 2148–2153. doi:10.1021/ja208706c.

[151] S.B. Simonsen, I. Chorkendorff, S. Dahl, M. Skoglundh, J. Sehested, S. Helveg, Ostwald ripening in a Pt/SiO2 model catalyst studied by in situ TEM, J. Catal. 281 (2011) 147–155. doi:10.1016/j.jcat.2011.04.011.

[152] S. Porro, S. Musso, M. Giorcelli, a. Chiodoni, a. Tagliaferro, Optimization of a thermal-CVD system for carbon nanotube growth, Phys. E Low-Dimensional Syst. Nanostructures. 37 (2007) 16–20. doi:10.1016/j.physe.2006.07.010.

[153] G. Taguchi, System of experimental design: Engineering methods to optimize quality and minimize costs, UNIPUB/Kraus International Publications, 1987.

[154] B. Berginc, The use of the Taguchi approach to determine the influence of injection-moulding parameters on the properties of green parts, Manuf. Eng. 15 (2006) 63–70.

[155] G. Taguchi, Quality engineering (Taguchi methods) for the development of electronic circuit technology, IEEE Trans. Reliab. 44 (1995) 225–229. doi:10.1109/24.387375.

[156] C.L. Cheung, A. Kurtz, H. Park, C.M. Lieber, Diameter-controlled synthesis of carbon nanotubes, J. Phys. Chem. B. 106 (2002) 2429–2433. doi:10.1021/jp0142278.

[157] G. Zhang, D. Mann, L. Zhang, A. Javey, Y. Li, E. Yenilmez, et al., Ultra-high-yield growth of vertical single-walled carbon nanotubes: Hidden roles of hydrogen and oxygen, Proc. Natl. Acad. Sci. U. S. A. 102 (2005) 16141–16145. doi:10.1073/pnas.0507064102.

[158] P. Madhav, Quality Engineering Using Robust Design, Pearson Education, 2008. https://books.google.co.in/books?id=7leNc9ZEiOEC.

[159] H. Koji, T. Harigai, N. Nitta, H. Furuta, A. Hatta, Magnetron sputtering deposition of additional Ni thin films on the Fe/Al multi-layered catalyst film for the growth control of carbon nanotubes, Trans. Mater. Res. Soc. Japan. 37 (2012) 511–514. doi:10.14723/tmrsj.37.511.

[160] H. Koji, H. Furuta, K. Sekiya, N. Nitta, T. Harigai, A. Hatta, Increased CNT growth density with an additional thin Ni layer on the Fe/Al catalyst film, Diam. Relat. Mater. 36 (2013) 1–7. doi:10.1016/j.diamond.2013.02.002.

[161] A. Pander, A. Hatta, H. Furuta, Optimization of catalyst formation conditions for synthesis of carbon nanotubes using Taguchi method, Appl. Surf. Sci. 371 (2016) 425–435. doi:10.1016/j.apsusc.2016.02.216.

[162] P. Software Minitab 17 Statistical, Minitab 17 Statistical Software, (2010).

[163] T. De Los Arcos, M.G. Garnier, J.W. Seo, P. Oelhafen, V. Thommen, D. Mathys, The influence of catalyst chemical state and morphology on carbon nanotube growth, J. Phys. Chem. B. 108 (2004) 7728–7734. doi:10.1021/jp049495v.

[164] I. Sushumna, E. Ruckenstein, Role of physical and chemical interactions in the behavior of supported metal catalysts: Iron on alumina—A case study, J. Catal. 94 (1985) 239–288. doi:10.1016/0021-9517(85)90100-9.

[165] M. Cantoro, S. Hofmann, S. Pisana, V. Scardaci, A. Parvez, C. Ducati, et al., Catalytic chemical vapor deposition of single-wall carbon nanotubes at low temperatures, Nano Lett. 6 (2006) 1107–1112. doi:10.1021/nl060068y.

[166] M. Xu, D.N. Futaba, M. Yumura, K. Hata, Alignment control of carbon nanotube forest from random to nearly perfectly aligned by utilizing the crowding effect, ACS Nano. 6 (2012) 5837–5844. doi:10.1021/nn300142j.

[167] J. Walkowicz, J. Staśkiewicz, K. Szafirowicz, D. Jakrzewski, G. Grzesiak, M. Stępniak, Optimization of the ASPN process to bright nitriding of woodworking tools using the Taguchi approach, J. Mater. Eng. Perform. 22 (2012) 410–420. doi:10.1007/s11665-012-0288-y.

[168] M. Pancielejko, A. Czyżniewski, V. Zavaleyev, A. Pander, K. Wojtalik, Optimization of the deposition parameters of DLC coatings with the MCVA method, Arch. Mater. Sci. Eng. 54 (2012) 60–67.

[169] M. Wąsik, J. Judek, M. Zdrojek, A.M. Witowski, Limitations of blackbody behavior of vertically aligned multi-walled carbon nanotubes arrays, Mater. Lett. 137 (2014) 85–87. doi:10.1016/j.matlet.2014.08.141.

[170] H. Bao, B. Duvvuri, M. Lou, X. Ruan, Effects of randomness and inclination on the optical properties of multi-walled carbon nanotube arrays, J. Quant. Spectrosc. Radiat. Transf. 132 (2014) 22–27. doi:10.1016/j.jqsrt.2013.04.015.

[171] E. Lidorikis, A.C. Ferrari, Photonics with multiwall carbon nanotube arrays, ACS Nano. 3 (2009) 1238–1248. doi:10.1021/nn900123a.

[172] G. Taguchi, S. Chowdhury, Y. Wu, Taguchi's quality engineering handbook, John Wiley & Sons, Inc., Hoboken, NJ, USA, 2004. doi:10.1002/9780470258354.

[173] A. Kawabata, T. Murakami, M. Nihei, N. Yokoyama, Long length, high-density carbon nanotube film grown by slope control of temperature profile for applications in heat dissipation, Jpn. J. Appl. Phys. 52 (2013) 110117. doi:10.7567/JJAP.52.110117.

[174] P.B. Amama, C.L. Pint, M. Kim, L. Mcjilton, K.G. Eyink, E.A. Stach, et al., Influence of alumina type on the evolution and activity of alumina-supported fe catalysts in single-walled carbon nanotube carpet growth, ACS Nano. 4 (2010) 895–904. doi:10.1021/nn901700u.

[175] S. Sakurai, M. Inaguma, D.N. Futaba, M. Yumura, K. Hata, Diameter and density control of single-walled carbon nanotube forests by modulating Ostwald ripening through decoupling the catalyst formation and growth processes, Small. 9 (2013) 3584–3592. doi:10.1002/smll.201300223.

[176] B. Zhao, D.N. Futaba, S. Yasuda, M. Akoshima, T. Yamada, K. Hata, Exploring advantages of diverse carbon nanotube forests with tailored structures synthesized by supergrowth from engineered catalysts, ACS Nano. 3 (2009) 108–114. doi:10.1021/nn800648a.

[177] M.S. Dresselhaus, G. Dresselhaus, R. Saito, A. Jorio, Raman spectroscopy of carbon nanotubes, Phys. Rep. 409 (2005) 47–99. doi:10.1016/j.physrep.2004.10.006.

[178] S. Costa, E. Borowiak-Palen, M. Kruszyńska, A. Bachmatiuk, R.J. Kaleńczuk, Characterization of carbon nanotubes by Raman spectroscopy, Mater. Sci. 26 (2008) 1–9. doi:10.1155/2010/603978.

[179] Y.Y. Wang, S. Gupta, R.J. Nemanich, Role of thin Fe catalyst in the synthesis of double- and single-wall carbon nanotubes via microwave chemical vapor deposition, Appl. Phys. Lett. 85 (2004) 2601–2603. doi:10.1063/1.1796529.

[180] H. Dai, Carbon nanotubes: Opportunities and challenges, Surf. Sci. 500 (2002) 218–241. doi:10.1016/S0039-6028(01)01558-8.

[181] H. Furuta, T. Kawaharamura, K. Kawabata, M. Furuta, T. Matsuda, C. Li, et al., High-density short-height directly grown CNT patterned emitter on glass, E-Journal Surf.

Sci. Nanotechnol. 8 (2010) 336–339. doi:10.1380/ejssnt.2010.336.

[182] C. Emmenegger, J.-M. Bonard, P. Mauron, P. Sudan, A. Lepora, B. Grobety, et al., Synthesis of carbon nanotubes over Fe catalyst on aluminium and suggested growth mechanism, Carbon N. Y. 41 (2003) 539–547. doi:10.1016/S0008-6223(02)00362-7.

[183] A. Pander, H. Miyaji, A. Hatta, H. Furuta, Water-assisted low-temperature growth of carbon nanotubes on aluminum foil, in: CNT 25 Conf. Tokyo, 2016.

[184] H. Furuta, T. Kawaharamura, M. Furuta, K. Kawabata, T. Hirao, T. Komukai, et al., Crystal structure analysis of multiwalled carbon nanotube forests by newly developed cross-sectional X-ray diffraction measurement, Appl. Phys. Express. 3 (2010) 1–4. doi:10.1143/APEX.3.105101.

[185] D.J. Yang, S.G. Wang, Q. Zhang, P.J. Sellin, G. Chen, Thermal and electrical transport in multi-walled carbon nanotubes, Phys. Lett. A. 329 (2004) 207–213. doi:10.1016/j.physleta.2004.05.070.

[186] Y. Murakami, E. Einarsson, T. Edamura, S. Maruyama, Polarization dependence of the optical absorption of single-walled carbon nanotubes, Phys. Rev. Lett. 94 (2005) 87402. doi:10.1103/PhysRevLett.94.087402.

[187] T.P. Butler, H. Butt, T.D. Wilkinson, G.A.J. Amaratunga, Visible diffraction from quasi-crystalline arrays of carbon nanotubes, Nanoscale. 7 (2015) 13452–13457. doi:10.1039/c5nr03245h.

[188] H. Butt, A.K. Yetisen, R. Ahmed, S.H. Yun, Q. Dai, Carbon nanotube biconvex microcavities, Appl. Phys. Lett. 106 (2015) 121108. doi:10.1063/1.4916236.

[189] A.E. Nikolaenko, N. Papasimakis, A. Chipouline, F. De Angelis, E. Di Fabrizio, N.I. Zheludev, THz bandwidth optical switching with carbon nanotube metamaterial, 20 (2012) 534–537. doi:10.1364/OE.20.006068.

[190] S. Fan, M.G. Chapline, N.R. Franklin, T.W. Tombler, A.M. Cassell, H. Dai, Self-oriented regular arrays of carbon nanotubes and their field emission properties, Science. 283 (1999) 512–514. doi:10.1126/science.283.5401.512.

[191] H.K. Kyeong, G.K. Tae, L. Seok, M.J. Young, H.K. Sun, T.B. Young, Simple assembling technique of single-walled carbon nanotubes using only photolithography, J. Korean Phys. Soc. 58 (2011) 1380–1383. doi:10.3938/jkps.58.1380.

[192] J. Wu, A. Antaris, M. Gong, H. Dai, Top-down patterning and self-assembly for regular arrays of semiconducting single-walled carbon nanotubes, Adv. Mater. 26 (2014) 6151–6156. doi:10.1002/adma.201401108.

[193] Y. Chen, H. Chen, J. Yu, J.S. Williams, V. Craig, Focused ion beam milling as a

universal template technique for patterned growth of carbon nanotubes, Appl. Phys. Lett. 90 (2007) 93126. doi:10.1063/1.2710785.

[194] A. Tselev, K. Hatton, M.S. Fuhrer, M. Paranjape, P. Barbara, A photolithographic process for fabrication of devices with isolated single-walled carbon nanotubes, Nanotechnology. 15 (2004) 1475–1478. doi:10.1088/0957-4484/15/11/017.

[195] J. Choi, K. Koh, J. Kim, Scalable and number-controlled synthesis of carbon nanotubes by nanostencil lithography, Nanoscale Res. Lett. 8 (2013) 281. doi:10.1186/1556-276X-8-281.

[196] J.D. Beard, J. Stringer, O.R. Ghita, P.J. Smith, High yield growth of patterned vertically aligned carbon nanotubes using inkjet-printed catalyst, ACS Appl. Mater. Interfaces. 5 (2013) 9785–9790. doi:10.1021/am402942q.

[197] S. Hofmann, M. Cantoro, B. Kleinsorge, C. Casiraghi, A. Parvez, J. Robertson, et al., Effects of catalyst film thickness on plasma-enhanced carbon nanotube growth, J. Appl. Phys. 98 (2005) 1–8. doi:10.1063/1.1989432.

[198] J. Jiao, L. Dong, S. Foxley, C.L. Mosher, D.W. Tuggle, Selected-area growth of carbon nanotubes by the combination of focused ion beam and chemical vapor deposition techniques., Microsc. Microanal. 9 (2003) 516–21. doi:10.1017/S1431927603030460.

[199] A. Emplit, E. Tooten, V. Xhurdebise, I. Huynen, Multifunctional material structures based on laser-etched carbon nanotube arrays, Micromachines. 5 (2014) 756–765. doi:10.3390/mi5030756.

[200] S. Huang, L. Dai, A.W.H. Mau, Controlled fabrication of large-scale aligned carbon nanofiber/nanotube patterns by photolitography, Adv. Mater. 14 (2002) 1140–1143. doi:10.1002/1521-4095(20020816)14:16<1140::AID-ADMA1140>3.0.CO;2-5.

[201] G. Jeong, N. Olofsson, L.K.L. Falk, E.E.B. Campbell, Effect of catalyst pattern geometry on the growth of vertically aligned carbon nanotube arrays, Carbon N. Y. 47 (2008) 696–704. doi:10.1016/j.carbon.2008.11.003.

[202] S. Huang, A.W.H. Mau, Selective growth of aligned carbon nanotubes on a silver-patterned substrate by the silver mirror reaction, J. Phys. Chem. B. 107 (2003) 3455–3458. doi:10.1021/jp034282b.

[203] Y. Wang, X. Zhao, G. Duan, X. Zhang, Broadband extraordinary terahertz transmission through super-aligned carbon nanotubes film., Opt. Express. 24 (2016) 15730–41. doi:10.1364/OE.24.015730.

[204] W.J. Yu, Y.S. Cho, G.S. Choi, D. Kim, Patterned carbon nanotube field emitter using the regular array of an anodic aluminium oxide template, Nanotechnology. 16 (2005)

S291–S295. doi:10.1088/0957-4484/16/5/029.

[205] C. Enkrich, F. Pérez-Willard, D. Gerthsen, J. Zhou, T. Koschny, C.M. Soukoulis, et al., Focused-ion-beam nanofabrication of near-infrared magnetic metamaterials, Adv. Mater. 17 (2005) 2547–2549. doi:10.1002/adma.200500804.

[206] A.A. Tseng, Recent developments in micromilling using focused ion beam technology, J. Micromechanics Microengineering. 14 (2004) R15–R34. doi:10.1088/0960-1317/14/4/R01.

[207] A. Pander, A. Hatta, H. Furuta, FIB secondary etching method for fabrication of fine CNT forest metamaterials, Nano-Micro Lett. (2017) In press.

[208] F. Yongqi, N.K.A. Bryan, Investigation of 3D microfabrication characteristics by focused ion beam technology in silicon, J. Mater. Process. Technol. 104 (2000) 44–47. doi:10.1016/S0924-0136(00)00544-6.

[209] H.-W. Li, D.-J. Kang, M.G. Blamire, W.T.S. Huck, Focused ion beam fabrication of silicon print masters, Nanotechnology. 14 (2003) 220–223. doi:10.1088/0957-4484/14/2/323.

[210] A. Pander, K. Takano, M. Nakajima, A. Hatta, H. Furuta, Infrared properties of patterned CNT forest for metamaterials, in: 2016 IEEE Nanotechnol. Mater. Devices Conf., IEEE, 2016: pp. 1–2. doi:10.1109/NMDC.2016.7777129.

[211] M.S. Dresselhaus, A. Jorio, M. Hofmann, G. Dresselhaus, R. Saito, Perspectives on carbon nanotubes and graphene Raman spectroscopy, Nano Lett. 10 (2010) 751–758. doi:10.1021/nl904286r.

[212] M.S. Dresselhaus, G. Dresselhaus, A. Jorio, A.G.S. Filho, R. Saito, Raman spectroscopy on isolated single wall carbon nanotubes, Carbon N. Y. 40 (2002) 2043–2061. doi:10.1016/S0008-6223(02)00066-0.

[213] M.S. Dresselhaus, G. Dresselhaus, A. Jorio, A.G. Souza Filho, G.G. Samsonidze, R. Saito, Science and applications of single-nanotube Raman spectroscopy., J. Nanosci. Nanotechnol. 3 (2003) 19–37. doi:10.1166/jnn.2003.189.

[214] V.W. Brar, G.G. Samsonidze, M.S. Dresselhaus, G. Dresselhaus, R. Saito, A.K. Swan, et al., Second-order harmonic and combination modes in graphite, single-wall carbon nanotube bundles, and isolated single-wall carbon nanotubes, Phys. Rev. B. 66 (2002) 155418. doi:10.1103/PhysRevB.66.155418.

[215] M. Wąsik, J. Judek, M. Zdrojek, Polarization-dependent optical reflection from vertically aligned multiwalled carbon nanotube arrays, Carbon N. Y. 64 (2013) 550–552. doi:10.1016/j.carbon.2013.07.068.

[216] X.J. Wang, L.P. Wang, O.S. Adewuyi, B.A. Cola, Z.M. Zhang, Highly specular carbon nanotube absorbers, Appl. Phys. Lett. 97 (2010) 163116. doi:10.1063/1.3502597.

[217] S. Linden, C. Enkrich, M. Wegener, J. Zhou, T. Koschny, C.M. Soukoulis, Magnetic response of metamaterials at 100 terahertz., Science. 306 (2004) 1351–3. doi:10.1126/science.1105371.

[218] N. Feth, M. König, M. Husnik, K. Stannigel, J. Niegemann, K. Busch, et al., Electromagnetic interaction of split-ring resonators: The role of separation and relative orientation, Opt. Express. 18 (2010) 6545. doi:10.1364/OE.18.006545.